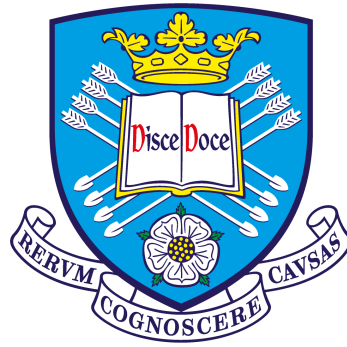


# **Investigation into the Effects of Pulsed Laser Sintering on Inkjet-Printed Functional Materials for Printed Electronics**



**Vimanyu Beedasy**

Department of Mechanical Engineering  
The University of Sheffield

This dissertation is submitted for the degree of  
*Doctor of Philosophy*

July 2021



”Il semble que la perfection soit atteinte non quand il n’y a plus rien à ajouter,  
mais quand il n’y a plus rien à retrancher.”

– Antoine de Saint-Exupéry



## **Declaration**

I hereby declare that except where specific reference is made to the work of others, the contents of this dissertation are original and have not been submitted in whole or in part for consideration for any other degree or qualification in this, or any other university. This dissertation is my own work and contains nothing which is the outcome of work done in collaboration with others, except as specified in the text and Acknowledgements. This dissertation contains fewer than 65,000 words including appendices, bibliography, footnotes, tables and equations and has fewer than 150 figures.

Vimanyu Beedasy  
July 2021



## **Acknowledgements**

First and foremost, I have to thank my industrial sponsors, Dr. David Anderson and Dr. Peter Choi, from FuseJet-3D for the invaluable opportunity I was offered. While it lasted for a couple of years, they have provided invaluable guidance and assistance within their means, for which I am grateful.

I would also like to extend my deepest gratitude to my supervisor, Dr. Patrick Smith, who has been a mentor, and more importantly a friend, throughout this journey which began at an even earlier stage. In spite of all the unpredictable years, both academically and personally, his patience, support and guidance has been paramount in my achievements today. I would also like to extend my sincere thanks to the Royal Exchange elites, who have, in many ways, been secondary supervisors at different stages of my research: Dr. Kamran Mumtaz, Professor Patrick Fairclough, Dr. Candice Majewski and her invaluable team comprising Ms. Wendy Birtwistle and Mr. Kurt Bonser. I very much appreciate the conversations with the colleagues at the D14 research office, which have ultimately sparked many research ventures.

I am also incredibly grateful to my teaching coordinator from the Advanced Manufacturing Technology at The Diamond, Mr. Martyn Aspinall, for all the invaluable opportunities for learning, teaching and development, whilst always bringing an enjoyable element to every session.

Getting through this journey required more than academic support, and I have been blessed with a very supportive family: my grandparents, my parents, my brother, and my sister. They somehow always believe and support me in various ways despite being separated by thousands of miles. I have reached here today thanks to the unconditional love and encouragement, in their own words, over the years.

More importantly, none of this could have happened without the incredible day-to-day support of my friends who stood by my side: Răzvan (for your wise words and being my *bro-in-crime*), Büşra (for the brightening joy you bring every.single.day), Cindy (for the warm companionship and kind-heartedness), Özgün (for the normality you bring in everyday situations, a quality I aspire to possess one day) and Karl & Ezra (for a friendship built upon dedication and perseverance).

The last year of this research coincided with the start of the COVID-19 pandemic which turned the world upside-down, but yet I am very grateful as it taught me many things other than independence and adaptation. I had taken many things for granted in this fast-paced world, but the abruptness of the lockdowns opened my eyes (and heart) to better enjoying the simpler things in life, with the people that matter the most.

”Et puis, il y a ceux que l’on croise, que l’on connaît à peine, qui vous dissent un mot, une phrase, vous accordant une minute, une demi-heure et changent le cours de votre vie.”

– Victor Hugo



## Abstract

Inkjet printing is a technology available since the late 90's, and has shown widespread adoption in various fields beyond graphics printing, including printed electronics due to the rising availability of functional materials such as metallic nanoparticle-based inks. However, the functional materials require some level of heat treatment, and recently, since the early 2000's, alternative methods of delivering that particular thermal energy have been explored, including the use of lasers for their ability to deliver localised thermal energy.

The thesis describes the novel use of pulsed laser sintering combined with inkjet printing of functional materials of a conductive nature (e.g. metallic nanoparticle-based silver and copper inks), with the aim of forming interconnects after laser irradiation. The printed copper patterns were successfully made conductive at ambient conditions by optimising the laser processing parameters, and also without showing any structural degradation of the substrate. Furthermore, thermo-sensitive substrates such as PET and paper were explored to demonstrate the novelty and feasibility of this alternative manufacturing method. The effects following the laser treatment on the printed patterns and the substrates were investigated, namely the electrical performance and mechanical properties such as the adhesion, morphology, heat affected zone and structural integrity.

It was found that the patterns achieved comparable electrical performance up to 38.7 % and 24.9 % bulk conductivity of copper and silver, respectively, on the thermo-sensitive substrates at ambient conditions. The adhesion was evaluated by an improved standardised test method which incorporated a digital perspective to eliminate subjective bias, and the samples were categorised as *3B* and above, hence targeting mid-range electronics applications.

The outcome of this innovative fabrication method was applied to a scenario where copper sensors in the form of multi-layer inductance coils were applied to carbon fibre actuators to detect strain for structural health monitoring purposes, and compared to commercially-available sensors. The results indicated superior performance of the inkjet-printed coils.



# Table of contents

<b>List of figures</b>	<b>xv</b>
<b>List of tables</b>	<b>xxi</b>
<b>Symbols</b>	<b>xxiii</b>
<b>1 Inkjet Printing: A background and prospects in the field of Printed Electronics</b>	<b>1</b>
1.1 Introduction . . . . .	2
1.2 A brief history . . . . .	2
1.3 Inkjet Printing Mechanisms . . . . .	5
1.3.1 Continuous Inkjet Printing . . . . .	5
1.3.2 Drop-on-Demand Inkjet Printing . . . . .	7
1.4 Current and emerging market trends . . . . .	11
1.5 The inclusion of Inkjet technology in Printed Electronics . . . . .	13
1.5.1 The added benefits of Inkjet technology to Printed Electronics . . . . .	16
1.5.2 Some challenges Inkjet Printing faces in Printed Electronics . . . . .	16
1.6 Motivation for Printed Electronics . . . . .	18
1.7 Questions and key points to address in the following chapters . . . . .	20
<b>2 Functional Inks and Sintering Mechanisms</b>	<b>21</b>
2.1 Functional Inks . . . . .	22
2.1.1 Survey of inks for Printed Electronics . . . . .	24
2.1.2 Functional ink formulation and rheology . . . . .	27
2.1.3 Theory and mechanics of drop formation . . . . .	30
2.1.4 Droplet-substrate interaction . . . . .	32
2.1.5 Goniometry . . . . .	34
2.2 Sintering Mechanisms . . . . .	36
2.2.1 Alternative sintering techniques . . . . .	38
2.2.2 LASER sintering . . . . .	41

2.2.3	Continuous wave and pulsed lasers . . . . .	44
2.2.4	Laser sintering in Inkjet applications . . . . .	46
2.3	Conclusions and questions to address in the next chapters . . . . .	48
<b>3</b>	<b>Combining Inkjet Printing and Pulsed Laser Sintering</b>	<b>51</b>
3.1	Materials . . . . .	52
3.1.1	Substrate compatibility . . . . .	55
3.2	Inkjet Printing . . . . .	56
3.2.1	Drop formation process and optimisation . . . . .	56
3.2.2	Pattern resolution . . . . .	61
3.3	Laser system . . . . .	63
3.4	Analytical methods . . . . .	69
3.4.1	Rheology: Viscometer and Circulation bath . . . . .	69
3.4.2	Contact angle . . . . .	70
3.4.3	Atomic Force Microscopy . . . . .	70
3.4.4	Spectrophotometry . . . . .	71
3.4.5	Scanning Electron Microscopy . . . . .	71
3.4.6	Conductivity comparison . . . . .	73
3.4.7	The ASTM F1842-15 Cross-cut test . . . . .	75
<b>4</b>	<b>Setting the baseline using conventional methods</b>	<b>83</b>
4.1	Experimental - Conventional thermal sintering . . . . .	84
4.1.1	Materials and methods . . . . .	84
4.1.2	Characterisation . . . . .	86
4.1.3	Results and discussion . . . . .	87
4.1.4	Conclusions . . . . .	95
<b>5</b>	<b>Pulsed Laser Sintering</b>	<b>97</b>
5.1	Experimental I - Pulsed Laser Sintering Investigation . . . . .	99
5.1.1	Materials and methods . . . . .	99
5.1.2	Characterisation . . . . .	102
5.1.3	Results and discussion . . . . .	103
5.1.4	Conclusions . . . . .	115
5.2	Experimental II - Adhesion Investigation . . . . .	117
5.2.1	Materials and methods . . . . .	118
5.2.2	Characterisation . . . . .	119
5.2.3	Results and discussion . . . . .	120

---

5.2.4	Conclusions . . . . .	133
5.3	Experimental III - Heat Affected Zone evaluation . . . . .	135
5.3.1	Materials and methods . . . . .	136
5.3.2	Characterisation . . . . .	137
5.3.3	Results and discussion . . . . .	138
5.3.4	Conclusions . . . . .	148
<b>6</b>	<b>Applications</b>	<b>151</b>
6.1	Introduction . . . . .	152
6.1.1	Magnetostriction . . . . .	153
6.1.2	Sensors . . . . .	154
6.2	Experimental Section . . . . .	155
6.2.1	Introduction . . . . .	155
6.2.2	Materials and methods . . . . .	156
6.2.3	Results and discussion . . . . .	166
6.2.4	Conclusions . . . . .	174
<b>7</b>	<b>Conclusions and Further works</b>	<b>177</b>
7.1	Conclusions . . . . .	177
7.2	Further works . . . . .	181
	<b>References</b>	<b>185</b>
	<b>Appendix A Chapter 3 Supporting Information</b>	<b>207</b>
A.1	Python script for pulse overlap % calculation . . . . .	207
A.2	Pulsed Laser Sintering station . . . . .	209
A.3	Optical Output Power vs. Current - 905D1S3J09UA . . . . .	211
A.4	Four Point Probe test station . . . . .	212
A.5	Sheet Resistance formula derivation . . . . .	214
A.6	Cross-cutter Assembly and Technical Drawing . . . . .	216
	<b>Appendix B Chapter 5 Supporting Information</b>	<b>219</b>
B.1	Pulse overlap variation analysis . . . . .	219
B.2	Heat Affected Zone RAW SEM data . . . . .	220
	<b>Appendix C Chapter 6 Supporting Information</b>	<b>223</b>
C.1	Summary of the fitted values for the change of inductance plots of each coil	223
C.2	Dimensions of the three inkjet-printed copper coils . . . . .	224



# List of figures

1.1	An extract from the original patent showing a drawing of the telegraph recorder by William Thomson. . . . .	3
1.2	Example of the Rayleigh instability. . . . .	3
1.3	An extract from Hansell's patent from 1946 which depicts the first drop-on-demand piezo-electric device. . . . .	4
1.4	Illustration of the two modes of operation of continuous inkjet (CIJ) printers. . . . .	6
1.5	Illustration of the three modes of operations of drop-on-demand (DOD) inkjet printers. . . . .	7
1.6	Illustration of the four piezoelectric mechanisms for drop-on-demand (DOD) inkjet printers. . . . .	9
1.7	A branch diagram of the classification of inkjet printers. . . . .	10
1.8	A comparison of the production of an intergrated circuit using photolithography and inkjet printing. . . . .	14
1.9	Chart showing the conductivity trends over the last decade of silver and copper patterns aimed at printed electronics . . . . .	19
2.1	Illustration of a time-dependent surface tension measurement for a fluid with a surfactant. . . . .	27
2.2	A graphical representation of the relationship between applied shear rate, shear stress and viscosity for different types of fluids. . . . .	28
2.3	Graph of the range of values for a fluid to be usable in a DOD inkjet system, highlighting the four scenarios which may occur in the event of improper selection of parameters. . . . .	31
2.4	Representation of the sequences involved from the moment of droplet impact onto a solid surface. . . . .	33
2.5	Analysis of the interfacial forces acting on a droplet on a substrate. . . . .	34
2.6	Illustration of the motion of the particles inside a droplet during evaporation, from the deposition of the droplet to the evaporation stage. . . . .	35

---

2.7	Effects of particle diameter on the melting point of gold nanoparticles and other metals . . . . .	36
2.8	An illustration of the different stages in thermal sintering of metallic nanoparticles. . . . .	37
2.9	Detailed description of a semiconductor laser and a typical emission curve.	43
2.10	Comparison between the output of a pulsed and a continuous wave laser. . .	44
2.11	Comparison between conventional thermal sintering and laser sintering. . .	49
3.1	Representation of the change of state for an amorphous and semicrystalline material under a change of temperature. . . . .	55
3.2	Stages of the acoustic wave propagation in a glass capillary for a piezoelectric drop-on-demand inkjet printer, and the typical waveform used for the droplet ejection process. . . . .	57
3.3	Typical waveform used for the generation of a droplet from a piezoelectric printhead. . . . .	58
3.4	Effects of controlling the applied voltage and duration of the applied voltage on the drop formation process, comparing a standard waveform and a triple pulse waveform for the droplet ejection process. . . . .	59
3.5	Effects of varying the applied voltage and pulse width of a piezoelectric printhead. . . . .	60
3.6	Effects of changing the droplet spacing on the drop density for a printed square array. . . . .	61
3.7	Effects of changing the drop spacing for a track. . . . .	62
3.8	Schematic of the pulsed laser sintering setup and the sintering mode. . . . .	64
3.9	Example of the pulse overlap variation. . . . .	64
3.10	Snapshot of the graphical user interface used for programming the laser sintering pattern. . . . .	65
3.11	A schematic of the custom-built pulsed laser sintering station. . . . .	66
3.12	A snapshot of the SV-1A viscometer and the circulating bath used for viscosity measurements. . . . .	69
3.13	A snapshot of the jetting station with a micro-syringe attached, and the relevant measurement window. . . . .	70
3.14	(a) A snapshot of the AFM used to quantify the thickness of the samples, and (b) the output of the analysis. . . . .	71
3.15	Snapshot of the application of the LUT image processing filter ( <i>mpl-viridis</i> ) used to highlight the region of interest, in this case the partially sintered area after pulsed laser irradiation. . . . .	72

---

3.16	A snapshot of the custom-built four-point probe test station used to quantify the conductivity of the samples, and technical specifications of the probes. . . . .	73
3.17	Snapshot of the multi-blade cutter purchased from an online retailer, highlighting the alignment of all the cutting edge of the blades and the blade angle. . . . .	76
3.18	Illustration of rendered 3D model of cross-cutter. . . . .	76
3.19	Snapshot of the in-house 3D printed cross-cutter. . . . .	77
3.20	Illustration of the cross-cut procedure and the 3-step process of evaluating the adhesion. . . . .	78
3.21	Classification of the different adhesion levels as a result of the cross-cut test. . . . .	79
3.22	Snapshot of the 3-step process of evaluating the detached area of the grid after the tape has been peeled off. . . . .	81
4.1	Optimised waveform for inkjet printing of the three different inks using the FUJIFILM Dimatix DMP-2831 printer. . . . .	85
4.2	Conductivity improvement as a function of temperature for the silver inks. . . . .	87
4.3	Conductivity improvement as a function of time for the silver inks. . . . .	88
4.4	Snapshot of the silver samples showing the colour change before and after heat treatment. . . . .	89
4.5	Result of the SEM analysis of the voids improvement of the silver inks as the sintering time increases. . . . .	90
4.6	Graphical representation of the change in particle size for each silver ink. . . . .	92
4.7	Graph showing the reduction in voids of the silver samples at optimum sintering conditions. . . . .	92
4.8	Surface topology from AFM analysis of the silver inks. . . . .	94
5.1	Jetting parameters and a droplet using the Microdrop MD-K-130 piezoelectric dispenser head. . . . .	101
5.2	Snapshot of the silver and copper nanoparticle-based inks following inkjet printing, prior to pulsed laser sintering, on all four substrates. Scale bar is 5 <i>mm</i> . . . . .	101
5.3	Absorption spectrum of silver and copper nanoparticle inks. . . . .	104
5.4	Graphical representation of the height profile of the laser sintered silver nanoparticle test sample on each substrate. . . . .	105
5.5	Graphical representation of the height profile of the laser sintered copper nanoparticle test sample on each substrate. . . . .	106

---

5.6	Snapshot of the silver and copper nanoparticle-based inks following pulsed laser sintering on all four substrates. Scale bar is 5 <i>mm</i> . . . . .	107
5.7	Bulk resistivity comparison of the inkjet-printed silver patterns after pulsed laser sintering. . . . .	108
5.8	Bulk resistivity comparison of the inkjet-printed copper patterns after pulsed laser sintering. . . . .	110
5.9	Example of unsintered regions due to a low pulse repetition rate and a high laser scanning speed. . . . .	111
5.10	Example of the pulse overlap variation, from no overlap to a large overlap, and the effects on the sintered copper nanoparticles. . . . .	113
5.11	Detailed SEM view of a partially sintered region after the pulsed laser fluence below the optimum sintering threshold, and a sintered region. . . . .	114
5.12	Snapshot and SEM observation of the ablation of copper nanoparticle ink as a result of a large overlap of 30 % between each row of sintered copper at optimum fluence levels. . . . .	114
5.13	Jetting parameters and a droplet using the JetLab piezoelectric dispenser head at room temperature. . . . .	119
5.14	Graphical representation of the different adhesion evaluation in terms of the detached area as a percentage of the total printed area for the copper nanoparticle-based ink printed on the four different substrates, as a function of the laser fluence variation. . . . .	122
5.15	Graphical representation of the optimum adhesion classification values and the variation shown with error bars on each substrate when sintered at the optimum laser fluence. . . . .	123
5.16	Representation of the comparison between a rough and smooth surface. . .	124
5.17	Snapshot of the contact angle of a drop of copper nanoparticle-based ink on the four substrates, highlighting the spreading of the ink on the surfaces. . .	126
5.18	Illustration of the different failure modes for a coating on a substrate. . . .	127
5.19	Design of experiment for the oxidation evaluation of pulsed laser sintered copper NPs. . . . .	128
5.20	Snapshot of the oxidised copper sample printed on paper which was left at ambient conditions for seven days, after which the pulsed laser sintering was performed followed by the cross-cut test. . . . .	129
5.21	Analysis of the different stages of sintering, crack formation, ablation, HAZ and failure on the PET substrate. . . . .	138

---

5.22	Analysis of the different stages of sintering, crack formation, ablation, HAZ and failure on the Kapton PI substrate. . . . .	140
5.23	Analysis of the different stages of sintering, crack formation, ablation, HAZ and failure on the paper substrate. . . . .	142
5.24	Results from the SEM analysis at laser fluence variation above the optimum sintering threshold, highlighting thermal and structural damage to the PET substrate. . . . .	143
5.25	Results from the SEM analysis at laser fluence variation above the optimum sintering threshold, highlighting thermal and structural damage in the form of cracks to the Kapton PI substrate as well as the vaporised deposits around the plume. . . . .	144
5.26	Results from the SEM analysis at laser fluence variation above the optimum sintering threshold, highlighting the ablation of the nanoparticles on the paper substrate at the irradiated area as well as the formation of a recast layer and vaporised deposits surrounding the plume, without any thermal or structural damage to the paper substrate. . . . .	145
5.27	Illustration of the heat affected zone (HAZ) created as a result of laser machining processes, showing the use of a continuous wave, and a pulsed laser.	148
6.1	Illustration of the domains in a ferromagnetic material. . . . .	153
6.2	Graphical representation of the various stages in the curing cycle of the carbon fibre laminates, and a snapshot of the vacuum bagging process. . . .	157
6.3	Snapshot of the three inkjet printed coils, the hand-wound coil, and an AMR sensor. . . . .	159
6.4	Illustration of the testing procedure of the carbon fibre samples on the bending jig. . . . .	160
6.5	Snapshot of the dual deposition system using the Jetlab IV printer from MicroFab Technologies. . . . .	161
6.6	Jetting waveform using the JetLab piezoelectric dispenser head at 40 °C for the copper and insulator ink, and a plot of the viscosity variation as a function of temperature. . . . .	162
6.7	Illustration of the process steps involved in the printing of each set of coils.	163
6.8	Emission spectrum of the Phoseon Firefly FF200 UV LED lamp, and the irradiance as a function of distance from the output window. . . . .	164
6.9	Snapshot of the laser sintering process for the monofilar_5n coil, highlighting the distinction between unsintered copper as a dark-brown coating, and sintered copper as a reddish-brown coating. . . . .	166

---

6.10	Graphical representation of the inductance response of each sensor on the bending jigs (300, 400, 500 & 600) when actuated with the different composite laminates containing the magnetic component. The results from the inkjet-printed sensors are in the first three rows (monofilar_5n, monofilar_10n and bifilar_5/5). . . . .	167
6.11	Graphical plot of the gradients for each sensor and actuator design from their inductance response. . . . .	169
6.12	Graphical representation of the size distribution of the iron and nickel particles used for impregnating the epoxy layer for the carbon fibre laminates. . .	170
6.13	Snapshot of printed copper coils showing the selective pulsed laser sintering of copper to only render the pattern printed on top of the insulator ink conductive. . . . .	171
6.14	Snapshot of a partially sintered copper coil as a result of a height variation. . .	172
6.15	Snapshot of the contact angle measurement for the copper nanoparticle-based ink printed on the cured insulator layer. . . . .	174
7.1	Flow chart of the process steps involved in the design of experiment for the “smart” CFRC samples. . . . .	183

# List of tables

1.1	A summary of the key drivers and trends and the relevance of inkjet to the field.	12
1.2	A comparison of inkjet printing with screen printing and photolithography, highlighting their key advantages and limitations. . . . .	15
2.1	A survey of the recent state-of-the-art results achieved using inkjet-printed functional silver and copper inks sintered using LASER (continuous wave, <i>cw</i> , and pulsed). . . . .	47
3.1	List of relevant properties of the different substrates used throughout the experiment. . . . .	52
3.2	Details of relevant properties of the different inks used throughout the research.	53
3.3	Summary of the pulse laser sintering parameters varied at 6000 <i>Hz</i> . . . . .	67
3.4	Summary of the pulse laser sintering parameters varied at 8000 <i>Hz</i> . . . . .	68
4.1	Summary of the results achieved using the three silver inks. . . . .	96
5.1	Results of AFM analysis of the test samples, showing the mean value of thickness. . . . .	104
5.2	Summary of the bulk conductivity values obtained when compared with relevant bulk metal at optimum laser sintering conditions. . . . .	115
5.3	Summary of the adhesion evaluation using image processing software, and the classification result based on the F1842-15 standard table. . . . .	121
5.4	Summary of the pulsed laser parameters used to sinter the copper nanoparticle ink on the four different substrates, the conductivity comparison and the adhesion classification. . . . .	134
6.1	Table summarising the laser processing parameters for sintering the copper nanoparticle-based ink on the paper substrate. . . . .	165



# Symbols

## Roman Symbols

$d$	Characteristic length
$I$	Current
$I_{th}$	Threshold current
$R_s$	Sheet resistance
$T_g$	Glass transition temperature
$V$	Voltage
$v$	Velocity

## Greek Symbols

$\beta$	Spreading ratio
$\delta\theta$	Angular broadening
$\delta_v$	Viscous boundary layer thickness
$\eta$	Dynamic viscosity
$\gamma$	Surface tension
$h$	Planck's constant
$\lambda$	Wavelength
$\omega$	Angular frequency
$\Omega$	Ohms

$\rho$  Density

$\rho_s$  Sheet resistivity

$\theta$  Contact angle

$\nu$  Frequency

### Acronyms / Abbreviations

CIJ Continuous inkjet

cw Continuous wave

DOD Drop-on-demand

FWHM Full Width Half Maximum

HAZ Heat affected zone

IJP Inkjet printing

IPL Intense pulsed light

MOD Metal organic decomposition

NPs Nanoparticles

$Oh$  Ohnesorge number

PC Polycarbonate

PEN Polyethylene naphthalate

PES Polyether sulfones

PET Polyethylene terephthalate

PI Polyimide

PMMA Polymethyl methacrylate

PPHM High modulus polypropylene

R2R Roll-to-roll

$Re$  Reynolds number

RFID Radio Frequency Identification

ROM Reactive organometallic

RSI Reactive silver

$We$  Weber number

Z Z number



# Chapter 1

## **Inkjet Printing: A background and prospects in the field of Printed Electronics**

### **Summary**

This chapter begins by first describing the inkjet printing (IJP) technique, diving briefly into its history and the relevant key points which made the technology rise to its current widespread adoption in research and industry. Then, the advances of inkjet printing beyond graphics printing are elaborated upon, with particular focus on printed electronics.

The application of inkjet printing in the field of printed electronics is then discussed; with a brief comparison with other printing techniques. A survey of some of the key drivers and trends of the printed electronics field is mentioned, followed by the advantages and challenges the inkjet technology faces in the field of printed electronics.

Finally, the chapter is concluded with the motivation for printed electronics which discusses the latest trends in printing conductive functional inks since the last decade, thereby highlighting areas of improvements, and ending with the questions which will be addressed in the following chapters.

This chapter has been published: (1) Beedasy, V.; Smith, P.J. Printed Electronics as Prepared by Inkjet Printing. *Materials* **2020**, 13, 704.

## 1.1 Introduction

Inkjet printing (IJP) is one of the most widely used methods of digital printing. It is a versatile manufacturing tool which has numerous applications in sectors ranging from graphics printing to printed electronics with a range of formats from high speed printing systems to small office printers. The features of an inkjet printing device allow the dispensing and precise positioning of tiny volumes of liquid (1-100 *picolitres*,  $10^{-12}$  L, equating to a droplet diameter of 62-288 *microlitres*,  $10^{-6}$  L) in the form of an ink on a substrate before transformation to a solid. Perhaps the most familiar is the commercially available desktop inkjet printer in the office or at home where pigmented ink (*cyan, magenta, yellow* and *black*) from a cartridge is deposited onto a sheet of paper to produce a readable text, or an image. In the last couple of decades, scientists have investigated applications beyond standard ink being printed on paper, and one example of this is “printed electronics”. The ability to investigate such an area of manufacturing is made possible by the advances in the deposition of functional materials [1], which is gaining an increasing amount of interest despite the core principles of inkjet printing being discovered over a century ago.

## 1.2 A brief history

In 1867, a patent [2] which was filed by William Thomson was granted and “marked” the course of history for the years to come. The patent described a technology which uses electrostatic forces to control the release of ink onto paper. Later in 1870, Thomson invented the telegraph recorder device [3] which can be considered the first application of in-situ ink deposition, and an application of his patented technology. The invention consisted of a marking needle such as a capillary tube, one end dipped into a stationary reservoir of fluid and the other freely suspended over a rotating spool of paper. Once the ink was drawn from the reservoir using electric force, the current caused the needle to move perpendicular to the motion of the spool, hence writing lines that translated to the intensity of the current. This method, as it made use of electrostatic forces, is considered contactless. The Figure 1.1 below is an extract from the filed patent [3] by Thomson which depicts the invention and the key components.

In 1873, Joseph Antoine Ferdinand Plateau, a Belgian scientist, published his book titled “*Statique expérimentale et théorique des liquides soumis aux seules forces moléculaires*” in which he described a phenomenon where a free stream of liquid will become unstable and will form periodic droplets. It was only five years later that Lord Rayleigh first modelled the instability of free-flowing liquid [4].

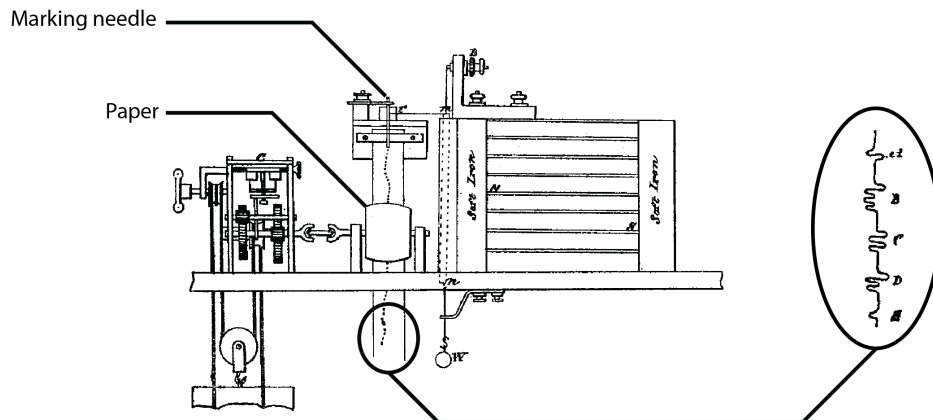


Fig. 1.1 A schematic drawing of the telegraph recorder by William Thomson adapted from the original patent [3], highlighting the marking needle hanging over the spool of paper. To the right is an enlarged view of the writing capabilities of the technology.

This phenomenon, known as the Plateau-Rayleigh instability [4] explains how a growth in sinusoidal perturbations of a stream of fluid causes differences in pressure waves, and in turn the production of small uniform droplets in a steady stream under the influence of surface tension – as shown in Figure 1.2. The Rayleigh instability, nowadays, is at the base of inkjet devices. Therefore, it can be said that the foundation concerning the basics governing ink jetting has been in place for more than a century.



Fig. 1.2 Example of the Rayleigh instability.

In the 1940's onwards, there have been some notable developments in contactless deposition technology using inks. In 1946 Clarence Hansell invented the DOD device at the Radio Corporation of America [5]. His invention, shown in Figure 1.3, made use of a piezo-electric quartz crystal which exerted the necessary force in the form of supersonic vibrational waves on the surface of the exposed liquid, hence producing a jet on demand. In 1951, Siemens patented a galvanometer [6] which had a similar working principle to the telegraph recorder invented by Thomson earlier, although it had a better sensitivity to the driving current, making it more accurate. Sweet in 1965 [7] combined electrostatics for the positioning of the droplets together with a gutter for deflection and line break, which resulted in the continuous inkjet printing system.

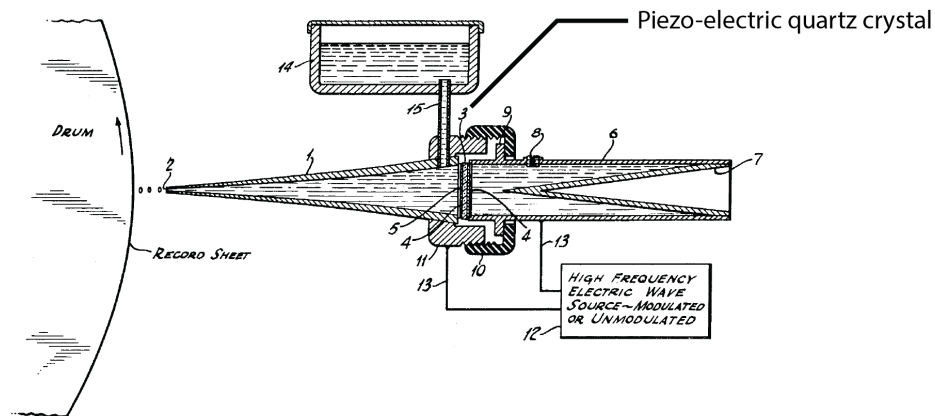


Fig. 1.3 An extract from Hansell's patent [5] from 1946 which depicts the first drop-on-demand piezo-electric device. The quartz crystal, located between the reservoir and the conical tube, strikes the liquid and causes a pressure wave to be formed, eventually leading to the ejection of a fine spray of liquid in the form of droplets.

It was not until 1971 when the first DoD device, the model 500 Typuter by Casio Company, was released, and comprised an electrostatic pull device [8] to produce drop-on-demand droplets. In 1977, Siemens came up with the first product, the PT80i, a dot-matrix printer which used 12 piezo tubes to create dots on paper [9]. The device, as expensive as it was at the time, not only offered a significant improvement in speed at 270 characters per second but was also noiseless. In 1981, the P2131 printhead was developed for the Philips P2000T microcomputer [10], and improvements in the printing system increased the droplet-ejection rate to 6,000 drops per second. This doubled the rate of printing compared to other DOD printing systems at the time. In 1985, Hewlett-Packard was the first company to introduce the "BubbleJet" – an inkjet printing technique which plays to the advantage of the expansion and contraction of an air bubble in a confined space owing to changes in temperature, resulting in a drop being forced out of the nozzle when required [9].

Over the course of history, the development of the inkjet printing technology has highlighted the following:

1. It is a method used to produce drops of small volumes ranging from picolitres ( $pL$ ,  $10^{-12} L$ ) to microlitres ( $\mu L$ ,  $10^{-6} L$ );
2. The drops are produced through differences in pressure waves in the fluid chamber;
3. There is a separation of a few millimetres ( $mm$ ,  $10^{-3} m$ ) from the orifice where the drops are ejected and the deposited surface, as such making it a contactless printing method;
4. The devices which make use of this technology are either continuous inkjet printers (CIJ) or drop-on-demand (DOD) inkjet printers.

The following section describes the two distinct categories of inkjet printing mechanisms and their current applications.

## 1.3 Inkjet Printing Mechanisms

### 1.3.1 Continuous Inkjet Printing

Continuous inkjet (CIJ) printing involves a continuous ejection of droplets onto a substrate, only in specified locations, when there is a demand for the ink as determined by the pattern to be printed. The remaining droplets which are not required are recycled through a gutter which pumps them back to the reservoir, as shown in Figure 1.4 below.

Depending on the drop deflection methodology, the jetting of the fluid can be controlled either by a binary or a multiple deflection system [11]. The binary deflection system (Figure 1.4(a)) relies on gravity and on the charging of the droplets. Upon ejection, the charged drops are deposited on the substrate where required, while the uncharged drops gravitate towards the gutter for recirculation. The droplets in the binary deflection system are only subject to a constant charge. In contrast, in the multiple deflection system (Figure 1.4(b)), the droplets are subject to varying charges to steer them to different positions on the substrate which allows for multiple dot positions per nozzle, and consequently much faster prints [12].

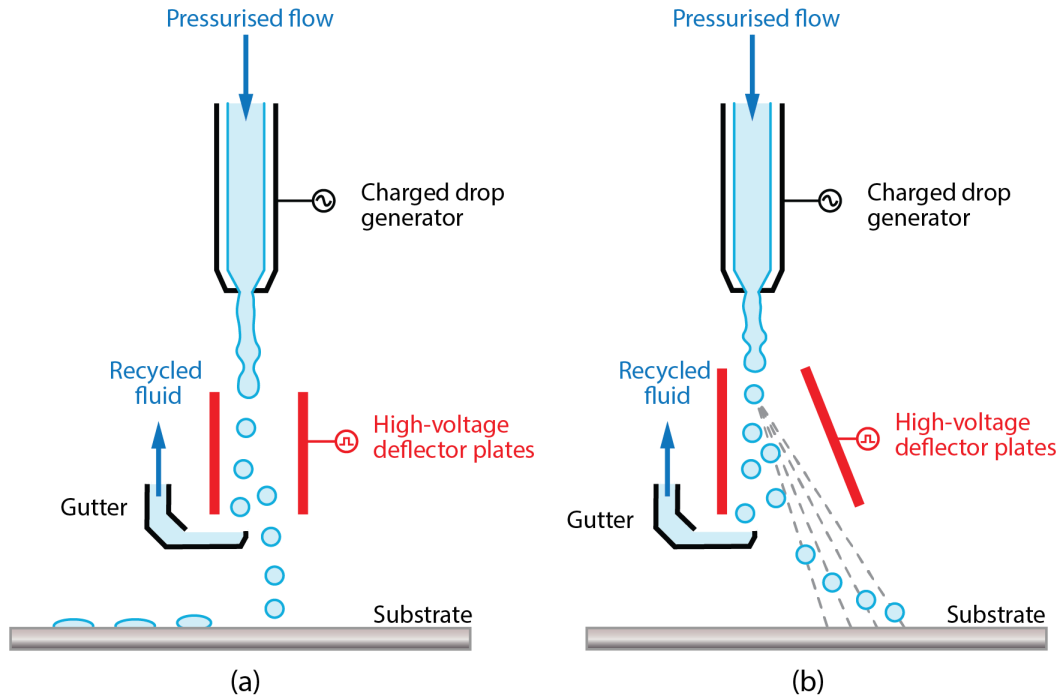


Fig. 1.4 Illustration of the operation of a continuous inkjet (CIJ) printer under the (a) binary deflection system; and (b) multiple deflection system. The stream of droplets is deposited onto the substrate (bottom), and those which are not required are deflected into a gutter.

CIJ printing systems have complicated hardware associated with their successful and reliable functionality, and risk contamination when recycling of inks is involved after exposure to the environment. This makes CIJ printing a potentially wasteful process, and for the reasons aforementioned the research industry has focussed on drop-on-demand inkjet printers [13–15]. However, for mass-production applications, CIJ systems are superior as their printing speeds are far greater than their DOD counterpart. CIJ printers operating at megahertz ( $MHz$ ,  $10^6$ ) frequencies are being investigated [16] with typical drop velocity at the nozzle greater than  $10\text{ ms}^{-1}$ . This allows for a relatively greater distance between the printhead and the substrate which is useful for industrial applications due to the bulkier machinery involved in high-speed production. On a final note, historically CIJ is renowned for the use of volatile solvents in fast-paced industrial applications where rapid drying is a critical advantage to minimise delays in production steps. However, the inconveniences such as the requirement for an electrically chargeable ink, the relatively lower print resolution and higher maintenance machinery have led to CIJ being perceived as not being an environmentally friendly print technology, and rather messy.

### 1.3.2 Drop-on-Demand Inkjet Printing

Drop-on-demand (DOD) inkjet printers have the ability to control the amount of ink they can deposit at a time. Owing to their principle of operation, DOD inkjet printers are more economical with ink usage than the CIJ printers. The mechanism of droplet formation and ejection behind each DOD printer is relatively simpler as compared to the CIJ printer. The drops are formed after the propagation of a pressure pulse throughout the fluid held in the capillary tube behind the printing nozzle. If this pressure pulse exceeds the minimum threshold for droplet formation at the nozzle, a drop is ejected. This minimum threshold for droplet ejection is discussed later in Chapter 2.1.3. The meniscus level is either controlled by the surface tension of the liquid or the static back pressure of the print head assembly. As compared to CIJ systems, the frequencies associated with DOD systems are normally in the range of 1 – 20  $kHz$  with resonance within the capillary tube strongly influencing the pressure pulse and drop formation according to Antohe [17]. Drop positioning is done by either moving the print head assembly over the fixed substrate at the desired location, or by moving the substrate under the printer nozzle. Drop-on-demand inkjet printers can be further categorised into three sections: *thermal* inkjet (or BubbleJet), *piezo-electric* inkjet and *electrostatic* inkjet based on the actuation method employed for the droplet formation from the print head [18]. Figure 1.5 is an illustration of the three types of DOD inkjet mechanisms along with the components which make them unique.

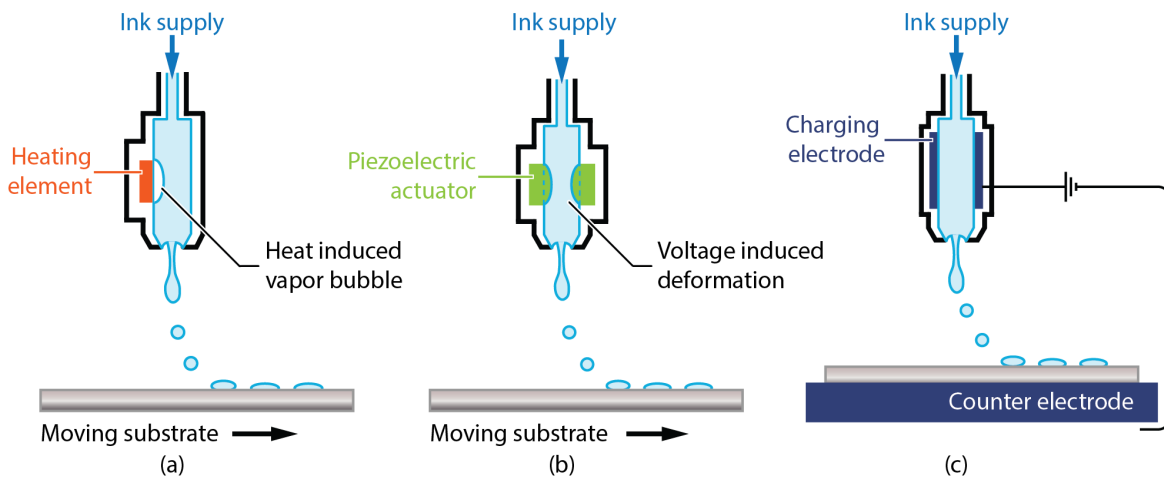


Fig. 1.5 Illustration of the operations of drop-on-demand (DOD) inkjet printers. In (a) the droplet is squeezed out of the nozzle by the formation of a bubble upon heating the ink to its vapourisation temperature; (b) the expansion-contraction cycle of the piezo-electric crystal causes the pressure wave to propagate and eject a droplet; (c) the droplet is ejected owing to the electric field generated between the print head assembly and the substrate.

In thermal DOD (Figure 1.5(a)), a small heater is located within the print head assembly inside the capillary tube which carries the liquid. When current flows through the heater, the liquid in contact with the heating element heats up to beyond its boiling point and forms a small vapour pocket (or bubble). When the heater is switched off, the liquid cools and contracts, hence causing the instant collapse of the vapour pocket. This rapid expansion-contraction cycle causes the formation of a pressure wave which is directly related to the formation of a drop.

The core component of piezo-electric DOD inkjet printers is a crystal (quartz or lead zirconate titanate), shown in Figure 1.5(b), which acts as an actuator. Upon the application of an electric pulse to the crystal, it expands and squeezes the capillary tube which contains the ink in such a way that it ejects a tiny amount of liquid in the form of a drop. When the electric pulse is removed, the crystal returns to its original shape and replenishes the capillary tube. The distinction between the crystal element being separated from the ink is advantageous as it allows a much wider range of inks to be used, and at the same time increases the lifespan of the print head. However, the cost of the print head and the software to control the core components is considerable, particularly when combined with the time required for the user to master the software interface for printing. Altogether, these contribute to an increase in the capital expenditure.

In the case of electrostatic inkjet (Figure 1.5(c)), the printing is controlled not only by the print head but also manipulated via both the nozzle and a translation stage, both of which are connected to a voltage. The electric field generated between them creates an electrohydrodynamic phenomenon that exceeds the meniscus' surface tension and causes ink to be ejected onto the substrate. This dual-controlled jetting mechanism enables the electrostatic inkjet printer to achieve nano-sized spots. However, this limits the range of inks which can be used as only conductive inks can be utilised for this type of inkjet printer [12]. The jetting position of ink on the matrix can be controlled by varying the electrical potential applied on the plate. This allows deposition of droplets much smaller than the orifice diameter, producing finer droplets of a sub-femtolitre ( $fL$ ,  $10^{-15} L$ ), volume than the piezoelectric inkjet printer [19], although the placement accuracy of the drops is inferior to other drop-on-demand inkjet mechanisms [20]. This technique has been demonstrated for a variety of materials such as  $THz$ ,  $10^{12} Hz$  planar metamaterials [21], 3D microbatteries [22] as well as metallic electrode materials [23].

For the scope of this research, only piezo-electric drop-on-demand printing is considered, mainly for its versatility and the small volume required. The ink need not be heated to its boiling point unlike thermal DOD, hence preventing degradation of functional material and the use of a wider range of solvents present in the ink. Moreover, the investment and

maintenance costs of an electrostatic DOD inkjet printer is considerably higher, and the printing method is still relatively in its infancy as compared to piezo-electric DOD inkjet printing [18].

There are four mechanisms behind piezo-electric droplet generation, which vary based on the distortion of the piezo-ceramic plate and include (a) squeeze mode; (b) bend mode; (c) push mode and; (d) shear mode; all of which are explained with the help of Figure 1.6 below [24].

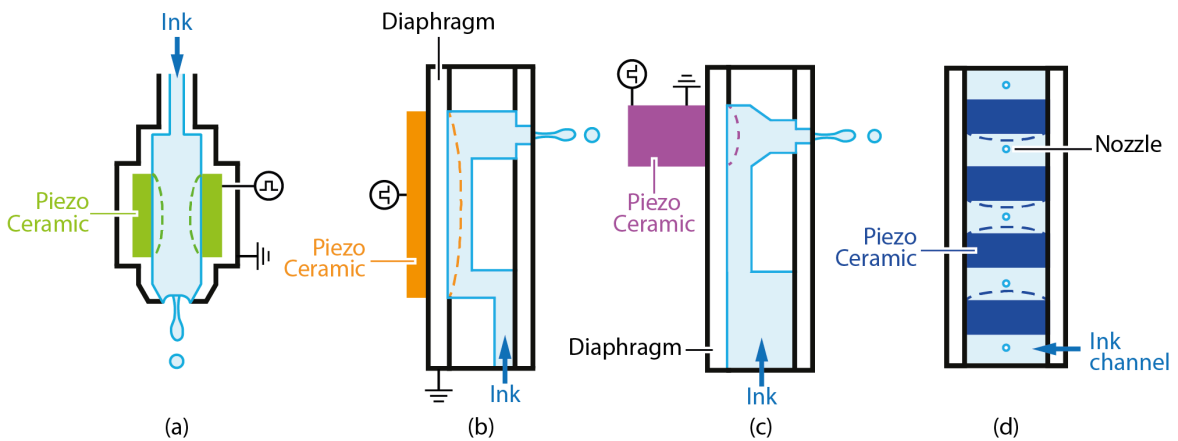


Fig. 1.6 Illustration of the different drop-on-demand piezo-electric mechanisms with (a) squeeze mode, (b) bend mode, (c) push mode and (d) shear mode.

The first, the squeeze mode (Figure 1.6(a)), comprises a radially polarised piezo-ceramic tube which surrounds the nozzle. Upon the application of a pre-determined voltage, the piezo-electric crystal squeezes the ink from the chamber. The squeeze method nowadays is mainly used in the Microdrop [25] and MicroFab [26] printing devices. The second, the bend mode (Figure 1.6(b)), uses the bending of the wall of the ink chamber to produce a droplet, and is common in Epson printers. The third, the push mode (Figure 1.6(c)), involves the piezo-electric element pushing against the ink chamber wall to eject a droplet, and is common in Trident, Brother and some Epson printers. In both the bend and push mode, the direction of the electric field and piezo-ceramic plate deformation are parallel [27]. In the fourth, the shear mode (Figure 1.6(d)), the electric field is designed to be perpendicular to the deformation of the piezo-ceramic plate. Nowadays, Xaar, Dimatix and Spectra printheads typically rely on this method of droplet ejection.

In all four modes, the applied voltage, the duration of the pulse and the orifice diameter influence the size of the ink droplets [12]. These print heads from different manufacturers each serve a specific purpose: Brother (*push mode*) and Epson heads (*bend mode*) are typically made for office desktop inkjet printers as they can deliver small drops, hence

high resolutions, at very high speeds using inexpensive heads. The Xaar (*shear mode*) and Trident (*push mode*) heads specialise in large scale applications as their heads can be customised for maximum adaptability to original equipment manufacturer (OEM) systems, hence minimising the development and production costs [28]. In addition to this, Xaar heads are stackable to create large printing multi-head blocks and reliable printing speed and resolution. The Microdrop and MicroFab heads (*squeeze mode*) are made for experimental and research purposes as they only have a single nozzle. Compared to other heads they are relatively slower, but the advantage lies in their flexibility and control in relation to the fluidic parameters of the chosen ink. This is significantly important in experimental research as this enables scientists to gain a better understanding of the droplet generation process from start to end.

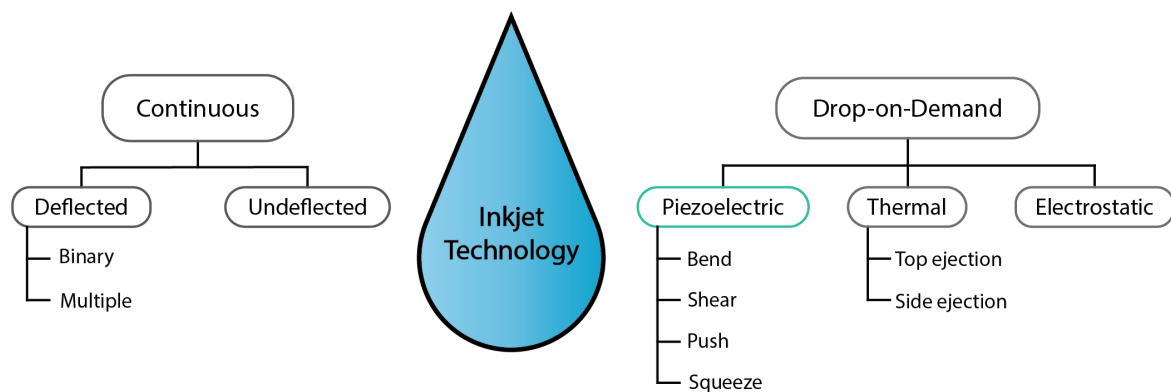


Fig. 1.7 A classification of widely popular and available inkjet printing technologies, adapted from [11]. The focus of the thesis will be on piezoelectric IJP technology.

Figure 1.7 represents a classification of the inkjet printing technology available nowadays. CIJ printers were a popular choice for high-throughput, high speed, low quality graphical application such as banners and textile printing but incur high investment costs to gain a sufficiently decent quality product. DOD printers were well-known for their better print quality which came at the cost of the print speed – although, this could be compensated with a multi-printhead assembly, but it came at an increased production cost. Thermal DOD inkjet printers dominate the graphical colour printing market nowadays [18], but they are limited to specific types of inks, especially because the rapid heating and cooling of the ink induces thermal stress on the ink. Printers which use **piezo-electric DOD** technology are more compatible with a variety of inks and solvents, hence are the preferred choice for scientific research purposes – which will be the focus of this thesis henceforth.

## 1.4 Current and emerging market trends

It is widely known that inkjet printing was first applied to graphics printing as a contactless, direct-write technology. The contactless aspect is valued for the highly minimised risk of ink contamination and being a direct-write driven approach does not require any masks, and the pattern to be printed can be switched rapidly from one to another. These two key criteria led to the implementation of IJP in various industries such as graphics, e.g. marking of packages, mail addressing, wide format posters, billboards, banners; and textiles for haute couture and decorations [29, 30]. In many cases, inkjet has replaced analogue manufacturing processes such as screen printing, gravure, spraying, dripping and roll coating. In more popular fields such as life sciences which receive increased resources and media attention, inkjet has been successfully implemented into tissue engineering [31], cell printing [32, 33], glucose biosensors [12] and proteomics [34]. With further advances in chemistry and material science [35], functional inks compatible with inkjet printers have been developed and opened the gateway to the field of printed electronics. Prior to the adoption of inkjet printers, the deposition of functional inks was done via spin-coating or screen printing. The earliest use of IJP in this area includes the work by Vest et al. [36, 37] for photovoltaic applications and microcircuits, but the resolution obtained did not compare to other manufacturing methods for printed electronics. The first comparable demonstration by Sirringhaus et al. [38] in early 2000s sparked interest in piezoelectric DOD inkjet producing a minimum functional feature size of 5 $\mu$ m after hydrophobic surface treatments. Since then, other ventures into electrical interconnects made using IJP on printed circuit boards (PCB) [39], radio frequency identification (RFID) tags [14, 40], sensors, liquid crystal displays (LCD) functional layers [41], solar panels [42, 43], transistors [44], antennas [45], and even batteries [22] have been made. Table 1.1 below provides a brief survey of the trends and market outlooks in this digital revolution, and how inkjet is implemented and made to cope accordingly.

Table 1.1 A summary of the key drivers and trends and the relevance of inkjet to the field.

Key drivers and trends	Role of inkjet
Big Data, Internet of Things (IoT), and digitalisation	Personalisation in the digital revolution is the new norm – QR codes connecting high-end consumers with brands in an interactive fashion, with links to product details, social media, virtual reality, etc. in real-time can be achieved via inkjet technology.
Digital printing and rapid prototyping	Inkjet allows for rapid customisation of three-dimensional products in an agile response to varying customer requirement. Additionally, inkjet eliminates the requirement for an inventory of masks, rolls, or screens for a quick turnover and a reduced footprint.
Non-impact printing	Inkjet can be used to print on delicate, irregular, and curved surfaces allowing for intelligent re-engineering of parts and processes for significant time and cost savings.
Sustainability	Inkjet minimises waste of costly material during printing and the use of harmful chemicals during post-printing processes, such as acidic solutions for cleansing the mesh used in screen printing. Consumers can be educated how to recycle responsibly through intelligent packaging.

## 1.5 The inclusion of Inkjet technology in Printed Electronics

In this digital revolution it is without a doubt that the field of electronics is gaining an increasing amount of interest and resources. Printed electronics is a field which comprises various fields of science and engineering to produce electronic devices and systems based on existing printing techniques such as gravure, and over the last decade it has proven to be a potential application of inkjet printing. Inkjet has the potential to significantly reduce the process steps through its ability to deposit materials in a spatially logical manner, which can greatly benefit the design process and overall reduce the cost of the producing electronics. To better illustrate the potential of inkjet, Figure 1.8(a) below depicts the process steps involved for producing an integrated circuit (IC) using the photolithography process, while Figure 1.8(b) depicts the manufacturing of a similar IC using inkjet technology. Prior to the start of each process, there are some additional steps involved in preparing the substrate through a combination of rinsing (water or a solvent such as acetone) and a drying step (using heat from an oven or clean compressed air).

During the photolithography process in Figure 1.8(a), the cycle can be described as such – (1) the functional material is deposited in a blanket layer typically via vacuum-based processes such as chemical vapor deposition [46] or physical vapor deposition [47]; (2) a photoresist coating is then applied; (3) the photoresist is then exposed to ultraviolet (UV) radiation through a mask; (4) the photoresist is then developed and the resist removed; (5) the remaining film is then etched away using chemicals in regions where the photoresist had been developed and a heat treatment is applied to “hardbake” the functional material; (6) the final coating of resist is stripped away to expose the now-patterned film. The finished film is then cleaned to remove any residual chemicals or coatings, and the process is repeated multiple times to create more complex integrated circuits. Steps (1) – (3) are additive by function, while the remaining steps (4) – (6) are subtractive. In contrast, the inkjet printing process depicted in Figure 1.8(b) is purely additive as it drastically reduces the steps involved: the functional ink is deposited at predetermined locations which conform to the pattern followed by a heat treatment operation.

The photolithography process is a subtractive manufacturing method since subsequent patterns are created through the removal of materials. Additional process steps are required to produce the final pattern as a result of subtractive manufacturing, which altogether increase the duration of the workflow, the expenditure and the equipment required. The environmental implication is also questioned given the wasteful approach of production as well as the use of harsh chemicals, which eventually need to be neutralised safely before disposal.

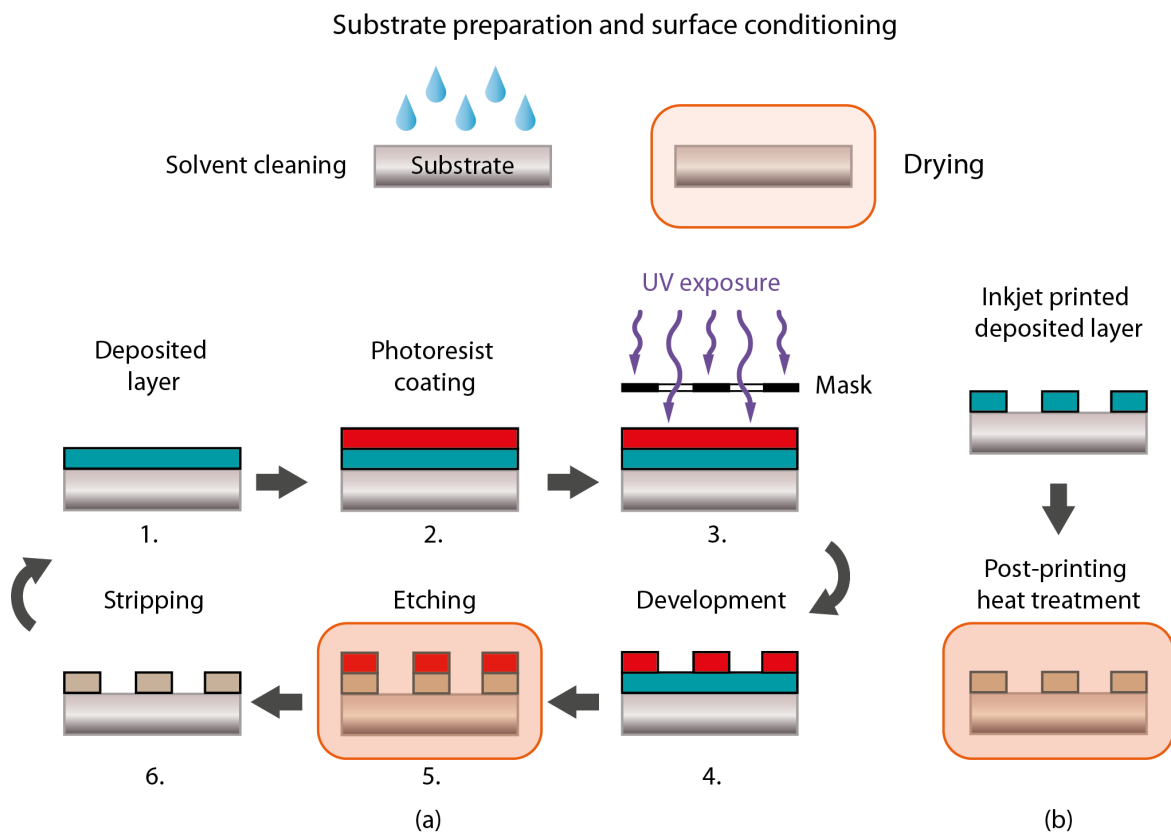


Fig. 1.8 An illustration comparing the steps involved in the production of an integrated circuit (IC) using (a) the photolithography process, and (b) a direct-write deposition technique such as inkjet printing. Note that the drying step in the substrate preparation, and step 5 in (a) and step 2 in (b) are heat treatment operations (typically 80 - 400 °C), indicated by a shaded translucent rectangle.

In comparison, the inkjet printing technology functions in an additive paradigm where the deposition of materials is carefully controlled locally, which means a predetermined amount of material is placed where desired. As such, through the inkjet additive manufacturing process, the number of steps per pattern has conceptually decreased from six steps to a single one. Table 1.2 provides a brief comparison of inkjet with screen printing on one end, and photolithography on the other end. The "duration" category describes the typical time taken to produce a printed pattern for printed electronics purposes.

On the lower end, during screen printing the setup cost is relatively low as the material used for the mesh is made out of polyester, which is a relatively cheap material in comparison to the materials used for making an inkjet printhead (glass, piezoelectric crystal, metal housing). Once a design has been selected, it is masked on the screen using a photo-sensitive lacquer which only develops selective regions determined by the pattern, thereby creating the stencil which can then be used for printing. A paste is then forced through the mesh to create

the pattern, although the resolution is relatively very low with the finest features of only a few *mm*. In comparison with inkjet printing, there is a limited choice of colours which can be used for screen printing, and colour gradients tend to add to the complexity of the process. Additionally, the stencil cannot be altered on the fly as compared to the inkjet printing process. Functional inks deposited using screen printing are relatively under-researched due to the high risk of contamination which can ultimately degrade the functional aspect of the ink or paste.

On the higher end, lithography is often seen as the premium printing process due to the extremely high printing resolutions down to a few *nm*, without creating any pixelation. However, the investment cost is relatively higher due to the requirement of an aluminium plate onto which the pattern is etched, as well as the setup and optimisation of the printing process which results in the production of waste material. While accounting for the print and dry time, the lead time to produce a completed pattern is relatively much longer as compared to inkjet printing, and there is little customisability once the aluminium plates are manufactured. However, the lithography process is highly adapted for functional inks, and manufacturers rely on this technique for producing integrated circuits.

Table 1.2 A comparison of inkjet printing with screen printing and photolithography, highlighting their key advantages and limitations.

	<b>Screen printing</b>	<b>Inkjet printing</b>	<b>Photolithography</b>
Cost	\$ 0.50 – \$ 5.00	\$ 0.50 – \$ 5.00	\$ 5.00 – \$ 500.00
Duration	Two days	Same day	Five days
Lifecycle	Limited print runs	Continuous coverage due to roll-to-roll expansion	Continuous coverage using rolls and high-resolution masks
Resolution	Minimum line width $\approx$ <i>mm</i> , $10^{-3}$ <i>m</i>	Minimum line width $\approx$ $\mu$ <i>m</i> , $10^{-6}$ <i>m</i>	Minimum line width $\approx$ <i>nm</i> , $10^{-9}$ <i>m</i>

### 1.5.1 The added benefits of Inkjet technology to Printed Electronics

One of the most significant advantages of inkjet printing is the scalability to match large-scale industrial manufacturing processes which involve a roll-to-roll (R2R) approach capable of reaching a printed coverage area of hundreds of square metres per hour – for example, the Fujifilm Acuity Ultra is capable of reaching a printed coverage area of up to  $400\text{ m}^2/\text{hr}$  using UV based inks. More realistically, at this current stage, the work done by Sowade et al. [48] explored the compatibility of R2R with inkjet-printed silver nanoink on a flexible substrate at printing speeds of up to  $1\text{ ms}^{-1}$ , which can be promising for printed electronics. The feed rate of the rollers is not limited by the inkjet deposition speed as an array of multiple printheads can be used, which altogether will drastically increase the throughput, lower the cost of production and the final-end product, and eventually allows for the exploration into a multi-layer integrated circuits [49, 50], and flexible circuits [51–53]. Being a contactless deposition technique, this can be further implemented to printing directly onto irregular surfaces with the proper machinery, thereby eliminating the need for intermediate process steps involving the use of stencils or adhesives. Overall, with the reduction in process steps and the controlled use of production materials, inkjet-printed electronics are one step closer to a more sustainable manufacturing technique.

### 1.5.2 Some challenges Inkjet Printing faces in Printed Electronics

The field of printed electronics consists of a range of products including ultra-high-end devices such as displays [54], computer processor hardware down to a feature size of  $10\text{ nm}$  [55] produced by lithography which inkjet is unable to compete with currently (except for mid- to low-end applications). These resolutions are produced with such a degree of precision that it guarantees the reliability and functionality of the devices. The inkjet printing technology, despite being reliable, is unable to achieve such a degree of precision even with intermediate process steps such as surface treatments [56], sacrificial coatings [57] or exploiting the chemical properties of inks [58]. To date, sub-nanometre precision matching the lithography process cannot be replicated via the inkjet printing technology. Additionally, the material deposited by inkjet technology does not match the surface finish as that produced via lithography techniques owing to surface roughness and overlap of interconnects, creating weak points in the printed pattern. This may eventually lead to charge leakage or electrical degradation at these locations, highlighting the inferiority of inkjet technology compared to ultra-high-end lithography processes.

One could argue the composition of the functional ink for deposition can be tailored to better improve the surface finish of the printed pattern, but this highlights the other limitation

of the inkjet technology which is the material. Some of the changes which must be made upon conversion of a screen printing ink include a significant decrease in viscosity [59], and, for inks of a particulate nature such as metallic nanoparticle inks, a decrease in particle size from orders of a few  $\mu m$  to  $nm$  [20]. These two ink properties are interconnected as a decrease in viscosity without reducing the particle size would lead to particle agglomeration, which would eventually clog the inkjet printheads. These requirements bear true to the creation of a functional ink for inkjet printing purposes and can be rather challenging as the sub-micrometre particles (metallic, ceramic, etc.) are not always readily or commercially available.

Rheological properties such as viscosity and surface tension have a crucial impact on the printability of the functional ink. The formulation of the ink needs to not only meet the printer requirements but also prevent damage to the printer itself. One of the parameters which can be modified is the viscosity of the ink – and this can vary depending on the printhead. An ink with a high viscosity generally above  $25\text{ cP}$  will be very difficult to print due to the requirement of a larger actuating waveform to eject a droplet, greater than the capabilities of a piezo-electric actuator, and can potentially damage the inkjet printing head, whereas one with a viscosity lower than  $1\text{ cP}$  will flow through the printhead and be rather difficult to print and control reliably. The surface tension of the ink needs to be accounted as it determines the drop formation process from satellites (low surface tension) to large droplets (high surface tension), and also the spreading on the substrate which, in turn, affects the resolution and surface roughness of the pattern.

Semiconductor inks are highly desired for printed electronics but given the high expectations such as the desired high charge mobility crucial for efficient transistors (the higher the charge mobility the faster the switch in a transistor), this narrows the choice for semiconductor materials. Inorganic semiconductor materials such as carbon nanotubes have recently been developed and demonstrate substantial performance improvement over existing semiconductor materials, but the challenge remain in getting a printable ink at a competitive price [60].

## 1.6 Motivation for Printed Electronics

Functional inks often require a form of heat treatment after being printed to improve the characteristics of the final pattern, which can either be the electrical properties, mechanical structure, surface finish or a combination. The chemical composition of the ink is crucial for successful and reliable printing, and at the same time prevent the conducting components from agglomerating. For example, in functional inks with a conducting element such as a nanoparticle-based silver ink, the dispersant maintains the separation of the nanoparticles and upon a thermal energy input, the heat incites the consolidation of conductive pathways for the flow of electrons, and hence the conduction of electric current. This process is called sintering and must not be mistaken for curing. For inks composed of particles, curing relates to the process by which the particles lose their organic shell and exhibit a conductive behaviour upon direct physical contact. This curing process takes places at a temperature determined by the flash point of the organic additives in the ink [61], which is lower than the melting point of the particles. Sintering, in contrast, occurs at a higher temperature after all the organic components in the ink have been burnt off and a combination of particles growth and grain-boundary relocation, also known as necking, begins. The method of application of heat can vary significantly, ranging from hot plates or convection ovens [62–65], microwaves [66, 67], radiation in the form of UV exposure [68] or LASER [69–71], electric current sintering [72, 73] and even high temperature plasma sintering [74]. There have also been reports of the use of chemicals for the sintering process [75, 76]. Some of these conventional methods such as using a convection oven and chemical sintering have been thoroughly researched, are very well-established and are currently being used for industrial applications, while others such as microwave, plasma and electric current are still in their infancy and require thorough research before implementation. In the last few decades, advances in LASER physics have improved our understanding and reliability on lasers and have since been increasingly targeted for implementation in manufacturing processes. Figure 1.9 below represents the conductivity trends over the last decade, starting from the well-established conventional oven sintering, and notable ventures in alternative photonic sintering techniques using intense pulse light or LASER. Some of the notable improvements in conductivity of silver are described in the work by Jahn et al. in 2010 [77], followed by Halonen et al. in 2013 [78] and Black et al. in 2016 [79] with 40 % bulk conductivity of silver and above reported. The work by Balliu et al. in 2018 [80] reported 26 % bulk conductivity of silver by using laser sintering. In terms of copper, Kang et al. in 2010 [81] reported superior conductivity values of copper using an oven, followed by Zenou et al. in 2013 [82] and Niittynen et al. in 2015 [83] who both used alternative photonic sintering methods.

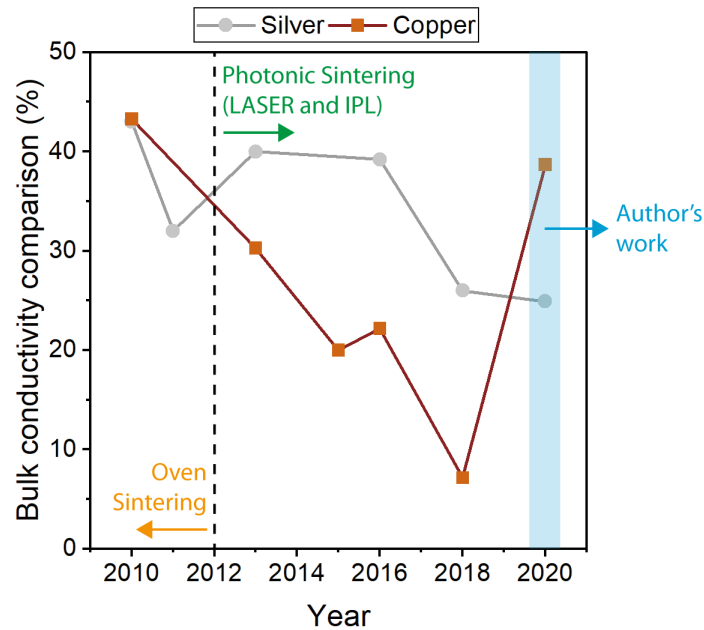


Fig. 1.9 Chart showing the conductivity trends over the last decade of silver and copper patterns aimed at printed electronics. The region in highlighted in blue shows the author's contributions to the research field.

The recent increased research output into LASER sintering with inkjet printing of functional inks has highlighted grounds for further investigation. As such, the focus of the thesis lies in the investigation of LASER sintering with inkjet-printed components for printed electronics applications.

Despite the niche market of ultra-high- and high-end electronics made by complex photolithography processes where inkjet printing lacks the capabilities to challenge, the mid- to low-end electronics markets can benefit from a boost in manufacturing and expansion to printed electronics. Electronic systems fabricated using IJP can benefit from a reduced cost per unit area, particularly with high throughput roll-to-roll processes as demonstrated by Grubb et al. [58] and Sowade et al. [48]. This can be further expanded to flexible and stretchable electronics which Huttunen et al. [84] investigated using a stretchable silicone substrate. The mid- to low-end printed electronics market which shows promises includes, and is not limited to, sensors and integrated smart systems (smart labels, temperature monitoring, health monitoring systems, etc.) which require layers of sensing material which can be printed onto substrates of varying mechanical and elastic properties; RFID communication devices with links to the Internet of Things (IoT); flexible OLED displays where waste reduction and management is crucial during the manufacturing process; and, more importantly, printed transistors which comprises conductive electrodes, semiconducting channels and an insulating gate dielectric [44, 85].

## 1.7 Questions and key points to address in the following chapters

Inkjet printing has proven benefits and has been adopted in many large-scale manufacturing processes as a replacement for lithography, for example in the making of optical elements such as lenses [86, 87], electroluminescent devices [88], and organic light emitting devices [89] to name a few. Prior to their adoption, these manufacturing processes had been rigorously trialled and tested to be reliable and provide cost-saving opportunities to the industry. Hence, for IJP to set foot in additional areas of manufacturing such as printed electronics, there are many factors which need to be understood and proven reliable, and the post-printing heat treatment operation is a major one. The simple traditional method of applying heat by placing the pattern in an oven has proven benefits, but the major drawback is the limitation of the substrate as the latter must withstand thermal damage during that lengthy heat treatment process. High temperature-tolerant substrates such as polyimide can withstand temperatures of up to 400 °C whilst maintaining their robust mechanical properties and flexibility, but are expensive compared to other polymeric substrates such as polyethylene terephthalate (PET) and polyethylene naphthalate (PEN) which have a lower heat tolerance (glass transition temperature of PET and PEN are 70 °C and 120 °C, respectively). This drives the research focus for alternative sintering methods which are better able to direct the applied energy towards the printed pattern, limiting any thermal damage to the substrate.

LASER sintering is a promising field, particularly after the recent advances in the industry which improved the understanding, control, and reliability on the LASER processing parameters. This method of irradiating the printed pattern has attained a proof-of-concept stage and requires additional resources and research into an in-depth study between the interaction of radiation and the printed pattern.

Hence, the focus of this thesis lies in the investigation of laser sintering inkjet-printed components, with a focus on printed electronics patterns. Functional inks of a conductive behaviour such as copper and silver nanoparticle inks are focussed on given their attractiveness to the mid- to low-cost manufacturing. Some of the questions which can be asked at this stage include:

1. Can laser sintering be done on inkjet-printed metallic nanoparticles to form thin films?
2. Does the thin film experience any damage during the laser sintering process?
3. What are the effects of the laser sintering process on the printed pattern, and also the thin film?

## **Chapter 2**

# **Functional Inks and Sintering Mechanisms**

### **Summary**

In this chapter, functional inks and their interaction with a variety of substrates are investigated. First an overview of inks used for inkjet purposes is provided, then follows a brief overview of the categories of inks used for printed electronics, with more focus laid on conductive inks. The formulation of a functional ink is discussed in detail, and also compared to the quantifiable theory in literature which has been used as a guide for years, albeit not relied upon fully. The droplet deposition process is also discussed in relation to its influence on the performance of the functional ink and geometry of the printed pattern.

The next section dives into the sintering process for printed electronics, defining the term and using an illustrative approach to explain the process. Some of the most recent works of sintering inks for printed electronics applications using alternative methods to conventional thermal sintering are discussed. The focus of this section is then shifted towards laser sintering due to its recent success, yet lack of understanding in the interaction with the printed patterns. A brief explanation of the principle of operation of a laser is given, after which a review of some of the most recent works using laser sintering is presented.

This chapter concludes with questions surrounding the use of pulsed lasers for manufacturing processes, and their potential inclusion for the post-processing of inkjet-printed functional materials. The areas seeking further investigation such as the mechanical and electrical performance of the laser sintered features are highlighted, with the aim of being investigated in the next chapters.

## 2.1 Functional Inks

Inkjet printing as a technique is a reliable direct-write method of depositing an ink on a surface. In the case where a typical desktop inkjet printer is not performing, a closer look will reveal that it is most likely the ink which is misbehaving instead of the printhead system (unless there is a paper jam, in which case the carriage of the printer itself is faulty). There are many factors which influence the printing performance of an ink, therefore setting the bar for the requirements of an ink to be very high. For graphics printing at home or in an office, the typical requirements for such an ink generally involves a long shelf life (home users replace an ink cartridge between two to six times a year), stability at a range of temperatures and humidity, and more importantly an accurate colour rendition on paper (which relies on the quality of the pigments in an ink). Therefore, when formulating an inkjet ink for graphics printing, the chemical composition of an ink is the determining factor for reliability.

Nowadays, inkjet printing has evolved from graphics printing for the home user to more advanced printing processes, such as printed electronics, which require specially formulated inks comprising a functional element. This trend towards functional inks can be attributed to advances in nanoscience material technology, enabling a more widespread range of materials of different sizes and properties to be more commercially available. These inks for printed electronics consist of an electrically relevant component which has one of the following properties:

- (i) conducting;
- (ii) semiconducting;
- (iii) dielectric;
- (iv) insulating.

Consequently, functional inks have more requirements to fulfil and can make their synthesis a more complicated process. There has been an increasing amount of novel materials of sub-micrometre and nanometre dimensions that have been discovered in the last few decades, and prompted a revised classification mechanism proposed by Pokropivny and Skorokhod [90]. This revised classification includes *0D*, *1D*, *2D* and *3D* materials which conform to certain nanostructures, explained below:

### *0-D* (zero-dimensional)

Zero-dimensional materials are those which conform to the nanoscale ( $nm$ ,  $10^{-9}m$ ). In recent years, physical and chemical micro-manufacturing processes have produced well-defined materials which conform to the *0-D* scale, such as quantum dots and nanoparticles of less than  $100\text{ nm}$ .

### *1-D* (one-dimensional)

One-dimensional materials include materials outside the nanoscale, such as nanowires, nanorods, nanotubes, etc. They are commonly used in the layering of interconnects for printed electronics (displays, solar cells) and security printing [91].

### *2-D* (two-dimensional)

Two-dimensional materials are those which exhibit plate-like shapes, such as nanoplates (graphene), nanodisks, nanowalls, etc. These class of materials are key to the understanding the mechanism of nanostructure growth and are the prime choice to investigations into developing novel sensors and other 2D structures of materials [92].

### *3-D* (three-dimensional)

Three-dimensional materials have been reported to have a well-defined structure and morphology, and, due to their larger surface area to volume ratio, create large absorption sites for molecules at distinct microscopic locations [93, 94], with applications in the transport of molecules due to their inherent porosity in three dimensions [95].

The synthesis of nano-dimensional materials is of great interest due to their inherent novel physical and chemical properties which differ from their larger dimensional bulk counterparts. There are many methods of synthesis, many of which are still under investigation, that can be split between physical and chemical processes. The physical synthesis process is advantageous due to its eco-friendliness, although the chemical synthesis process produces materials that can be refined into a final end product and have a good chemical homogeneity. However, there are additional process steps to filter the by-products at the end of the chemical synthesis process, which altogether increase manufacturing costs and duration. For an in-depth review of the synthesis of each type of nanomaterial, the reader is directed toward the article by Tiwari et al. [96].

In this chapter, inks for printed electronics will be discussed, with a particular focus on zero-dimensional nanoparticle inks as they are the most commonly used materials for printed electronics, particularly for inkjet printing purposes. Functional inks of a conductive behaviour will be focussed upon.

### 2.1.1 Survey of inks for Printed Electronics

This section provides a brief overview of the use of each category of functional ink used for printed electronics purposes from an inkjet printing perspective.

#### Conductor inks

Conductor inks can be of a metallic suspension, metallic solution, polymer or carbon based. The most commonly used inks of this category for printed electronics are metallic-based nanoparticle inks (zero-dimensional) due to their vast availability. The important advantages of metallic-based inks are their stability over a range of storage and printing conditions, and the high loading of the ink (generally between 30 – 40 *wt. %* of particulate material) which results in more conductive material being deposited per pass. In addition to nanoparticulate materials, nanowires (one-dimensional) have also been used for printed electronics due to their similar advantages, but are less favoured for inkjet printing purposes due to their high aspect ratio and lower volume fraction which may cause printability issues and require multiple passes to produce an electrically conductive pattern. Metallic nanowires exhibit better mechanical performance when subjected to tension, torsion, bending or compression due to their ductility [97], hence are the preferred material for flexible and stretchable electronics [98, 99]. Other types of metallic inks can be solution based such as metal-organic decomposition (MOD) inks where a metallic salt is dissolved in a solvent, resulting in a solution free of particulate matter. Upon deposition, the post-processing step (heat treatment) is used to “activate” the metal compounds which become conductive. The use of a metallic solution for inkjet printing eliminates any blockages in the printhead, and generally the loading of MOD inks is inferior to nanoparticle-based inks.

#### Choice of metal for ink formulation

In terms of which metal to use, the choice is primarily dictated by cost, performance, and ease of handling. Silver, although the most conductive of metals, is expensive, whereas copper, which is much more affordable, often requires a controlled atmosphere in order to prevent the formation of copper oxide. In terms of bulk resistivity, silver has the lowest,  $1.59 \times 10^{-8} \Omega \cdot m$ , copper has the next lowest  $1.72 \times 10^{-8} \Omega \cdot m$ , then gold  $2.44 \times 10^{-8} \Omega \cdot m$ . Even though these three metals have excellent values of conductivity, when the cost of the metal is factored in the decision, the choice becomes more complicated. Gold (as expected is most expensive) costs about a thousand dollars per ounce, silver

is about twenty dollars an ounce, whereas copper is only about twenty cents an ounce. Other metallic based inks have been researched, such as aluminium (resistivity of  $2.82 \times 10^{-8} \Omega \cdot m$ , and about ten cents per ounce), although it undergoes even faster oxidation than copper to form a thick, non-conductive aluminium oxide layer. This makes the ink formulation more complex and less stable, as compared to formulating printable copper nanoparticle inks [100]. Nickel (resistivity of  $6.99 \times 10^{-8} \Omega \cdot m$ , about fifty cents an ounce) has also been considered as a metallic-based ink for printing conductive patterns [101], and metal oxides such as Tungsten oxide [102, 103] (about five dollars an ounce) and Zinc oxide [104, 105] (about fifty dollars an ounce) are also being investigated for printed electronics applications.

Polymer-based conductor inks for printed electronics are favoured for applications where optical transmission is a key criterion. The most common type is Poly(3,4-ethylenedioxythiophene):polystyrene sulfonate (PEDOT:PSS), which is commonly used for inkjet applications and in roll-to-roll (R2R) manufacturing of displays as the optimised formulation of the ink has an optical transparency of around 80 % [106], although recent reports mention an optical transmittance of above 90 % for ultra-thin coats of PEDOT:PSS [107], making it extremely suitable for interfacial layers of optoelectronics devices. Printed PEDOT:PSS films are also chemically stable and structurally elastic [108] and biocompatible, making them another candidate for flexible, stretchable and wearable electronics [109, 110]. Other polymer-based conductor inks include polyaniline (PANi) [111] and polypyrrole (PPy) [112], and they have been explored with similar endeavours due to their superior flexibility to metallic based inks, low-cost and biocompatibility [113].

A third category of conductor inks is carbon-based, where graphene is the most commonly used conductor ink for applications in printed electronics. As an allotrope of carbon, graphene (two-dimensional) has been of peak research interest in the recent decade due to its distinctive electrical, mechanical, and optical capabilities. The high charge mobility of graphene makes it an ideal candidate for nanoelectronics in high-frequency applications [114], and due to the unique mechanical properties, they have been reportedly used in nanomechanical sensors [115, 116], thin-film transistors [117], conductive composites and electrodes [118]. Recent reports have also demonstrated graphene being combined with PEDOT:PSS for biocompatible applications [119]. Despite the superior elastic and biocompatible properties of polymer-based conductor inks, their inherent electrical performance does not match metallic or carbon-based conductor inks.

### Semiconductor inks

Semiconductor inks can be of either an organic or inorganic nature, with the main difference being in their charge transport mechanism. For inks of an organic nature, the charge transport mechanism is based on the charge carriers “hopping” between localised states, while for ink of an inorganic nature the charge carriers move in wide delocalised planes. The interest for organic inks is based on the fact that they are biodegradable, cheaper, and easier to fabricate as compared to inorganic inks which have a more rigorous and sensitive processing condition, but results in more stable inks. Some organic semiconductor inks which have been reportedly used for printed electronics applications include PBTTT – Poly(2,5-bis(3-alkylthiophen-2-yl)thieno[3,2-b]thiophenes [120], TIPS-Pentacene [121], P3HT – Poly(3-hexylthiophene) [122] and DH4T –  $\alpha$ ,  $\omega$ -dihexylquaterthiophene [123]. As for the inorganic semiconductor inks, the most popular and reliable ones are silicon-based [124], although due to the recent interest in flexible electronics, other formulations have been explored including carbon-based (graphene or single-walled carbon nanotubes) [125, 126] or ionic metal oxides [127] as a base.

### Dielectric inks

Dielectrics are a key component in thin film capacitor and transistor circuits as they are used to maintain an electrostatic field between the conductor layers while minimising heat loss. In printed electronics, the dielectric layer is in the form of a printed polymer film as compared to solid ceramics or metal oxides in large scale applications. The most commonly available dielectric used in thin film transistors (TFTs) is crosslinked PVP – poly(4-vinylphenol) [128], PMF – poly(melamine-co-formaldehyde) and PGMEA – propylene-glycol-monomethyl-ether-acetate [129, 130].

### Insulator inks

Insulator inks play a vital role in ensuring the proper function and durability of printed electronics, particularly when two or more stacked or adjacent layers are involved. Insulator inks prevent cross-talk between different charge carriers and can also be used as an encapsulating layer to prevent damage or contamination from external sources. The most commonly used insulator in printed electronics is SU-8 [131–133]. Another silicone-based encapsulating agent which doubles as an insulating layer is PDMS – polydimethylsiloxane, and it has reportedly been used in several studies involving printed electronics [98, 134, 135].

### 2.1.2 Functional ink formulation and rheology

To guarantee the superior properties of functional inks over regular dye-inks for at-home inkjet printers, there are several parameters associated with the rheology of an ink, that is, the science involving the flow characteristics of the fluid including its behaviour under stress (during printing), which must be carefully tailored. Some of the rheological parameters include the surface tension and viscosity, and for functional inks the solid content, particle size and shelf life must be also addressed.

#### Surface tension

The surface tension of an ink is an important criterion to consider for the droplet formation process and the interaction with the targeted surface once deposited. It is defined as the work required to expand a surface by a certain amount, due to direction dependent forces of molecules residing at, or close to, the interface. The surface tension can be tailored by the addition of surfactants and a careful solvent composition. Surfactant can contain either hydrophobic or hydrophilic substances which affect the molecules at the surface or interface. For example, to improve the “wetting” of a fluid on a surface, surfactants which lower the surface tension are used. Surface tension measurements can be either static or dynamic. For a static surface tension measurement, the value of the measurement method is associated with the thermodynamic equilibrium independent of time, as compared to the dynamic surface tension which refers to a particular surface at a given time. In the case where a new surface is formed (during a drop formation process, or the spreading of a drop on a surface), the dynamic surface tension must be considered when a surfactant is involved. Figure 2.1 below shows the change from static to dynamic surface tension for a fluid containing a surfactant. While the surfactant is dispersed inside the fluid, the dynamic surface tension is much higher and decreases until equilibrium as the surfactant is adsorbed at the surface.

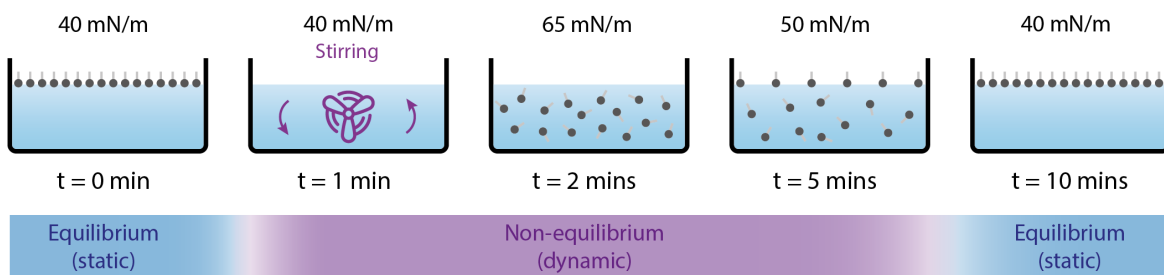


Fig. 2.1 Illustration of a time-dependent surface tension measurement for a fluid with a surfactant, showing the progression from static to dynamic surface tension due to the diffusion and adsorption of the surfactant.

## Viscosity

Viscosity is a parameter which mediates the flow of a fluid, and for inkjet printing this parameter is critical as it determines the flow through a nozzle. It is affected by factors such as the solvent composition, concentration of additives, surfactants, and flocculation. Most inkjet inks are Newtonian, i.e. their viscosity is constant over a range of shear rates. However, inks which contain additives can change this behaviour in a way that the viscosity varies as a function of the applied shear rate. This behaviour is termed “non-Newtonian” – a fluid where its viscosity decreases with an increased shear rate is called “pseudoplastic, or shear-thinning” whereas one where its viscosity increases as the shear rate is increased is called a “dilatant, or shear-thickening”. This is due to the structural reorganisation of the fluid molecules during flow, which is not always uniform as compared to Newtonian fluids where the reorientation of the molecules is symmetrical in shape and properties. An exception to these categories is a “Bingham plastic” fluid which requires a minimum shear stress before it flows, only after which it behaves as a Newtonian fluid. An example of such a Bingham plastic fluid is mayonnaise. Figure 2.2 below is a graphical illustration of the different types of fluids discussed above.

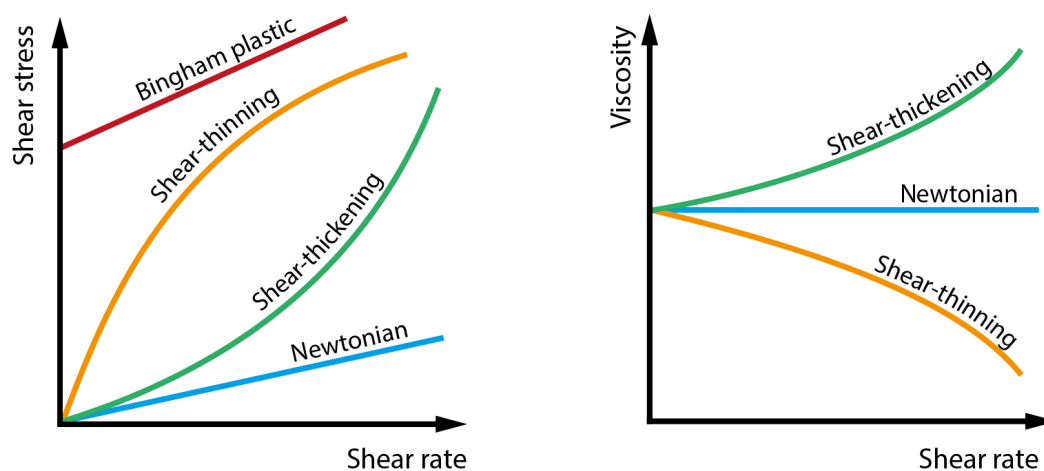


Fig. 2.2 A graphical representation of the relationship between applied shear rate and [left] shear stress and [right] viscosity for different types of fluids.

Typically for inkjet applications the viscosity of fluids is in the range of between 5 – 20  $cP$ , depending on the method of drop ejection (up to 3  $cP$  for thermal drop-on-demand). The particle content of an ink may also cause a change in viscosity due to the flocculation of particles, hence a balance between loading, viscosity and surfactant content must be maintained.

### **Solid content and particle size**

Particulate content in a functional ink must be carefully controlled in terms of mass or volume fraction as it directly affects the rheological properties of the ink. Generally, a high particle content in an ink increases contact between the particles, although they are more susceptible to agglomeration which can cause printability issues such as clogs in a printhead during jetting. In addition to the amount of particles present in the ink, the size of the particle must be given adequate consideration. Generally, the size of the particle present in the ink must be at least twenty times smaller [136] than the diameter of the nozzle orifice in a printhead to ensure reliable printing, although inks with a larger particle size have been successfully printed in very dilute concentrations, or rely on the physical act of “stirring” by using a back pressure (negative pressure difference). As solvents are used to formulate these functional inks, volatile inks are produced as a result which is undesirable during printing (although considerably more desirable during drying) as they can cause clogs at the nozzle orifice. Humectants, chemical compounds which retard the evaporation of liquids, are used to control the drying rate of the ink inside the printhead as well as the printed pattern. They are a substantial portion of the solvent in the range of 10 – 30 *wt.%* of the ink.

### **Shelf life**

The shelf life (storage) of an ink is another important criterion to consider during formulation as the chemicals (solvent, surfactant) used may decompose over time. An ink with an excellent shelf life would have the same overall properties after a prolonged period of time (typically two years of storage) at room temperature, and these would qualify as stable inks. In contrast, unstable inks are affected by several environmental factors such as temperature or light sensitivity, and often times other factors such as the storage vessel walls reacting with the ink can be the cause of ink degradation. Additionally, an imbalance in the chemical composition (e.g. pH) of a particle-based ink may lead to sedimentation due to lengthy storage times. Surfactants often cause the formation of bubbles which are highly undesirable in functional inkjet inks as they cause printability issues. To alleviate this problem, chemists use defoamers which are a chemical compound that reduce the surface tension at localised regions to very low values and facilitate the flow of liquid between particle surfaces. Defoamers are used in minuscule concentrations to avoid the separation of molecules during prolonged storage, which can be detectable during and after printing.

### 2.1.3 Theory and mechanics of drop formation

In inkjet printing, the generation of droplets is a complex phenomenon which is governed by numerous laws of physics and fluid mechanics, and they are still being researched nowadays [30]. The behaviour of these liquids can be quantified and characterised by a number of dimensionless physical constants, of which the Reynolds ( $Re$ ), Weber ( $We$ ) and Ohnesorge ( $Oh$ ) numbers are the most useful. The Reynolds number, given in Equation 2.1, compares the inertia forces to viscous forces within a droplet; the Weber number, given in Equation 2.2, is a measure of the influence of the kinetic energy relative to the surface energy of the fluid; and the Ohnesorge number, given in Equation 2.3, compares the viscous forces to the surface tension forces.

$$Re = \frac{vd\rho}{\eta} \quad (2.1)$$

$$We = \frac{v^2d\rho}{\gamma} \quad (2.2)$$

$$Oh = \frac{We^{\frac{1}{2}}}{Re} = \frac{\eta}{(\gamma d\rho)^{\frac{1}{2}}} \quad (2.3)$$

where  $\rho$ ,  $\eta$  and  $\gamma$  are the density, dynamic viscosity and the surface tension of the fluid respectively,  $v$  is the velocity of the fluid and  $d$  is the characteristic length.

Both the  $Re$  and  $We$  number are important to define the droplet characteristics [137]. In 1984, Fromm's work [138] was the first to provide a significant understanding through numerical methods for the mechanism of drop generation, and he used the Ohnesorge number for this purpose. However, he introduced the  $Z$ -number ( $Z = 1/Oh$ ) as a parameter to better illustrate his findings, and proposed that  $Z > 2$  for the generation of stable drops. However, to date, this range has proven to be unreliable as it has been demonstrated that solvents with a  $Z$ -number up to 91 could be inkjet-printed successfully [139]. Reis et Derby [140] argued that at low values of  $Z$  viscous dissipation, a mechanism which occurs when the fluid converts its kinetic energy into internal energy, prevents drop ejection whereas higher values of  $Z$  result in long liquid tails and numerous satellite drops occur behind the main drop.

Viscous dissipation occurs at low values of  $Z$ -number and is a result of the kinetic energy of the fluid being converted into its internal potential energy. The air-to-fluid barrier at the nozzle orifice introduces a surface tension which the droplet has to overcome to separate from the filament. For this separation to happen, Duineveld et al. [141] suggested that there needs to be a minimum velocity,  $v_{min}$ , which allows the ejection of a droplet with the least possible kinetic energy, and this is given in Equation 2.4 below:

$$v_{min} = \left( \frac{4\gamma}{\rho d_n} \right)^{\frac{1}{2}} \quad (2.4)$$

where  $d_n$  is the diameter of the nozzle.

When the velocity increases, the impact of the droplet onto the substrate must be considered. Even though the droplet volume is in picolitres, the large separation between the nozzle orifice and the substrate causes the drop to gain kinetic energy and consequently it spreads upon contact [142]. There is a considerable amount of ongoing research into understanding the mechanisms of splashing of a fluid, but the relationship explained by Stow et al. [142] in Equation 2.5 is well-established.

$$We^{\frac{1}{2}} Re^{\frac{1}{4}} > f(R) \quad (2.5)$$

where  $f(R)$  is a function of the surface roughness of the substrate only. This relationship has been the subject of numerous investigations by several scientists [143–146] and it was determined that for flat, smooth surfaces  $f(R) \approx 50$  [147].

By rearranging Equation 2.4 in terms of the Weber number, and a combination of Equations 2.4 and 2.5, Derby [148] plotted the range of values which determine the fluid properties that can be used in a DOD inkjet system in Figure 2.3.

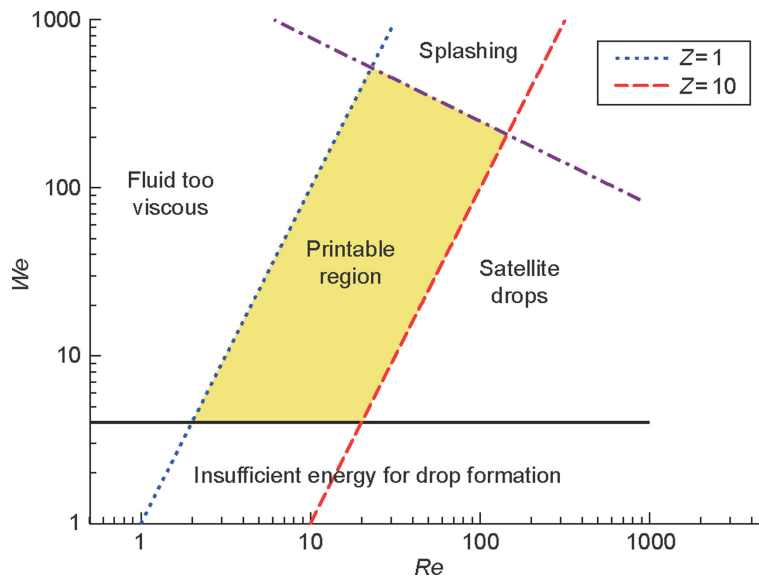


Fig. 2.3 Graph of the range of values for a fluid to be usable in a DOD inkjet system, highlighting the four scenarios which may occur in the event of improper selection of parameters. Note that the graph was corrected and redrawn by Derby from ref. [1] with permission from the journal. Reprinted from Derby [148] under Creative Commons open access license.

### 2.1.4 Droplet-substrate interaction

The deposition of an ink from the ejection of a droplet to contact with the substrate has many implications which altogether determine the spreading of a drop on the substrate through dynamic processes, which has been of significant research interest [144]. Typically, when a drop impacts a surface, its kinetic energy is converted into interfacial surface energy which eventually determines the degree of spreading. In inkjet printing, since the volume of the drops are in picolitres, the unstable splashing and bouncing energy dissipation methods are generally not discussed as the drops are minuscule and generally have a low in-flight velocity in the range of  $1 - 10 \text{ ms}^{-1}$ . Instead, the degree of spreading is determined by more stable energy dissipation methods that can then be classified into two regimes: impact driven based on inertial forces; and capillarity driven, based on capillary forces which are unaffected by the initial drop velocity. The research by Yarin et al. [144] investigated the impact of Newtonian liquid drops within a range of velocity ( $1 - 30 \text{ ms}^{-1}$ ) and droplet diameters ( $100 - 3000 \mu\text{m}$ ). Even though the range is much wider than for typical inkjet printing purposes, the experimental analysis can be used as a close approximation for reference to inkjet printing.

The evolution of the diameter of spreading can be classified into four distinct phases: the kinematic phase, the spreading phase, the relaxation phase, and the equilibrium phase. The first stage of impact is driven by kinematic behaviour and the liquid is compressed, forming a shock wave [149, 150] which detaches after reaching a critical angle. This stage lasts for less than  $1 \mu\text{s}$  in the case of inkjet printing owing to the dimensions and velocities involved. After this stage, the spreading phase is characterised by the formation of a radially expanding film. Levis and Hobbs [151] and Cheng [152] demonstrated that the maximum diameter achieved by the spreading film increases with the impact velocity. The relaxation phase is due to the surfactant which dampens the wave, and this dampening phenomenon is governed by viscous and surface tension forces which become more important in controlling behaviour. Capillary forces become increasingly dominant in controlling spreading and become solely responsible between  $0.1 - 1.0 \text{ ms}$  after impact, after which spreading continues due to relaxation and oscillation, and finally the equilibrium phase is reached after  $10 \text{ ms}$ . Figure 2.4 below is an illustration showing the different stages following the impact of a Newtonian drop which has been deposited on a surface by inkjet-printing methods. The last stages of the behaviour of the drop has been explained using a smooth surface to demonstrate complete wetting, and a hydrophobic surface to demonstrate incomplete wetting through the retraction of the drop from the surface.

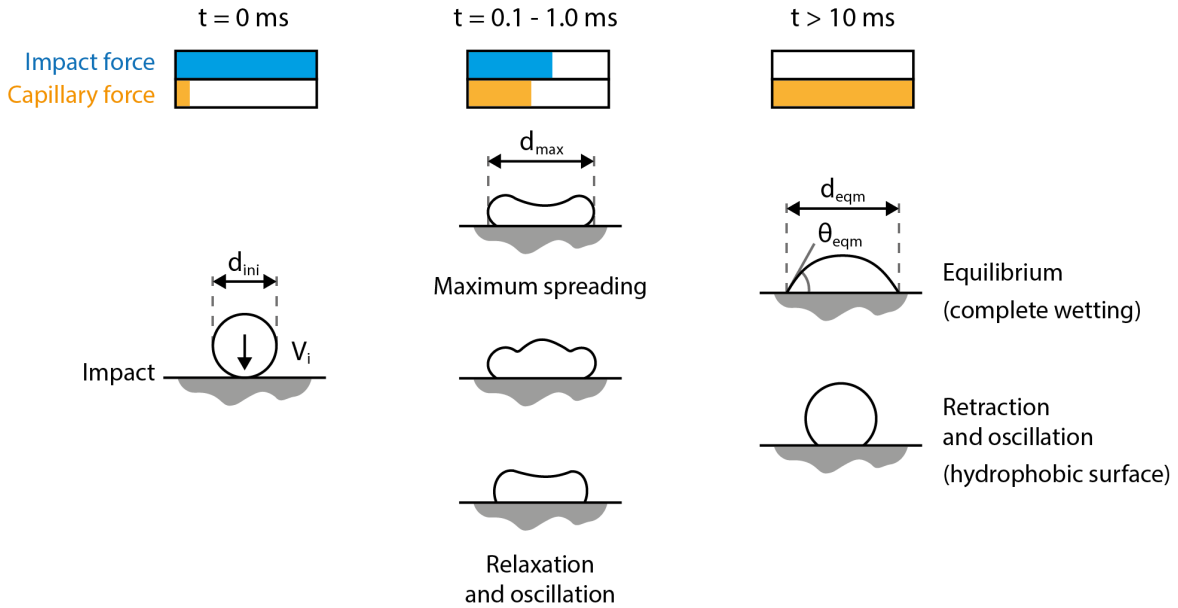


Fig. 2.4 Representation of the sequences involved from the moment of droplet impact onto a solid surface. Initial impact occurs and is followed by a series of damped oscillations before capillary-driven flow occurs.  $d_{ini}$  is the initial droplet diameter,  $d_{max}$  is the maximum diameter to which a droplet spreads during impact,  $V_i$  is the droplet velocity at impact,  $\theta_{eqm}$  is the equilibrium contact angle, and  $d_{eqm}$  is the droplet diameter when equilibrium is reached.

After equilibrium, the final droplet will have a contact diameter,  $d_{eqm}$ , determined by its volume and the equilibrium contact angle,  $\theta_{eqm}$ . In inkjet printing the drop volume, diameter and surface tension are so small that gravitational effects become negligible. Hence, the shape of the final spread drop can be estimated as a segment of a sphere of equal volume of the initial ejected droplet. This can be written in terms of the initial drop diameter,  $d_{ini}$ , to obtain the spreading ratio,  $\beta_{eqm}$ , given by Equation 2.6 below.

$$\beta_{eqm} = \frac{d_{ini}}{d_{eqm}} = \sqrt[3]{\frac{8}{\tan \frac{\theta_{eqm}}{2} (3 + \tan^2 \frac{\theta_{eqm}}{2})}} \quad (2.6)$$

This relationship has been shown to reliably predict the diameter of the printed droplets and shows that it is a linear function of the diameter of the drop in-flight.

### 2.1.5 Goniometry

The final shape of the printed feature is highly dependent on the contact angle of the drop onto the substrate, and this can be used to describe the “wetting” of a surface – a phenomenon which describes how well a liquid spreads across a surface. After deposition onto the substrate, during the spreading phase the drop advances over the dry surface in which case the contact angle mentioned in Equation 2.6 previously is the static contact angle. This is represented in Figure 2.5 which shows the interfacial tensions,  $\gamma_{xy}$ , acting on the drop from the three liquid-gas ( $\gamma_{LG}$ ), solid-gas ( $\gamma_{SG}$ ) and solid-liquid ( $\gamma_{SL}$ ) interfaces.

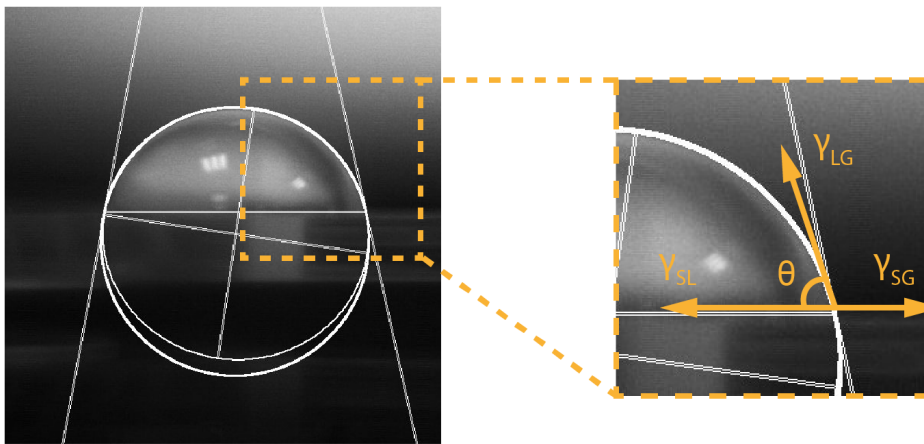


Fig. 2.5 Representation of the interfacial forces acting on a droplet on a substrate. The contact angle,  $\theta$ , is less than  $90^\circ$ , indicating a partial wetting of the substrate. The substrate in this case is the solid boundary in the interfacial tension.

If the drop stops spreading after deposition, the final angle can be easily measured through contact angle goniometry principles. This angle is called the static contact angle,  $\theta_s$ . During the spreading, the angle measured is called the dynamic contact angle,  $\theta_d$ . The contact angle of a droplet on a substrate is highly dependent on the composition of the ink, the surface roughness of the substrate and the surrounding environment. The interfacial tensions,  $\gamma_{xy}$ , determine the shape of the droplet from the three interfaces liquid-gas ( $\gamma_{LG}$ ), solid-gas ( $\gamma_{SG}$ ) and solid-liquid ( $\gamma_{SL}$ ). The equilibrium contact angle can then be calculated using these energies into the static Young’s equation [153], shown in Equation 2.7:

$$\cos(\theta) = \frac{\gamma_{SG} - \gamma_{SL}}{\gamma_{LG}} \quad (2.7)$$

It is important to note that for a liquid drop to reach thermodynamic equilibrium, the drop should not undergo any significant phase change such as solidification or evaporation during the spreading process, and this may cause the contact line to be pinned. This is

often the case for systems where the substrate temperature is raised. However, the use of an elevated substrate temperature is often advantageous during printing so as to prevent the over-spreading of droplets onto the surface, thereby tailoring the morphology of the printed feature. The surface roughness of the substrate plays a significant role in this aspect given that a droplet gets pinned at its boundary upon deposition and consequently forms a ring as the solvent dries. This phenomenon, called “coffee staining”, is often observed in everyday life and the study lead by Deegan et al. [154] resulted in three required conditions for ring formation: (1) the solvent meets the surface at a non-zero contact angle, (2) the contact line is pinned to its initial position, and (3) the solvent evaporates. In 2006, however, Hu and Larson [155] supplemented these conditions with an addition which states that the Marangoni effect resulting from the latent heat of evaporation be suppressed.

The coffee staining effect has been explained by Deegan [154] and it follows that when a thin, dilute drop of a suspension ink is deposited onto a dry solid surface, the geometric nature of the pinning and the increased rate of evaporation at the edge of the drop owing to a thinner geometry cause the particles to move to the edge and create a build-up of solute. This is illustrated in Figure 2.6 below where the transition from a deposited drop to an evaporated one is shown. The length of the dashed arrows represents the rate of evaporation of the drop, and the particles inside the drop can be seen to move closer to the edge to prevent shrinkage of the drop diameter through capillary flow. The coffee staining effect can be altered or even prevented in some cases by the use of a two-solvent system [156], or by changing the temperature or vapour pressure of the atmosphere.

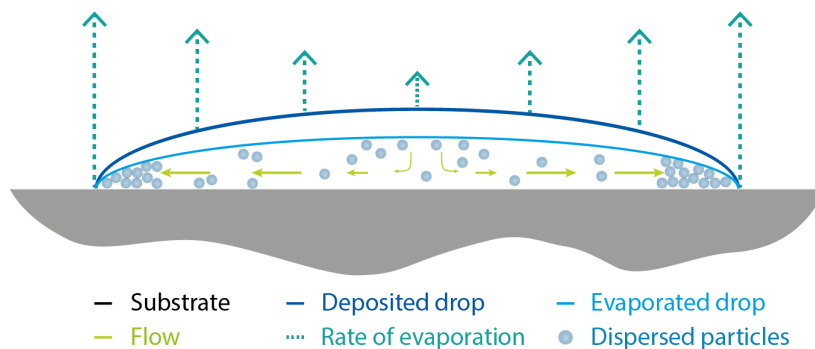


Fig. 2.6 Illustration of the motion of the particles inside a droplet during evaporation, from the deposition of the droplet to the evaporation stage. The rate of evaporation of the droplet is represented by the length of the upward facing dashed arrows.

Functional inks often require a heat treatment process to significantly improve their functional characteristics. For conductive nanoparticle-based inks, this process is called sintering, and will be discussed in the next section.

## 2.2 Sintering Mechanisms

Sintering is a processing technique in which discrete particles fuse together under the application of thermal energy (traditionally through heated ovens) to produce a density-controlled component from metal powders. This concept has been extensively studied in powder metallurgy since the 1940s [157] and since then, significant progress and development have been made in sintering science which have led to the technique being applied to smaller metal particles to join at temperatures below their melting point.

One example is the sintering of a dispersion of metal nanoparticles in the form of an ink for printed electronics applications to form conductive pathways. The dispersion generally consists of metallic nanoparticles with a diameter ranging from 1 and 100 nm. In a study conducted by Buffat & Borel [158], gold nanoparticles of a diameter below 100 nm were found to melt at a significantly lower temperature than their bulk metal properties with a reduction from 1064 °C to well below 300 °C, especially when their diameter is below 5 nm, depicted in Figure 2.7(a) below. This is due to the thermodynamic size effect as the surface area exposed to heat is significantly larger [159]. A follow-up study conducted by Allen et al. [160] extended this validity for other metals such as bismuth, indium, lead and tin, as shown in Figure 2.7(b). The results of these studies confirm that metallic nanoparticles are ideal for creating a dispersion in a liquid form for inkjet printing applications.

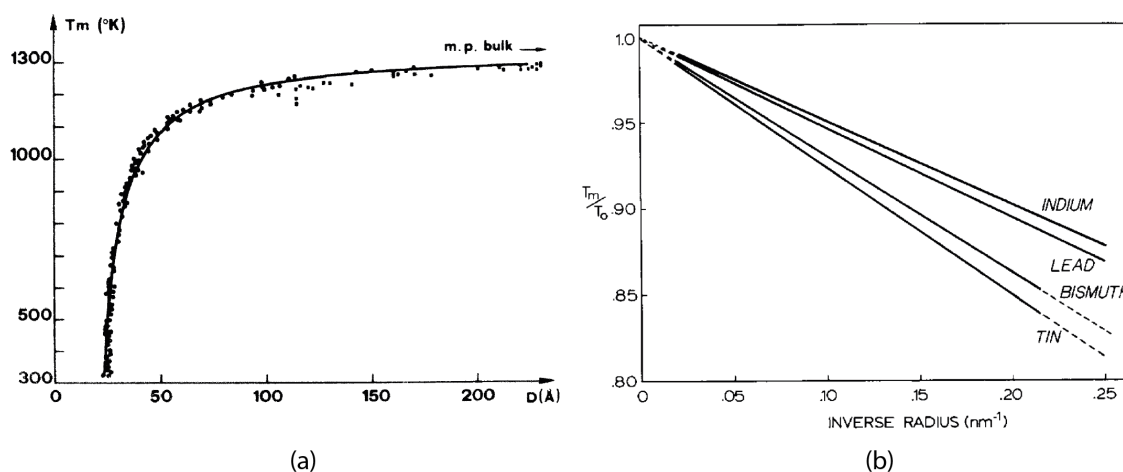


Fig. 2.7 Effects of particle diameter on the melting point of gold nanoparticles (a) and similar experiments on bismuth, indium, lead and tin (b). Reprinted with permission from ref.[158] for (a) and ref.[160] for (b).

The composition of the ink is vital for both the printing and the sintering process. Chemical additives such as dispersants, organic binders and solvents are required to ensure a smooth printing process, although as the sintering process is initiated by the application

of heat, these chemical additives need to be removed as they inhibit the flow of electrons throughout the printed feature. Using Figure 2.8 below, an illustrative summary of the stages of solid-phase sintering can be explained once a nanoparticle-based ink is deposited on a substrate in the form of a pattern and the heat treatment phase begins.

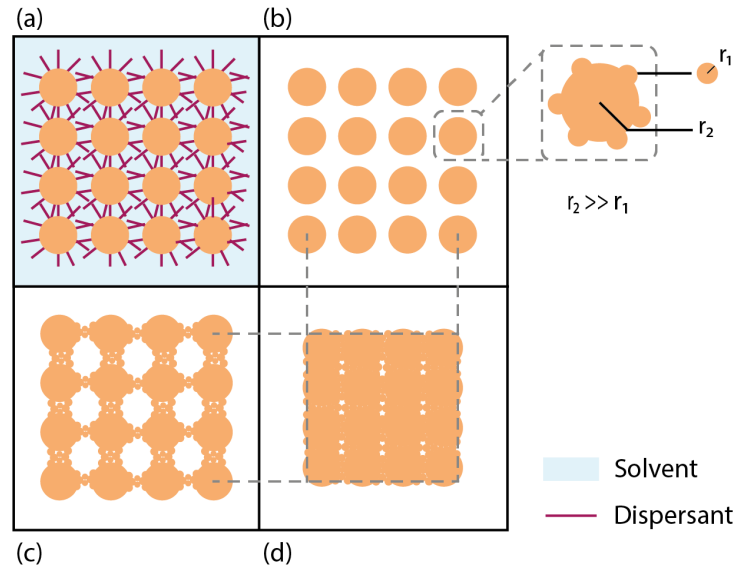


Fig. 2.8 An illustration of the stages in thermal sintering with (a) the ink, as printed, prior to the application of heat; (b) the removal of the solvent and dispersant; (c) Ostwald ripening; (d) lattice diffusion. Note that in real life applications, the arrangement of the particles is not so orderly. The sintering process has been simplified for illustrative purposes.

When the pattern is heated, the first stage (a) illustrates the evaporation of the solvent as well as the thermal decomposition of the organic dispersant, thereby releasing the nanoparticles from their protective cells. In this relatively low temperature regime, the sintering process is mainly driven by the surface diffusion from the small particles to the larger ones through a process called Ostwald ripening [161], as shown in stage (b). In layman's terms, it is assumed that the larger metal particles are immobile, and the macroscopic driving force of sintering originates from the higher chemical potential of the small metallic atoms due to their smaller radius of curvature, causing a redistribution towards the larger particles. This phenomenon initiates a surface and grain boundary diffusion within the agglomerated particles, which eventually leads to neck formation and an increase in the neck radii, as shown in stage (c). The Ostwald ripening process stalls after a growth of approximately 150 % the original size of the particle is achieved [39], leaving behind a porous structure with higher conductivity values prior to the heat treatment but still lower than the bulk conductivity of the metal. The Ostwald ripening process does not cause densification as the distance between the large metal particles remains unchanged.

In the final stage (d), the use of reference guides from the centre of the larger particles from previous stages clearly illustrates a reduction of the size of the pores and densification through lattice diffusion [162]. This process, described as particle migration and coalesce, causes the atoms on the grain boundary with sufficient energy to detach and move towards each other so that the centre of the spheres can coalesce. As the distance between the centres decreases, the neck formation grows leading to an increase in the contact area and eventually an increase in conductivity. The effectiveness of this process depends on the duration of the applied thermal energy, which can be for several hours depending on the functional ink, resulting in final density values between 95 – 99 % as the presence of impurities or surface imperfections often slow the grain boundary mobility. The movement of particles eventually leads to a shrinkage in the overall dimensions of the printed geometry due to a decrease in porosity.

Activation energy plays a vital role in determining which process dominates throughout the stages of sintering. For surface diffusion, the activation energy is the lowest as the smaller atoms require the least energy to travel to the large metal particles, and consequently prevails during the initial sintering stages where the density is almost unchanged. During lattice diffusion, however, the activation energy is much higher for the larger particles to migrate towards each other, hence only occurs at higher sintering temperatures resulting in an increase in density at the cost of shrinkage of the component [163]. This highlights the importance of the sintering temperature for the metallic nanoparticles. On the one hand the higher the temperature, the higher the energy input and the faster the sintering process as the particles relocate more vigorously; but on the other hand, the thermal limitation of the substrates must be compatible with the temperature selected.

The sintering process is generally done through exposure to heat and there are many methods of heat application, other than the conventional thermal sintering using ovens. The next section briefly describes some alternative sintering methods which have been successfully used to produce printed electronics.

### **2.2.1 Alternative sintering techniques**

During the conventional sintering process which uses a hotplate or an oven, the application of heat starts from the bottom to the top of the substrate via conduction as well as convection assisted by the atmosphere or a fan in an oven. Heat is also transferred via radiation from the internal walls of the oven to the substrate. This radiation-conduction-convection heat transfer process is well established, but poses a limitation to the substrate of choice. Hence, researchers have investigated alternative techniques which can be applied to thermo-sensitive substrates. These are briefly discussed in the following sections.

### **Microwave heating**

Microwave heating uses electromagnetic radiation (wavelength in the range of  $1\text{ mm} - 1\text{ m}$ ) which are directed towards the printed pattern to absorb the radiation. Metals are known to reflect microwaves and generate electrical discharges in the form of arcs or sparks, whereas metal powders, on the contrary, having a particle size of around a few micrometres, are proven to be good absorbers of microwave radiation [164, 165]. This is because the penetration depth of the microwave radiation at  $2.54\text{ GHz}$ , ( $10^9\text{ Hz}$ ) for metals such as silver, gold and copper is approximately  $1 - 2\ \mu\text{m}$ , as theoretically explained by the Maxwell-Wagner polarisation effect. Perelaer et al. [166, 66, 67] have attempted to bridge this theoretical gap through experimental studies on microwave sintering of inkjet printed conductive inks on polymeric substrates with reliable and comparable results obtained in very little time (20 % bulk silver in less than 5mins). Additional studies [167–169] further highlighted the applicability to high throughput roll-to-roll (R2R) production for printed electronics applications.

### **Chemical sintering**

The core attribution to the success of chemical sintering relies on the meticulous chemical composition of the ink, and sometimes to the substrate of choice. The initial grounding work by Valton et al. [170] in 2010 investigated the room temperature curing of conductive silver features following inkjet printing, and eventually led to a patent as it was the first reported technique of chemical-assisted curing on polymer substrates. Further research exploiting the meticulous chemical composition of the ink to form conductive printed features have been reported [76, 171, 172, 75], with comparable bulk conductivity of silver achieved (up to 20 %). However, due to better results achieved solely by thermal sintering, the prospects of chemical sintering for large-scale expansion are less probable mainly due to the strict discipline in the chemical composition of the inks, the numerous process steps, and the cost and environmental considerations for the use and treatment of harsh chemicals prior to safe disposal.

### **Electrical sintering**

Another distinct method of sintering nanoparticles is via the application of a voltage across a printed pattern. In a study by Allen et al. [72], a direct current (DC) voltage was applied across a pattern made out of inkjet-printed silver nanoparticle-based ink on photo paper. The pattern was subjected to 50 volts and the sample resistance significantly decreased by several orders of magnitude within  $2\ \mu\text{s}$ . Upon comparison with identical samples which had been thermally sintered at  $120\text{ }^\circ\text{C}$  for 20 min, the electrically sintered sample was found to be

superior in terms of electrical performance with a maximum of 58.7 % bulk conductivity of silver obtained under optimum sintering conditions on photo paper. Further experimental modelling [173] and validation [174–176] have demonstrated the advantages of electrical sintering with comparable electrical performance, although this method can only be applied to conductive inks of a nanoparticle-based nature, and consequently there has not been many applications of this sintering method to date.

### **Plasma exposure sintering**

Plasma sintering exposes conductive inks to low-pressure Argon plasma, and if the duration of the exposure is optimised, the ink can be sintered to high bulk conductivity values. This technique, developed by Reinhold et al. [177], initiates decomposition of the organic elements in the printed feature from a top-to-bottom approach, resulting in a bulk resistivity of less than one order of magnitude higher than the value of bulk silver achieved on polymer films such as PET after 60mins. Additional studies by Wolf et al. [178] and Wunscher et al. [179, 180] reported high conductivity values of up to 40 % bulk silver and an applicability to thermo-sensitive substrates. However, in a study by Niittynen et al. [181], the importance of precise control of the plasma sintering process was highlighted – a printed sample which has not been completely sintered can create a surface delamination due to the poor adhesion of the bottom layer with the substrate, while an “over-sintered” sample can crack due to the rapid material shrinkage and vaporisation of the organic stabilisers.

### **Intense pulsed light sintering**

Intense pulsed light (IPL) sintering, also referred to as flash light sintering, relies on a flash lamp which delivers pulses of energy over a broad range of wavelengths (ranging between 380 – 950 nm) within a predetermined area, which is usually a few  $cm^2$ . The aforementioned success of this method relies on the careful control of the pulsing frequency and power of the lamp in order to control the amount of energy delivered to the sample. This technique has proven to be advantageous due to its applicability to polymer inks, ceramics [182], and metallic nanoparticle-based inks such as silver [168, 183] and copper [184–187, 83] with conductivity values of up to 43 % silver and 30 % copper achieved. These studies also demonstrated applications using thermo-sensitive substrates such as PEN films and expansion to R2R. However, a flash light sintering system can be a costly addition to printing systems, especially due to their bulky size and narrow processing window. Moreover, these systems often require sophisticated cooling capabilities (e.g. water cooling) to operate safely and reliably.

### 2.2.2 LASER sintering

Intense pulsed light (IPL) sintering makes use of light within a certain range of wavelengths to perform the sintering process. These form part of a process called photonic sintering, a process whereby light is pulsed repeatedly to deliver the energy within a confined area. The advantage of this method of delivering energy is for its efficiency and more defined control of the energy delivery process parameters as compared to other forms of conventional sintering such as thermal. LASER (Light Amplification by Stimulated Emission of Radiation) sintering is remarkably similar to photonic sintering, with the main difference being in the emission area and the wavelength of the incident radiation. In the case of laser sintering, the processing area is in the range of  $mm^2$  or less, and due to the nature of the laser radiation, the range of wavelength is significantly more defined to within  $\pm 5\%$  of the stated emission wavelength.

The promising photonic sintering method highlights grounds for investigation to better understand the interaction of the radiation with the printed patterns from a printed electronics point of view. As such, the following section describes the use of lasers for sintering from a printed electronics perspective as the emission area is much smaller and the effects of the incident radiation can be better quantified. On a grander scale, laser sintering has the advantage of being selective as compared to flash or IPL sintering due to the much more defined area, and consequently may lead to the fabrication of conductor-insulator composite patterns. Some of the latest developments using lasers in inkjet printing are also surveyed at the end of this section.

#### Laser systems

A laser is a *high intensity* light source which is not only *monochromatic* but also *coherent* with a unique *directionality*. The high intensity aspect of the laser allows the laser beam to be focussed to a high power density, within a narrow bandwidth (due to the monochromatic beam), over a long distance due to the coherence and directionality. Altogether, these four properties of the laser occur simultaneously during a stimulated emission, and not in the ordinary flashlight. There are numerous types of laser and these can be sub-categorised as:

1. Solid-state lasers
2. Gas lasers
3. Dye lasers
4. Semiconductor lasers

### **Solid-state lasers**

Solid-state lasers contain materials which can either be transparent crystals or glass which are heat resistant and contain rare-earth elements as active ions. Currently, the most practical solid-state laser used for material processing and machining is the YAG laser which contains a  $\text{Y}_3\text{Al}_5\text{O}_2$  (yttrium aluminium garnet) crystal composed of neodymium  $\text{Nd}^{3+}$  ions, also known as the Nd : YAG laser. It can be found in industrial sites welding heavy metals, in the surgical suite performing delicate surgery, in the research laboratory making precise spectroscopic measurements, and on a satellite orbiting the planet Mars measuring the detailed topography.

### **Gas lasers**

Gas lasers consist of a glass tube filled with a mixture of gases which act as the laser medium. The most common gas laser is the Helium-Neon laser, but there are different types such as Argon-ion, Carbon dioxide, Carbon monoxide, Nitrogen and excimer lasers to name a few. The laser medium, in this case the type of gas used, determines the laser wavelength and efficiency. Currently,  $\text{CO}_2$  lasers are the most efficient (up to 20 % efficiency) and are generally used for processing materials in industrial applications, while others are around 1 % efficient. Excimer lasers are frequently used in the semiconductor photolithography manufacturing process.

### **Dye lasers**

Dye lasers use complex organic dyes diluted in a solvent such as a pure alcohol (e.g. methanol) as the laser medium. Some of the dye molecules include rhodamine 6G, stilbene and coumarin. However, dye lasers are not very common due to their impracticability – the dye molecules cannot survive without being constantly circulated by a pump in a reservoir, and the dye-solvent mixture must be changed regularly as it degrades over time due to light sensitivity. They are mainly used for dermatology.

### **Semiconductor lasers**

A semiconductor laser, also referred to as a diode laser, consists of a  $p$ - $n$  junction made out of a semiconductor material. When the  $p$ -type junction is positively biased with respect to the  $n$ -type junction through the application of a current, electrons flow easily from the  $n$ -type junction to the  $p$ -type junction. When these electrons meet, they combine and, in the process, emit a photon of energy almost equal to the band-gap energy.

Generally, the semiconductor materials can have different band-gap energies resulting in a different emission wavelength, such as GaAs (Gallium Arsenide, 904 nm), AlGaInP (Aluminium Gallium Indium Phosphide, 760 nm) and InGaN (Indium Gallium Nitride, 405 nm) to name a few. Diode lasers are much cheaper, smaller and consume less power when operated as the emission process within the  $p$ - $n$  junction is highly efficient.

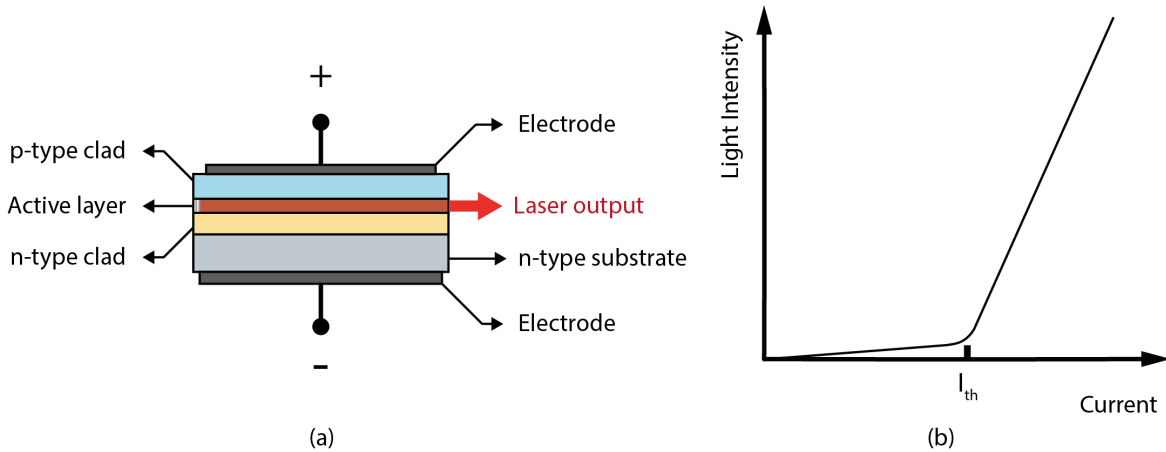


Fig. 2.9 Schematic of a simple semiconductor laser showing the different components. Note that the active layer contains a reflective surface to the left, opposite to the direction of the laser output. (b) represents the minimum excitation current required for stimulated emission.

In Figure 2.9(a) above, the two parallel facets of a direct-transition semiconductor are perpendicular to the plane of the  $p$ - $n$  junction, where a positive potential is applied to the electrode on the  $p$ -type semiconductor and a negative to the  $n$ -type. When the photons are emitted from the electrons which recombine, they bounce back and forth the active layer. Note that, in Figure 2.9(a), the active layer contains a highly reflective end on the left, while on the opposite side it contains a partially mirrored surface which allows only certain photons through in the form of a laser output at wavelengths equal to the band-gap energy. The intensity of the emitted light is a function of the injection current, as shown in Figure 2.9(b). It can be seen that the intensity increases rapidly above a certain current  $I_{th}$ . This current,  $I_{th}$ , is called the threshold current and is the starting current for laser oscillation. Below  $I_{th}$  the directivity of the emitted light is poor, and the spectral width is broad, similar to a light-emitting diode (LED) and can be described as a spontaneous emission. Above threshold, however, the laser light has a narrower spectral width and sharper directivity [188] and is described as a stimulated emission.

### 2.2.3 Continuous wave and pulsed lasers

The emission of lasers can be sub-categorised under continuous wave (CW) emission or pulsed emission. As their name suggests, CW lasers output an uninterrupted beam of light, ideally with a stable output power and at the exact wavelength depending on the laser medium. By controlling the power at the threshold current, the output of the CW laser can also be controlled whenever required to output the laser beam.

Pulsed lasers, on the other hand, operate via the switching “ON” and “OFF” of the laser output repeatedly. When turned “ON”, the pulsed laser delivers the laser energy in a single pulse for the entirety of the duration – which can vary from as little as a few femtoseconds to as much as a few milliseconds, after which the output of the laser goes to zero, i.e. the “OFF” state. The laser is then switched “ON” and the cycle repeats. The rate at which the cycle between switching “ON” and “OFF” the output of the laser is determined by the repetition rate of the laser, typically given in hertz ( $Hz$ ), and is defined as the number of pulses of energy emitted by the laser in one second.

When comparing the power output of a laser, for a CW laser module the output power will be relatively lower. For a pulsed laser, since it emits burst of energy in a very short time, the output power is generally defined as “peak power”. The pulse energy emitted during this period is shown in the shaded region of Figure 2.10 below. Pulse width, repetition rate and peak power are not characteristics of a CW laser.

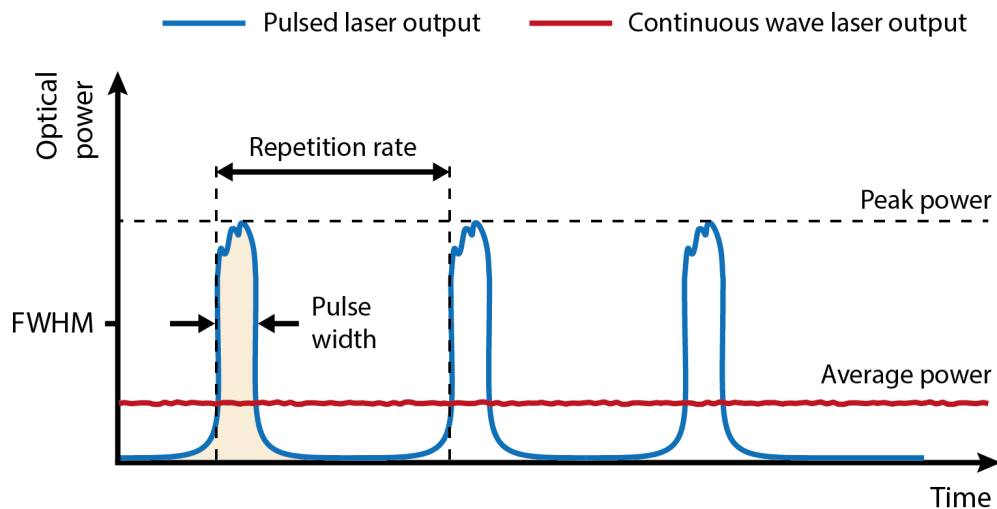


Fig. 2.10 Representation of a typical output for a pulsed laser, denoted by the blue strokes, showing the pulse width, repetition rate and peak power output; and that of a continuous wave laser, denoted by a red stroke, which is only typically characterised by the average power output. Note that the area shaded under the pulsed laser represents the energy delivered in that pulse.

Over the years pulsed lasers have mainly been used for machining processes as their peak power output can be contained to very short durations. Mafuné et al. [189, 190] used a 532 *nm* pulsed laser to produce silver nanoparticles from a silver metal plate irradiated at nanosecond intervals in an aqueous solution. Similarly, Kabashin et al. [191] used an 800 *nm* femtosecond laser for the synthesis of gold nanoparticles via laser ablation. Ablation, in the context of laser physics, is the process by which finer materials are removed from a larger source. Typically, pulsed lasers are used due to their high energy density in a pulse, which is significantly higher than that of a continuous wave laser. There are many factors which influence the ablation process, including the absorption spectrum of the incident laser irradiation, the penetration depth of the radiation, and the pulsing parameters of the laser.

Despite laser ablation being a subtractive manufacturing technique, there are many advantages of this method. The heat affected zone (HAZ), probably the most significant and distinguishable as compared to other subtractive manufacturing methods such as milling or turning, is significantly minimised during the process. This makes this technique very attractive for applications where heat-sensitive substrates are preferred, including surface treatments such as cleaning or texturing [192]. The process leading to the minimising of the HAZ first requires the optimisation of the "ablation threshold" of the material, the point beyond which material is removed from the surface, as described by Gamaly et al. [193] and Shirk et al. [194] who described the threshold levels for several metals.

However, prior to reaching the ablation threshold, the laser irradiation can be used to deliver precise amounts of energy into a pattern. In the case of polymers, that energy may lead to internal reactions causing cross-linking, photo-induced oxidation or depolymerisation [195], whilst minimising the thermal energy diffusion to the substrate due to the short duration of the pulse [196]. In metals such as nanoparticles, on the other hand, this irradiation prior to the ablation threshold level, can be utilised to induce sintering provided the energy irradiated is sufficient to match the activation energy of the nanoparticles for relocations, as explained in the earlier section on the sintering mechanisms.

As this thesis details the use of pulsed lasers for sintering of metallic nanoparticle-based inks, the ablation threshold is of significant importance in order to avoid damage to the pattern as well as the excessive heat diffusion to the underlying substrate. This very concept will lead to the formation of the hypothesis of whether the thermal mass of the substrate contributes to the thermal energy diffusion during pulsed laser sintering whilst avoiding damage to the substrate. The following chapters will further elaborate on these, with experimental data used to test the hypothesis.

### 2.2.4 Laser sintering in Inkjet applications

Continuous wave lasers have been successfully, and reliably used to perform the sintering process in patterns printed from nanoparticle-based inks. Table 2.1 below represents a survey of the latest inkjet-printed experiments using high performance conductive inks for printed electronics applications, along with the respective results achieved via LASER sintering methods including the use of continuous wave (*cw*) and pulsed lasers. The survey includes experiments involving silver and copper inks which are printed on a variety of substrates, including borosilicate glass, polyimide (PI), polyethylene terephthalate (PET), silicone wafers, and a glass-epoxy composite.

The work by Niittynen et al. with silver and copper NPs resulted in the most promising work with alternative LASER sintering methods using an 808 *nm cw* laser, although the substrate of choice was generally polyimide due to its high temperature resistance ( $T_g \approx 400$  °C). When a silicon wafer was used for printing and *cw* laser sintering, the substrate showed thermal damage due to the high temperature rise of the laser, and concluded with the requirement of an insulator layer.

Some notable works with copper functional ink which were laser sintered but not inkjet-printed, and instead used other deposition methods such as spin coating and screen printing, resulted in relatively inferior conductivity values achieved as compared to the works by Niittynen et al. and Halonen et al. However, the laser sintering process was successfully done on PET films which have a much lower glass transition temperature as compared to polyimide ( $T_g \approx 80$  °C), thereby demonstrating application to thermo-sensitive substrates, and also the feasibility of pulsed laser sintering even though patterns were made via the screen-printing technique.

The study by Niittynen et al. [69] further elaborated on the theory of laser sintering and thermal modelling of the samples during the irradiation process. They used finite element method (FEM) modelling to simulate the printed samples under the sintering temperature provided by a laser and attempted to correlate their theoretical findings with actual experimental data. In their experiments with the laser sintering of the copper nanoparticle patterns, they used an 808 *nm* continuous wave semiconductor laser to irradiate the samples of varying thicknesses, over a range of laser scanning speeds. Their study concluded with theoretical data matching experimental data and highlighted several areas, in addition to sintering temperature, which need further investigation to better understand the thermal energy variation during the laser sintering process. This understanding is key to prevent the excessive heat dissipation into the substrate, which would eventually allow the use of laser sintering of printed metallic nanoparticle inks on thermo-sensitive substrates.

Table 2.1 A survey of the recent state-of-the-art results achieved using inkjet-printed functional silver and copper inks sintered using LASER (continuous wave, *cw*, and pulsed).

Author	Ink type and substrate	Sintering method	Result (% bulk conductivity)
Niittynen et al. [181], 2014	Silver NPs on polyimide	<i>cw</i> laser (808 <i>nm</i> )	35.0 %
Ji et al. [197], 2017	Silver nanoflakes on PET	<i>cw</i> laser (532 <i>nm</i> )	25.2 %
Zhao et al. [198], 2020	Silver MOD on FR4 fibre-glass	<i>cw</i> laser (532 <i>nm</i> )	23.0 %
El Hajjaji et al. [199], 2021	Silver NPs on polyimide	<i>cw</i> laser (1064 <i>nm</i> ) and IPL	10.3 %
Joo et al. [200], 2011	Copper paste on polyimide ( <i>screen printed*</i> )	Pulsed laser (355 <i>nm</i> ) under N <sub>2</sub> atmosphere	9.2 %
Halonen et al. [201], 2013	Copper NPs on polyimide	<i>cw</i> laser (808 <i>nm</i> )	19.1 %
Niittynen et al. [69], 2014	Copper NPs on silicon wafer	<i>cw</i> laser (808 <i>nm</i> )	15.9 %
Niittynen et al. [83], 2015	Copper NPs on polyimide	<i>cw</i> laser (808 <i>nm</i> ) and IPL	20.1 %
Rahman et al. [202], 2018	Copper Oxide NPs on glass ( <i>spin coated*</i> )	<i>cw</i> laser (532 <i>nm</i> )	17.6 %
Hernandez-Castaneda et al. [203], 2020	Copper NPs on PET ( <i>screen printed*</i> )	<i>cw</i> laser (808 <i>nm</i> ) and pulsed laser (523 <i>nm</i> )	3.8 %

## 2.3 Conclusion and questions to address

The use of a pulsed laser to successfully sinter metallic nanoparticles raised questions such as how to deliver the precise amount of energy to encourage sintering and not vaporise the nanoparticles through ablation. The process of pulsed laser sintering has been successfully performed on substrates which can withstand high temperatures such as glass and polyimide ( $T_g \approx 1200$  °C and  $\approx 400$  °C respectively), but not on thermo-sensitive substrates. Intense pulsed light (IPL) sintering has proven successful on thermo-sensitive substrates mainly due to the short pulse duration which restrict the energy irradiated to the printed conductive pattern, thereby protecting the substrate from excessive heat accumulation and thermal damage. In theory, IPL and laser sintering are methods of photonic sintering, with the only difference being in the emission area. IPL sintering has a much larger area and can sinter parts quicker and on larger scale, suitable for high-throughput manufacturing processes. Laser sintering, on the contrary, has a much smaller emission area and can precisely control the deposition of the emitted radiation, which highlights the possibility of selective sintering.

Pulsed lasers have been used for laser micro-machining of minuscule features such as a fine line width in which a metallic nanoink can be deposited by inkjet printing, but there have been no reports of the use of pulsed lasers for the sintering of inkjet printed patterns on thermo-sensitive substrates. The work by Joo et al. [200] opens ground for investigation as they report the pulsed laser sintering, under reduced atmosphere, of screen-printed copper paste on a heat resistant substrate (in their report, polyimide) by avoiding laser ablation levels. Prior to the ablation threshold, the irradiated energy from a pulsed laser can be used as a heat treatment process similar to *cw* laser irradiation, given that the energy in a pulse matches the energy required to initiate sintering in a metallic nanoink. Despite the inherent difference in the principle of operation of a *cw* and pulsed laser, the use of radiation to initiate sintering has proven to be successful. Continuous wave lasers have proven to cause damage to the substrate and an equivalent heat affected zone due to the inability of the substrate to dissipate the thermal energy during the irradiation process. With pulsed laser, since the output of the irradiation is repeatedly switched ON/OFF, the damage to the substrate may be minimised during the irradiation process.

The top-down approach to sintering via lasers (Figure 2.11(b)), as compared to the bottom-up approach via conventional thermal sintering (Figure 2.11(a)) may also prompt the reflection into a change in the mechanical and electrical properties of the printed features. Incomplete sintering via a top-down approach has proven to have adverse effects on the adhesion of the samples to the substrates, as reported by Niittynen et al. [181]. Consequently, this top-down approach of laser sintering may have similar adverse effects on the electrical properties of the samples.

The research hypothesis as a result of the literature survey is as follows:

**Can pulsed laser sintering of inkjet-printed metallic nanoparticle inks in the form of thin films be done on a thermo-sensitive substrate without causing ablation? If it is possible, then what are the implications on the substrate, and the mechanical and electrical properties of the thin film following irradiation?**

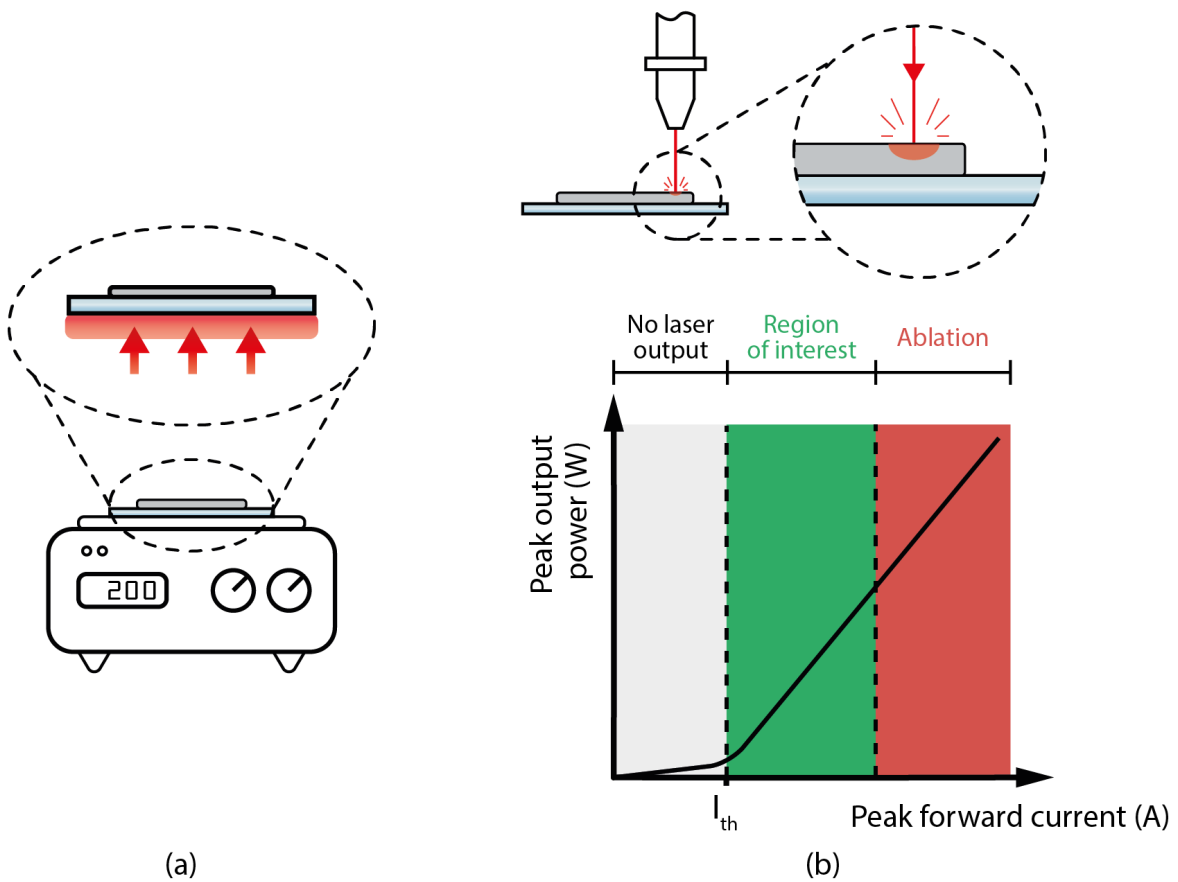


Fig. 2.11 Illustration of the (a) bottom-up approach of conventional thermal sintering (e.g. using a hotplate); and (b) the top-down approach of laser sintering, with the graph showing the region of interest for sintering prior to ablation.



# Chapter 3

## Combining Inkjet Printing and Pulsed Laser Sintering

### Summary

This chapter describes the methodology used throughout this research to enable the investigation of combining inkjet printing with pulsed laser sintering to produce printed electronics. As printed electronics can be produced on a variety of substrates for different applications, a wide variety of materials are investigated for inkjet deposition using functional inks. The relevant properties of these materials are described in detail, followed by the constituents of the functional inks used for inkjet printing.

Additionally, the inkjet printing process is described in more detail with the aim of achieving the best resolution as well as the optimum performance of the pattern. The droplet formation process is further elaborated upon based on the prior literature described in Section 2.1.3. Then, the laser system used for the pulsed laser sintering process is further detailed, particularly due to the bespoke configuration of the system, and the laser sintering parameter variation is explained.

Finally, the last section of this chapter covers the analytical approach of characterising the samples, with a particular focus on the custom-built testing rigs such as the four-point probe station to evaluate the conductivity of the samples, and the cross-cutter based on the ASTM F1842-15 standard to evaluate the adhesion of the printed samples to the substrate.

### 3.1 Materials

Throughout this research, four different substrates were used to demonstrate different applications of the inkjet printing process. The thermal and mechanical properties of these substrates are detailed in Table 3.1 below. The first substrate is a standard laboratory glass slide which has a rigid, smooth and non-porous surface; the second is a polymer film made out of polyimide which has a flexible and non-porous surface; the third a similar polymer film made out of polyethylene terephthalate which exhibits flexibility and non-porosity; and the last substrate is specially designed out of 250 *gsm* paper with a thin resin hydrophilic polymer coating to improve surface coating adhesion. All samples, except for paper, were prepared first by a deionised water rinsing process followed by another rinse with acetone, and finally dried under a flow of clean air.

Table 3.1 List of relevant properties of the different substrates used throughout the experiment.

Substrate	Manufacturer	Thickness ( <i>mm</i> )	Glass transition temperature, $T_g$ ( $^{\circ}\text{C}$ )	Thermal conductivity ( $\text{Wm}^{-1}\text{K}^{-1}$ )
Glass	Academy	1.0 – 1.2	1,200	0.8 – 1.0
Polyimide (PI)	DuPont <sup>TM</sup> Kapton <sup>©</sup>	0.125	400	0.12
Polyethylene terephthalate (PET)	Goodfellow	0.35	80	0.15 – 0.40
Paper	Hewlett-Packard	0.40	–	–

As the substrates were used during pulsed laser sintering at 905 *nm*, the absorption of the irradiation must be addressed. Several research outputs have investigated the effects of irradiation on the substrates used throughout this research, and it was found that the absorption spectrum of the substrates are less than 0.2 a.u in the 905 *nm* range for glass [204, 205], polyimide [206, 207], PET [208] and paper [209, 210].

Five different types of functional inks were investigated at different stages. As they constitute a functional element, either of a conductive or an insulative nature, the post-printing process differs due the composition of the ink. Table 3.2 shows the relevant properties of each ink used in this research. In the case of conductive inks, the sintering process was performed based on either the manufacturer's specifications, or, when unspecified, the analysis of the constituents of the ink to determine a starting range for sintering in terms of temperature and duration.

Table 3.2 Details of relevant properties of the different inks used throughout the research.

<b>Ink</b>	<b>Viscosity (cP)</b>	<b>Particle content (wt.%)</b>	<b>Surface tension (<math>mNm^{-1}</math>)</b>	<b>Recommended sintering temperature (<math>^{\circ}C</math>)</b>	<b>Recommended sintering duration (min)</b>	<b>Manufacturer</b>
AgNPs	18 at 20 $^{\circ}C$	30 – 35	35 at 20 $^{\circ}C$	150	30	Sigma-Aldrich (no. 736465)
AgMOD	4.04 at 20 $^{\circ}C$	40	30.2 at 20 $^{\circ}C$	140	5	Strem Chemicals (no. 68683-18-1)
RSI	12 at 20 $^{\circ}C$	12 – 14	28.4 at 20 $^{\circ}C$	80	15	Sigma-Aldrich (no. 745707)
CuNPs	22 at 25 $^{\circ}C$	35 – 37	35.2 at 20 $^{\circ}C$	–* <sup>1</sup>	–* <sup>1</sup>	Dycotec Materials (DM-CUI-5001)
Insulator	16 at 40 $^{\circ}C$	–	34 – 36 at 40 $^{\circ}C$	–* <sup>2</sup>	–* <sup>2</sup>	Dycotec Materials (DM-INI-7003)

\*<sup>1</sup>: The recommended sintering temperature and duration cannot be specified as the ink is specially designed for flash sintering.

\*<sup>2</sup>: The recommended sintering temperature and duration cannot be specified as the ink is specially designed for UV curing.

The first ink is the silver nanoparticle-based (NPs) ink which was purchased from a commercial supplier, Sigma-Aldrich (product no. 736465). It contains 30 – 35 *wt.%* of silver nanoparticles of a particle size of less than 50 *nm* dispersed in triethylene glycol monomethyl ether. The ink has a matt grey colour, with a tint of yellow from the triethylene glycol. The viscosity of the ink was measured to be 18 *cP* and surface tension of 35 *mN/m* at 20 °C, which was the room temperature during printing.

The second ink, the silver neodecanoate metallorganic decomposition (MOD) ink was prepared by dissolving 40 *wt.%* silver neodecanoate (68683-18-1, Strem Chemicals) into p-xylene (296333, Sigma-Aldrich). The mixture was constantly stirred for 60 *min* until all the silver had dissolved in the solvent. The ink was colourless as it is a solution. Further analysis of the ink revealed the viscosity to be 4.04 *cP* and surface tension of 30.2 *mN/m* at 20 °C.

The third ink, the reactive silver ink (RSI) was also purchased from a commercial supplier on special order (745707, Sigma-Aldrich). It is formulated by dissolving silver acetate into an amine solution and diluted with formic acid. The resultant mixture appeared slightly yellow due to the presence of the amine complex. Further analysis showed that the silver has a loading of 12 – 14 *wt.%* and a viscosity of 10 – 12 *cP* and surface tension of 28.4 *mN/m* at room temperature [211].

The fourth ink is an experimental copper nanoparticle-based ink which was developed by a commercial supplier (Dycotec Materials Ltd.) specially for flash sintering processes. It contains 35 – 37 *wt.%* of copper nanoparticle stabilised in a mixture of diethylene glycol monoethyl ether and benzyl alcohol. The ink has a matt brown colour from the copper nanoparticle. The viscosity of the ink measured 22 *cP* at 25 °C and surface tension of 35.2 *mN/m*.

The final ink, the insulator, was also purchased from the same supplier (Dycotec Materials Ltd.) and was specially designed for inkjet printing applications as well as providing a smooth, hydrophilic surface for overprints using other types of inks from the same supplier. However, the insulator ink needed to be heated to 40 °C to be successfully printed, and as such the viscosity of the ink measured 16 *cP* at 40 °C and surface tension of 35 *mN/m*.

Prior to filling the reservoirs for inkjet-printing, the inks were filtered using a 0.20  $\mu\text{m}$  PTFE filter to eliminate the presence of potential contaminants which may clog the nozzle. The silver MOD and reactive silver inks both appeared to be light-sensitive, so they were filled in reservoirs which were coated with a light-repellent adhesive tape on the external surface to prevent degradation.

### 3.1.1 Substrate compatibility

There are some additional factors which need to be considered during the choice of printing a functional ink on a substrate. One of the most important factors to consider is the substrate compatibility with the heat treatment process. As a general rough indicator, the melting point ( $T_m$ ) of materials is used to determine whether the applied heat is a limiting factor. However, in the case of polymers, the glass transition temperature ( $T_g$ ) of the material is more important as structural changes at a molecular level occur at this temperature. Polymers can be amorphous or crystalline, with the main difference being in the molecular arrangement of the molecules. Before heating, polymers remain in their glassy state which is generally rigid and brittle before reaching  $T_g$ . Amorphous polymers have a randomised arrangement which cause gradual softening as the applied temperature rises. Crystalline (or semi-crystalline) polymers have a highly ordered arrangement which do not soften when heated and instead have a defined melting point. The key difference between the glass transition temperature and the melting point of the polymer is in the region in which it occurs – glass transition occurs in the amorphous region, while melting occurs in the crystalline region. In the amorphous region, the molecular chains begin sliding past one another in a disorderly fashion (softening) until it reaches a rubbery state, while in the crystalline region the entire molecular chain flows and separates through viscous flow (melting), as shown in Figure 3.1 below. For example, polymers such as polyethylene terephthalate (PET) have a  $T_g$  around 80 °C, after which the PET films deform plastically. The choice of the substrate must be done carefully to ensure its mechanical, optical, and electrical properties remain unchanged during the heat treatment process, particularly for printed electronics where polymers are preferred for their optical clarity and flexibility.

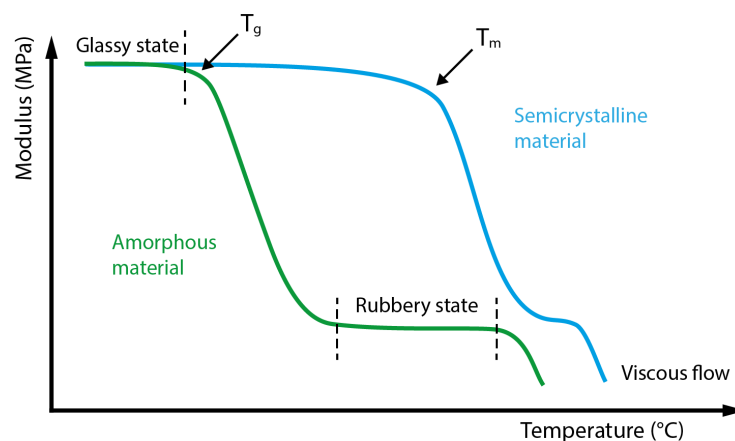


Fig. 3.1 Representation of the change of state for an amorphous and semicrystalline material, highlighting the glass transition temperature ( $T_g$ ) and the melting temperature ( $T_m$ ).

## 3.2 Inkjet Printing

The droplet formation process was theoretically explained in the earlier section of Chapter 2.1.3, and this section elaborates on the waveform optimisation for the deposition process using a piezoelectric printhead. Prior to this, a more detailed description of controlling each waveform parameter such as applied voltage and pulse width is provided in this section, which ultimately broadens the understanding of the droplet optimisation process.

### 3.2.1 Drop formation process and optimisation

The drop formation process is heavily influenced by the parameters (viscosity and surface tension) mentioned earlier. In a drop-on-demand piezo-electric printhead, a drop is formed by controlling the pressure wave formation inside the capillary tube. Within the inkjet head, upon the application of an electric field the piezo-ceramic surface is deformed which subsequently induces a pressure wave into the fluid and causes a droplet to be ejected [212]. The surface tension of the fluid normally prevents the drop from separating at the orifice, hence the pressure wave is important to overcome but in a controlled manner. Figure 3.2 shows an illustration of the principle behind the pressure wave formation inside the glass capillary tube upon deformation of the piezo-ceramic plate.

The applied voltage and the delay between each change in voltage play a significant role in controlling the drop generation process. Upon application of a voltage, the piezo-electric element expands outwards (Figure 3.2(a)) and a pressure wave travels in two opposite directions (Figure 3.2(b)). When the wave arrives at the nozzle (the right end of the capillary tube), it is conserved since the orifice is considered a closed end being a fraction of the diameter of the glass capillary tube, based on Bogy's acoustic wave theory [212]. On the other end the wave travelling towards the reservoir is reflected as the reservoir acts as an open end (Figure 3.2(c)) [212]. The moment that both pressure waves return to the centre of the nozzle the piezo-electric actuator contracts (Figure 3.2(d)) and creates a compressive pulse which propagates in phase and increases the amplitude of the reflected wave, thus cancelling the returning wave. This enhanced compression wave causes the ejection of a droplet from the nozzle orifice (Figure 3.2(e)). The design of printheads, particularly the nozzle dimension, greatly influences the propagation and reflection of pressure waves inside the capillary tube. After fine tuning the voltage and delay of the piezo-electric actuator, the desired waveform (Figure 3.2, rightmost) can be achieved, resulting in a reliable droplet ejection process.

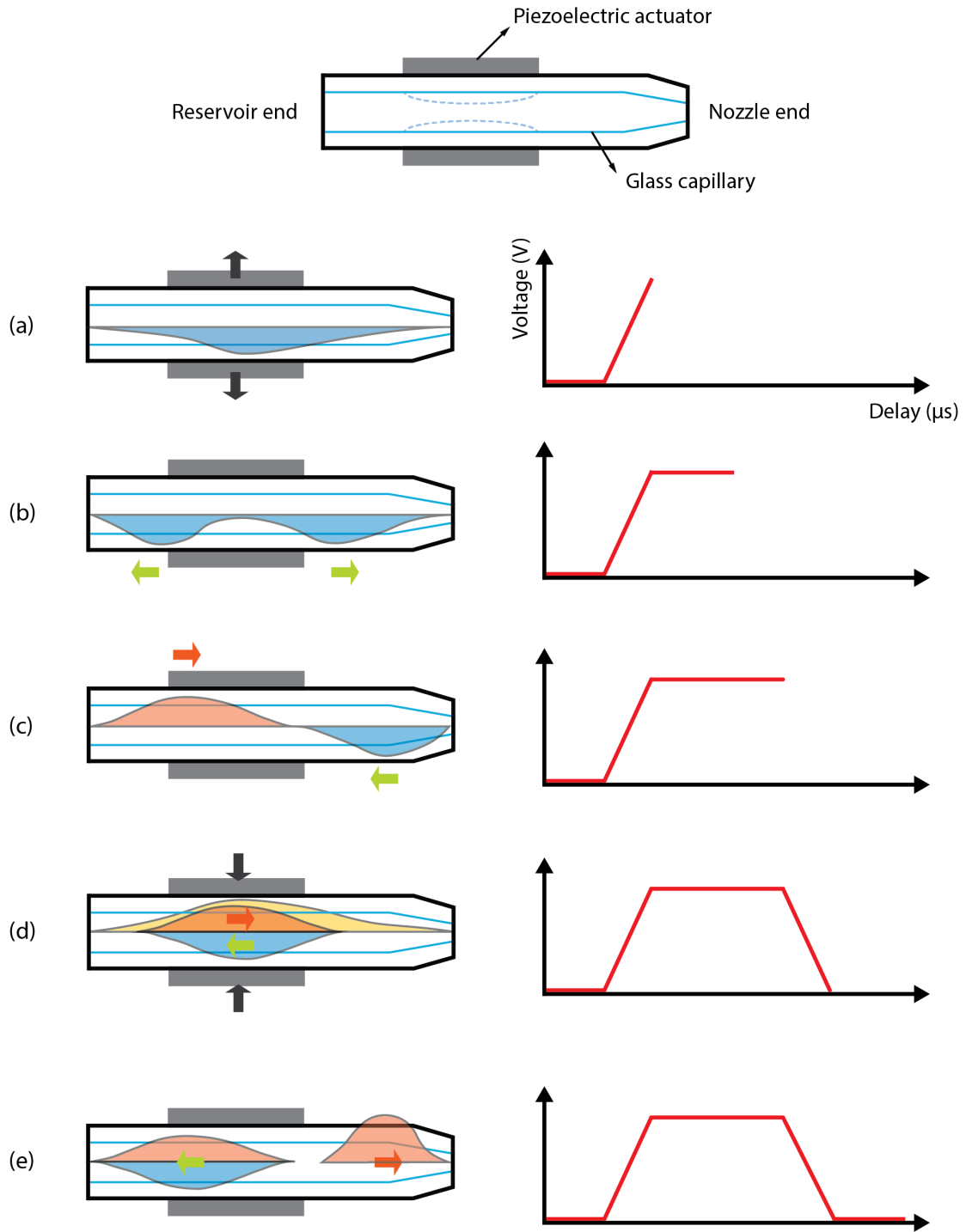


Fig. 3.2 [Left] Schematic of the acoustic wave propagation in a glass capillary used in a piezo-electric drop-on-demand inkjet printer. [Right] Representation of the typical waveform showing the effects of voltage and delay involved in the droplet ejection process, each corresponding to the individual stages (a) – (e) from the illustrations.

The characteristic waveform of a piezo-electric DOD actuator somewhat resembles a trapezoid, as shown in Figure 3.3. The duration over which the voltage goes from zero to  $V$ , is maintained, and drops from  $V$  to zero is called the voltage rise time ( $t_r$ ), the dwell time ( $t_d$ ), and the fall time ( $t_f$ ) respectively. This duration (the pulse width) typically lasts a few microseconds, and with the correct parameters corresponds to the formation of a single droplet. As mentioned previously, the right balance between the applied voltage and the delay allows a separate droplet to form.

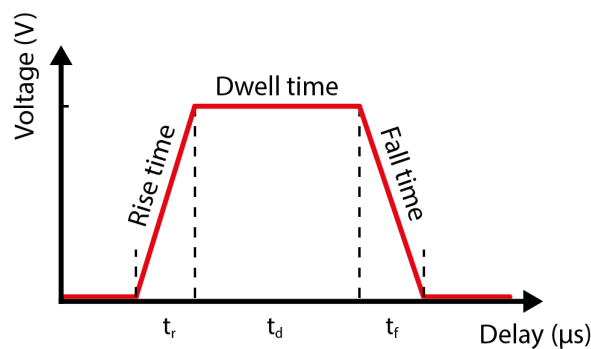


Fig. 3.3 Typical waveform used for the generation of a droplet from a piezoelectric printhead.

A typical drop formation process is shown in Figure 3.4 below which is formed of a series of sequences of images. Figure 3.4(a) is a typical representation of the early stages of exploring the parameters for successfully obtaining a drop, as per the waveform used in Figure 3.3 above. As a result of a single pulse, the typical diameter of a drop is about the same as the diameter of the nozzle orifice. A considerably smaller drop can be formed after further experimenting to find the optimum jetting parameters, as shown in Figure 3.4(b) which shows the drop formation when oppositely directed triple pulses are used.  $V_n$ ,  $P_n$  and  $D_n$  are the applied voltage, duration of the applied voltage and the duration of the recovery voltage respectively, and  $n$  is a representation of the various stages.

Initially, the pressure wave from inside the capillary causes a small volume of liquid to be ejected, which forms a sphere due to the surface tension of the liquid [213]. This volume remains attached to the nozzle by a “tail” which is highly affected by fluid viscosity and the geometry of the nozzle. Eggers [214] found that highly viscous inks show long symmetric tail shapes whereas moderately viscous inks form long asymmetric tails and low viscosity inks show short tails. The tail elongates as the droplet falls and at a certain point necking occurs and the tail separates from the main drop [215]. This is called the break-off point and at this instance satellite drops can be formed, especially if the droplet has a higher velocity than its tail. This is an example of the Rayleigh instability as the drops are initiated by the surface tension driven capillary waves which have to overcome inertia and viscous effects.

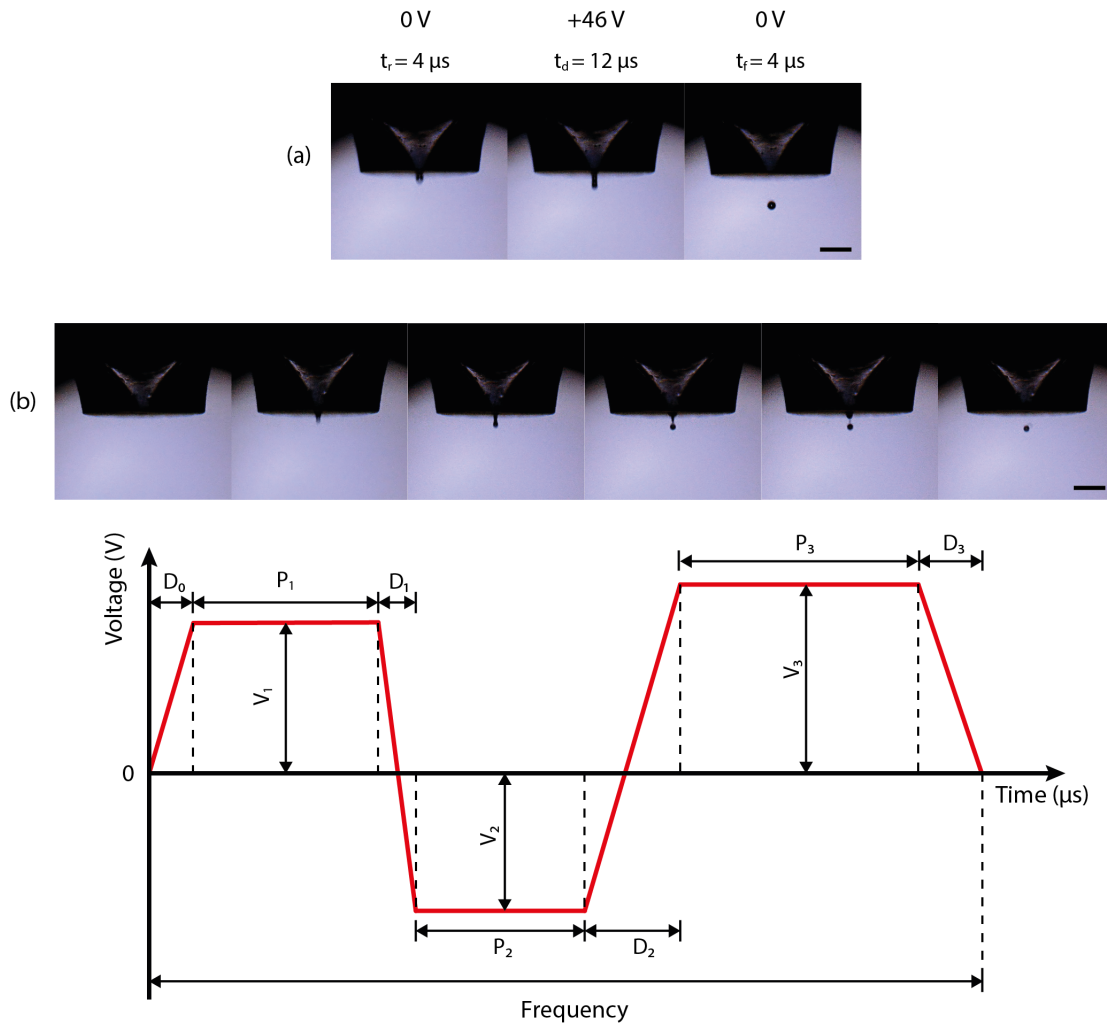


Fig. 3.4 Effects of controlling the applied voltage and duration of the applied voltage on the drop formation process. The sequence of images in (a) represents the application of single pulse of 46V and the effects on the drop formed, while (b) represents a detailed precise control over the application of oppositely directed triple pulses and the corresponding effect on a smaller drop formed. Scale bar is 500  $\mu m$  for each image in the sequences, both for (a) and (b).

Satellite drops also cause the formation of a secondary tail, which has been modelled by Wijshoff [216]. The small secondary tail may eventually break up in even smaller droplets which are dragged along the air flow induced by the firing sequence of the drops [217], resulting in a fine “spray-like” effect. The satellite droplets have a smaller volume than the main droplet, and hence have a larger velocity. As such, they can merge with the main droplet, provided they are in the same line of travel. Upon merging, the combined droplet oscillates and eventually stabilises into a stable spherical shaped drop.

Figure 3.5 below shows the effects of varying the voltage and pulse width on the drop formation process. When a large voltage is used to eject a droplet, this results in the formation of a long tail as well as a droplet with a large ejection velocity, as shown in Figure 3.5(a). As the voltage is reduced, the length of the tail is also reduced along with the ejection velocity, thereby minimising the possibility of satellite drop formation, as shown in Figure 3.5(b). In Figure 3.5(c), a large pulse width is used to produce a droplet at an optimum voltage, resulting in a large drop formation due to the additional volume. As the pulse width is also optimised, an optimum droplet is formed with a smaller volume and smaller ejection velocity, as shown in Figure 3.5(d).

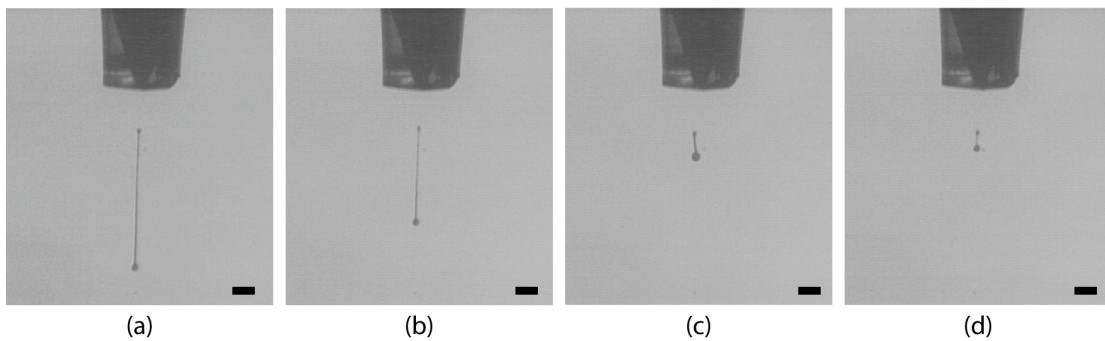


Fig. 3.5 Effects of varying the applied voltage and pulse width of a piezoelectric printhead. The high voltage used in (a) results in a long tail and high velocity of droplet ejection, and (b) reducing the voltage results in a shorter tail and lower velocity. Snapshot (c) represents a large drop due to a large pulse width, while (d) represents the optimum drop formation. Scale bar is 100  $\mu\text{m}$ .

Once the droplet has been formed, the time between ejection and deposition is crucial, especially in a piezo-electric DOD system, as it affects the resolution of the printed pattern through the placement accuracy in between subsequent droplet. Being a non-contact technique, the separation between the nozzle orifice and the substrate influences the time taken for the droplet to reach the desired location on the target surface. The placement accuracy can also vary because of drag from the surrounding atmospheric currents which can deflect the drops from their desired trajectory. To avoid this undesirable effect, the stand-off distance is usually set to the minimum, in the order of a few millimetres, depending on the droplet velocity.

### 3.2.2 Pattern resolution

The idea behind inkjet printing is to obtain narrow lines by using minuscule drops (drop volume in picolitres), and this generally can be achieved using a printhead of a small nozzle orifice and an optimised waveform to generate the drop. The geometry of the line resolution is then determined by the separation of drops, a parameter known as the droplet spacing (DS). In regular “at-home” inkjet terminology, when a user prints a document, the quality of the features on the document is determined by the choice of “DPI” settings – i.e. the “dots per inch”, instead of the droplet spacing. The user generally does not have much control other than choosing between a print quality of *draft*, *normal* or *best*, with the difference being in the DPI settings (starting from around 150 DPI for *draft*, 300 DPI for *normal* and increasing up to 1200 DPI for *best* depending on the printer).

For applied inkjet printing, in contrast, there is much more control over this parameter using droplet spacing (DS) instead of dots per inch (DPI). Figure 3.6 below is a representation of how the droplet spacing affects the final resolution of a printed square pattern. The diameter of the drop,  $d$ , remains unchanged while the droplet spacing is altered. As the drop spacing decreases (illustration on the right), the drop density increases for the same area of deposition, resulting in more material per unit area.

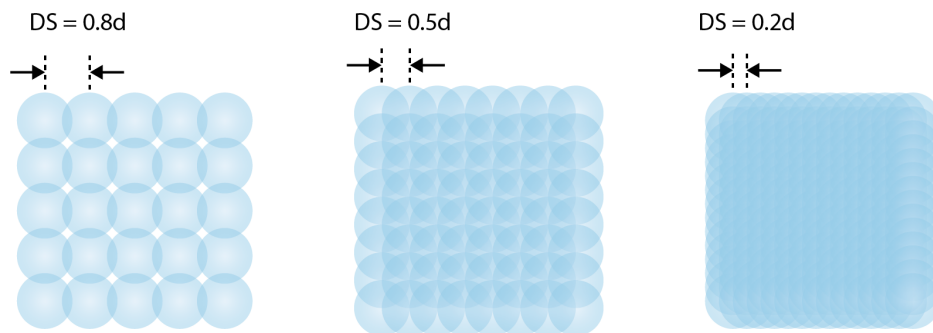


Fig. 3.6 Illustration of the effects of changing the droplet spacing (DS) on the density of drop for printing a square array. The diameter of the drop,  $d$ , remains unchanged.

A small droplet spacing is advantageous when printing conductive inks as there is more conductive material per unit area, which ensures a highly functional pattern. However, there are limits as to what defines a pattern with a high resolution. The choice of droplet spacing cannot be done randomly as the overlapping of drops can result in a variety of scenarios, as described by Soltman and Subramanian [218]. Figure 3.7 represents the droplet spacing optimisation process to yield a uniform track with an optimum resolution. As the droplet spacing is decreased from Figure 3.7(a) - (d), the droplets on the pattern merge to form a uniform smooth track with well-defined edges.

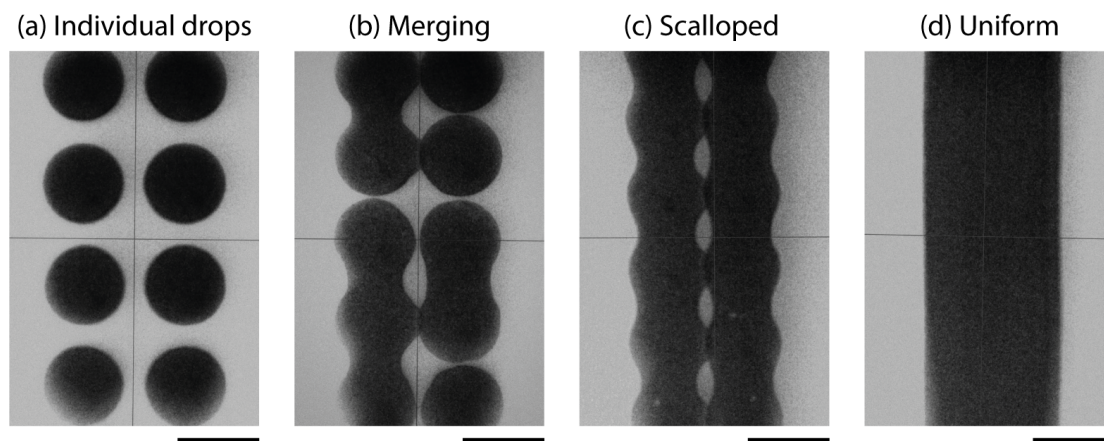


Fig. 3.7 Effects of changing the drop spacing for a track. (a) represents individual drops, (b) randomly merged drops, (c) scalloped track, and (d) uniform track. The droplet spacing decreases from left to right. Scale bar is 50  $\mu\text{m}$ .

When combined with a heated substrate, it is possible to print patterns with a high resolution by printing additional layers. It is critical to ensure the layer underneath has been pinned at the edges to prevent the overspreading due to the additional volume of ink from the subsequent layers, which ensures a high aspect ratio ( $h/w$ , where  $h$  is height and  $w$  is width) of the final pattern [219]. For functional inks of a conductive nature, the multiple layers enable more pathways for the electrons to flow (in both latitude and longitude), further consolidating the conductive electrical properties of the printed pattern. It is common to print patterns of a minimum of two layers to ensure reliability, while four-layer patterns are also favourable, although a compromise between optimum electrical functionality and an increased cost of material and duration accompanied with printing four layers has to be made.

### 3.3 Laser system

A pulsed laser sintering system was used to perform the laser sintering operation on the nanoparticle-based inks. A pulsed laser diode system from Laser Components Ltd. was purchased as it has a much smaller footprint and can hence be adapted to the printing system, with the aim of using the  $x$ - $y$  stage to control the irradiation pattern. The diode material is made out of AlGaAs (Aluminium Gallium Arsenide) and the wavelength of the emitted radiation is in the near infrared (NIR) region, with 905 nm at peak radiant intensity, with a minimum and maximum of 895 nm and 915 nm respectively. The peak power emitted from the diode is 75 W and this can be achieved by very precise control of the pulsing parameters, and through a stacked combination. The supplied diodes are triple junction devices, each junction emitting up to 25 W of peak power at  $I_{th} = 35$  A. The emitting area is confined to  $235 \times 10 \mu\text{m}^2$  with a beam spread of  $12^\circ$  parallel to the junction plane, and  $20^\circ$  perpendicular to the junction plane at 50 % peak intensity. However, the emitting area is further collimated by using a combination of aspheric and achromatic lenses, which reduce the beam dimension to  $200 \times 15 \mu\text{m}^2$ , ensuring the irradiated beam spread is reduced minimally and focussed on the sample.

First, an aspheric lens is used to collimate the beam without introducing spherical aberration into the transmitted waveform. To achieve perfect collimation, the separation between the output of the diode and the aspheric lens was controlled by using a 19.1 mm sliding cage plate with a 100 TPI (threads per inch) fine adjuster. Once the laser beam is collimated into parallel rays, a shortpass dichroic mirror placed at a  $45^\circ$  angle redirects the beam onto the  $x$ - $y$  stage. Dichroic mirrors spectrally separate light by transmitting and reflecting light as a function of the wavelength. Shortpass dichroic mirrors are highly transmissive below the cutoff wavelength and highly reflective above it, and in this case the mirror has a cutoff wavelength of 650 nm, providing  $> 85$  % absolute transmission between 400 – 633 nm and  $> 90$  % absolute reflection between 685 – 1600 nm.

Finally, a 20X microscope objective with a working distance of 8.80 mm is used to focus the laser beam to yield a higher on-target power density for optimum efficiency during sintering. A 5 megapixel CMOS image sensor (Basler AG) is used to capture the image of the sample under irradiation once collimated by another achromatic doublet lens, thus bringing the source image into focus at the CMOS sensor. The sensor has an active area of  $5.70 \times 4.78 \text{ mm}^2$ , and the focal length of the zoom lens is 50.2 mm. Altogether, it provides a viewing area of approximately  $10 \times 8 \text{ mm}^2$ . The CMOS sensor can control the aperture and exposure, and at the same time capture at 30 frames per second, thereby enabling the irradiation process to be monitored “live”.

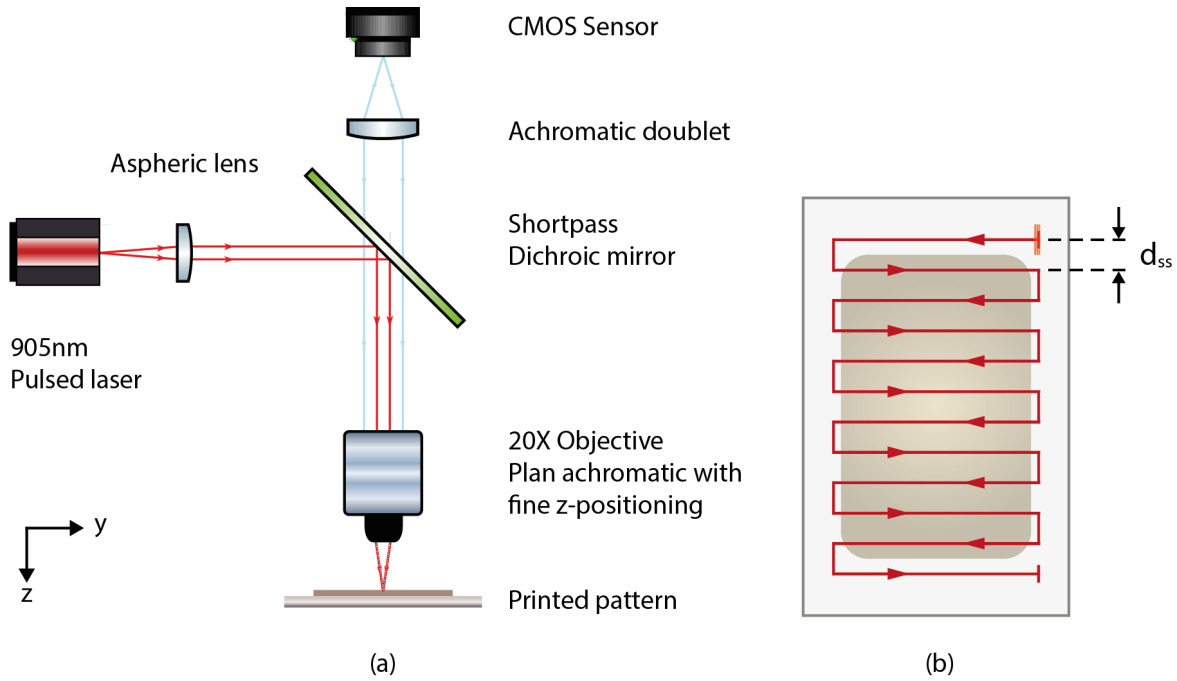


Fig. 3.8 (a) Illustration of the custom-built 905nm pulsed laser sintering system showing the key components. The printed pattern is placed on a fast-scanning  $x$ - $y$  stage. (b) represents the “snake scanning” approach for laser sintering of the printed pattern, highlighting the importance of fine tuning the overlap between each sintered row ( $d_{ss}$ ).

Due to the small rectangular spot size of the laser, a “snake scanning” approach (Figure 3.8) was used to sinter the patterns as a single lengthwise pass did not cover the entire area of the printed pattern. Due to the scanning approach, the overlap between each sintered row ( $d_{ss}$ ) is critical to ensure a continuously sintered pattern, hence the overlap percentage was also varied to determine the optimum overlap without leaving unsintered regions.

The overlap of the pulse was calculated from the area of beam profile between the separation of the two adjacent “rows”,  $d_{ss}$ , and quoted as a percentage based on the total area of the beam, as shown in Figure 3.9 below. The percentage of overlap was varied from 5 %, 15 %, and 30 %. A script was written to calculate the overlap percentage based on the total area superimposed (Appendix A.1) and fed back into the programming software for the pulsed laser sintering process, as shown in Figure 3.10.

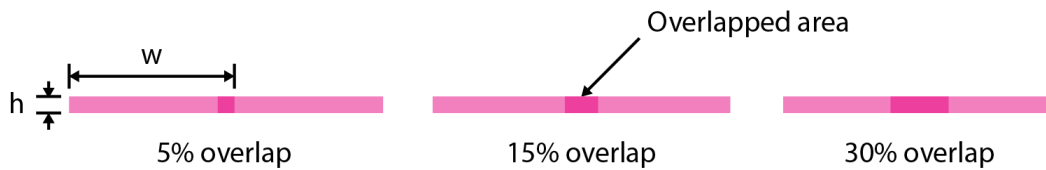


Fig. 3.9 Illustration of the variation of the pulse overlap between adjacent “rows”.

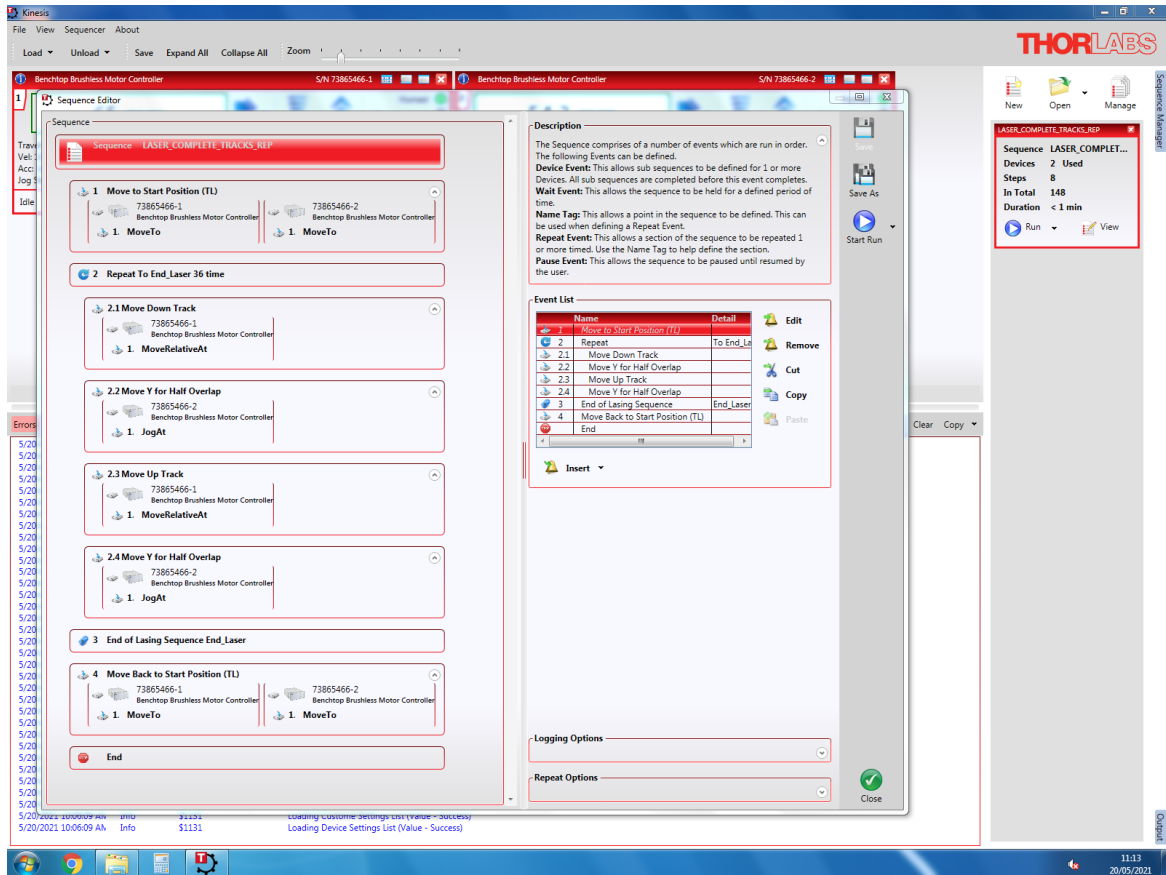


Fig. 3.10 Snapshot of the graphical user interface used for programming the laser sintering pattern.

The pulse parameters of the laser were varied in terms of pulse width and repetition rate, while the emitting current was maintained at 25 A. The variation in terms of pulse width and repetition rate had a direct impact on the laser pulse energy per effective focal spot area, i.e. the fluence. The variation in laser fluence strongly affects the sintering process for the nanoparticles due to the amount of radiation absorbed in the material during the interaction.

A schematic of the custom-built pulsed laser sintering station is shown in Figure 3.11. A more detailed rendered CAD model of the laser sintering system is included in Appendix A.2.

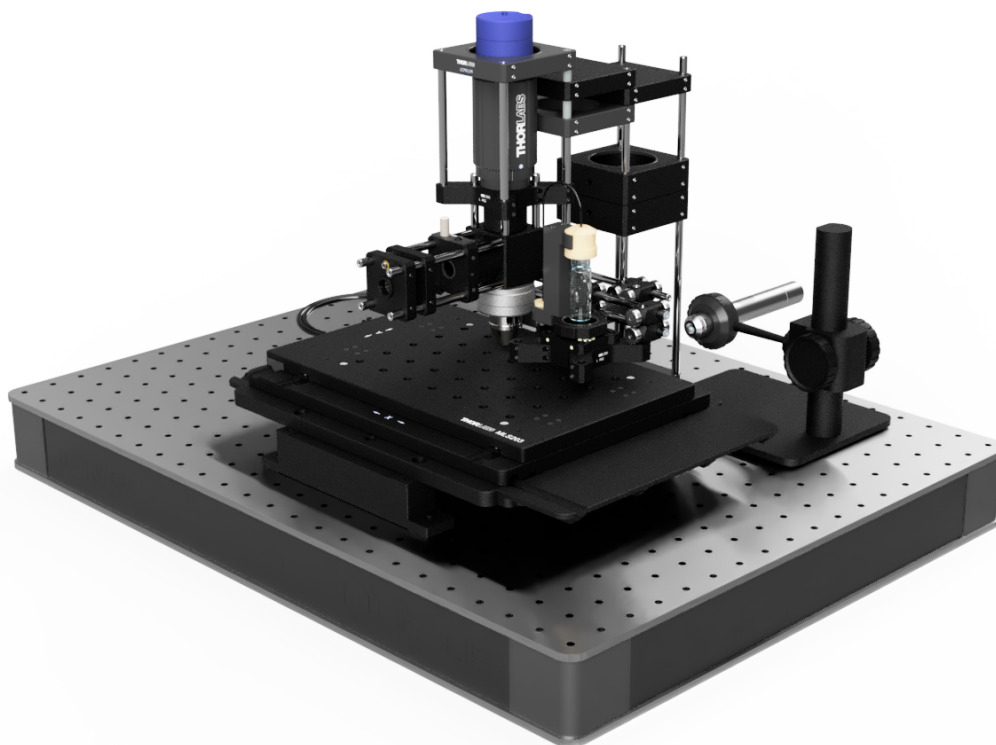


Fig. 3.11 A schematic of the custom-built pulsed laser sintering station.

Table 3.3 and 3.4 below shows the range of laser sintering parameters investigated during the experiments as a variation of pulse width. The diode has a maximum rated duty cycle of 0.25 %, hence this was the limiting factor of irradiation as exceeding this value would result in permanent damage of the diode, and the maximum fluence values are highlighted in red. The variation of pulse width directly increased the amount of energy delivered in the pulse, while the variation of repetition rate increased the frequency of the pulse delivery, and hence the average power delivered.

The AlGaAs semiconductor laser diode comes in a 5.6 mm hermetically sealed TO can housing to ensure reliability, precise chip alignment, and passive cooling during irradiation. The optical output power as a function of the applied forward current in the diode can be seen in Appendix A.3.

Table 3.3 Summary of the pulse laser sintering parameters varied at 6000 Hz.

<b>Pulse width (ns)</b>	<b>Repetition rate (Hz)</b>	<b>Current (A)</b>	<b>Duty cycle (%)</b>	<b>Pulse energy (<math>\mu J</math>)</b>	<b>Average power (W)</b>	<b>Peak power (W)</b>	<b>Fluence (<math>mJ/cm^2</math>)</b>
50	6000	25	0.0300	2.68	0.01607	53.57973036	89
75	6000	25	0.0450	4.02	0.02411	53.57973036	134
100	6000	25	0.0600	5.36	0.03215	53.57973036	179
125	6000	25	0.0750	6.70	0.04018	53.57973036	223
150	6000	25	0.0900	8.04	0.04822	53.57973036	268
175	6000	25	0.1050	9.38	0.05626	53.57973036	313
200	6000	25	0.1200	10.72	0.06430	53.57973036	357
225	6000	25	0.1350	12.06	0.07233	53.57973036	402
250	6000	25	0.1500	13.39	0.08037	53.57973036	446
275	6000	25	0.1650	14.73	0.08841	53.57973036	491
300	6000	25	0.1800	16.07	0.09644	53.57973036	536
325	6000	25	0.1950	17.41	0.10448	53.57973036	580
350	6000	25	0.2100	18.75	0.11252	53.57973036	625
375	6000	25	0.2250	20.09	0.12055	53.57973036	670
400	6000	25	0.2400	21.43	0.12859	53.57973036	714
<b>425</b>	<b>6000</b>	<b>25</b>	<b>0.2550</b>	<b>22.77</b>	<b>0.13663</b>	<b>53.57973036</b>	<b>759</b>

Table 3.4 Summary of the pulse laser sintering parameters varied at 8000 Hz.

Pulse width (ns)	Repetition rate (Hz)	Current (A)	Duty cycle (%)	Pulse energy ( $\mu$ J)	Average power (W)	Peak power (W)	Fluence ( $mJ/cm^2$ )
50	8000	25	0.0400	2.68	0.02143	53.57973036	89
75	8000	25	0.0600	4.02	0.03215	53.57973036	134
100	8000	25	0.0800	5.36	0.04286	53.57973036	179
125	8000	25	0.1000	6.70	0.05358	53.57973036	223
150	8000	25	0.1200	8.04	0.06430	53.57973036	268
175	8000	25	0.1400	9.38	0.07501	53.57973036	313
200	8000	25	0.1600	10.72	0.08573	53.57973036	357
225	8000	25	0.1800	12.06	0.09644	53.57973036	402
250	8000	25	0.2000	13.39	0.10716	53.57973036	446
275	8000	25	0.2200	14.73	0.11788	53.57973036	491
300	8000	25	0.2400	16.07	0.12859	53.57973036	536
<b>325</b>	<b>8000</b>	<b>25</b>	<b>0.2600</b>	<b>17.41</b>	<b>0.13931</b>	<b>53.57973036</b>	<b>580</b>

## 3.4 Analytical methods

This section covers the analytical tools and methods used to quantify the performance of the samples both from a quantitative and qualitative perspective. Numerous pieces of equipment are described, including the make & model, as well as any prior treatment performed before analysis.

### 3.4.1 Rheology: Viscometer and Circulation bath

The viscosity of the measured inks was quantified using the SV-1A viscometer by A&D Company Ltd, as shown in Figure 3.12. The viscometer consists of two oscillating paddles driven in opposing directions which measures the viscosity of the fluid through the tuning-fork measurement technique. In this technique, the plates are vibrated at a controlled frequency required to maintain a uniform displacement caused by the viscosity between the fluid and the sensor plates. Prior to the measurement of the inks, a two-point calibration was performed to ensure consistency between the results. Two fluids of known viscosity at a particular temperature were used, namely distilled water ( $0.8891 \text{ mPa} \cdot \text{s}$  at  $25 \text{ }^\circ\text{C}$ ) and a viscosity standard fluid (Paragon scientific) ( $0.2950 \text{ mPa} \cdot \text{s}$  at  $25 \text{ }^\circ\text{C}$ ). The temperature of the fluid was controlled by using a heated circulating water bath (Grant Optima TXF200) surrounding the ink reservoir jacket.

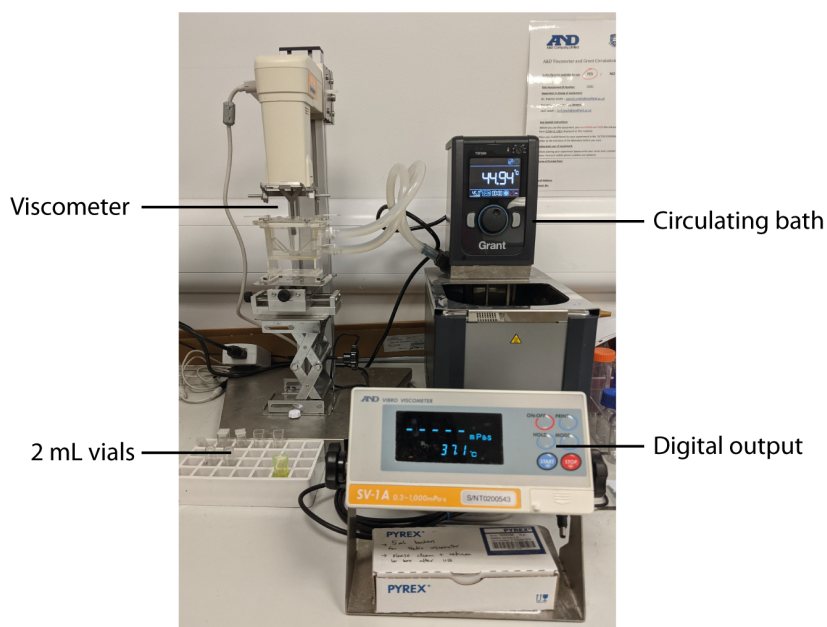


Fig. 3.12 A snapshot of the SV-1A viscometer and the circulating bath used for viscosity measurements.

### 3.4.2 Contact angle

The contact angle of the ink on the substrate was measured using the JetLab jetting station, with a micro-syringe attached. The back pressure was controlled using the built-in vacuum pump, and the droplet wetting process was visualised using the Thorlabs DCC1545M CMOS sensor fitted with a zoom lens. The Thorcam software was used to capture the image, followed by the measurement of the contact angle using an ellipse best-fit, as shown in Figure 3.13 below.

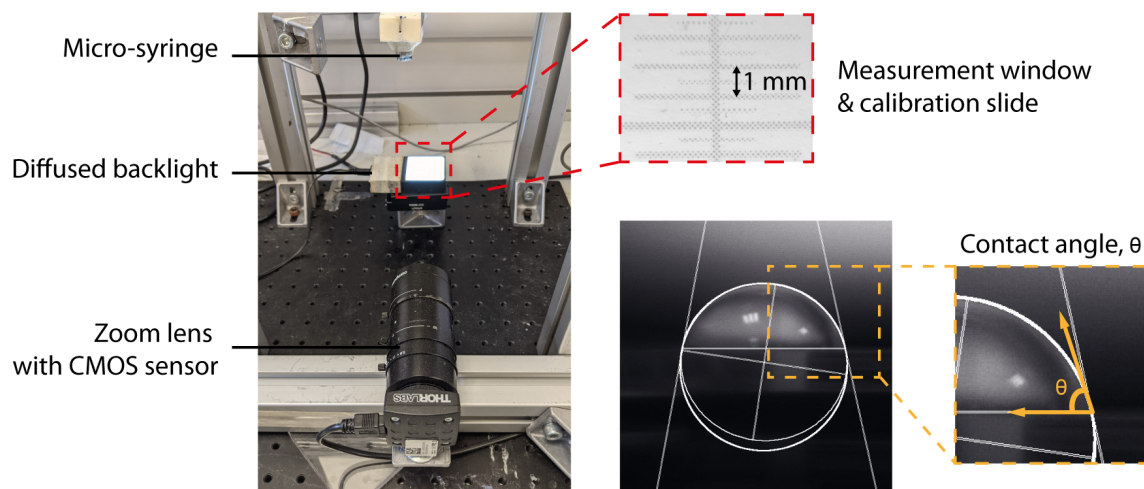


Fig. 3.13 A snapshot of the jetting station with a micro-syringe attached, and the relevant measurement window showing the contact angle measurement process.

### 3.4.3 Atomic Force Microscopy

The thickness of the printed samples was evaluated using atomic force microscopy (Nanoscope IV – TM-AFM, Bruker Inc., Kroto Research Institute) as shown in Figure 3.14 under the tapping mode technique which limits the chances of contamination of the tip from foreign substances such as unsintered nanoparticles, ablated nanoparticle patches, or simple dust particles. The longitudinal deflection resolution of the probe can detect instances as minuscule as a few *nm* in height. The lateral and vertical deflection of the cantilever is measured by using an optical lever which reflects a laser beam off the cantilever. The reflected laser beam is then captured on a position-sensitive photodetector which calculates the position of the laser spot, and hence the angular deflection of the cantilever.

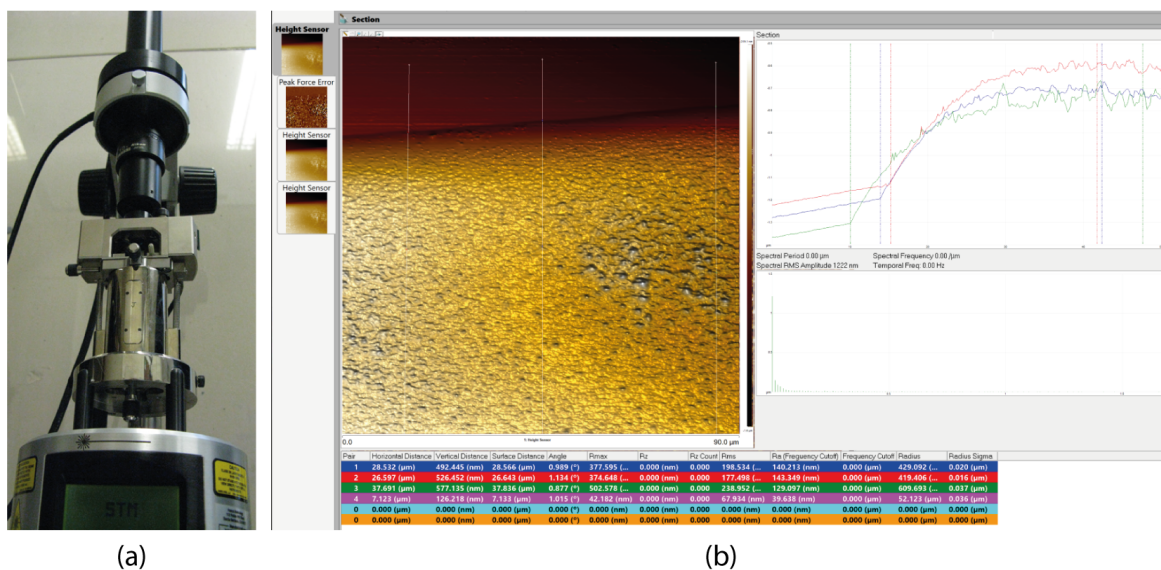


Fig. 3.14 (a) A snapshot of the AFM used to quantify the thickness of the samples, and (b) the output of the analysis.

### 3.4.4 Spectrophotometry

To gain a more thorough understanding of the laser sintering of both the silver and copper NPs ink used throughout this experiment, the optical absorption spectrum of both inks was quantified in the ultraviolet (UV), Visible light (Vis) and near infrared (NIR) range, i.e. from 240 *nm* – 2500 *nm* inclusive. These were performed with highly diluted doses down to 0.01 *wt.%* of both inks in their subsequent solvent (diethylene glycol) due to the high concentration of nanoparticles, and a small sample of the diluted ink (4*mL*) was deposited in a cuvette which was irradiated. Two distinct pieces of equipment were used (for UV-Vis: Cary50, Agilent Technologies Inc.; and for NIR: NIRQuest 2500, Ocean Optics Inc.) due to the limited range of measurements. UV-Vis and NIR measurements were carried out using an integration time of 10 *ms*, taking 10 scans to average.

### 3.4.5 Scanning Electron Microscopy

Scanning electron microscopy was used to obtain a closer analysis of the surface of the samples with an inspection window of a few  $\mu\text{m}^2$ . The SEM imaging facility at the Sorby Centre for Electron microscopy (Kroto Research Institute) was used. The samples, as they were conductive, required a 10 *nm* carbon coating and the addition of silver paint around the edges of the substrate to avoid excessive charge. A low electron acceleration voltage of 2 *kV* was used to produce a high resolution contrasting image.

Once imaged, the analysis of the SEM images include simple void analysis where a set of images at different locations on a sample with the same imaging parameters are inspected for voids, particularly to understand the sintering process of nanoparticle-based inks. Additionally, the heat-affected zone formation was quantified using digital imaging software to highlight regions of interest where the laser was pulsed, namely regions of partial or complete sintering along with the corresponding heat affected zone, if any. A look-up table (LUT) filter was applied based on the threshold brightness and contrast of all the images to aid in the calculation of the heat affected zone – the LUT converts each individual pixel based on its colour value and returns a new colour value based on the type of filter used (in this case, *mpl-viridis*). Figure 3.15 below shows an example of the LUT filter used to highlight the region treated with the laser to aid in the calculation of the HAZ.

Once the filter was applied, the particles corresponding to a range of values above a threshold set by the image background was used to evaluate the treated area. The determination between partial and complete sintering was done based on the critical evaluation by the user upon comparison with the effective irradiated area of the laser beam ( $200 \times 15 \mu\text{m}^2$ ). For example, in the Figure 3.15 below, the irradiated area is determined to only be partially sintered at only 30 %, while a completely sintered area would equate the geometry of the collimated laser beam. Higher values of irradiated area could cause damage to the printed layer or to the substrate, or a combination of both, and would indicate a formation of a HAZ which was also measured based on the size of the plume.

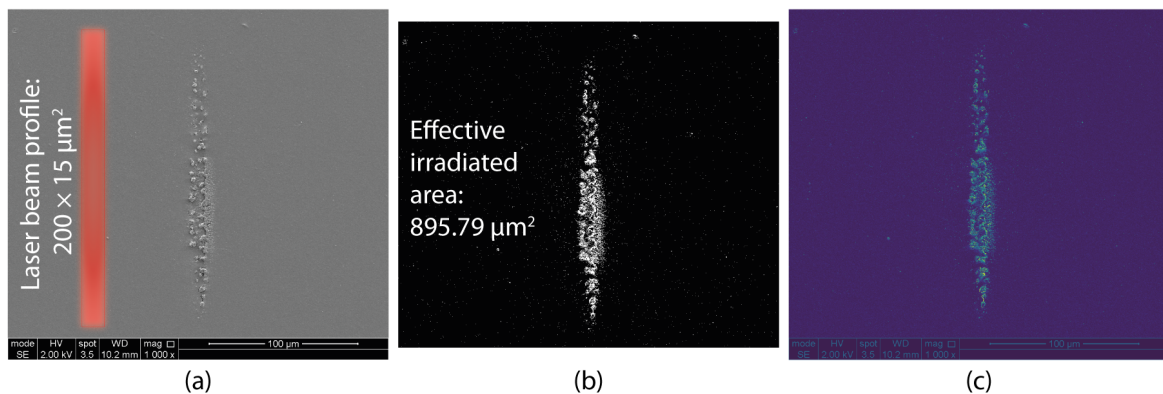


Fig. 3.15 Snapshot of the application of the LUT image processing filter (*mpl-viridis*) used to highlight the region of interest, in this case the partially sintered pattern after pulsed laser irradiation. Figure (a) shows the SEM image as captured, (b) shows the calculation step based on the ROI, and (c) shows the similar image after image processing. The copper nanoparticle layer is printed on paper.

### 3.4.6 Conductivity comparison

The electrical conductivity of the printed functional inks was used as a measure of success following the thermal sintering/curing process using the four-point probe method. By using four probes – two as source leads to supply the test current and the other two as sense leads to measure the voltage difference across the samples under test – it eliminates any systematic error of resistance due to the leads or contact between the probes and the sample. A custom-built four-point probe system was used for the precise measurement of the conductivity of the samples made out of silver. The probes were made out of gold-coated tubular barrel which was spring-loaded. They were connected to a four-terminal resistance meter (Applent Instruments Ltd.) and calibrated using known conductivity values from gold samples to eliminate any stray impedance within the leads. Figure 3.16 below shows a snapshot of the four-point probe test station, and technical details of the probes.

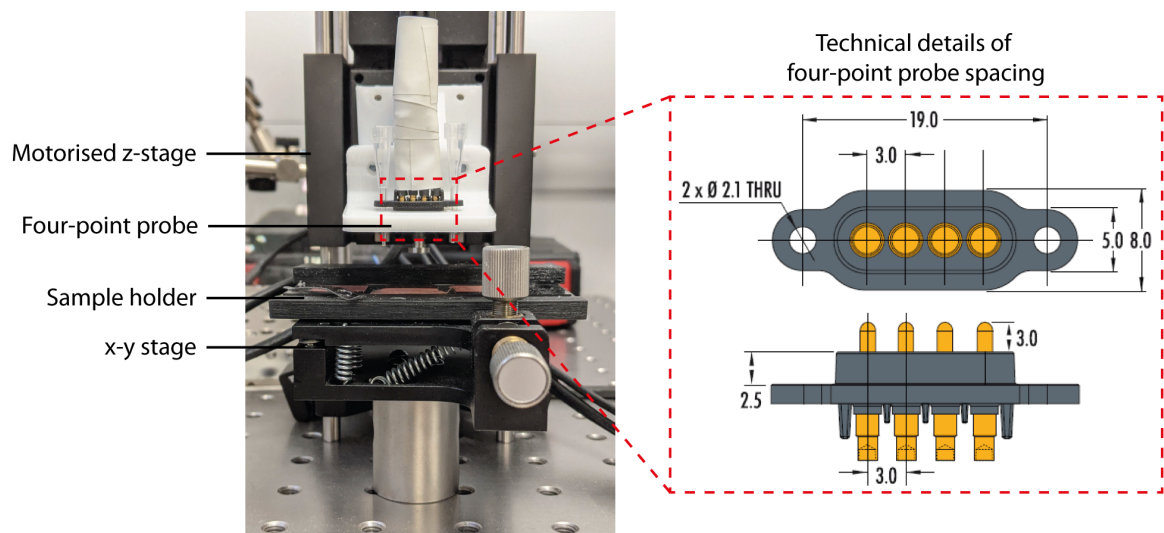


Fig. 3.16 A snapshot of the custom-built four-point probe test station used to quantify the conductivity of the samples, and technical specifications of the probes.

The four-point probe was mounted on a motorised test station to prevent any scratches to the test surface during measurement by the user. The test station allowed the four probes to be lowered in a controlled manner until contact was made with the sample, thereby preventing an excessive downward actuating force which could penetrate or damage the ink coating, or the substrate. As the probes were spring-loaded, the recommended actuating distance was 1.35 mm to ensure reliable contact was made with the sample to record a conductivity value. The contact location of the probes onto the surface was also controlled by fine tuning knobs in the *x-y* axis of the stage where the substrate was attached during testing.

A rendered CAD model of the four-point probe test station can be found in Appendix A.4.

The sheet resistance,  $R_s$ , of the samples can be calculated using the following Equation 3.1:

$$R_s = 4.532 \times \frac{V}{I} \quad (3.1)$$

where “ $V$ ” is the voltage and “ $I$ ” is the current measured across the samples, and provided the following conditions are met:

- (i) the spacing between the probes must be constant;
- (ii) the thickness of the film being tested is less than 40% of the probe spacing;
- (iii) the edges of the film are more than 4 times the spacing distance from the measurement point.

The derivation of the above Equation 3.1 can be found in Appendix A.5.

The sheet resistivity,  $\rho_s$ , can then simply be calculated by multiplying the sheet resistance by the thickness,  $t$ , of the printed pattern as shown in the following Equation 3.2, and the sheet resistivity value can be compared to the bulk resistivity value of silver ( $1.59 \times 10^{-8} \Omega \cdot m$ ) and copper ( $1.72 \times 10^{-8} \Omega \cdot m$ ).

$$\rho_s = R_s \times t \quad (3.2)$$

### 3.4.7 The ASTM F1842-15 Cross-cut test

The adhesion of the samples was tested according to the ASTM F1842-15 standard using scotch tape. It is a standardised test method for determining the ink adhesion on substrates for printed electronic devices [220], and it is based on the ASTM D3359 standard [221]. The ASTM standard F1842-15 described the apparatus required for the testing the adhesion of an ink on flexible substrates for printed electronics applications. The specification for the cutting tool, described as a multi-blade cutter (or cross-cutter) are extracted as follows:

- (i) The blade angle must be between  $15 - 30^\circ$ ;
- (ii) The cutter must perform 6 cuts at once;
- (iii) The blade spacing must be maintained  $2\text{ mm}$  apart;
- (iv) The cutting edges must be in good condition.

With these specifications, a multi-blade cutter can be easily purchased (or manufactured to specifications) from online retailers. However, there is no mention of the type of material which can be used for the blades, which in turn reflects on the durability of the cutter. This can potentially affect the last specification “the cutting edges must be in good condition” as the sharpness of the blades can suffer after multiple uses due to the formation of micro-cracks or micro-indentations along the blade profile, resulting in bluntness.

A multi-cutter was purchased from an online retailer which satisfied the four specifications mentioned earlier. However, the cutting edge of the blades deteriorated after multiple uses due to the “blade softness” or ductility of the material, which eventually led to inaccurate results. Figure 3.17(a) below is a snapshot of the multi-blade cutter. After a series of tests performed according to the procedure, the edge of the blade was found to have significantly deteriorated as shown in Figure 3.17(b). The blade edge deterioration resulted in the excessive removal of printed material from the substrate. At this stage, the validity of the adhesion test was questionable, and it was futile to regrind the edges to the correct alignment (shown in Figure 3.17(a), solid red line) as the spacing of the blades would increase and the planar alignment would be offset.

The ASTM F1842-15 standard is based on the existing D3359 test method, which is a similar test in terms of procedure and equipment required, with the only difference being in the thickness of the test specimens which can be used for printed electronics applications. In the D3359 methodology which describes the cross-cut tape test, the cutting tool mentioned in Section 10.1 can also be a sharp razor blade, scalpel or knife, as long as the blade angle is between  $15 - 30^\circ$  [221].

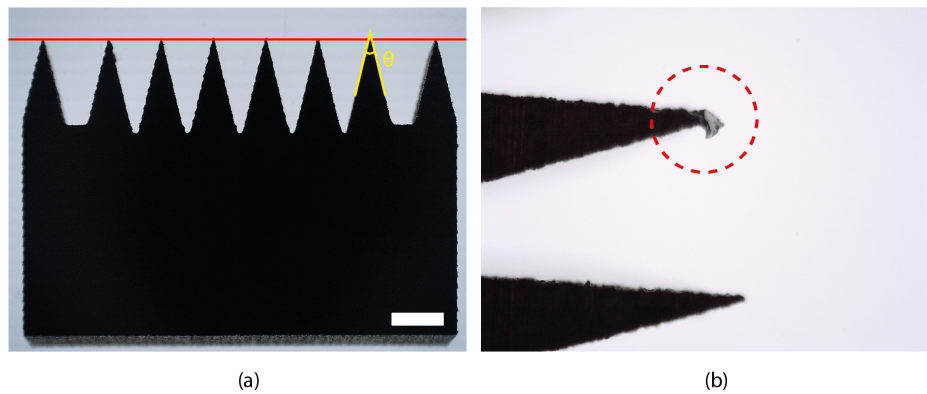


Fig. 3.17 Snapshot of the multi-blade cutter purchased from an online retailer, highlighting (a) the alignment of all the cutting edge of the blades (solid red line) and the blade angle of  $\theta = 30^\circ$  (yellow line), and (b) deterioration of the cutting edge due to the softness of the blade (dashed red circle). The white scale bar in (a) is 2 mm.

In order to conform to the testing standard, this section will describe the design and fabrication of an in-house cross-cutter made with scalpel blades. The selection of scalpel blades was made due to their precise blade angle, and the easy swappable nature of replacing the blades if they no longer satisfied the specifications due to misuse, or wear and tear. The design of the scalpel cutter is shown in Figure 3.18 below and consists of six scalpel blades separated by 2 mm. The blade angle was measured and was found to be  $20.6 \pm 0.1^\circ$ , hence satisfying all four criteria for the cross-cutter testing apparatus.

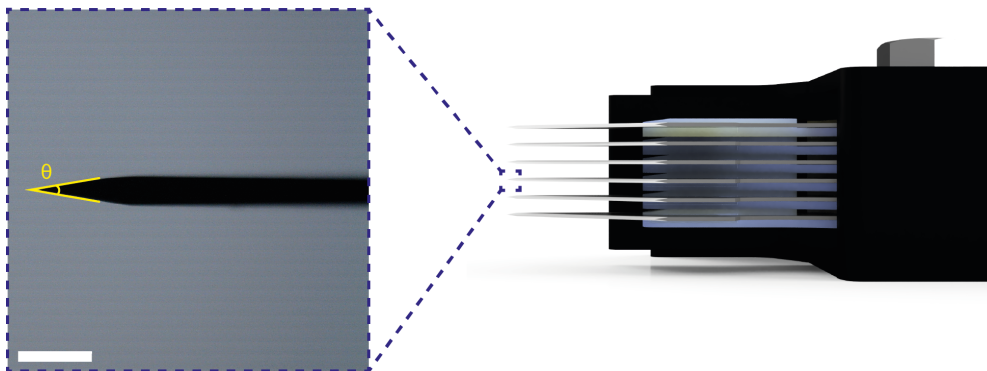


Fig. 3.18 Illustration of rendered 3D model of cross-cutter, showing the mechanism used to maintain a 2 mm separation between the 6 scalpel blades, and the detailed-view inset showing the measurement of the blade angle with  $\theta = 20.6^\circ$ . The scale bar in the inset is 2 mm.

The testing procedure relies on the precise alignment and contact of all six blades to the test surface to ensure a continuous cut was placed across the testing surface, as specified in Section 11.1 of the D3359 standard. The design of the handle contained an alignment plate (Figure 3.19) which was used to apply a uniform pressure over the surface of all six

blades, thereby ensuring the aligned downwards displacement of the blades during the testing procedure. The alignment plate is actuated using a spring mechanism to allow the blades to maintain an aligned state at rest.



Fig. 3.19 Actual snapshot of the in-house, 3D printed and assembled cross-cutter, highlighting the alignment plate used to maintain the planar alignment of the blades, and the spring mechanism to ensure a constant pressure is applied during the testing procedure.

The scalpel blades were mounted in a jig (Figure 3.19) which was used to maintain the spacing of the blades at 2 mm apart when compacted together inside the handle. An  $M5 \times 25$  mm bolt was used to tighten the mechanism together with all the components. All the components, except the blades, spring and fastener were 3D printed using an extrusion printer (Anet A8 using  $\emptyset 1.75$  mm filament) with a 0.40 mm extruder nozzle, allowing to precise features down to 0.10 mm to be printed. The high precision ensured the printed components conformed to the modelled specification and precision, thereby eliminating manufacturing imperfections. A full technical assembly drawing of the cross-cutter can be found in Appendix A.6 which details the overall dimensions of the design and the exploded view highlighting the fit of all the components together.

### Testing procedure

The procedure begins by brushing the blades to remove any debris, followed by cutting into the test sample in a straight line. The sample is then brushed off for any loose particles which may have been removed from the surface, and a second identical cut is placed, perpendicular to the first, to achieve a grid pattern. Similarly, the surface is brushed followed by the application of an adhesive tape to the cut sample, ensuring good contact is made with the specimen. After 90 seconds, the tape is removed by steadily peeling it off back upon itself as close to a  $180^\circ$  angle as possible. The grid area is then inspected and compared against the standard. Figure 3.20 below represents the procedure for the cross-cut test, and the cross-cutter used for this experiment.

The tape (product number Scotch 810-25) used throughout this experiment was purchased from the 3M company. The adhesive specification for the tape, which was mentioned in the ISO 2409 standard, indicates the peel strength must be between  $6N - 10N$  per  $25\text{ mm}$  [222], and the tape chosen for an experiment must be from the same batch and conform to some specifications such as the peel strength. Based on the data provided from the supplier, the peel strength of the tape measured  $6.5\text{ N}$  per  $25\text{ mm}$ . Additionally, the thickness and width of the tape are  $0.05\text{ mm}$  and  $19\text{ mm}$ , respectively, and it has a clear transparent colour which allows for the precise placement of the adhesive on top of the printed pattern. The application of the tape first begins with discarding one lap of tape around the roll to ensure reliability of the tape performance, followed by cutting a length of  $30\text{ mm}$  from the roll and immediately placing the centre on the printed square surface. The tape is then firmly pressed onto the surface, and after 90 seconds, the tape is peeled in a steady rate as depicted in Figure 3.20, *Step 2*.

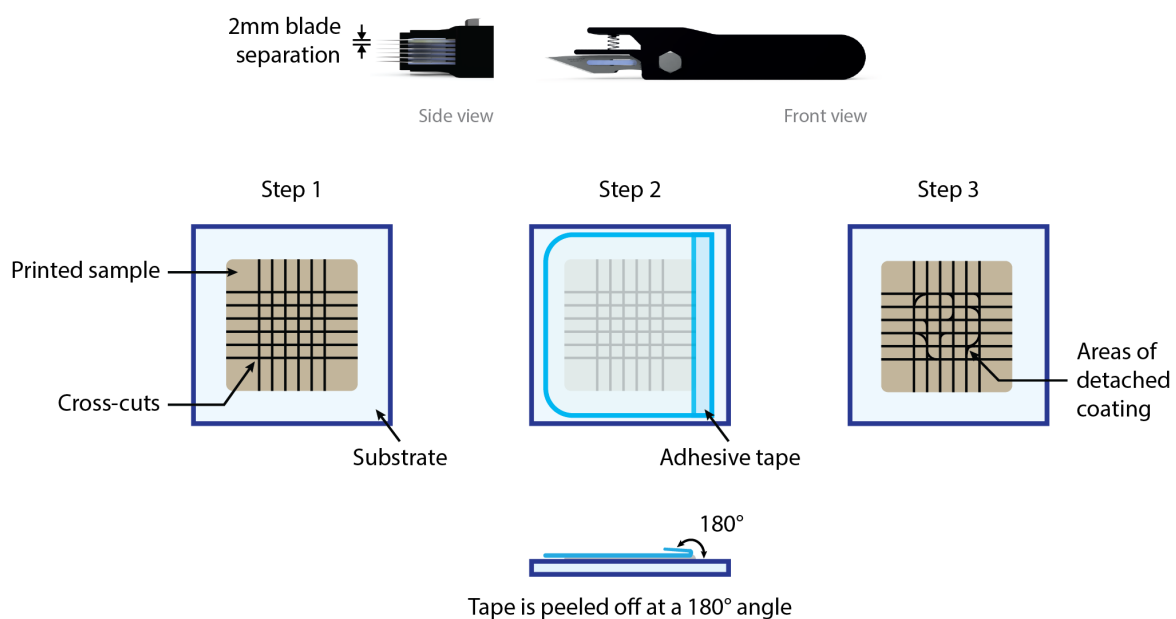


Fig. 3.20 Illustration of the cross-cut procedure, showing the in-house fabricated cutter used to maintain a  $2\text{ mm}$  separation between the blades, and the 3-step process of evaluating the adhesion of the printed sample.

### Adhesion classification: A digital perspective

The evaluation procedure after the cross-cut test is performed simply involves an inspection of the grid area of the cut sample, and a comparison with the standard test results table from Figure 3.21. The scale provides a classification of the adhesion level based on the amount of detached material (i.e. *flaking*) and the detached area.

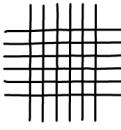
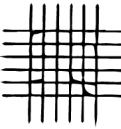
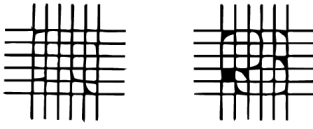
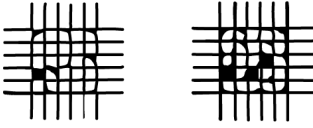
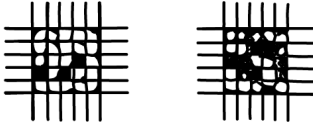
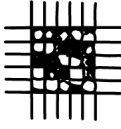
Classification of Adhesion Test Results		
Classification	Percent Area Removed	Surface of cross-cut area from which flaking has occurred for six parallel cuts and adhesion range
5B	0% None	
4B	Less than 5%	
3B	5 - 15%	
2B	15 - 35%	
1B	35 - 65%	
0B	Greater than 65%	

Fig. 3.21 Classification of the different adhesion levels as a result of the cross-cut test. The table has been adapted from reference [222] with permissions.

The classification of the results from Figure 3.21 introduces a relatively large margin for classifying the adhesion of the sample simply based on the subjective evaluation of the user. This can introduce some form of bias and inaccuracies due to human error. Lukacs

et al. [223] recently elaborated on the evaluation of the cross-cut tape test and explained the subjective bias in sampling the results due to human error. In their research output they compared results obtained from different individuals and found that the classification of the adhesion results in the mid-range was subjective and varied across different individuals. As a solution, they introduced an image processing software to evaluate the sample, which eventually eliminates the human bias and provides a more rigorous, systematic evaluation procedure.

The use of an image processing software to calculate the detached area can be done in a simple three-step process as shown in Figure 3.22 below. First, the image is imported and cropped according to the region of interest (ROI) in a monochrome format to allow for the optimal threshold to be adjusted. The threshold process can be done automatically through the software which uses the “IsoData” threshold calculation approach, implemented from the research output from Ridler and Calvard [224]. The procedure separates the image into an object and background based on an initial threshold value, followed by computing the average of the pixels at or below the threshold value, and the pixel above are computed. This iterative approach is repeated until the threshold is larger than the composite average. Next, the highlighted area is calculated, which reports the detached area based on the ROI. This detached area value is then used to classify the adhesion of the sample. This methodology provided an unbiased and a more systematic and reliable assessment of the adhesion.

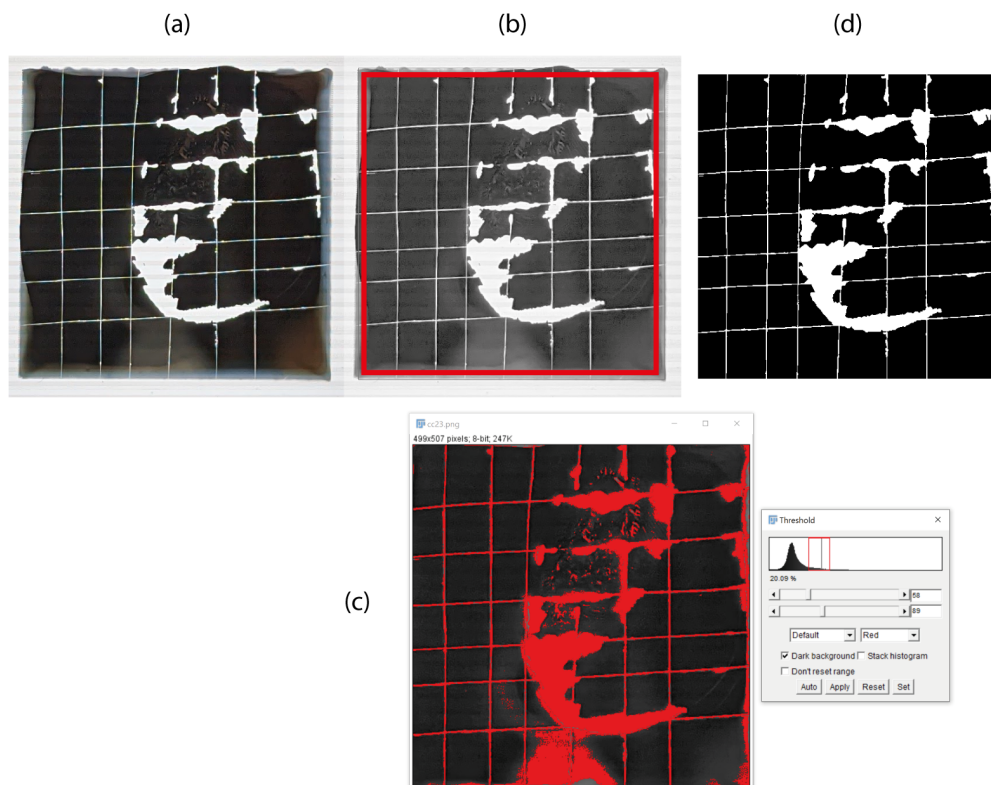


Fig. 3.22 Snapshot of the 3-step process of evaluating the detached area of the grid after the tape has been peeled off, starting with (a) importing the image, (b) cropping and converting to a monochrome picture, (c) adjusting the threshold to distinguish from the darker and lighter area, and (d) representation of the detached area.



# Chapter 4

## Setting the baseline using conventional methods

### Summary

In this chapter, a baseline for future comparison is set through experimental methods. A variety of silver inks of different compositions are inkjet-printed and converted to conductive features using conventional sintering via a hotplate. Three unique silver inks were tested, including a nanoparticle-based (NPs) suspension ink; a metallorganic decomposition (MOD) solution-based ink composed in-house using silver neodecanoate dissolved in a solvent; and a reactive silver ink, composed of silver acetate dissolved in an amine solution. The heat treatment process was determined to be optimised for each ink when the electrical performance did not exhibit any drastic changes.

The variation of the chemical composition of the inks was necessary to highlight the influence of particle or crystal size on the electrical performance of the printed patterns. The porosity and the particle size distribution were quantified, and this was used to correlate to the conductivity of the samples. It was found that the silver MOD ink was the most conductive at 30.7 % bulk conductivity, although it was the most porous at 31.08 % porosity. The reactive silver ink could be cured at a lower temperature of 120 °C and achieved only 12.2 % bulk conductivity and 6.13 % porosity. The best overall performance ink was the silver NPs ink with a bulk conductivity of 24.5 % and porosity of only 2.8 %.

*Manuscript in preparation: (1) Beedasy, V.; Lin, J.; Smith, P.J. Comparison of silver ink formulations and their electrical performance with morphology after flash thermal sintering, 2021.*

## **A comparison of different silver ink formulations and the relation of their electrical performance with morphology after flash thermal sintering**

In this chapter, the term “sintering” and “curing” is used alternatively as they refer to the heat treatment process, but they are inherently dissimilar processes. When applied to powders, in this case of a metallic nature, the term sintering is used to describe the heat treatment process which causes the powder to agglomerate into a bulk material via diffusion amongst the particles. Curing, on the other hand, is a heat treatment process which is responsible for accelerating a chemical process and is more commonly used in the context of liquids or polymeric materials and composites. As such, the term “sintering” is used to refer to the heat treatment of the silver nanoparticle ink while “curing” is used to refer to the heat treatment of the silver metallo-organic decomposition ink as well as the reactive silver ink.

### **4.1 Experimental - Conventional thermal sintering**

#### **4.1.1 Materials and methods**

##### **Substrates**

Two thermally stable substrates were used in this experiment, including glass slides and Kapton polyimide films (500HN, DuPont<sup>TM</sup> Kapton<sup>®</sup>), the details of which were also provided in Section 3.1 on p. 52. The sample preparation involved a dionised water rinsing process followed by another rinse with acetone, and finally dried under a flow of clean air.

##### **Inkjet printing**

The FUJIFILM Dimatix DMP-2831 printer was used for inkjet printing. The details of the three silver ink used in this experiment were described in Section 3.1 on p. 53. As a summary, the first ink is a silver nanoparticle-based (AgNPs) ink, the second a silver metallorganic decomposition (AgMOD) ink, and the last a reactive silver ink (RSI). The printer was fitted with cartridges capable of ejecting a droplet volume of 10 *pL*, and to ensure homogeneity a single nozzle was used for the printing process. A heated bed of 35 °C was used to avoid the spreading of the droplets on the substrate, and square patterns measuring 15 × 15 *mm*<sup>2</sup> were printed. The droplet spacing was optimised for each ink through trial and error and was maintained at 28 *µm*, ensuring comparable performance during analysis. Two layers of silver ink were printed to obtain comparable results while not sacrificing printing time and volume of ink.

The printing parameters for each ink was optimised separately, and the optimal waveform was found when an individual drop could be produced without satellites, ensuring repeatability, as theoretically described in Section 3.2.1 on p. 57 The waveform for each ink is shown in Figure 4.1 below along with the droplet formation process under the application of voltage. The difference due to the ink properties such as viscosity and surface tension requires a more elaborately composed waveform.

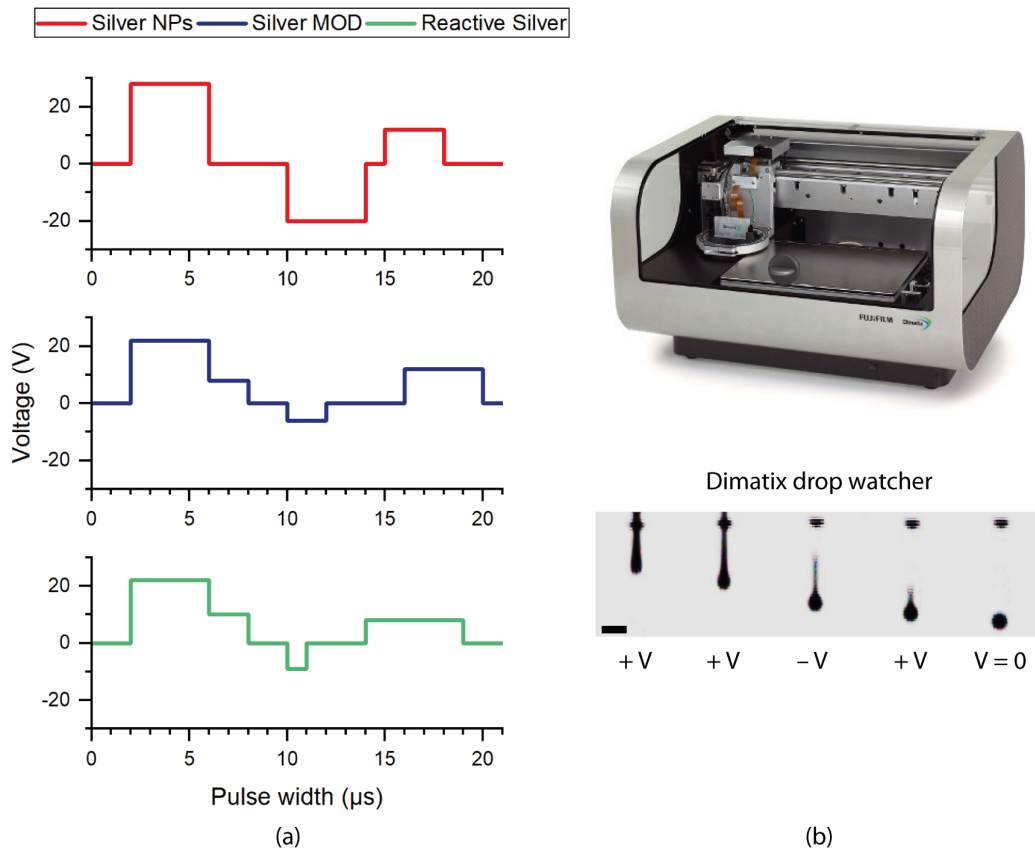


Fig. 4.1 (a) Optimised waveform for inkjet printing of the three different inks using the FUJIFILM Dimatix DMP-2831 printer, and (b) a view of the optimised droplet from the drop watcher. Note there is a slight delay of  $<1 \mu\text{s}$  from the application of a voltage to the piezoelectric actuator and the change to the waveform. Scale bar in (b) is  $100 \mu\text{m}$ .

## Sintering

The sintering conditions for each ink was found through trial and error, using some supplier information as a guideline. The optimum sintering condition was found when the best electrical conductivity was achieved, and both the sample and substrate appeared to be structurally viable.

For the silver NPs, the sintering temperature was varied between 100 – 150 °C for 30 – 60 min according to the guidelines from the manufacturer. However, the range of sintering temperature was increased up to 220 °C based on the previous literature survey which indicated the capability of silver NPs to sinter at a higher temperature.

The silver MOD ink was mainly composed of p-xylene, which has a boiling point of 138 °C so the initial temperature of curing was set at 140 °C. This was done to ensure all the solvent had evaporated, leaving behind the silver MOD salt crystals, which then decompose to form conductive links throughout the printed pattern. The temperature was varied up to 200 °C. The duration of this process was also optimised, starting from 1 min up to 10 min.

The reactive silver ink was designed to be cured at low temperatures while still exhibiting electrical performance equivalent to silver. An initial curing temperature of 80 °C was selected, and this was gradually increased to 160 °C. The duration of the curing process was varied between 4 – 15 min.

## 4.1.2 Characterisation

### Electrical properties

The electrical conductivity of the printed samples was used as a measure of success following the thermal sintering/curing process. As such, the conductivity was quantified using the four-point probe method, the details of which is provided in Section 3.4.6 on p. 73. By using four probes – two as source leads to supply the test current and the other two as sense leads to measure the voltage difference across the samples under test – it eliminates any systematic error of resistance due to the leads or contact between the probes and the sample.

### Thickness

The thickness of the patterns was calculated based on the mass of the drops deposited on the substrate and the remaining mass after evaporation. The density of each ink was measured for a given mass, which was then used to calculate the thickness of the printed samples after two layers. This value of thickness was then compared with the thickness obtained via atomic force microscopy (Nanoscope IV – TM-AFM, Bruker Inc., Kroto Research Institute), the details of which are provided in Section 3.4.3 on p. 70 and the profile of each pattern was then plotted. The profile of the pattern was also used as an indication of the morphology of the three inks after being optimally heat treated on the hotplate.

### Surface morphology

One sample for each ink which was optimally converted to conductive features was randomly chosen for SEM analysis. The surface morphology of the samples was captured and, using image processing, the void ratio was compared. The size, uniformity and coalesce of the silver samples were also observed. The void ratios and the size of the nanoparticles were directly derived from micrographs. The void ratio was determined by the ratio of area of voids to total analysed area; the nanoparticle size was estimated from the mean diameter of ten randomly chosen nanoparticles in the same image.

### 4.1.3 Results and discussion

#### Conductivity development of inkjet-printed silver inks

The results of optimising the conductivity of the printed silver inks for each type of ink is shown in Figure 4.2 and 4.3 below. For the silver nanoparticles, the optimum sintering conditions were actually found to be at 200 °C when sintered for 60 min, which was indicated when the pattern changed from a matt grey to shiny silver. The improvement in conductivity is significant in the first 30 min while the additional 30 min allowed an increase in conductivity by almost an order of magnitude.

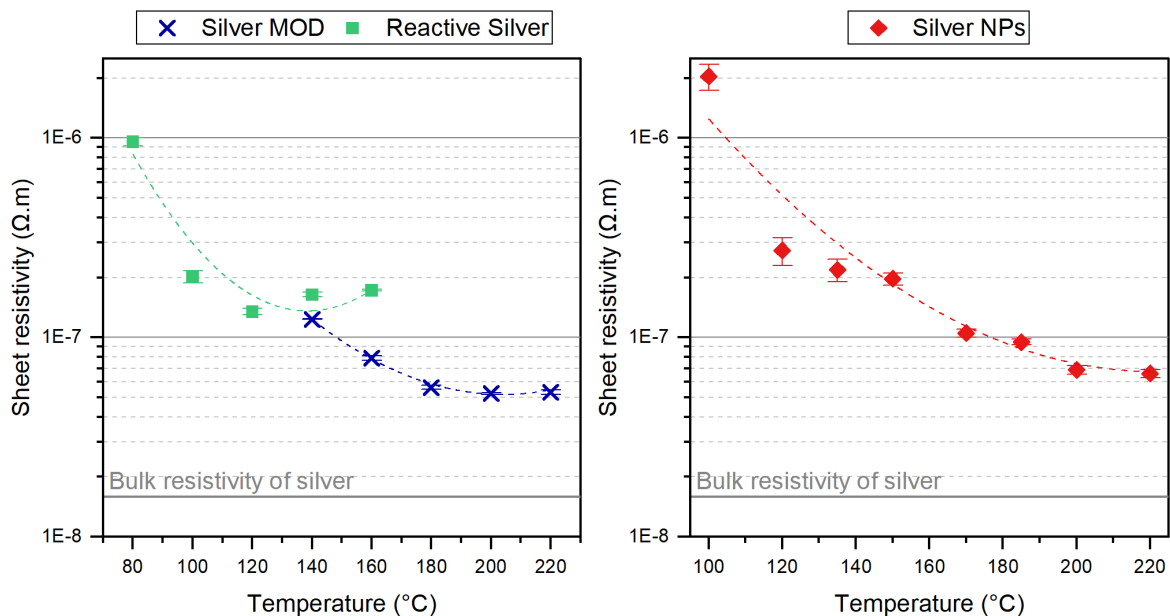


Fig. 4.2 Conductivity improvement as the temperature increases at optimum sintering time for each ink, until a plateau is reached.

Further analysis of the surface of the sintered silver NPs indicated significant neck formation between the NPs, which explained the improvement in conductivity. In the first stage of sintering, the application of thermal energy is used to first evaporate the solvent, in this case triethylene glycol monomethyl ether, followed by the decomposition of the nanoparticle stabilisers. This takes place beyond the flash point of the solvent (133 °C), which indicated the onset of sintering. Once the stabilisers are eventually decomposed, the nanoparticles are free to move once the thermal energy matches the activation energy of the electrons, allowing for the surface diffusion of the smaller metallic atoms towards the larger atoms, thereby forming a percolating network of NPs. It is at this stage that necks are formed in the printed pattern. The additional thermal energy input in the system is then used for the growth of necks, while simultaneously improving the sintering process through particle migration. In this process, the thermal energy input matches the activation energy required to agglomerate the larger atoms, thereby improving the centre-to-centre distance between the neighbouring nanoparticles. It is only during this process that the porosity of the structure is reduced while the density of the printed pattern is increased.

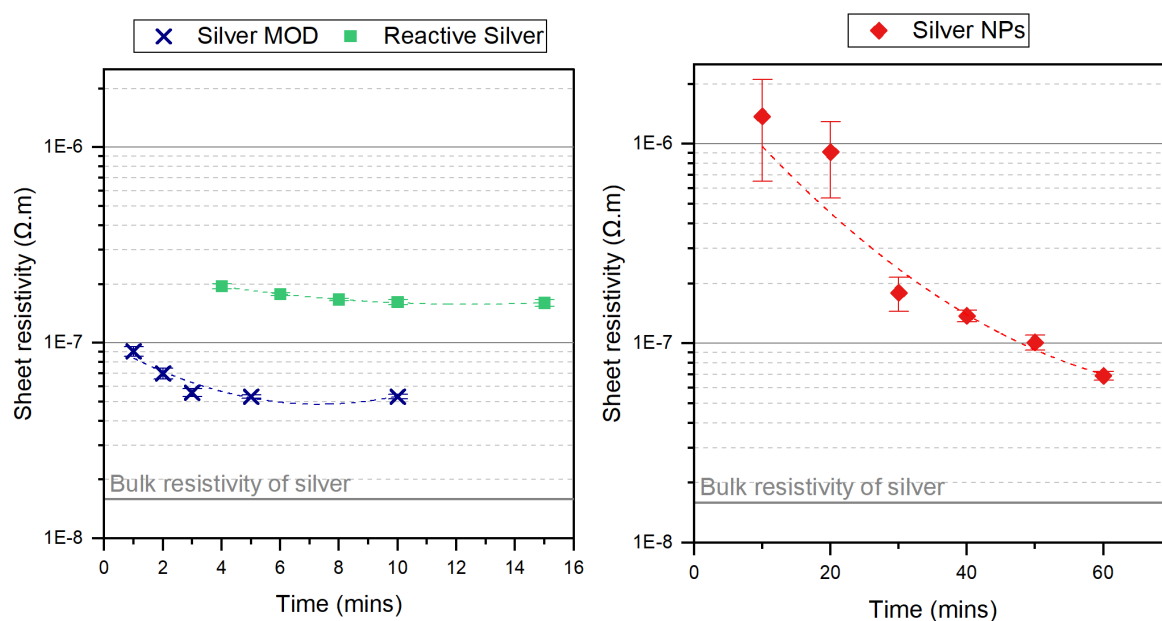


Fig. 4.3 Conductivity improvement as the duration of the sintering time increases for the printed silver samples, at the optimum sintering temperature for each ink.

Figure 4.4 below shows a snapshot of the printed patterns before and after heat treatment at the optimised sintering/curing time and temperature for each silver ink. The colour change from the silver NPs ink went from matt grey to shiny silver; the MOD ink from cloudy to silver; and the reactive silver ink from a yellow tint to silver.

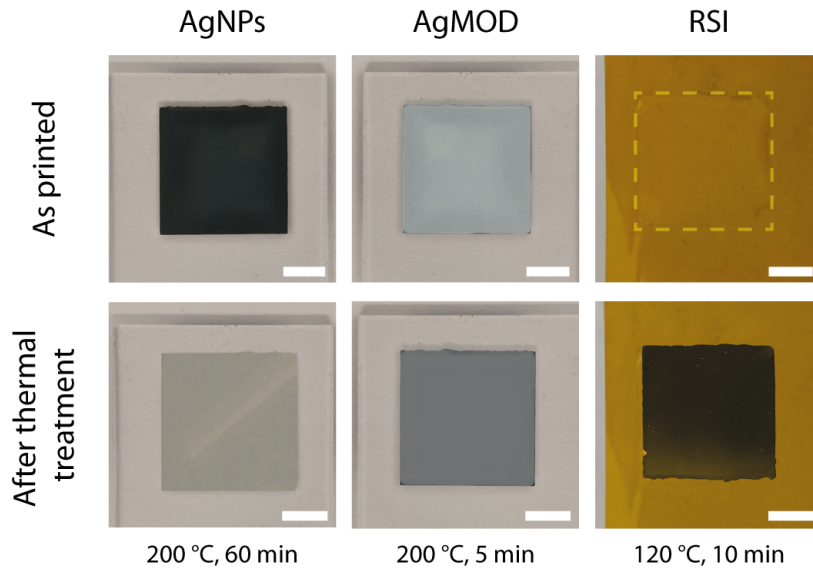


Fig. 4.4 Snapshot of the silver NPs, silver MOD and reactive silver samples showing the colour change before and after optimum heat treatment. The reactive silver ink, being rather translucent when printed, is highlighted with the dashed square lines. The scale bars are all 5 mm.

The improvement in conductivity of the silver MOD samples was much faster as compared to the metallic silver NPs ink as the optimum curing conditions were found to be at 200 °C for 5 min, at which point the pattern changed from cloudy silver to off-white/silver. As this is a salt-based solution, the change in surface morphology was drastic as soon as the solvent (in this case p-xylene) had evaporated, leaving behind the silver neodecanoate precipitation which immediately decomposed to form conductive silver colloids. From Figure 4.3 above, this process happened within a few minutes and any additional thermal energy input in the pattern was used to reinforce the silver colloid network up to a limit.

Similarly, the reactive silver ink formed an immediate precipitate after the evaporation of the solvent after a few minutes, as shown in Figure 4.3. In this case, the optimum sintering conditions for the reactive silver ink was found to be within 10 min when cured at 120 °C, after which the ink thermally degraded. The pattern changed from yellow to an off-white/silver pattern. An increase in the curing temperature resulted in a decrease in resolution of the patterns as the vapor pressure difference agitated the ink, causing additional spreading of the ink.

### Morphology and porosity of sintered patterns

Figure 4.5 are SEM micrographs of the printed silver inks. In Figure 4.5(a), the silver NPs sample had not been subjected to any heat treatment, indicating the actual shape and size of the nanoparticles present in the ink. Figure 4.5(b) was subjected to a heat treatment of 200 °C for 30 min which shows the increase in particle size. It also shows the neck formation at distinct locations within the sample, which incidentally indicates surface filled with voids. Figure 4.5(c) was thermally sintered at the same temperature but for a total of 60 min. At this stage, the voids in the sample can be observed to have decreased significantly, while the nanoparticle size increased.

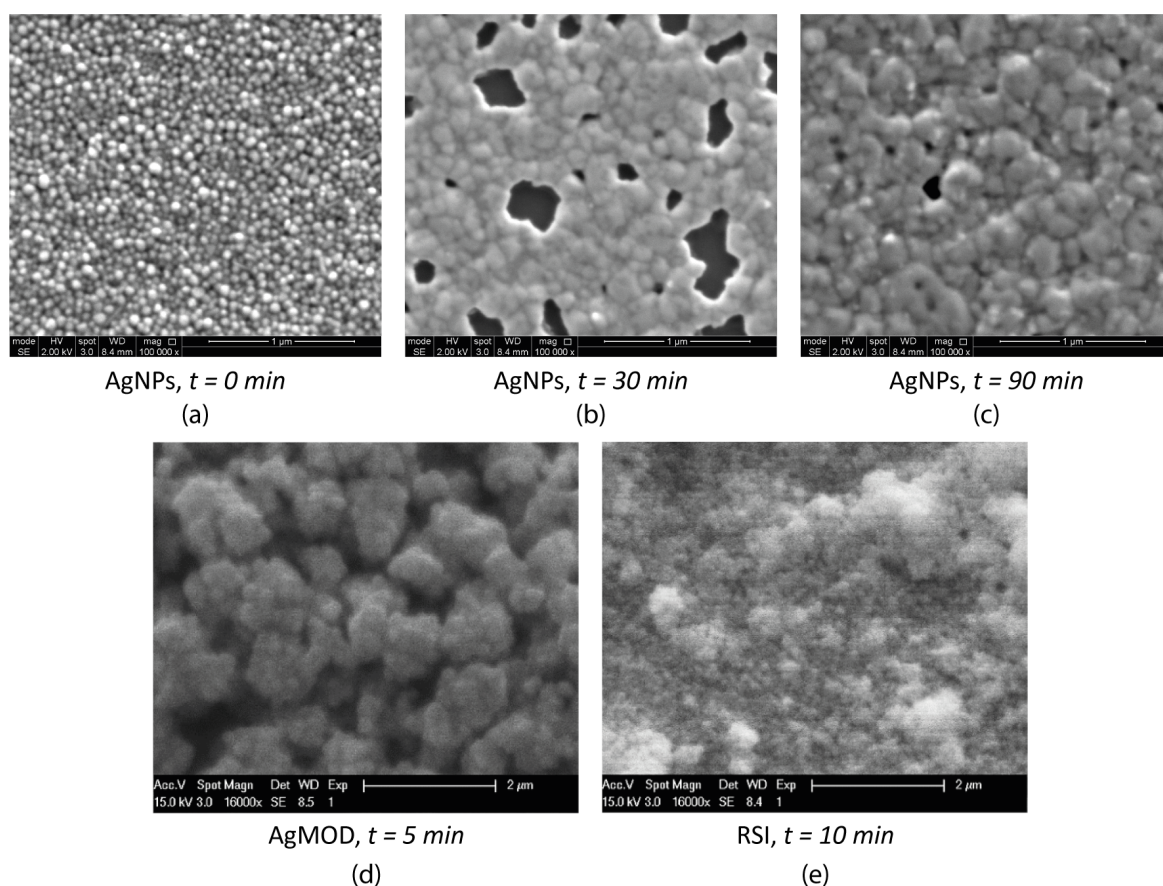


Fig. 4.5 Results of SEM analysis at different stages of sintering of the silver inks. Micrograph (a) represents the printed silver NPs ink without any heat treatment; (b) represents the surface of the pattern after 30 min of sintering, indicating necking and a porous surface; (c) represents the final sintered pattern after 60 min, showing a significant reduction in porosity; (d) represents the final sintered AgMOD ink after 5 min at optimum sintering temperature; and (e) represents the RSI ink after 10 min at optimum sintering temperature.

The silver NPs patterns appeared to be relatively smooth and shiny with a high resolution. Upon closer analysis, it was found that the optimally sintered NPs samples maintained a high uniformity in terms of shape and size. The SEM micrographs were used to further quantify the sample surface, particularly the void ratio and the size distribution of the nanoparticles. The void ratio of the samples had reduced from an average of 11.09 % to 2.80 % during the particle migration stage of sintering, indicating a 97.2 % dense structure based on an average of five samples. As for the size distribution, the optimally sintered nanoparticle measured an average of 162.90 *nm* in diameter, with a distribution range between 117 – 297 *nm*.

Upon closer analysis of the silver MOD patterns which were optimally cured, the particles were found to be closely packed with the widest particle size distribution. The formation of localised clusters which agglomerated randomly can be explained by the flash evaporation of the solvent which limits the movement of the silver particles, which is concurrent with the findings of Dearden et al. [225]. Further analysis using image processing software revealed individual particles having an average size of 215.80 *nm* with a size distribution in the range of 196 – 259 *nm*, and they agglomerate into clusters ranging from 397 *nm* to 1486 *nm* (Figure 4.5(d)). These clusters form the percolating network through which the electrons flow, resulting in a conductive pattern form. The voids of the optimally cured samples was relatively high as compared to the other ink formulations, with an average void ratio of 31.08 %, which indicated an uneven surface.

The reactive silver ink appeared to be less porous as compared to the silver MOD patterns, with a void ratio of only 6.13 %. The particle size distribution, however, was wide with individual particles measuring 161.20 *nm* on average, and a distribution range of 104 – 228 *nm*. They eventually formed clusters between 418 – 1356 *nm*, which can be observed on the top surface in Figure 4.5(e). This indicated a rather uneven surface which could be due to the difference in vapor pressure of the evaporating solvent during the heat treatment process.

The change in particle size as well as the distribution range during the heat treatment process for all three inks is represented in Figure 4.6 below. The change in voids of the samples is also plotted for the known values obtained upon further analysis of the SEM micrographs for each sample, shown in Figure 4.7 below.

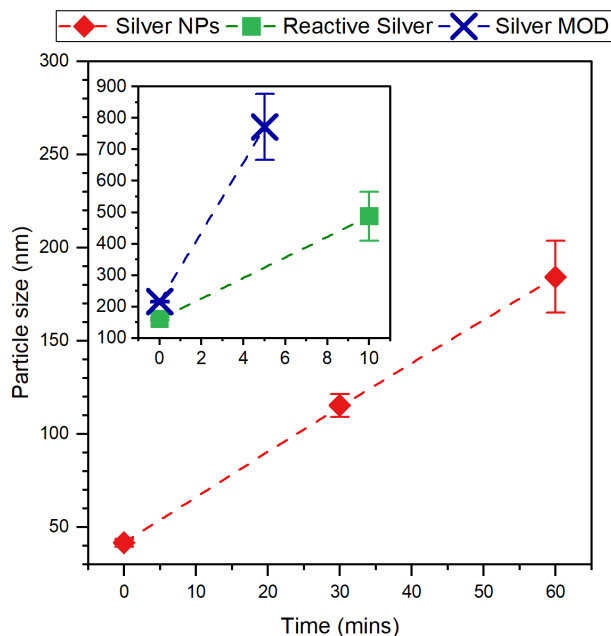


Fig. 4.6 Change in particle size for each ink, with the distribution range represented by means of error bars. The inset in the top left corner is for the particle size distribution of the reactive silver and silver MOD due to the smaller timescale involved, and the larger particle sizes.

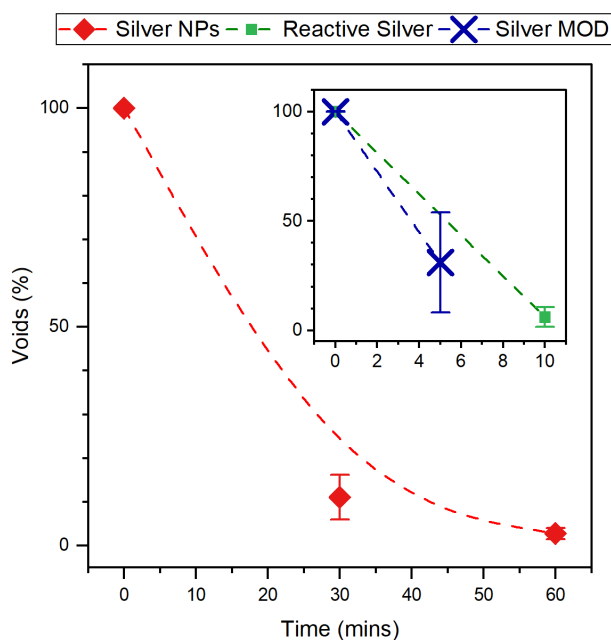


Fig. 4.7 Reduction in voids of the silver samples at optimum sintering conditions as the duration of the applied heat is increased. The inset in the top right corner represents the plot for reactive silver and silver MOD due to the smaller timescale involved for the optimum sintering.

### **Contact line pinning by using a heated bed**

The surface of the print bed was heated to 35 °C so as to accelerate the evaporation of the solvent, thereby pinning the contact line of the printed pattern. This contact line pinning was necessary to prevent the spread of the ink when the second layer was printed, as well as during the transfer to the hotplate for the heat treatment process. Contact line pinning has proven to result in a generally unwanted phenomenon called “coffee staining” where there is a difference in the evaporation rate of the liquid at the edge and the centre of the drop. The evaporation rate at the edge of a drop tends to be faster due to the contact angle of the drop on the printed surface, resulting in a flow of liquid from the centre to constantly replenish that at the edge. Consequently, the flow towards the edge carries the material in the same direction, causing the formation of a “stain”. However, the formulation of an ink with the addition of surfactants which reduce the surface tension of the ink has proven to reduce the coffee-staining effect [156], while the study by Deegan et al. [154] has exploited this effect to produce well defined polymer dots and arrays by controlling the flow mechanism. In a similar aim, the gentle heating of the substrate has been used to pin the contact line of the drop so as to prevent spreading, while the second layer replenishes the evaporated regions closer to the edge.

### **Relationship between surface morphology and bulk resistivity of samples**

The resistivities of the samples were compared to the bulk value of silver ( $1.59 \times 10^{-8} \Omega \cdot m$ ) once the thickness of the samples was measured using confocal microscopy. Each ink was printed in a track pattern measuring  $100 \mu m \times 2 mm$  and the height profile of each track was measured at different regions, and the mean value was calculated and plotted in Figure 4.8 below. The average thickness of the silver nanoparticle samples revealed to be 185 nm, the silver MOD ink at 257 nm and the reactive silver at 220 nm for two layers which had been printed and optimally heat treated. The bulk resistivity of each sample was compared to that of silver and the best sample was the silver MOD ink where a maximum of 30.7 % bulk conductivity of silver was achieved, while the silver NPs achieved 24.5 % and the reactive silver 12.2 % bulk conductivity of silver.

The height profile of the printed patterns revealed the silver NPs to have a relatively smooth morphology as compared to the silver MOD and the reactive silver inks. This can be explained by the dense percolating network of the patterns as the porosity of the silver NPs is only 2.8 % after being optimally sintered. Additionally, the particle size distribution within the printed silver patterns is evenly spread with the nanoparticles measuring an average of  $162.9 \pm 95 nm$ .

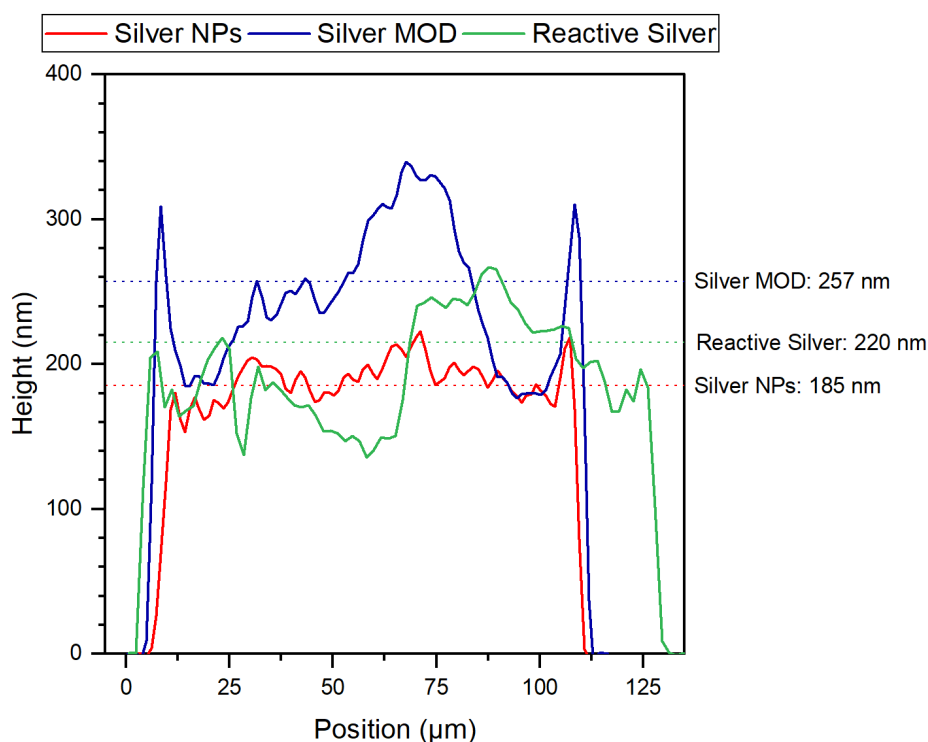


Fig. 4.8 Height profile variation of the silver NPs, silver MOD and reactive silver ink, optimally printed and sintered with two layers. The dotted lines represent the average value of thickness for each ink.

The silver MOD ink has a porosity of 31.08 %, which indicated a relatively rough surface as compared to the nanoparticles. The particle size distribution based on the clusters which were formed indicated a spread between 397 – 1486 nm, which can account for the highly porous structure. The silver MOD ink is the most conductive ink and can be cured in 10 min, but the conductivity values obtained can be attributed to the high silver content loading of 40 wt.% as compared to the silver NPs which has a silver loading of 30 – 35 wt.%. The high porosity of the silver MOD pattern can pose a limitation for being used in multi-layer components as the subsequent deposition surface after curing is highly porous, introducing areas of weak adhesion.

The reactive silver has a porosity of 6.13 %, with particles measuring an average of 161 nm which eventually formed clusters between 418 – 1356 nm. Similarly, when comparing the profile of the reactive silver patterns, the large clusters form regions of depressions along the surface of the pattern due to the large particles agglomerating rather unevenly. The sintering of the reactive silver can be done in 10mins, resulting in a conductivity of 12.2 % that of bulk silver and a better porosity than the silver MOD.

#### 4.1.4 Conclusions

In this experiment, the conventional heat treatment of three varieties of silver inks was performed, and an analysis on the influence of the heat treatment process was done by evaluating the void ratio, particle size distribution and conductivity of the samples. The commonly used silver nanoparticles ink, a silver metallorganic decomposition ink and a reactive silver ink were inkjet-printed on both glass and polyimide films with similar optimised printing parameters. The samples were then subjected to a series of heat treatment processes where the temperature and duration of the applied heat was varied in order to find optimum conditions to yield the most conductive yet structurally stable sample. The electrical conductivity measurements were calculated, and, with the aid of the thickness of the samples, the resistivity was calculated and compared to the bulk resistivity of silver. Further investigations using SEM analysis were performed, and with the aid of digital imaging software numerous sample properties were measured such as the particle size distribution as well as their surface porosity. These properties were then used to correlate between the electrical conductivity of the samples. Table 4.1 below shows a summary of the experimental results achieved.

It was found that the silver MOD ink was the most conductive (30.7 % bulk conductivity of silver) and can be cured the fastest (5 min) at elevated temperatures (200 °C). However, it was the most porous sample (31.08 % void ratio) and contains the highest silver content (40 wt.% silver neodecanoate). The reactive silver ink could be cured in twice the amount of time (10 min) but at a lower temperature (120 °C) which proved to be more compatible for thermo-sensitive substrate such as polyethylene naphthalate (PEN,  $T_g = 125$  °C), polycarbonate (PC,  $T_g = 145$  °C) or polyether sulfones (PES,  $T_g = 190$  °C) to name a few. The silver nanoparticle ink was sintered at a similar temperature of the silver MOD ink (200 °C) but for a much longer duration (60 min). It resulted in a very conductive (24.5 % bulk conductivity of silver) sample while being the least porous (2.8 % void ratio) despite having a comparable silver content (30 – 35 wt.% silver nanoparticles) to the silver MOD ink.

Table 4.1 Summary of the results achieved using the three silver inks.

<b>Ink</b>	<b>Optimum sintering temperature</b> (°C)	<b>Optimum sintering duration</b> (min)	<b>Conductivity comparison</b>	<b>Void ratio</b>	<b>Particle size distribution</b> (nm)
AgNPs	200	60	24.5 %	2.80 %	117 – 297
AgMOD	200	5	30.7 %	31.1 %	397 – 1486
RSI	120	10	12.2 %	6.13 %	418 – 1356

## Summary

This chapter sets the baseline for using silver inks, and the expected results to be achieved using conventional sintering techniques. This baseline is then used to establish a benchmark for the results achieved using pulsed laser sintering in the following chapter, as well as to test the research hypothesis mentioned in Section 2.3 on p. 48. Additionally, the silver nanoparticle-based ink is preferred for the following experiments as it was found to yield the most reliable pattern in terms of electrical conductivity and mechanical performance, and is the most commonly used silver ink for printed electronics based on the literature survey.

# Chapter 5

## Pulsed Laser Sintering

### Summary

This chapter describes the investigation into combining inkjet printing with pulsed laser sintering to produce printed electronics. As printed electronics can be produced on a variety of substrates for different applications, a wide variety of materials were investigated for inkjet deposition using functional inks such as silver and copper nanoparticle-based inks. Then, instead of conventional sintering, a bespoke pulsed laser system was used for converting the printed features into conductive patterns, which were quantified through conductivity and morphology techniques, as described in the first experimental section. The laser sintered silver NPs were found to exhibit similar electrical performance (17.9 % bulk conductivity of silver) as the conventionally sintered ones (24.5 % bulk conductivity of silver), while the laser sintered copper NPs exhibited exceptional performance with up to 38.7 % bulk conductivity of copper achieved. In comparison with literature, this performance surpasses the last reported value of 20.1 % bulk conductivity of copper.

Then, the second experimental section expands on the performance characterisation results of the inkjet-printed copper nanoparticle-based ink on various substrates, more specifically at the interface between the ink and the substrate with particular attention to the adhesive strength. A modified, more appropriate adhesion test – the cross-cut test – including a digital perspective, was selected for the analysis detailed in the second experimental section. The cross-cut test was done according to the ASTM International F1842-15 standard and the digital analysis of the results provided an unbiased evaluation. It was found that the pulsed laser sintering improved the adhesion of the copper nanoparticles on glass and the two polymer films from an adhesion classification of *3B* to *4B*, while the copper nanoparticle sintered on paper remained at *3B* with a marginal improvement in delamination area, despite showing the highest conductivity values. Finally, a discussion about the industrial applications

of the samples based on their adhesion classification results is done in relevance their mechanical properties, before concluding this experimental section.

The third experimental section focuses on the pulsed laser sintering parameter and the impact on the copper nanoparticle coating as well as the substrate. As pulsed lasers are often used for ablation processes, this section investigated the phenomenon prior to ablation and the heat affected zone. This experiment investigated the heat affected zone after laser irradiation and highlighted the influence of the thermal mass in heat conduction to the nanoparticle layer, as well as the formation and size of the heat affected zone. It was found that the two polymer substrates resulted in nanoparticle ablation, thermal degradation and substrate failure at high fluence values, while the paper substrate only resulted in nanoparticle ablation and the largest heat affected zone formation.

*Manuscript in preparation: (1) Beedasy, V.; Smith, P.J. Adhesion evaluation of inkjet-printed and pulsed laser sintered copper nanoparticles at ambient conditions on thin films for printed electronics applications, 2021.*

## **5.1 Experimental I - Pulsed Laser Sintering Investigation**

### **Bulk resistivity comparison of pulsed laser sintered copper and silver nanoparticle inks on a variety of substrates.**

In this experiment, two types of nanoparticle-based functional inks were inkjet-printed on different substrates and laser sintered using a nanosecond pulsed laser. The functional inks were each made out of copper and silver nanoparticles, and they were both designed for printed electronics purposes. Additionally, the copper nanoparticle ink was designed to be rapidly sintered via flash sintering. The silver nanoparticle ink was commercially available and designed to be converted into conductive features by conventional thermal sintering techniques.

The two inks were deposited using inkjet printing technology on a variety of substrates with different thermal and mechanical properties. These include standard laboratory glass slides, Kapton polyimide films, polyethylene terephthalate films, and a resin-coated paper. They were chosen particularly for their inherent difference in thermal properties which would serve as an indication of a failure mode during the pulsed laser sintering process.

The nanosecond pulsed laser system is custom-built to fit into an inkjet printing system. This was done to ensure the precise control over the positioning of the incident laser beam onto the printed features. Contrary to the conventional sintering method which heats up the entire pattern, the laser sintering process can be performed in a selective approach so as to prevent damage to the surrounding patterns which require no heat-treatment. The laser sintered patterns were then evaluated for their electrical performance and the substrates were investigated for any damage which may have been caused due to the sintering process. To conclude this section, a comparison between the bulk resistivity of the sintered samples and the laser sintering parameters is provided, followed by a discussion of the effects of laser sintering on the printed patterns.

#### **5.1.1 Materials and methods**

##### **Substrates**

The inks were printed on four different substrates, with their thermal and mechanical properties detailed in Section 3.1 on p. 52. As a summary, the first substrate is a standard laboratory glass slide, the second is a polymer film made out of polyimide (PI) which is flexible and has a high glass transition temperature, the third a similar polymer film made out of polyethylene terephthalate (PET) which exhibits flexibility and has a lower glass transition temperature,

and the last substrate is a specially designed paper with a thin hydrophilic coating to improve particle adhesion. All samples, except for paper, were prepared first by a deionised water rinsing process followed by another rinse with acetone, and finally dried under a flow of clean air.

### **Inkjet printing**

The inkjet printing was done using a modified Microdrop MD-K-130 dispenser head with a piezoelectric actuator. The shape of the nozzle orifice was designed to be used with metallic nanoparticle inks by reducing the “neck” length, which in turn reduces the chances of clogging due to the potential agglomeration of nanoparticles. The diameter of the nozzle orifice is  $50\ \mu\text{m}$  with a nominal drop volume of  $30\ \text{pL}$ . The dispensing parameters, shown in Figure 5.13 below, were optimised using triple oppositely-directed pulses to produce the smallest droplet ranging between  $30 - 35\ \mu\text{m}$  in terms of in-flight diameter. The optimisation process followed the similar theory described in Section 3.2.1 on p. 57.

Two metallic nanoparticle-based inks, a silver and a copper (details provided in Section 3.1 on p. 53), were printed using the Microdrop dispenser. Both inks were first filtered using a  $0.45\ \mu\text{m}$  PTFE filter before transferring to the inkjet reservoir for printing. This was done to eliminate any contaminants which may cause defects or clogs during printing. The reservoir was coated with a light-repellent adhesive tape on the external walls to prevent degradation of the inks due to light.

The substrate was heated to  $40\ ^\circ\text{C}$  to accelerate the evaporation of the solvent upon deposition and thereby pinning the contact line. The gentle heating of the substrate was beneficial in controlling the morphology of the printed patterns, and this was observed as the droplet spacing was reduced to ensure a higher loading per unit area. The optimum droplet spacing for all four substrates was maintained at  $75\ \mu\text{m}$  as it yielded the most uniformly printed pattern after the droplets spread on the substrates. Two layers of nanoparticle ink were printed to ensure an optimum coverage of the specified geometry, which was a square pad measuring  $15\ \text{mm} \times 15\ \text{mm}$  in this experiment. Figure 5.2 shows a snapshot of the samples following deposition via inkjet-printing before the pulsed laser sintering process.

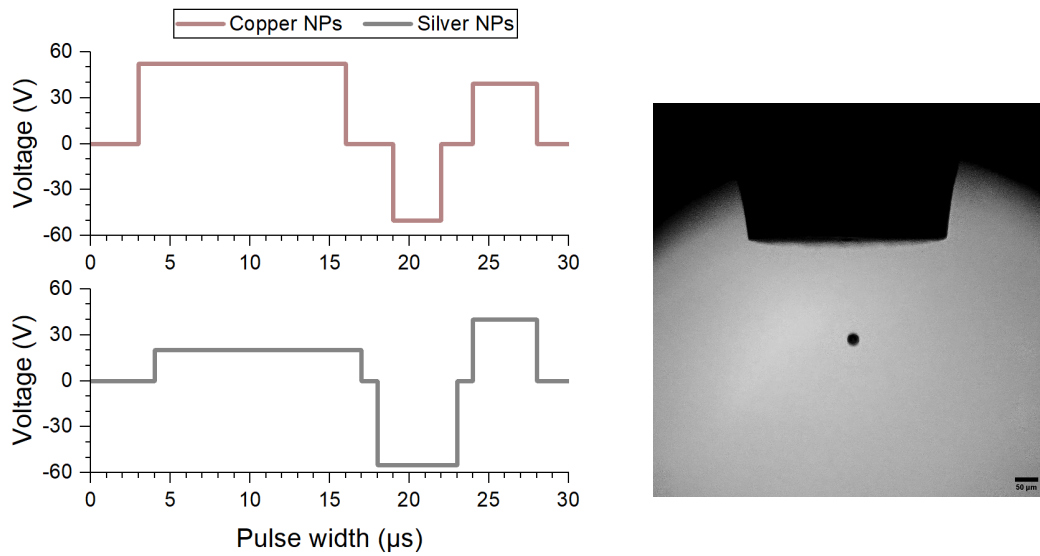


Fig. 5.1 [Left] Illustration of the waveform used for inkjet printing using the Microdrop MD-K-130 dispenser head fitted with a 50  $\mu\text{m}$  printhead. [Right] A snapshot of a 30  $\mu\text{m}$  droplet ejected from the Microdrop nozzle. The scale bar in this snapshot is 50  $\mu\text{m}$ .

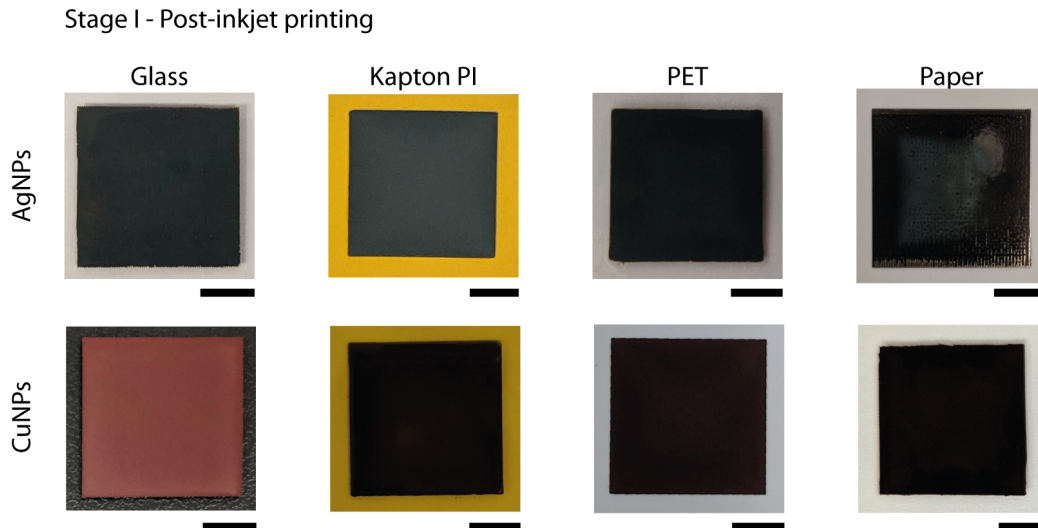


Fig. 5.2 Snapshot of the silver and copper nanoparticle-based inks following inkjet printing, prior to pulsed laser sintering, on all four substrates. Scale bar is 5 mm.

### **Pulsed laser sintering**

Once printed, the samples were left to first dry on the heated bed, followed by sintering using a nanosecond pulsed laser. The drying step is critical to allow laser sintering to occur as a wet sample requires additional energy to evaporate the carrier fluid, which may eventually vaporise the nanoparticles once they are exposed to the increased incident power.

The details of the laser system used to sinter the samples are provided in Section 3.3 on p. 66. As a summary, the laser uses a semiconductor laser diode to emit in the near infrared (NIR) region, with 905 nm at peak radiant intensity. The emitting area is collimated to produce a beam measuring  $200 \times 15 \mu\text{m}^2$ , and due to the small rectangular spot size of the laser, a “snake scanning” approach was used to sinter the patterns, and an overlap between each sintered row ( $d_{ss}$ ) was maintained to ensure a continuously sintered pattern.

The fluence of the laser was varied as it strongly affects the sintering process for the nanoparticles due to the amount of radiation absorbed in the material during the interaction. The scanning velocity of the laser is crucial to maintain an overlap between each pulse and hence effectively sinter the patterns without leaving “ridges” of unsintered ink. However, a low speed does not guarantee the patterns will be sintered evenly to achieve good mechanical and electrical properties as other factors such as the excessive heat dissipation within the pattern to the substrate must be considered, in addition to the excessive incident power which can cause cracks and ablation.

## **5.1.2 Characterisation**

### **Thickness**

The thickness of the patterns was obtained via atomic force microscopy (Nanoscope IV – TM-AFM, Bruker Inc., Kroto Research Institute), the details of which are provided in Section 3.4.3 on p. 70 and the profile of each pattern was then plotted. The profile of the pattern was used as an indication of the thickness of the inks after sintering.

### **Absorption spectrum of inks**

To gain a more thorough understanding of the laser sintering of both the silver and copper NPs ink used throughout this experiment, the optical absorption spectrum of both inks was quantified in the ultraviolet (UV), Visible light (Vis) and near infrared (NIR) range, i.e. from 240 nm – 2500 nm inclusive. The details of the process are described in Section 3.4.4 on p. 71.

### Electrical properties

The electrical conductivity of the printed samples was used as a measure of success following the thermal sintering/curing process. As such, the conductivity was quantified using the four-point probe method, the details of which is provided in Section 3.4.6 on p. 73. By using four probes – two as source leads to supply the test current and the other two as sense leads to measure the voltage difference across the samples under test – it eliminates any systematic error of resistance due to the leads or contact between the probes and the sample.

### 5.1.3 Results and discussion

#### Absorption spectrum of nanoinks

The method of sintering by using radiation had proven successful in several reports by Kim et al. [185], Ryu et al. [184], and Mitra et al. [226] to name a few. However, these reports mention the use of photonic sintering to enhance the conductivity of printed metallic nanoparticle-based patterns as a variation the intensity of the incident radiation. Subsequently, the wavelength of the exposed radiation matches the absorption of the metallic nanoparticles, as first reported by Ready in 1965 [227]. Additionally, Henglein [228] investigated the change in absorption of radiation of different sized copper nanoparticles, highlighting the dependence of particle size on the optical absorption spectrum.

Figure 5.3 below which is a plot of the variation of the absorption of the nanoparticle-based inks over a range of wavelengths. The emission range of the pulsed laser was superimposed on both plots as an indication of the absorption of both copper and silver nanoinks at that particular incident radiation wavelength (895 nm – 915 nm). The silver nanoparticle-based ink measured a peak absorption at 588 nm (529 nm – 639 nm at full width half maximum (FWHM) for that peak), although a more relevant peak was measured at 903 nm (880 nm – 943 nm FWHM) for this pulsed laser sintering application. However, there were other subsequent peaks observed during the experiment. The process was repeated three times and the results obtained showed a similar response to the testing equipment, which highlighted a potential systematic error at longer wavelengths. The copper nanoparticle-based ink measured a peak absorption at 253 nm (241 nm – 264 nm FWHM) and secondary peak at 888 nm (875 nm – 900 nm FWHM). The two distinct peaks indicate a better response to the testing equipment as compared to multiple peaks in testing the silver NPs ink, and ultimately validate the use of the pulse laser for this sintering application.

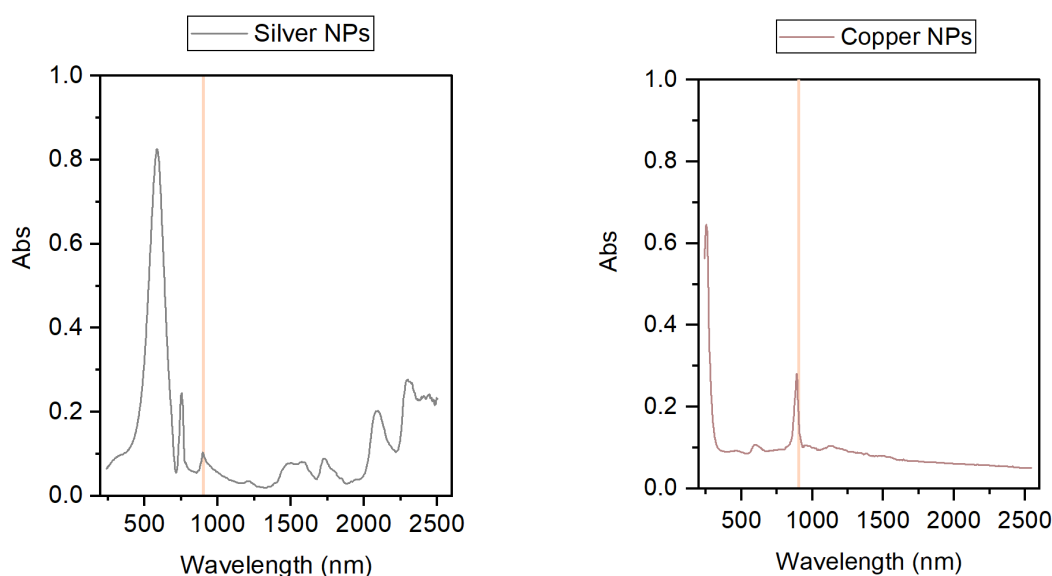


Fig. 5.3 Absorption spectrum of (left) the silver nanoparticle ink and (right) the copper nanoparticle ink over the UV-Visible light spectrum (240 nm – 800 nm) as well as the NIR range (850 nm – 2500 nm). The thin orange rectangular strip represents the range of the emission of the pulsed laser diode (895 nm – 915 nm).

### AFM measurements for thickness and morphology

In order to quantify the sheet resistivity of the samples, the thickness of each pattern is required and then used to calculate the resistivity from the sheet resistance measurements. Due to the limitations of the measurement window of only  $90 \mu\text{m}^2$ , the entire square pad of  $15 \text{mm}^2$  could not be measured, and hence an approximation of the thickness of two layers of metallic nanoink was used. Test samples of a single row of ink were printed out of two layers of nanoink followed by the laser sintering at optimum conditions, which will be discussed in the following section. These samples were then inspected under the AFM to gather the morphological parameters, particularly the thickness of two layers of nanoink, and the results from the analysis are shown in Table 5.1 below.

Table 5.1 Results of AFM analysis of the test samples, showing the mean value of thickness.

		Substrates			
		Glass	PET	Kapton PI	Paper
Thickness	AgNPs	466 nm	530 nm	525 nm	556 nm
	CuNPs	407 nm	426 nm	431 nm	468 nm

The AFM results also provide an indication of the overall surface morphology of the samples after laser sintering. Figure 5.4 and 5.5 below represents a topological plot of the laser sintered silver and copper nanoparticle test sample, respectively. The change in thickness from the unsintered and the sintered sample lies within the uncertainty range of each pattern, hence it was not plotted. From the graph, it can be seen that some coffee staining (albeit minimal) occurred for the sample printed on glass due to the spreading of the ink owing to the smooth surface.

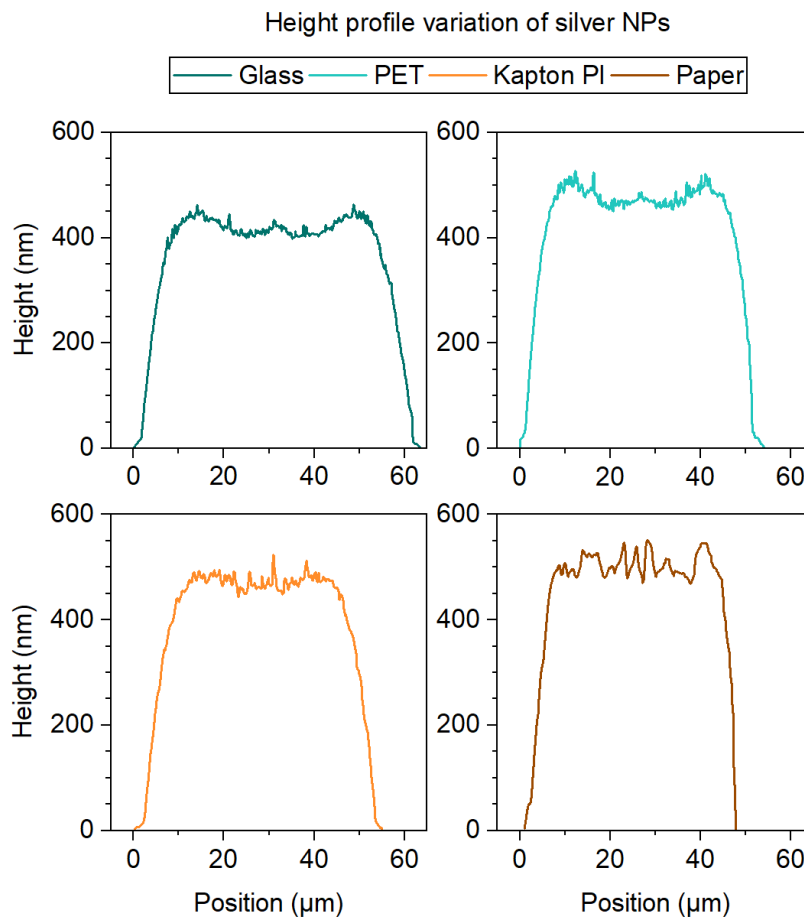


Fig. 5.4 Graphical representation of the height profile of the laser sintered **silver** nanoparticle test sample (two layers of a single row of droplet) on each substrate, highlighting the morphology on the surface.

The morphology of the sample printed on the PET film was subjected to some coffee staining, although the average thickness could still be calculated from the plots. Due to the nature of the tapping mode measurement technique, the tip was subjected to vertical deflections due to the surface of the sample under investigation, and also the presence of contaminants such as minuscule amounts of material removed from previous samples. This

limitation affected samples printed on paper as they were the last set of samples under investigation. As a result, the copper and silver nanoink samples printed on paper appeared to have a rougher surface, possibly due to the contamination of the AFM probe tip. Nonetheless, the results from the analysis provide a useful approximation of the sample thickness on paper as the overall edges of the pattern were accurately measured.

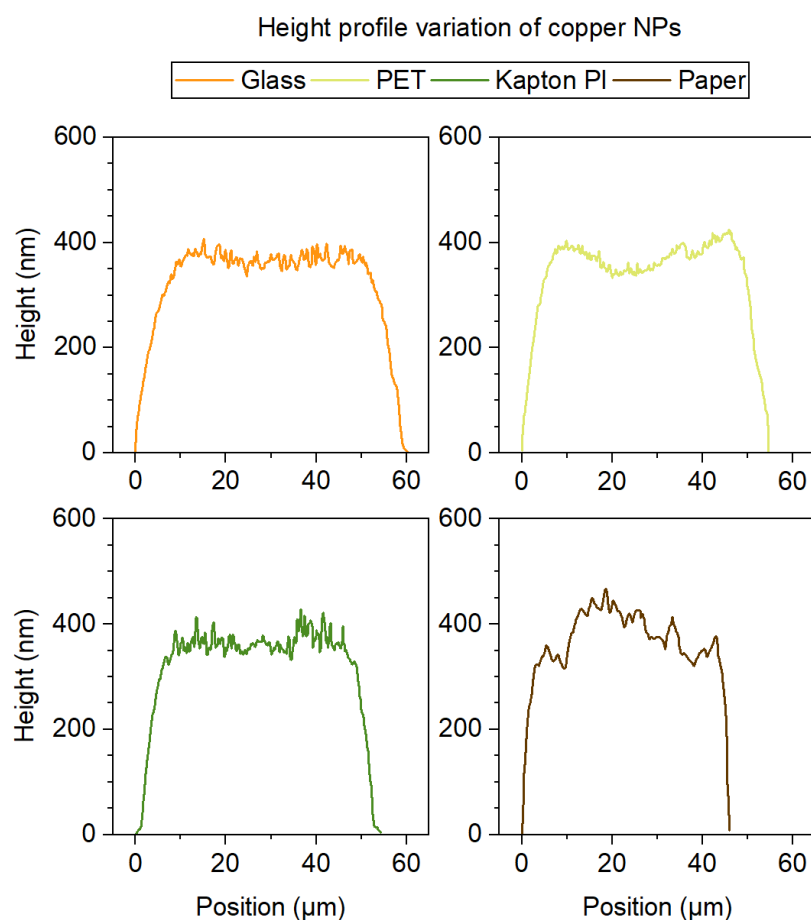


Fig. 5.5 Graphical representation of the height profile of the laser sintered **copper** nanoparticle test sample (two layers of a single row of droplet) on each substrate, highlighting the morphology on the surface. In this case, the samples printed on both glass and the PET film were subjected to coffee staining due to the spreading of the ink.

In comparison with the oven sintered silver NPs samples from Chapter 4 in Section 4.1.3 on p. 94 with the pulsed laser sintered silver NPs ink, it appears that the laser sintered samples printed on glass and the polymer films results in some minimal level of coffee staining, similar to that observed with the conventionally sintered silver NPs on p. 94, although this was not observed on the samples printed and laser sintered on paper. This could be due to the spreading phenomenon as a single row of two layers of silver NPs ink printed on glass

measured approximately  $63.53 \mu\text{m}$  wide, while on Kapton polyimide and PET  $55.44 \mu\text{m}$  and  $54.24 \mu\text{m}$  wide, respectively. The samples printed on paper measured  $48.67 \mu\text{m}$  wide, which is 23.3 % less than the width of the sample printed on glass. This reduction in width allows the silver NPs to spread out more evenly within the printed row, thereby reducing the coffee staining effect to produce a relatively smoother topology.

Based on the AFM topology of the samples, the pulsed laser sintered samples exhibit a smoother topology as compared to the conventionally sintered samples, possibly due to the inherent top-down sintering method as compared to the hotplate. Additionally, the use of a heated bed accelerated the rate of solvent evaporation, which in turn created a surface tension gradient resulting in a uniform morphology of the printed features [229].

### Conductivity development as a variation of laser fluence

With pulsed laser sintering, a high amount of energy confined in a very small area is transmitted to the nanoparticle ink in a short duration, thereby minimising the heat conducted to the surrounding environment. As the wavelength of the emitted pulses of radiation matches the absorption of the ink constituents, the energy emitted is absorbed within the ink, ultimately minimising the heat dissipation to the substrate which allows for sintering on thermo-sensitive substrates such as paper, or polymer films with a low glass transition temperature such as PET. Figure 5.6 shows a snapshot of the samples following pulsed laser sintering, showing the change in colour particularly for the copper samples (dark brown to copper).

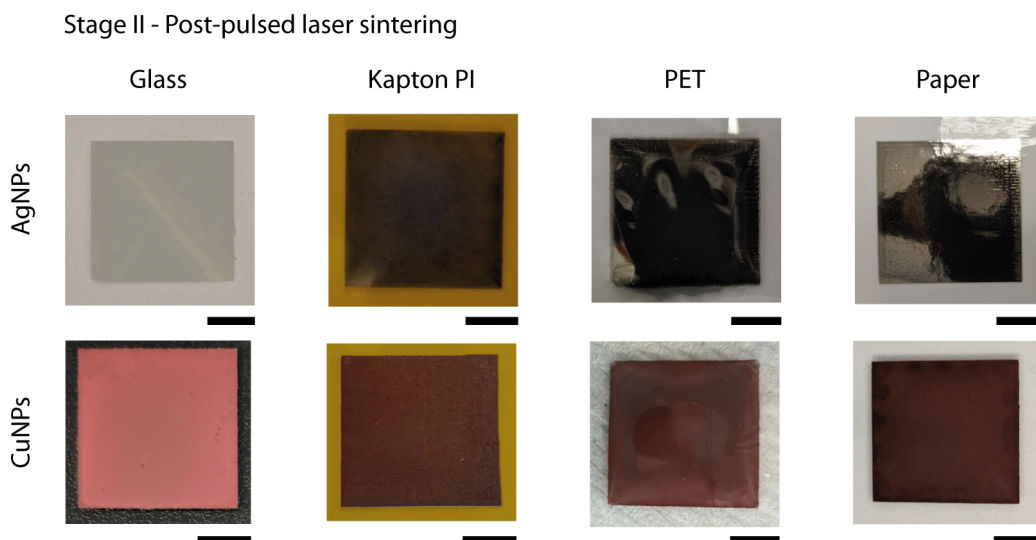


Fig. 5.6 Snapshot of the silver and copper nanoparticle-based inks following pulsed laser sintering on all four substrates. Scale bar is 5 mm.

The results in Figure 5.7 below show the change in resistivity of the silver nanoparticles as the laser fluence is increased for the four different substrates. In the case of laser sintering on glass, the resistivity of silver decreased by a few orders of magnitude until a maximum value of 17.9 % of bulk conductivity of silver was achieved. Similarly, the pulsed laser sintering performed on PET films resulted in comparable values of resistivity with a maximum of 19.5 % bulk conductivity of silver obtained. These values of bulk conductivity were achieved at a maximum fluence of  $446 \text{ mJ/cm}^2$ . When the laser was pulsed at higher fluence values greater than  $450 \text{ mJ/cm}^2$ , this resulted in the ablation of material with no values of conductivity recorded.

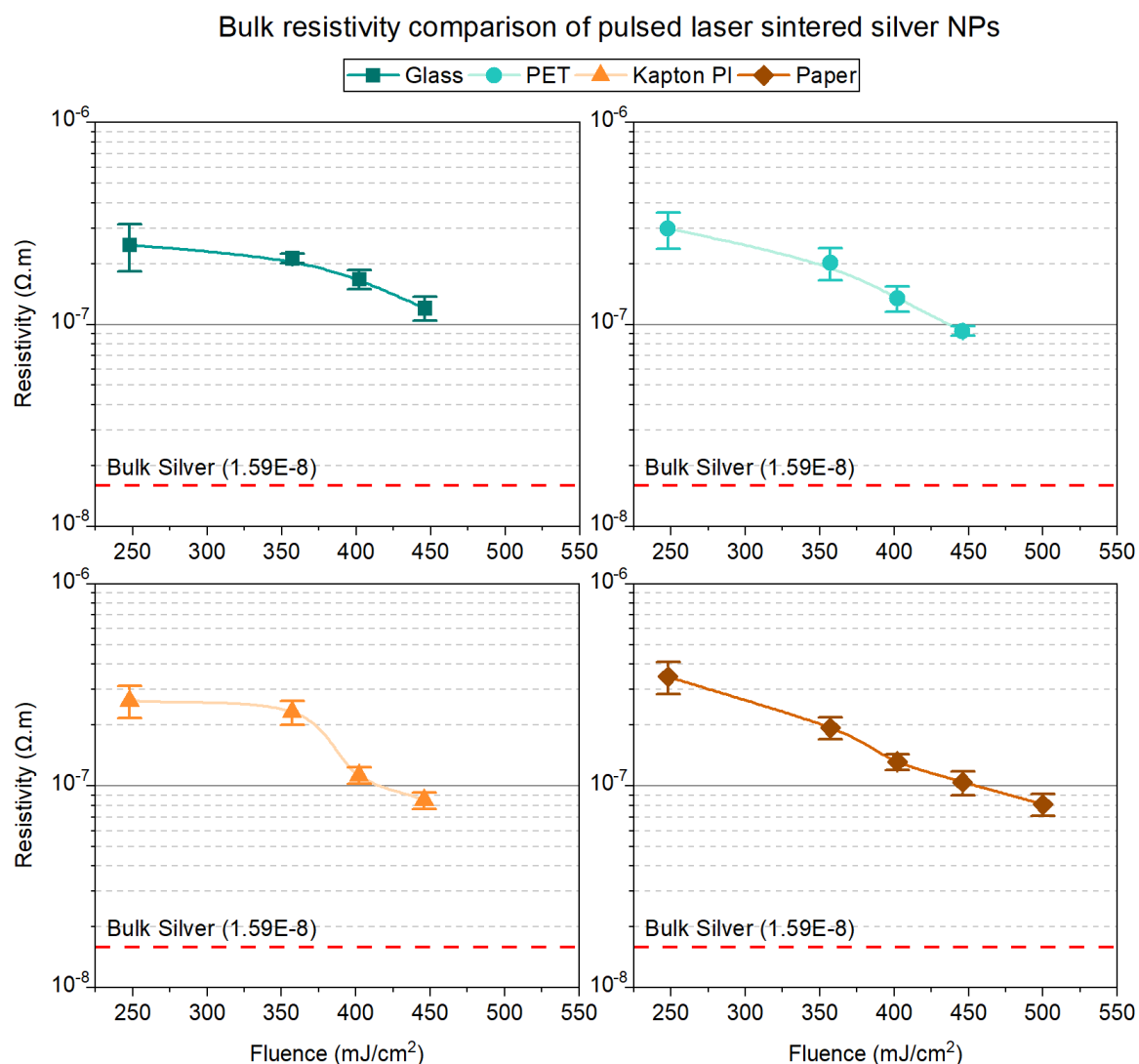


Fig. 5.7 Comparison of the change in resistivity of the silver nanoparticle ink as a variation of the laser fluence, on the four different substrates. The bulk resistivity of silver ( $1.59 \times 10^{-8} \text{ } \Omega \cdot m$ ) is indicated by the dotted red line.

The laser sintering performed on Kapton PI films and the paper substrate resulted in slightly more conductive patterns with a 22.4 % bulk conductivity of silver achieved on Kapton PI and 24.9 % on the paper substrate. However, in comparing the laser sintering process for the two substrates, it is worth noting that the increase in bulk conductivity obtained on the paper substrate was achieved at a higher fluence at  $500 \text{ mJ/cm}^2$ , as compared to the fluence of  $446 \text{ mJ/cm}^2$  used to sinter on the Kapton PI films. This increase in fluence was only made possible due to the coating on the paper substrate which enabled the nanoparticles to better adhere to the surface of the paper while being subjected to higher pulses of energy, preventing ablation.

The overall variation in the laser sintering appeared to decrease as the fluence increased up to the optimum level due to the increase in duration of the exposed incident radiation, thereby allowing for the nanoparticles being exposed to the sequential pulses to heat up and cool more evenly.

The laser sintering of the copper nanoparticle-based ink was performed successfully and Figure 5.8 below describe the conductivity improvement of the copper patterns which were sintered over a range of fluence on the four different substrates. The laser sintering performed on the glass substrate achieved a maximum of 16.2 % bulk conductivity of copper at a fluence of  $402 \text{ mJ/cm}^2$ , although the variation in the resistivity values obtained at a higher fluence was considerably larger compared to the samples printed on the other substrates. The copper NPs printed on the PET film, after laser sintering, achieved a maximum of 23.9 % bulk conductivity of copper at a fluence of  $446 \text{ mJ/cm}^2$ , while the other Kapton PI polymer film achieved a maximum of 26.6 % bulk conductivity of copper at a similar value of fluence. Similar to the silver ink, the copper patterns printed on the paper substrate achieved better bulk conductivity values of 38.7 % bulk copper when irradiated at higher fluence up to  $500 \text{ mJ/cm}^2$  due to the hydrophilic polymer topcoat which allowed for better adhesion during the laser sintering process. However, when irradiated at even higher fluence values, the resistivity of the copper patterns increased due to the localised ablation of the copper patterns, creating open circuits.

The pulsed laser sintered silver NPs can be compared with the baseline established in the earlier Section 4.1.3 on p. 87 where a maximum 24.5 % bulk conductivity of silver was achieved using conventional means on glass, while in the case of pulsed laser sintering a maximum of 17.9 % was achieved. As pulsed laser sintering can be performed on a wider variety of substrates, the printed silver NPs on paper were the most conductive with a maximum of 24.9 % as compared with bulk silver, clearly highlighting the advantages of pulsed laser sintering for compatibility with a wider variety of substrates. In comparison with the state-of-the-art results achieved to date, the work by Niittynen et al. [181] with a *cw* laser

achieved a maximum of 35 % bulk conductivity of silver in samples printed on polyimide. However, the use of the *cw* laser required thermally resistant substrates such as polyimide for the laser sintering to be performed without causing detrimental structural changes to the substrate. In comparison, Ji et al. [197] used a similar *cw* laser with PET samples and produced conductive silver patterns up to 25.2 % bulk conductivity of silver, although they used a silver nanoflakes ink and a much lower laser power (50 *mW*) and lower scanning speed (1 *mm/s*) to prevent damage to the thermo-sensitive substrate, which was PET.

Bulk resistivity comparison of pulsed laser sintered copper NPs

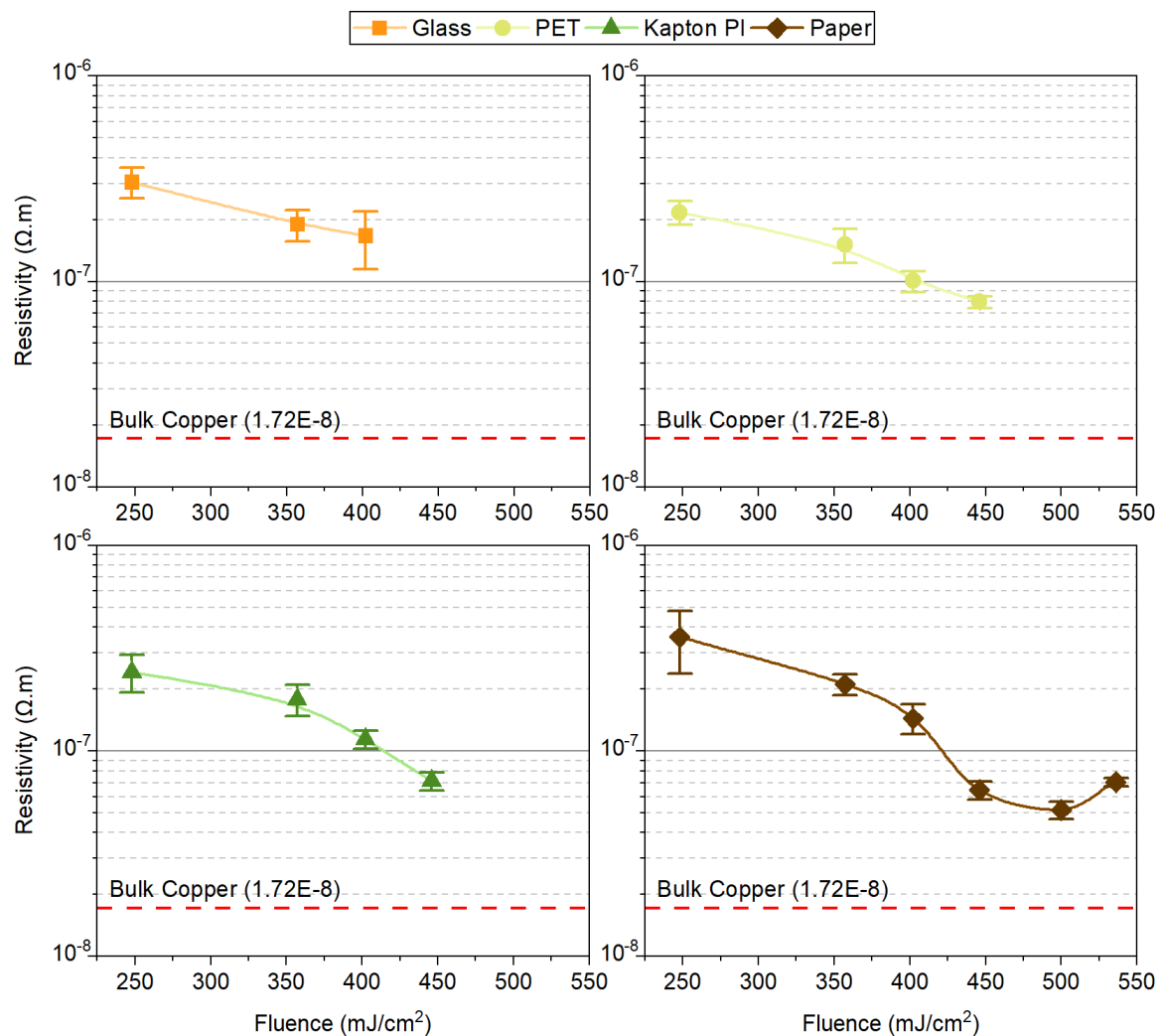


Fig. 5.8 Comparison of the change in resistivity of the copper nanoparticle ink as a variation of the laser fluence, on the four different substrates. The bulk resistivity of copper ( $1.72 \times 10^{-8} \Omega \cdot m$ ) is indicated by the dotted red line.

Finally, the pulsed laser sintered copper NPs can be compared to the state-of-the-art results achieved by Niittynen et al. [83] where they printed copper NPs on polyimide and used a *cw* laser and an IPL sintering system to produce conductive copper samples of up to 20.1 % bulk conductivity, without the requirement of an inert atmosphere. In comparison with the samples produced by pulsed laser sintering in this experiment, the samples produced on polyimide achieved a maximum 26.6 % bulk conductivity of copper, and the advantages of pulsed laser sintering were further extended by laser sintering on paper where a maximum of 38.7 % bulk conductivity was achieved.

### Relation between pulse overlap and laser scanning speed

One disadvantage of using a pulsed laser in comparison to a continuous wave laser is the pulse repetition rate which determines how often the output of the laser is toggled ON/OFF. In this case, the pulsed laser repetition rate can vary from 1 *Hz* to about 2 *MHz*, although the optimal pulsing frequency varied between 4.00 *kHz* to 6.60 *kHz* to ensure a continuous, optimally sintered pattern with pulses overlapping each other. A small pulse overlap will result in unsintered or partially sintered lines which can cause open circuits or an increase in resistivity at that particular region. The laser scanning speed is also vital in ensuring an overlap between the first pulse and the second pulse. A fast laser scanning speed combined with a low repetition rate will create areas of unsintered ink, as shown in Figure 5.9 below.

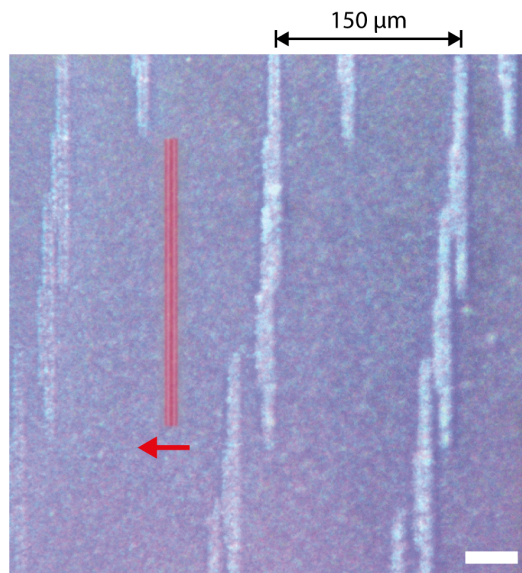


Fig. 5.9 Snapshot of an unsintered pattern as a result of a high laser scanning speed combined with a low pulsing frequency. The scale bar is 50  $\mu\text{m}$  and the separation between each sintered “column” is 150  $\mu\text{m}$ .

Increasing the repetition rate of the laser will generate more pulses per second which will overcome this issue, although a repetition rate above 8  $kHz$  has shown to cause the ablation of the ink due to the rapid pulsing of the laser, which was reported in similar findings by Mohammed et al. [230] where a pulsed laser above 6  $kHz$  was used to machine microchannels in ceramics. Consequently, the laser scanning speed is limited by the repetition rate so as to allow for the sequential pulses to overlap. An alternative method of using multiple passes to sinter the pattern can be used, although this increases the sintering time which ultimately makes laser sintering a less attractive method of manufacturing.

Additionally, the overlap between each sintered row of ink is vital to ensuring a continually sintered pattern. Even though the collimating lenses redistribute and attenuate the intensity due to the collimation and reshaping, the overlap between each row must be optimised to ensure an even power distribution of laser beam over the emitted area. Figure 5.10 below illustrates the effects of varying the overlap during the sintering. In a scenario of not including an overlap between each row of sintered copper ink (0 % overlap), this results in regions of unsintered copper ink which behave as open circuits. In contrast, having a large overlap of 30 % will result in areas of ablation due to the increased power distribution over the same region. The optimum pulse overlap was found to be at 15 % where the irradiated beam even sintered the copper NPs without causing ablation or unsintered regions.

### **Ablation threshold and pulse overlap**

The variation of the pulse overlap was found to also impact the ablation of the material due to the high intensity of focussed radiation exposed within a narrow gap. Upon varying the separation between each adjacent row,  $d_{ss}$ , with a smaller separation yielding a large overlap of up to 30 %, it was found that ablation occurred for samples sintered with a 30 % overlap. The optimum overlap was found to be 15 % where only a fraction of the beam was made to “re-scan” the previously sintered row of nanoparticle ink, resulting in a continuity in the sintering of the rows of nanoparticle ink to yield an optimum sheet resistance value in the sintered patterns, as shown in Figure 5.10 below. The full analysis of the overlap variation can be found in Appendix B.1. However, higher fluence values with a 15 % overlap, such as a fluence of 546  $mJ/cm^2$  in the case of copper printed on the paper substrate, resulted in the localised ablation of the copper nanoparticle ink which ultimately resulted in the increase in resistivity beyond the optimum, which can be seen in the bulk resistivity comparison plot for copper nanoparticle ink (Figure 5.8 above, comparing the fluence and bulk resistivity of copper nanoparticles printed on the paper substrate). Additionally, Figure 5.12 shows a snapshot of the sintered copper as a result of a 30 % overlap at optimum fluence levels, resulting in the ablation of copper on the surface. Following ablation, the vaporised material

is deposited on the surface of the substrate in the form of speckles of copper, which can be seen in the enlarged SEM image.

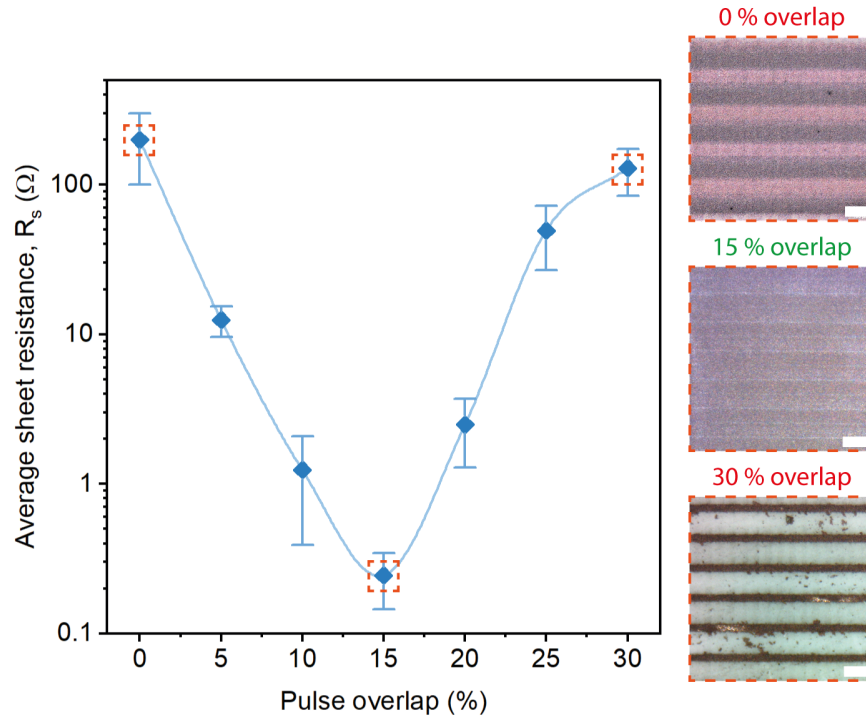


Fig. 5.10 Graph showing the pulse overlap variation optimisation and the effects on the sintered copper pattern through optical microscopy images of copper printed on paper, showing regions of unsintered copper in the darker regions (0 % overlap); optimum sintering (15 % overlap); and regions of ablation in the lighter regions due to a large pulse overlap (30 %) combined with a high fluence.

As the energy of the pulsed laser beam is more concentrated in the centre of the beam due to the stacked configuration of the diodes, the inclusion of an overlap is to prevent variation in the regions of sintering from the centre to the edges of the irradiated area. Figure 5.11 below represents a detailed SEM view of the comparison between a region of partial sintering taken at the edge of an irradiated area, and one of complete sintering, taken at the centre of the irradiated area. In order to improve the sintering mechanism without causing ablation in the centre of the irradiated area, the inclusion of an overlap between the sintered rows allows the laser to irradiate the partially sintered regions again and, in the process, supply sufficient energy to induce additional sintering of the nanoparticle at the edge of the laser beam, to eventually obtain a more evenly sintered pattern.

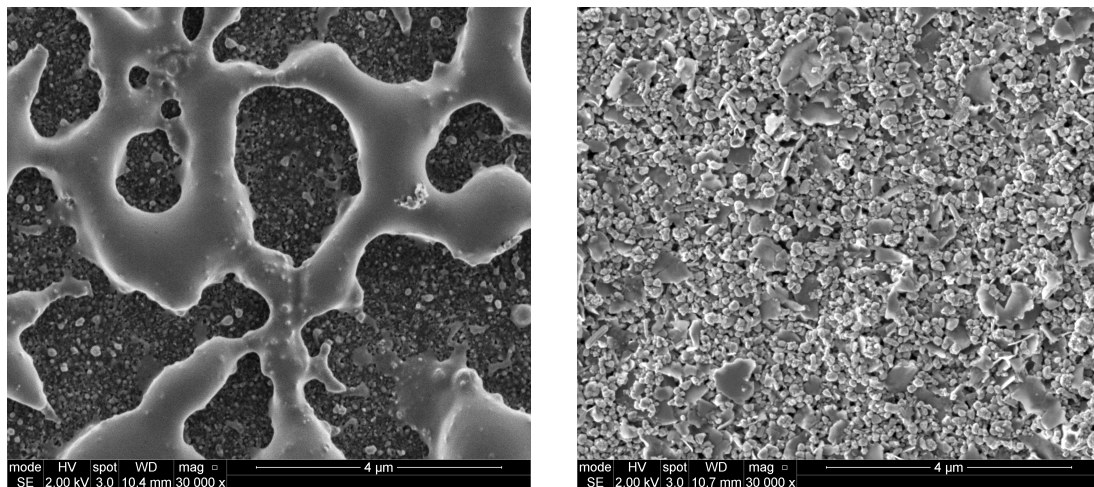


Fig. 5.11 Detailed SEM view of [left] a partially sintered region after the pulsed laser fluence below the optimum sintering threshold, highlighting the presence of the solvent and the partially unsintered nanoparticles in the background, and [right] a sintered region, showing the presence of coalesced nanoparticles to form a percolating network to improve conductivity.

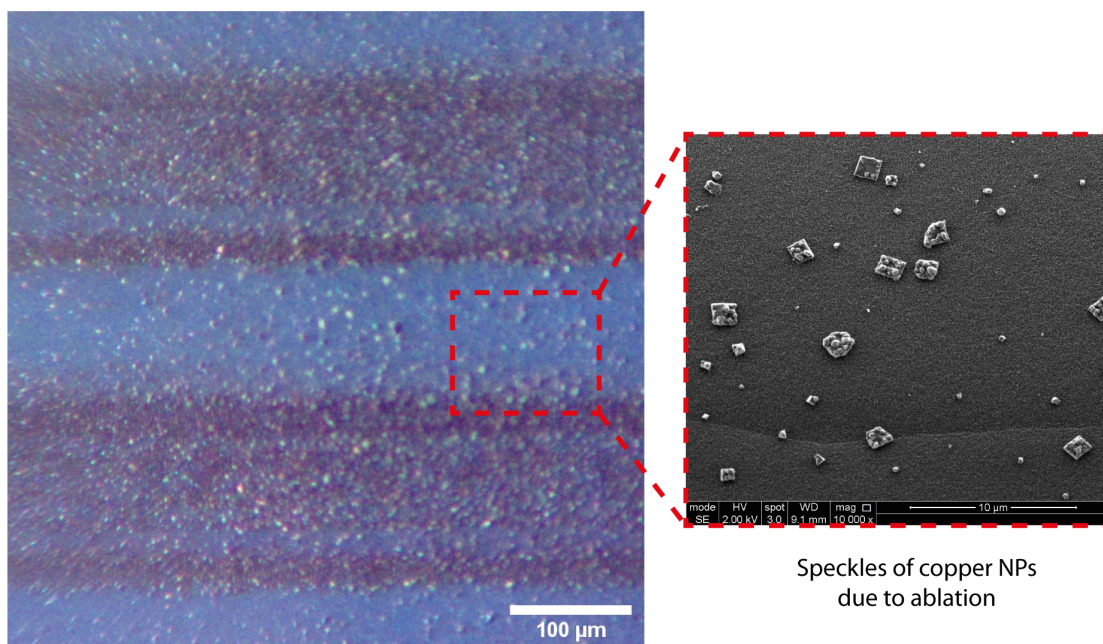


Fig. 5.12 Snapshot of the ablation of copper nanoparticle ink as a result of a large overlap of 30 % between each row of sintered copper at optimum fluence levels. The magnified view is the SEM of the speckles of copper produced as a result of ablation from the surface of the substrate, in this case paper.

### 5.1.4 Conclusions

In this experiment, a copper and a silver nanoparticle-based ink were inkjet-printed and sintered using a pulsed laser. Four substrates, each with varying mechanical and thermal properties, were subjected to the pulsed laser sintering process. The results from these tests indicate the successful pulsed laser sintering within a range of fluence parameters, above which the laser sintering results in the localised ablation of the nanoparticle layer. The results obtained from printing two layers of conductive ink are summarised in Table 5.2 below. From these experiments, the best conductivity results obtained were from the samples printed on paper due to the higher concentration of nanoparticles in a smaller section.

The samples printed on paper were, on average, 9.8 % thicker and 10.2 % narrower than the other samples printed on glass or the polymer films. The coating on the paper allowed for the better adhesion and concentration of nanoparticle on the surface, which combined with the higher resolution of print resulted in the better conductivity values.

Table 5.2 Summary of the bulk conductivity values obtained when compared with relevant bulk metal at optimum laser sintering conditions.

		Silver		Copper	
		<i>Conductivity comparison</i>	<i>Fluence, mJ/cm<sup>2</sup></i>	<i>Conductivity comparison</i>	<i>Fluence, mJ/cm<sup>2</sup></i>
Substrates	Glass	17.9 %	446	16.2 %	402
	PET	19.5 %	446	23.9 %	446
	Kapton PI	22.4 %	446	26.6 %	446
	Paper	24.9 %	500	38.7 %	500

The pattern sintered on the polymer films showed similar acceptable results. PET, being a transparent polymer film with a low glass transition temperature as compared to the Kapton polyimide film (80 °C as compared to 400 °C), showed no apparent damage during the laser sintering process. In this case, the choice of PET as compared to the Kapton PI film is advantageous due to its optical clarity and obvious low cost, with similar mechanical properties.

In terms of the duration of the laser sintering process, even though the “snake scanning” approach is more time consuming due to the limitation of the repetition rate of the laser as compared to a continuous wave laser, it outweighs the benefits as there is still a reduction in

the overall duration of sintering and the clear advantage of using a thermo-sensitive substrate, which would not be feasible via conventional sintering techniques.

Since the pulsed laser sintering was successfully done thermo-sensitive substrates, the next questions to address are the implications on the mechanical properties of the substrate. Pulsed laser ablation was observed on some substrates with the nanoparticle layer vaporised from the surface, raising the question of the effects of the penetration depth of the laser to the surface. In the case of the optimally sintered nanoparticle patterns, how does the fluence from the pulsed laser affect the adhesion of the nanoparticle layer to the substrate due to its inherent top-down sintering approach?

## 5.2 Experimental II - Adhesion Investigation

### **Adhesion evaluation of inkjet-printed and pulsed laser sintered copper nanoparticles at ambient conditions for printed electronics applications**

The determination of the success of a manufacturing process is highly subjective to the specification of the user. For example, the nowadays simple process of printing a document at home is deemed “successful” when the printer recreates the digital content sent from the computer onto the sheet of paper, with levels of clarity of text deemed decent by the end-user. When it comes to printed electronics, this assessment process becomes more thorough and complicated as other factors, such as electrical performance, are considered. In inkjet printing of functional material for printed electronics purposes, the list of specifications is much longer and will often include a specific requirement of resolution or line width, conductivity, and some level of robustness depending on the application (e.g. flexural strength for flexible electronics). However, the long-term viability of printed electronics is rarely considered as they are perceived to be as robust as the devices produced by industrial processes such as photolithography. For example, functional metallic nanoparticle-based inks of a conductive nature are assumed to have similar properties as their bulk counterparts, and the study by Guo et al. [231] clearly demonstrates a variation in mechanical properties of nanoparticles as compared to the bulk material.

Printed electronics differ in mechanical integrity due to their method of production (e.g. inkjet printing from nanoparticulate suspensions). Consequently, these printed electronics are more susceptible to failure due to mechanical or thermal stresses involved either in manufacturing, post-processing step or usage, particularly at the interface between the substrate and the deposited layer of functional material. High performance printed electronics are highly dependent on the adhesive strength at the interface for robustness during a flexible or stretchable application. The adhesion mechanisms of a coating to a substrate deserves an appropriate consideration in order to successfully fabricate printed devices, especially when different types of materials are considered (e.g. metals and polymers). Failure to properly quantify or understand these mechanisms often lead to device failure in the long-term, which is often overlooked in the early stages of fabrication.

The focus of this section lies on the adhesion characterisation of inkjet-printed copper nanoparticle-based inks on a variety of substrates. The copper nanoink tracks are printed and pulsed laser sintered, and the adhesion of the copper ink to the substrates is evaluated. The effects of different irradiation regimes on the adhesion are then expanded upon and a conclusion provided.

## 5.2.1 Materials and methods

### Substrates

Four different substrates were tested, including standard clear laboratory glass slides, DuPont™ Kapton® HN polyimide (PI) sheets of 125  $\mu\text{m}$  film thickness and polyethylene terephthalate (PET) sheets measuring 350  $\mu\text{m}$  in thickness. Additionally, a 250 *gsm* paper measuring 400  $\mu\text{m}$  thick and manufactured by Hewlett-Packard was also tested. The paper has a thin hydrophilic coating made of a polymer resin which enhances the print resolution for inkjet applications as it allows the liquid content of the ink to dissipate throughout the paper whilst allowing the pigments or particles to remain on the top surface. All of the samples, except for paper, were prepared for inkjet printing by a thorough rinse with deionised water followed by another rinse with acetone before drying under a clean, pressurised flow of air. The details of the substrates are described in Section 3.1 on p. 52.

### Inkjet printing

The ink chosen for this experiment was an experimental grade copper nanoparticle suspension ink (Dycotec Materials Ltd.) which was specially designed for flash sintering systems, described in Section 3.1 on p. 53. Prior to filling the inkjet reservoir, 3 *mL* of ink was filtered using a 0.45 *m* PTFE filter to eliminate the presence of any contaminants which may cause defects or clogs during printing. The reservoir was coated with a light-repellent adhesive tape on the external walls to prevent degradation of the inks due to light.

A drop-on-demand inkjet printer (JetLab-4XL, MicroFab Technologies Inc.) fitted with a printhead measuring 60  $\mu\text{m}$  at the nozzle orifice was used for all the printing trials. The in-flight diameter of an ejected droplet measured between 40 – 45  $\mu\text{m}$ , hence a droplet spacing of 75  $\mu\text{m}$  was maintained for all the specimens. The ink was printed to form square samples measuring 15×15  $\text{mm}^2$  with two layers of copper at ambient room conditions, the temperature of which ranging from 23 °C to 26 °C. The printing waveform shown in Figure 5.13 below was used for dispensing individual droplets from the printhead, along with a snapshot of the droplet produced. The optimisation process followed the similar theory described in Section 3.2.1 on p. 57. The substrate temperature was maintained at 40 °C to accelerate the evaporation of the solvent upon deposition, thereby creating a pinned geometry to prevent the overspreading of the ink.

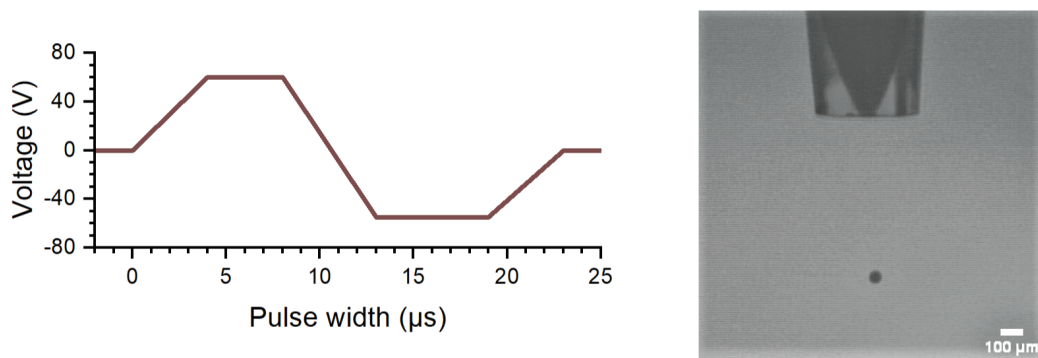


Fig. 5.13 [Left] Illustration of waveform used to eject a droplet of copper nanoparticle ink from the  $60\ \mu\text{m}$  printhead at  $25\ ^\circ\text{C}$  (room temperature), and [right] a snapshot of the droplet measuring an in-flight diameter between  $40 - 45\ \mu\text{m}$ .

### Pulsed laser sintering

A similar pulsed laser sintering process, as described in the previous Experimental Section I - Pulsed Laser Sintering Investigation on p. 102, was used. The percentage of overlapped area was maintained at 15 % as this was found to be optimum, as explained in Section 5.1.3 on p. 112. The variation of the pulsed laser fluence was done to determine the optimum fluence parameters to obtain the best adhesion of the copper nanoparticle ink to the substrate. The fluence was varied from  $286 - 500\ \text{mJ}/\text{cm}^2$  on all the substrates, as higher values of fluence resulted in ablation.

## 5.2.2 Characterisation

### Contact angle analysis

To understand the mechanics of adhesion when the copper ink is printed on the various substrates, the equilibrium contact angle of the droplet can give an indication of the wetting of the substrate. The contact angle (CA) of the drop of the different substrates was averaged based on five measured numerical values obtained by analysing the contact angle on the substrate, the methodology of which is described in Section 3.4.2 on p. 70.

### Cross-cut test procedure

The adhesion of the samples was tested according to the ASTM F1842-15 standard using scotch tape, and a full description of the procedure can be found in Section 3.4.7 on p. 75. As a summary, a cutter is used to make six simultaneous cuts into the sample, then the sample is brushed off for any loose particles which may have been removed from the surface, and a

second identical cut is placed, perpendicular to the first, to achieve a grid pattern. The surface is brushed one last time, followed by the application of an adhesive tape to the cut sample, ensuring good contact is made with the specimen. After 90 seconds, the tape is removed by steadily peeling it off back upon itself as close to a 180° angle as possible. The grid area is then inspected and compared against the standard.

### **Adhesion evaluation and classification**

The grid inspection after the tape was peeled was done through digital image processing software to avoid the human assessment bias. The samples were first photographed using a high-resolution camera, followed by digital manipulation involving a monochrome conversion and the areas of delamination quantified as “voids” from the overall selected sample area. This methodology provided an unbiased and a more systematic and reliable assessment of the adhesion, as detailed in the earlier section 3.4.7. The delaminated area was then compared to the standard test results table from Figure 3.21 on p. 79.

## **5.2.3 Results and discussion**

### **Laser fluence variation and adhesion classification**

The variation in the laser fluence was done to determine the optimum level of adhesion for the different substrate, and the results are shown in Table 5.3 below. The increase in the laser fluence resulted in an increase in the conductivity of the copper nanoparticle-based ink. The increase in conductivity can be explained by the absorption of the irradiation, resulting in the sintering of the copper nanoparticles, thereby increasing the concentration of pathways for the transfer of electrons throughout the printed sample. At the lowest fluence values, the adhesion of the printed copper ink on all the substrates can be classified as *3B* due to the removal of between 6 – 12 % of the sintered copper layer. As the laser fluence increases (resulting in an increase in the conductivity of the printed copper layer), the amount of copper removed following the cross-cut test decreases until the ablation threshold is reached, as shown in Figure 5.14 below. Beyond this threshold, ablation occurred, and the remaining printed copper layer was defective and unsuitable for the cross-cut testing and evaluation as the removed area was significantly higher at above 70 % of the total printed area. However, for the paper substrate, the highest fluence which was used was at  $500 \text{ mJ/cm}^2$ , and it was found to yield a more conductive printed pattern as well as a slight decrease in the average area detached by 0.29 %. Even though the decrease is marginal, it indicates that the ablation threshold for the paper substrate was not reached, and an overall higher resistance to ablation at  $500 \text{ mJ/cm}^2$  fluence as compared to the other substrates.

Table 5.3 Summary of the adhesion evaluation using image processing software, and the classification result based on the F1842-15 standard table. Note that the “\*” denotes a lack of area detached due to the ablation of the printed copper ink, resulting in defective samples unsuitable for adhesive characterisation.

Substrate		Fluence ( $mJ/cm^2$ )				
		286	357	402	446	500
Glass	%average area detached	6.66	2.42	1.70	1.60	*
	Classification	3B	4B	4B	4B	–
PET	%average area detached	6.54	6.53	2.68	0.61	*
	Classification	3B	3B	4B	4B	–
Kapton PI	%average area detached	6.93	5.85	3.55	0.65	*
	Classification	3B	3B	4B	4B	–
Paper	%average area detached	11.81	11.66	10.29	9.94	9.65
	Classification	3B	3B	3B	3B	3B

The optimum fluence values used for sintering the copper nanoparticles on the various substrates which led to the least areas of delamination (hence, indicating the most adhesive strength at the interface) is plotted for all four substrates in Figure 5.15 below. It was found that none of the samples were categorised in the 5B section which indicates that none of the copper ink was delaminated from the surface, although the copper ink optimally sintered on glass, PET and Kapton PI were categorised in the 4B section as a result of the F1842-15 cross-cut test. A more intricate look at these three samples shows that those printed glass had an average delamination of 1.60 % at optimum sintering, while the samples on the polymeric substrates, PET and Kapton PI, had an average delamination value of only 0.61 % and 0.65 %, respectively.

As this method of sintering is novel, and given the nature of delivering the sintering energy in the form of irradiation from a top-down approach as compared to other conventional sintering methodologies, the adhesive properties of the inkjet-printed copper NPs cannot be compared to other experimental output. Nonetheless, the recent work by Son et al. [187] describes the inkjet printing of copper nanoparticles on a plasma treated polyimide substrate, followed by sintering in a reduced atmosphere using a flash lamp, and the results showed a relatively more adhesive copper layer as compared to a heat sintered control sample after bending, although this was not quantified.

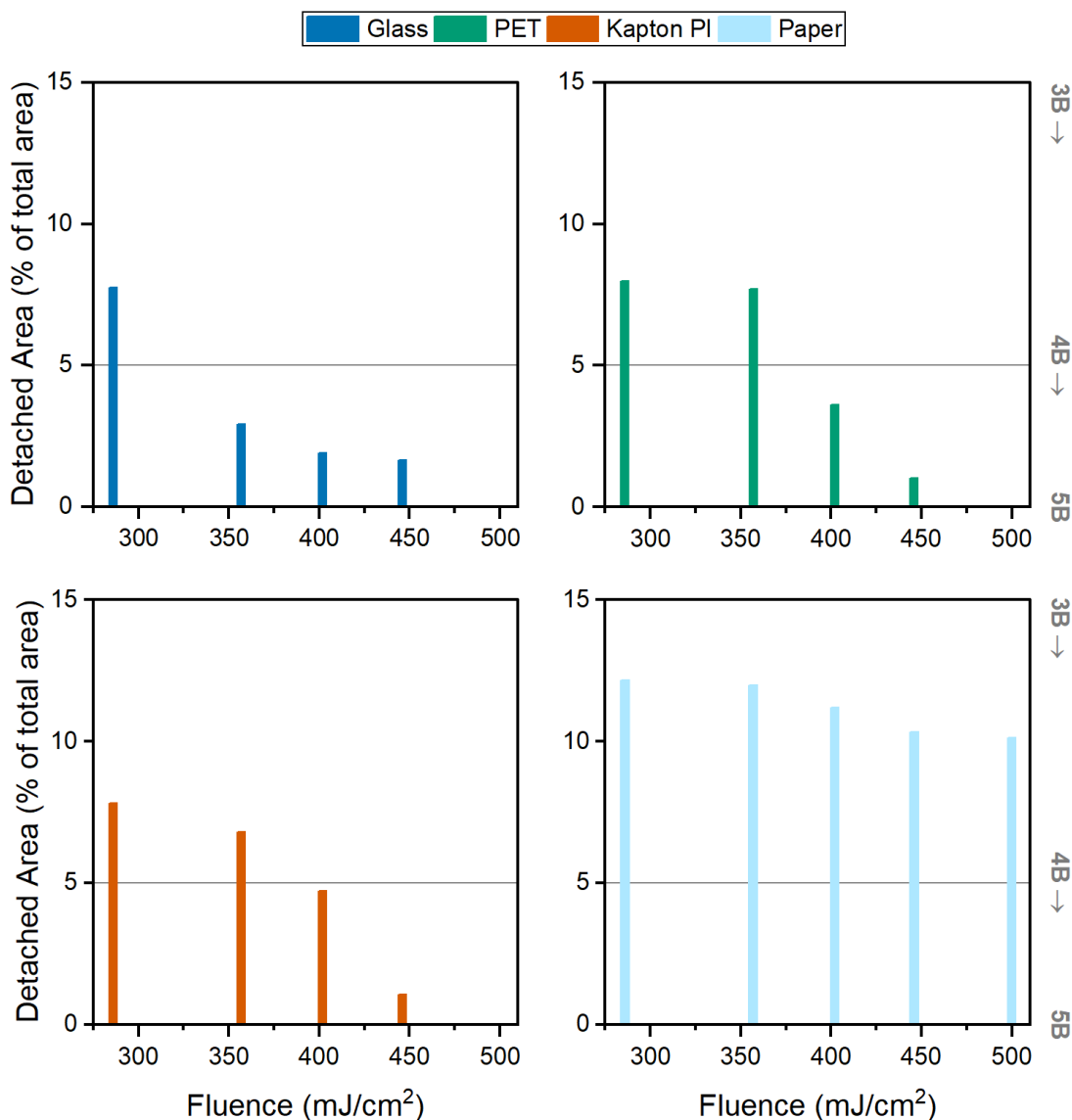


Fig. 5.14 Graphical representation of the different adhesion evaluation in terms of the detached area as a percentage of the total printed area ( $15 \times 15 \text{ mm}^2$ ) for the copper nanoparticle-based ink printed on the four different substrates, as a function of the laser fluence variation. The right y-axis represents the adhesion classification based on the F1842-15 standard, starting from 5B to 4B and 3B in this set of experiments.

Another contribution by Kim et al. [185] used an intense pulsed light setup to sinter a deposited copper nanoink on low-temperature polymer substrates at ambient conditions, and explained an improvement in the conductivity of the copper without damage to the substrate. In their contribution, a scratch test using a diamond tip was performed as a means to evaluate the adhesion and revealed “good adhesion” to the substrates.

Zenou et al. [82] explored the combined use of a continuous wave and a pulsed laser to produce spin-coated copper patterns at ambient conditions. The continuous wave laser output was used to sinter the patterns, while the pulsed laser was used for ablation, hence resulting in the formation of fine features with line width under  $5 \mu\text{m}$ . However, their adhesion evaluation method is questionable given their evaluation is based on a “pass or fail” after rinsing in water or a solvent.

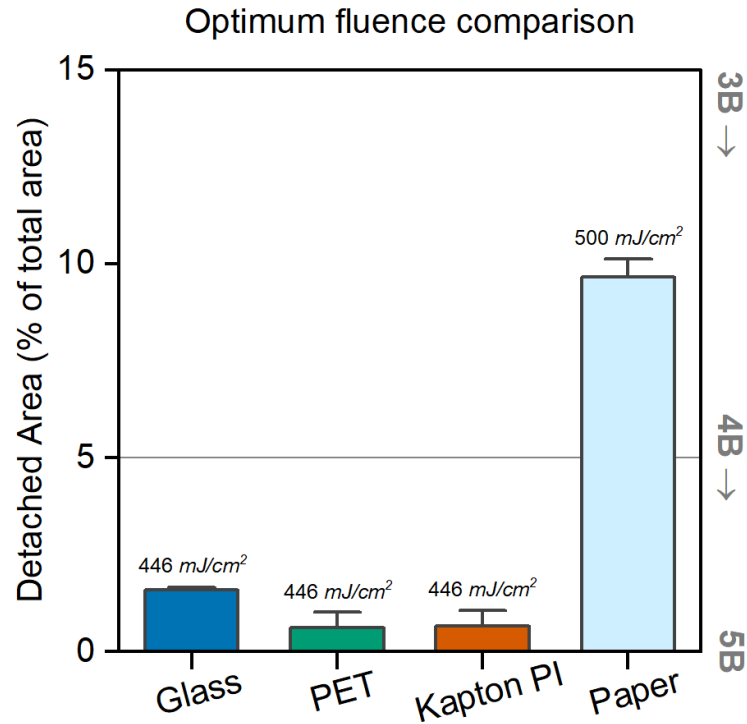


Fig. 5.15 Graphical representation of the optimum adhesion classification values and the variation shown with error bars on each substrate when sintered at the optimum laser fluence. The right y-axis represents the adhesion classification based on the F1842-15 standard, starting from 5B to 4B and 3B in this set of experiments.

### Adhesion mechanisms

There are several factors which can be used to describe the adhesion mechanics, although the two major contributors in a metal-polymer system have been found to be mechanical interlocking and chemical bonding [232–234], while other factors such as electrostatic forces, physical adsorption and diffusion have been found to have negligible effects when applied to this system under study. Mechanical interlocking adhesion mechanism is due to the anchoring of the ink constituents, in this case nanoparticles, within microscopic cavities found in the substrate, as shown in Figure 5.16. As a result, additional energy is required to separate the printed copper coating from the surface.

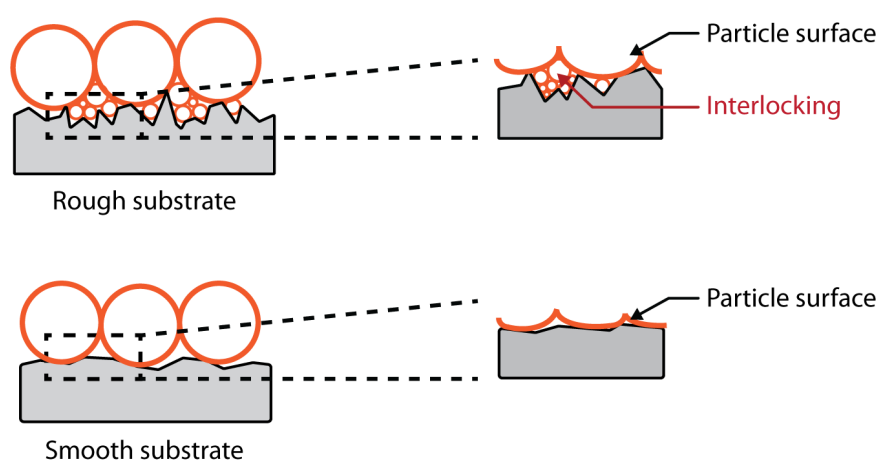


Fig. 5.16 Representation of the comparison between a rough and smooth surface, highlighting the presence of voids due to micro-gaps on a rough surface, resulting in a mechanical interlocking of NPs.

The surface roughness of the substrate plays a major role in the mechanical interlocking mechanism due to the interface – a relatively smooth surface with uniformly-sized voids ensure the consistent anchoring of nanoparticles of a uniform particle size within the substrate, thereby increasing the adhesive strength which is observed with the copper ink printed on glass. In contrast, a relatively rougher surface can result in the creation of voids due to an increased localised concentration of nanoparticle agglomeration around a hollow region, while other regions which contain smaller cavities have a low nanoparticle concentration, which ultimately leads to a poor adhesive strength at the latter regions. This phenomenon can be used to explain the adhesive property on the polymer substrates. Additionally, the variation of the size of the cavities at the surface of the substrate can create regions of moisture accumulation due to the failure of the nanoparticle to penetrate the cavities uniformly, which eventually is detrimental to the adhesive strength of the printed copper ink on that particular substrate – in this case the paper substrate.

Chemical bonding mechanisms can occur as a result of the formation of ionic, covalent, and metallic bonds at the metal-polymer interface [235]. However, the identification of the particular type of chemical bond at the interface is not well understood due to the complexity of each bond type, and the nanoscale involved in the analysis [236]. As a result, experimental quantifications of chemical bonds generally refer to a set of chemical bonds, and in a metal-polymer system, it usually occurs due to the transfer of a charge from the copper nanoparticle to the substrate after surface treatment such as chemical vapor deposition or plasma treatment [237]. These surface modification methods impart a functional aspect (e.g. hydrophilicity) to the substrate, which eventually enhances the chemical bonding properties of the polymer to the metal layer. However, as surface modification techniques were not used throughout this experiment for the polymer substrate, the adhesive strength due to chemical bonding mechanisms is assumed to be negligible as compared to mechanical interlocking mechanisms, particularly as metallic NPs ink were used.

### **Contact angle and substrate wetting characteristics**

Some other factors which influence the adhesion of the nanoparticles at the substrate interface include the wetting and spreading of the deposited functional material, the penetration within the substrate and, in the case of nanoparticulate suspensions, the size distribution of the nanoparticles. A poorly wetted surface (e.g. an ink printed on a hydrophobic substrate) has a smaller surface contact area as compared to a well-wetted surface (e.g. an ink printed on a hydrophilic substrate) which has a larger surface contact area. For suspension inks, a homogenous particle size distribution results in a larger contact area when printed on a surface, as compared to suspension inks with an uneven particle size distribution.

The equilibrium contact diameter of the drop on the substrates can be used as an indication of the spreading of an ink on the substrate after deposition. Figure 5.17 represents the results of the contact angle analysis on the substrates. In the case of glass being a relatively smooth, non-porous surface, the ink spreads considerably (shown by a CA = 18.7°) indicating a highly wetted surface which can result in coffee staining after sintering. For the polymer substrates, the wetting characteristics indicate a moderately well-wetted surface due to their smoothness and similar non-porous property (CA = 33.1° and 32.7° for PET and Kapton PI, respectively). The highest contact angle calculated for paper (CA = 37.6°) indicates a well-wetted surface, although this could be attributed to the resin coating and the porosity of the paper which prevents the spreading after deposition. Despite the variation in contact angle, the wetting characteristics for all four substrates follow a well-wetted surface, particularly when two layers of the copper ink were printed to ensure the optimal coverage of the 15 × 15 mm<sup>2</sup> surface area.

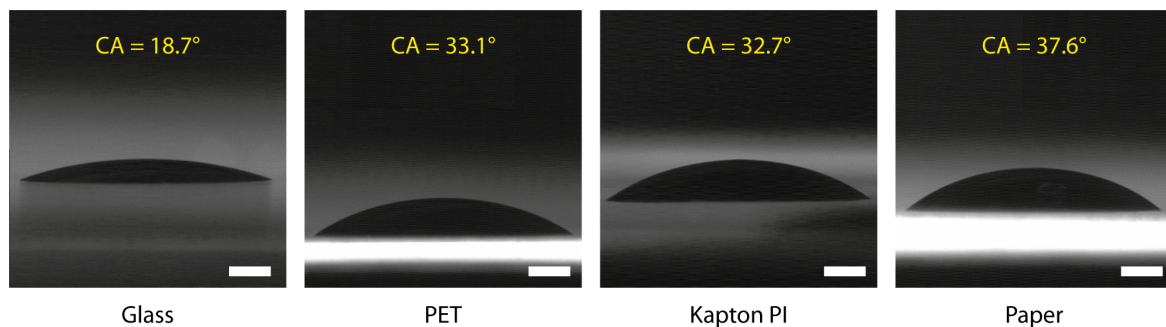


Fig. 5.17 Snapshot of the contact angle of a drop of copper nanoparticle-based ink on the glass, PET film, Kapton polyimide and the paper substrates used throughout this experiment, highlighting the spreading of the ink on the surfaces. Scale bar is 10  $\mu\text{m}$ .

### Types of failure modes

The adhesion test can also be used as an indication of the types of failure modes which can be observed while evaluating the performance of a coating (in this case, an inkjet-printed layer). These can be of four categories, which are described with the help of Figure 5.18 below:

(a) cohesive failure;

Perhaps the most tolerable out of all the failure modes, cohesive failure indicates a strong bond to the substrate and failure arises due to internal delamination within the converted ink structure due to the weak internal bonds of the particles (e.g. weak bonds between nanoparticles).

(b) adhesive failure;

Perhaps the least desirable, adhesive failure of the substrate and the ink which indicates a poor bonding of the ink to the substrate.

(c) mixture of both cohesive and adhesive failure modes;

(d) substrate or testing apparatus failure.

In this case, the substrate (or testing apparatus) detaches from the coating due to the excellent bonding of the ink, indicating a higher fracture or peel strength as compared to the flexural or tensile strength of the substrate (or testing apparatus).

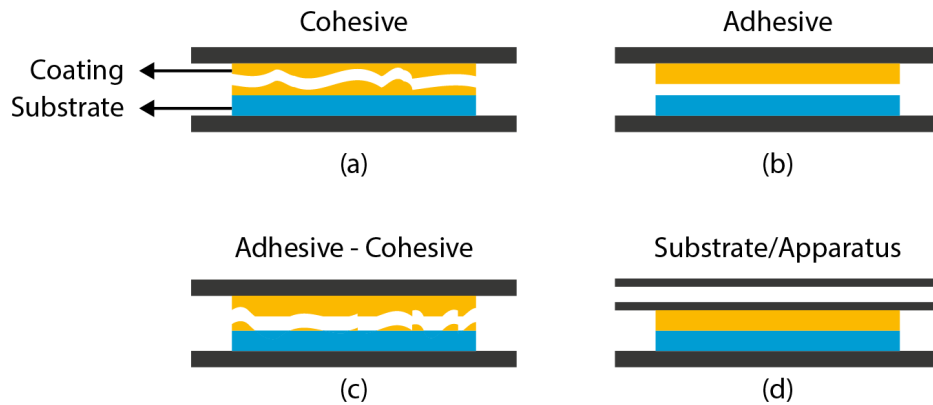


Fig. 5.18 Illustration of the different failure modes for a coating on a substrate. The testing equipment is represented by the black rectangular strips.

### Oxidation of copper nanoparticle on paper

During the adhesion evaluation, the delamination of the copper samples exposed the inter-layers of copper. Since copper is prone to oxidation, the question about the stability of the printed copper film at ambient conditions must be addressed. A design of experiment as shown in Figure 5.19 illustrates the procedure for evaluating the oxidation of copper. In stage I, the copper ink, once printed, was left at ambient conditions (21 – 25 °C) for *seven* days, after which the pulsed laser sintering at optimum fluence parameters was done on each substrate. It was found that the copper printed on glass and the polymer substrates (PET and Kapton PI) was successfully sintered and achieved similar mechanical and electrical properties after testing for adhesion and conductivity. However, the paper sample suffered from severe delamination following sintering and the cross-cut test due to the oxidation of the copper ink, as shown in Figure 5.20 below. After seven days at ambient conditions, the copper layers were completely dried, and despite exhibiting no colour changes in that period of time, the pulsed laser sintering process revealed otherwise, particularly after the cross-cut was performed.

As a comparison, stage II represents the procedure for the samples which were immediately laser sintered after drying (within one hour), and were left at similar ambient conditions for seven days. Then, the cross-cut test was performed, and the results were distinctively different. It was found that all the immediately sintered samples achieved similar mechanical and electrical properties after testing for adhesion and conductivity, as compared to the previous stage I of the experiment where the samples printed on paper suffered from oxidation. Additionally, stage III extends the experiment to a duration of *twenty-eight* days to validate the claim, and no significant change was observed for those samples, after which the experiment was concluded.

## Copper oxidation - Design of Experiment

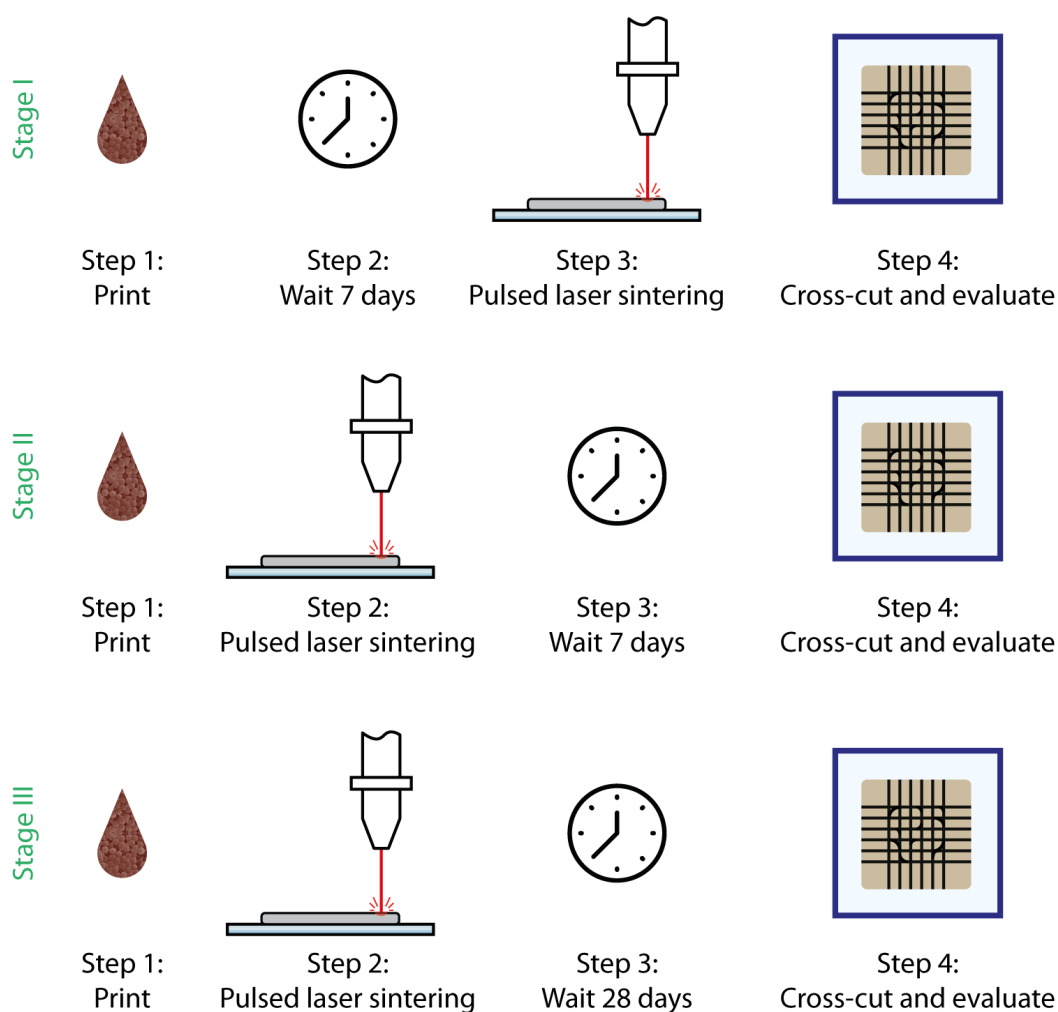


Fig. 5.19 Design of experiment for the oxidation evaluation of pulsed laser sintered copper NPs.

The oxidation of the copper ink which was printed on paper and left at ambient condition for seven days can be explained by the porous nature of the paper which allowed oxygen molecules to penetrate through the constituents of the stable nanoparticle-suspension ink. Moreover, the hydrophilic coating which promotes an improved resolution of the printed pattern creates a distinct separation of the nanoparticles and dispersant from the chemical solvent which is used to prevent the oxidation of the copper nanoparticle-based ink. As a result, the lack of oxygen-inhibitors from the ink causes the oxidation of copper nanoparticles as the chemical solvent evaporates through the underneath of the fibres of the paper substrate, resulting in a cohesive-adhesive delamination of the copper from the paper substrate, as shown in Figure 5.20.

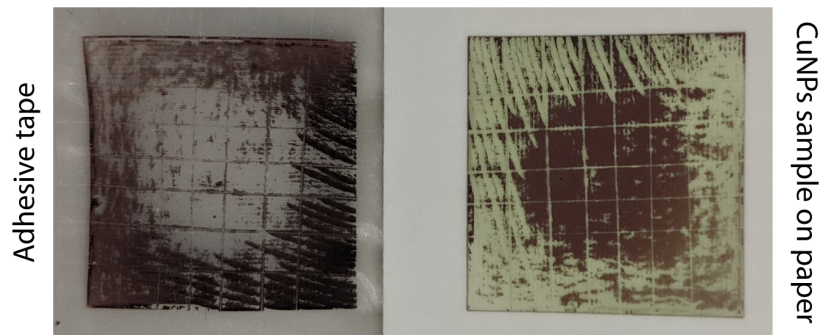


Fig. 5.20 Snapshot of the oxidised copper sample printed on paper which was left at ambient conditions for seven days, after which the pulsed laser sintering was performed followed by the cross-cut test.

In comparison with previous literature which evaluate the oxidation of copper, Zenou et al. [238] reported that no oxidation of copper was observed with their samples, provided the laser irradiation process was done fast enough at the correct fluence parameters depending on the NPs ink. In their case, they printed copper NPs on glass and performed the irradiation process using a *cw* laser, with an exposure time of a few milliseconds. Similarly, Halonen et al. [239] supported this conclusion when they performed the sintering of copper NPs with a *cw* laser and did not observe any oxidation as the irradiation was limited to very short durations.

### Applications and significance

The classification of the adhesion results from *5B* to *0B* can be interpreted in various ways, and for some scientists these results might not provide sufficient information concerning the kind of applications which the specimen under test can be aimed at. This raises the question of “*What do these classification results mean?*”, and this section aims at providing some indication to best answer the question. This discussion is facilitated by a qualitative survey with different ink suppliers which state the adhesion characterisation in their ink specification sheets, e.g. Dycotec Materials Ltd.

Starting from the lowest, a classification of *0B*, being the least desired outcome of the cross-cut test, indicates that there is a very high probability that the sample will fail when subjected to external stimuli such as a force acting on its surface, a vibrating environment, or a bending moment. At this stage, there are not many applications for such a sample due to its limited performance, although it can be made useful for temporary solutions on rigid surfaces. For example, this type of sample can be used as a quality control for short-term transport applications to verify the integrity of a shipment which unfavourably underwent

extensive fatigue in the form of bending or friction cycles. In the long term, to mitigate the failure of the sample, a surface treatment is highly recommended to improve the adhesion of the coating/ink to the substrate. Alternatively, the chemical composition of the coating/ink can be modified to include an adhesion promoter [240] which is an additive that improves the strength of the coating at the interface without impacting the performance of the end-product.

Next, a classification of *1B* indicates that there is also a high probability of the coating to detach from the substrate when subjected to similar external stimuli. However, depending on the amount of delamination (*1B* indicates between 35 % – 65 % delamination), there are several options which can be considered. On the lower end of the delamination, the use of adhesion promoters can only marginally improve the adhesion of the coating/ink while other factors such as a surface treatment, preparation prior to coating and carefully optimising the curing or sintering environment of the coating/ink can prove to be more beneficial for improving the adhesion. Some of the applications for a sample exhibiting such adhesive strengths can be targeted at temporary rigid coating such as wallpapers, posters, or banners.

Higher on the adhesion chart, a rating of *2B* indicates the delamination area is between 15 % – 35 %, which is acceptable for static applications such as a coating on a rigid surface (e.g., wallpapers and paints) in the long-term. However, similar external stimuli may not be favourable for the long-term viability of the coating/ink on that surface, hence the use of a surface treatment and an optimised curing cycle is recommended to improve the adhesive strength at the interface.

As we approach the higher rating of *3B* indicating a delamination of between 5 % and 15 % (only a 10 % range), coating/inks which fall into this category can be aimed at low- to mid-end applications such as printed electronics for static applications. For example, functional inks in this category can be printed on various surfaces without the need of a surface treatment as long as the curing or sintering process is optimised to promote a higher adhesion mechanism (either through mechanical interlocking or chemical bonding). Applications can be targeted at simple printed circuits which are not subjected to external stimuli such as extensive bending or fatigue cycles. However, a certain level of exposure from external forces on the surface of the coating/ink can be maintained without having a detrimental impact on the performance of the device. At this stage, the addition of an encapsulation layer is recommended to protect the coating/ink in the long-term, which can eventually be aimed for applications in the mid- to high- end electronics [241].

At the even higher end of the chart, a rating of *4B* indicates that less than 5 % of delamination occurs after testing, indicating the suitability of the coating/ink for high-end applications such as flexible printed electronics. These devices can sustain external forces, vibrations and bending cycles in the long-term with minor impact on their performance,

although an encapsulation layer is recommended for applications in high-stress dynamic environments.

Finally, at the top tier, a rating of *5B* indicates that no delamination occurs at all, and applications of such coating or inks can be aimed at ultra-high end electronics for flexible or even stretchable printed electronics.

### **Suitability of adhesion evaluation technique**

As printed electronics are classified as thin films due to their geometries, the evaluation of their adhesive strength is a complicated process which can increase in complexity due to the use of the test apparatus.

The earlier work by Mittal in 1976 [242] expanded on the importance of evaluating the adhesion of thin films ( $< 1 \mu\text{m}$ ) and reviewed some test methodologies such as the pull test, highlighting grounds for further improvement such as the use of centrifugal dispersion of the adhesive layer for the pull-test method. Other suggestions included further investigations in normalising the use of standard test equipment, cross-comparison of various techniques and the adhesion measurement of thin polymeric films. These suggestions were then discussed in detail by Bowling [243] who analysed the adhesive strength of particles ranging from  $0.1 \mu\text{m}$  to  $100 \mu\text{m}$  in diameter on semiconductor surfaces, and discussed the types of forces such as van der Waal and capillary acting at the interface, and can increase due to an increase in surface area after deformation.

The report by Gerberich and Cordill [244] expanded on the physics of adhesion based on different scenarios which ultimately contributed to a broader understanding on the topic. In their report, the authors focused on the metal-semiconductor and metal-ceramic interface due to the developments in thin film technology, and performed a series of simulations and quantitative experiments to determine the adhesive strength.

Quantitative experiments are aimed at finding the adhesive energy in  $J/m^2$ , and these can be done using pull tests, scratch tests, nanoindentation and four-point bend tests. These experiments often require the use of rather complicated equipment to visualise the testing procedure, and there is often a minimum requirement on the sample geometry. For example, Marshall and Evans [245] investigated the fracture analysis of thin films using indentation-induced delamination techniques and provided an explanation on controlling the indentation for a suitable response in contact-induced damage for thin films. Despite the testing area being minimal in size, the equipment involved to capture the delamination process is significantly larger and resource-intensive. Following this, Litteken and Dauskardt [246] investigated the adhesion of polymer thin films using nanoindentation and four-point bend techniques. Each of the specimens for these qualitative tests required careful preparation (e.g. machining a

100  $\mu\text{m}$  central notch for the bending test) in addition to the patterning on the substrate, and conform to thin film geometries much bigger in aspect ratio as compared to inkjet-printed specimens. Birringer et al. [247] further elaborated on the proper technique required for the four-point bend test, highlighting the importance of the grain alignment along the beam axis for composite structures.

The research by Dupont et al. [248, 249] investigated the adhesive strength of roll-to-roll processed polymer solar cells using a pull-off test, while the geometries of the deposited layers were obtained using inkjet printing techniques. In order to perform their test, further preparation in the form of epoxy bonding the samples to the testing beams, and the use of a delaminator system was required. The results of these experimental techniques provided a clear, calculated value of the adhesive force between the interfaces. The suitability to printed electronics is questionable due to the pre-testing machining requirements (surface preparation, test equipment bonding, notch machining at a micro scale), and the geometries required for these tests. The most suitable quantitative experiment which can relate to printed electronics is the pull-off test, and despite the requirements for high-end delaminator systems, it has proven useful in many printed electronics applications [250, 251].

The pull-off tests rely on the addition of an epoxy adhesive between the layers under investigation (ink-substrate interface, and substrate-test baseboard) as highlighted by the previously mentioned reports. The curing of the epoxy layer is crucial in obtaining meaningful results, without compromising the investigation due to the improper delamination of the specimen. The choice of epoxy has to satisfy the specification of having an adhesive strength stronger than the dolly-epoxy adhesive strength as well as the test specimen-epoxy adhesive strength, in such a way that the test specimen fails either via cohesive failure of the printed layers, or adhesive failure at the printed layers-substrate interface. A final criterion the epoxy must satisfy is that its cohesive strength must be stronger than either the cohesive strength of the printed layers, or the adhesive strength at the printed layers-substrate interface. Once these specifications have been met, the pull-off test can be performed and the outcome deemed quantifiable.

It is worth mentioning that the long list of specifications introduces very minimal margins for exploration, and eventually requires great control over epoxy application, curing stages and testing procedure. Additionally, prior testing must be performed on the samples to investigate the chemical compatibility of the glue with the test specimen to prevent physical or chemical changes to the printed layers during the epoxy curing cycle, particularly when investigating thin films in this application. Furthermore, flexible soft substrates are susceptible to deformation during a mechanically stressful pull-off test method, which can inevitably distort the test results.

Finally, the cross-cut test based on ASTM International standard D3359 “Standard Test Methods for Measuring Adhesion by Tape Test” [221] is a less stress-inducing test method for thin films, particularly printed electronics. The procedure is less stress-inducing as it provides an indication of the adhesion of a coating in the form of a film to a substrate by applying a pressure-sensitive tape over a series of cuts made into the film. Joo and Baldwin [235] applied this test methodology for their investigation into the adhesion mechanisms of silver nanoparticle which was deposited on a variety of organic and inorganic substrates. Similar research outputs by Schirmer et al. [252] investigated the adhesion of a screen-printed silver paste on flexible PET substrates using both the pull-off and the cross-cut tape test.

In all of these findings, the cross-cut test can be done quickly, without the need for expensive specialised equipment and is the preferred method of obtain quick and reliable results in the research and development industry, and this is highlighted in the specification sheet of many functional ink manufacturers [253–259].

#### 5.2.4 Conclusions

In this experiment, an inkjet-printed copper nanoparticle-based ink was deposited on four different substrates (glass, PET, Kapton PI and paper), after which pulsed laser sintering was done to render the printed pattern conductive. In order to further characterise the performance of the copper patterns, a cross-cut adhesion test was performed to replicate a stressful environmental application for the copper patterns for all four substrates based on the ASTM F1842-15 standard. However, in this experiment, an improved, more systematic, and unbiased method of evaluating the adhesion was used based on digital image processing techniques which automatically calculate the areas of delamination from the printed copper pattern. As a comparison, the laser fluence was varied for each sample until the optimal pulsed laser sintering parameters were found. Table 5.4 below provides a summary of the optimum fluence values used to perform the pulsed laser sintering process for each substrate, and the corresponding average power and bulk resistivity comparison with bulk copper.

The polymer samples were found to exhibit the best mechanical and electrical properties combined due to their inherent non-porous surface which prevents the oxidation of the copper layers, contrary to the paper substrate which was found to leak oxygen through the porous paper fibres and eventually causing a cohesive-adhesive failure of the printed copper samples. However, the electrical properties of the copper pattern printed on paper was found to be superior to the other samples at the expense of a lower adhesion classification at *3B* as compared to *4B* for all the other samples optimally sintered. Nonetheless, since the delamination was found to be cohesive, the addition of an encapsulation layer can be used as

a means to limit the damage to the surface of the pattern, thereby improving the adhesive property of the printed copper film on each substrate and eventually its lifespan.

Table 5.4 Summary of the pulsed laser parameters used to sinter the copper nanoparticle ink on the four different substrates, highlighting the optimum fluence values and average power used to obtain the most conductive copper, indicated by the bulk conductivity comparison with copper and the relevant adhesion classification based on the ASTM F1842-15 standard.

		<b>Fluence</b> ( $mJ/cm^2$ )	<b>Average</b> <b>power (W)</b>	<b>Conductivity</b> <b>comparison</b>	<b>Adhesion</b> <b>classification</b>
Substrates	Glass	446	0.0804	16.2 %	4B
	PET	446	0.0804	23.9 %	4B
	Kapton PI	446	0.0804	26.6 %	4B
	Paper	500	0.0999	38.7 %	3B

### 5.3 Experimental III - Heat Affected Zone evaluation

#### Analysis of the heat affected zone due to pulsed laser sintering of inkjet-printed copper nanoparticles on thin films for printed electronics

Printed electronics which have been treated with a laser during the post-processing step can often be subjected to some unwanted deformation, or a limited performance due to the formation of a heat affected zone (HAZ). The HAZ must be minimised to prevent the unwanted stress concentration areas within the printed pattern, which can ultimately lead to crack formation, especially for flexible electronics.

Pulsed (*ns*, *ms*) and ultrashort (*ps*, *fs*) pulsed lasers have been used mainly for the micromachining processes by exploiting their ability to remove material from a surface in a very precise and accurate manner through a process called ablation. Hirayama and Obara [260] used a femtosecond pulsed laser for the ablation of a variety of bulk metals such as gold, silver, copper and iron and found that during ablation the crystalline structure of the metal changes to an amorphous structure, which leads to the formation of a melt zone, indicating the formation of a HAZ. In a later research by the same authors [261], they used femtosecond pulsed lasers for the ablation of bulk copper, and focussed their study on the formation of the HAZ prior to the ablation threshold, where they described the incident laser energy is absorbed in the copper, without any noticeable change on the surface. At the ablation threshold and higher, the ablation of copper was found to be dependent on the absorption coefficient, while the remaining energy unused for ablation was found to be absorbed in the sample. Additionally, in another study [261], they found that the heat affected zone was dependent on the laser fluence.

Le Harzic et al. [262] explored the use of nanosecond and femtosecond pulsed lasers for the microdrilling of aluminium samples, with the aim of quantifying the HAZ produced as a result of the interaction. Their research found that the nanosecond pulses produced a HAZ dependent on the laser fluence, while the femtosecond pulses produced a HAZ significantly smaller and much less visible based on their observation limit, with a width smaller than 2  $\mu\text{m}$ . Chang et al. [263] used nanosecond pulsed laser for high-precision micromachining at very high repetition rates (*kHz*). They successfully machined metals and ceramics with  $\mu\text{m}$  accuracy, producing high aspect ratio structures with negligible HAZ after optimising the laser processing parameters (fluence and intensity). Similarly, they reported the melt zone formation and material ejection from the surface of the sample due to irradiation at high intensities, leading to the formation of a large HAZ. Hermann et al. [264] used femtosecond pulsed lasers to study the ablation dynamics on bulk copper and gold surfaces, with particular

attention laid on the ablation plume properties. They found that the heat affected zone produced was dependent on the thermal diffusivity of the metals, which was larger for gold, and nanoparticles were vaporised from the surface during short-pulse laser ablation.

From this survey, the key criteria based on the use of lasers for ablation are as follows:

- (i) Continuous wave lasers are used for machining relatively large features ( $mm^2$ ) as compared to pulsed lasers, and also produce a relatively larger heat affected zone;
- (ii) Nanosecond pulsed lasers are used for micromachining precise fine features ( $\mu m^2$ ) through material ablation, and produce a heat affected zone dependent on the laser fluence. Below the ablation threshold, the laser energy is absorbed in the material;
- (iii) Femtosecond and picosecond (ultrashort) pulsed lasers are similarly used for micromachining of precise and high aspect ratio features ( $\mu m^2$ ) through ablation, although the heat affected zone produced is very minimal.

Based on these observations, the following experiment is devised to investigate the formation of the heat affected zone by using a nanosecond pulsed laser at a range of fluence regimes on a variety of substrates. The samples under investigation are inkjet-printed copper nanoparticles on various thermo-sensitive substrates. The aim of the experiment is to find the optimum laser fluence parameters to produce the least HAZ, and the effects on the substrate as well as the surrounding nanoparticle layer.

### 5.3.1 Materials and methods

This materials and methods section resembles the earlier one "Experimental II – Adhesion Investigation" on p. 119 due to the similarity in the substrates used throughout the experiment to ensure a continuity in the investigation. The cross-cut experiment required much larger samples of a few  $mm^2$  printed out of copper nanoparticles, while this experiment investigates the heat affected zone at a much smaller scale of a few  $\mu m^2$  in order to clearly see the relevant changes at that scale. The printing procedure is the same, while the laser sintering procedure onwards is varied.

#### Substrates

Three different substrates were tested, including DuPont™ Kapton® HN polyimide (PI) sheets of 125  $\mu m$  film thickness and polyethylene terephthalate (PET) sheets measuring 350  $\mu m$  in thickness. Additionally, a 250 *gsm* paper measuring 400  $\mu m$  thick and manufactured

by Hewlett-Packard was also tested. All of the samples, except for paper, were prepared for inkjet printing by a thorough rinse with deionised water followed by another rinse with acetone before drying under a clean, pressurised flow of air. The details of the substrates are described in Section 3.1 on p. 52.

### **Inkjet printing**

The choice of ink, waveform and deposition process resembles the same as per the previous experimental section methodology on p. 119, hence this was not repeated here. As a summary, a copper NPs ink was printed to form square samples measuring  $15 \times 15 \text{ mm}^2$  with two layers on the substrates at ambient conditions. The substrate temperature was maintained at  $40^\circ\text{C}$  to accelerate the evaporation of the solvent upon deposition, thereby creating a pinned geometry to prevent the overspreading of the ink.

### **Fluence variation**

The samples were left to dry on the heated bed prior to sintering. A custom-built nanosecond pulsed laser system as described in the previous Experimental Section I - Pulsed Laser Sintering Investigation on p. 102, was used. The peak power output of the laser was maintained at  $55 \text{ W}$ , while the pulsing parameters were varied based on the number of pulses emitted from the laser diode to vary the laser energy delivered per unit area, i.e. the fluence. The number of laser shots were varied from 1 shot to 100,000 shots, which correspond to a fluence variation from  $40.18 - 4,020,000 \text{ mJ/cm}^2$  on all the substrates, and the effects on the relevant substrate was recorded. Additionally, closer examination revealed the difference between the partially evaporated solvent, partially sintered nanoparticles, sintered nanoparticles, and vaporised nanoparticles.

## **5.3.2 Characterisation**

### **Analysis of the heat affected zone**

The samples were recorded using SEM imaging at each location where the laser was pulsed on the copper nanoparticle surface, followed by digital image processing to highlight and compute regions of interest where the laser was pulsed, namely regions of partial or complete sintering along with the corresponding heat affected zone, if any. The complete details of the procedure can be found in Section 3.4.5 on p. 71.

### 5.3.3 Results and discussion

#### Heat affected zone as a variation of laser fluence

The results from the analysis of the heat affected zone show that as the laser fluence is increased beyond the optimum threshold, sintering of the irradiated nanoparticles still occur at the cost of a large HAZ formation, as shown in Figure 5.21 below.

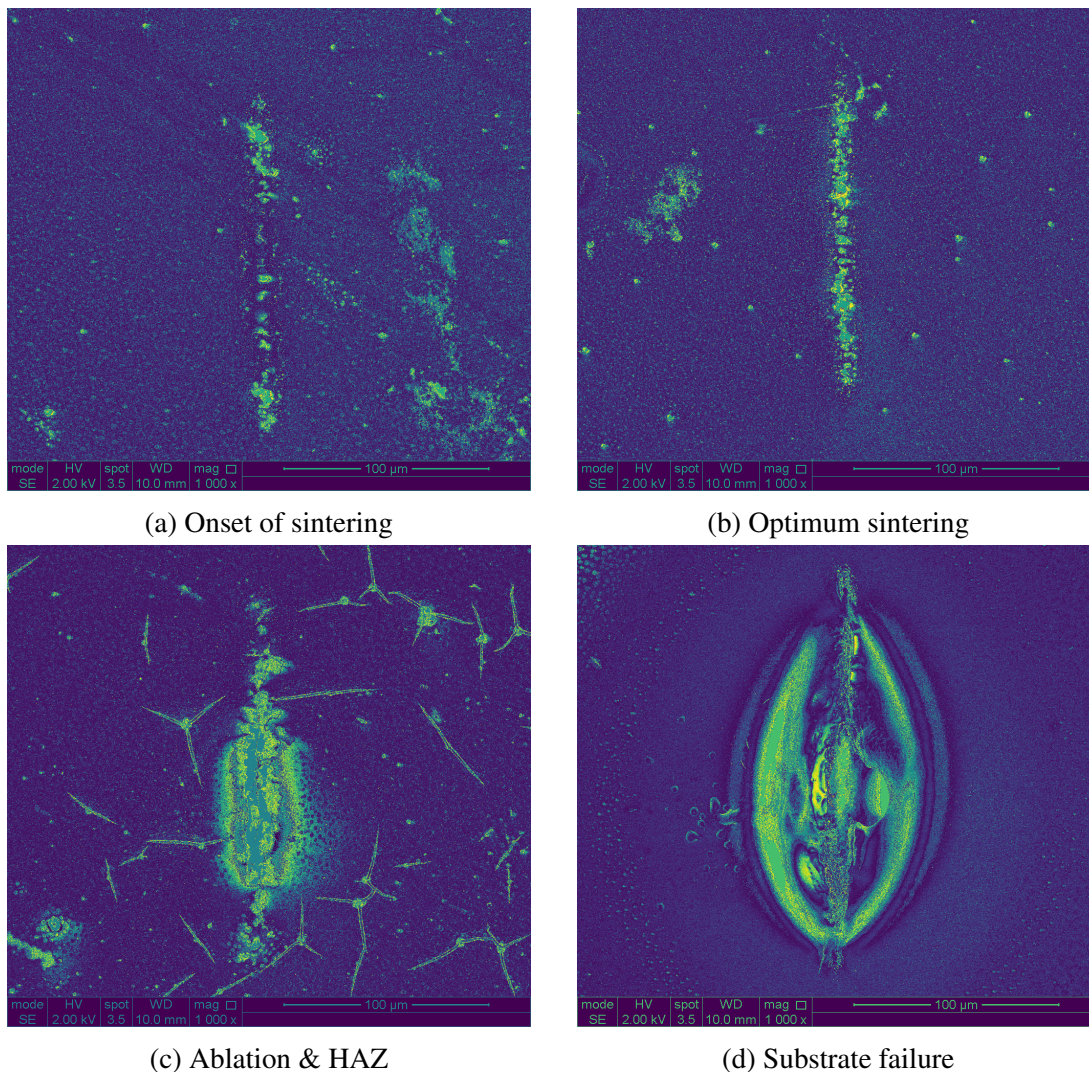


Fig. 5.21 Figure (a) represents the onset of sintering of copper nanoparticles on the PET substrate, (b) represents the completely sintered nanoparticle with the minimal HAZ formation of only 15 % the total irradiated area, (c) represents the completely sintered nanoparticles with a large HAZ (60 %) and crack formation at high fluence values ( $J/cm^2$ ), and (d) represents damage to the substrate at extremely high values of fluence ( $kJ/cm^2$ ) with the laser beam penetrating through the **PET substrate**, showing ablation, failure and vaporised material deposits on the surrounding plume.

At lower threshold values below the optimum, partial sintering occurs and the HAZ formation is negligible, as shown in the SEM analysis from Figure 5.21(a). Additionally, at the optimum fluence value, the sintered area increases drastically until due to the optimum absorption of the irradiation through the coating, although the HAZ formation is noticeable and ranges from 15 % up to 35 % of the total irradiated area, as shown in Figure 5.21(b). The laser fluence variation reflected clearly on the substrate. As PET has a low glass transition temperature of  $T_g = 80$  °C, the effects of increasing the fluence on the substrate were very obvious. At the lower fluence regime, the substrate was able to withstand the sudden temperature rise due to the irradiation from the laser beam, and the energy transfer from the radiation to the nanoparticle appeared to be successful with partial or complete absorption into the nanoparticle layer. However, at laser fluences above the optimum sintering threshold in the  $J/cm^2$  range, the typical crack formation phenomenon was observed due to the duration of the irradiation on pattern, which can be seen in Figure 5.21(c), in addition to a large HAZ formation of around 80 % of the irradiated area. As the laser fluence is further increased in the  $kJ/cm^2$  range, the penetration depth of the irradiation increases beyond the thickness of the printed pattern and the substrate combined, and results in the penetration through the PET film due to the excessive increase in the thermal energy at this location, as shown in Figure 5.21(d). The HAZ formation at this stage is excessive and undesirable at more than 100 % of the irradiated area, resulting in the thermal damage and obliteration of the substrate as the PET film is unable to dissipate the excessive energy.

In comparing the Kapton PI polymer film, at a low laser fluence below the optimum sintering threshold, only partial sintering of the nanoparticles occurs, and the formation of a HAZ is negligible as shown in Figure 5.22(a). As the laser fluence increases up to the optimum sintering threshold, the HAZ formation increases to between 10 % to 60 % (Figure 5.22(b)), although the energy in the laser beam is absorbed in the nanoparticle layer, resulting in a more complete sintering of the copper layer, thereby indicating the optimal energy required for sintering.

Similarly, the fluence variation beyond the optimum sintering threshold affected the structural integrity of the substrate, although the change was less apparent as compared to the PET film. This can be explained by the higher glass transition temperature of the Kapton PI film at  $T_g = 400$  °C in comparison to the PET which has a  $T_g = 80$  °C. Further increasing the laser fluence beyond the threshold in the  $J/cm^2$  range results in a complete sintering of the nanoparticles while the HAZ formation is still noticeable at a range of up to 60 %, although not as pronounced in comparison to the PET film, as shown in Figure 5.22(c). However, at this fluence regime beyond the optimum, the formation of cracks is observed and is detrimental to the performance of the printed layer. At even higher laser

fluence values in the  $\text{kJ}/\text{cm}^2$  range, the HAZ formation is very excessive above 100 % of the total irradiated area, depicted in Figure 5.22(d). In this case, the excessive fluence results in a large penetration through the combined thickness of the polymer film and the nanoparticle layer, with a large noticeable damage to the substrate due to the excessive thermal energy at that particular location.

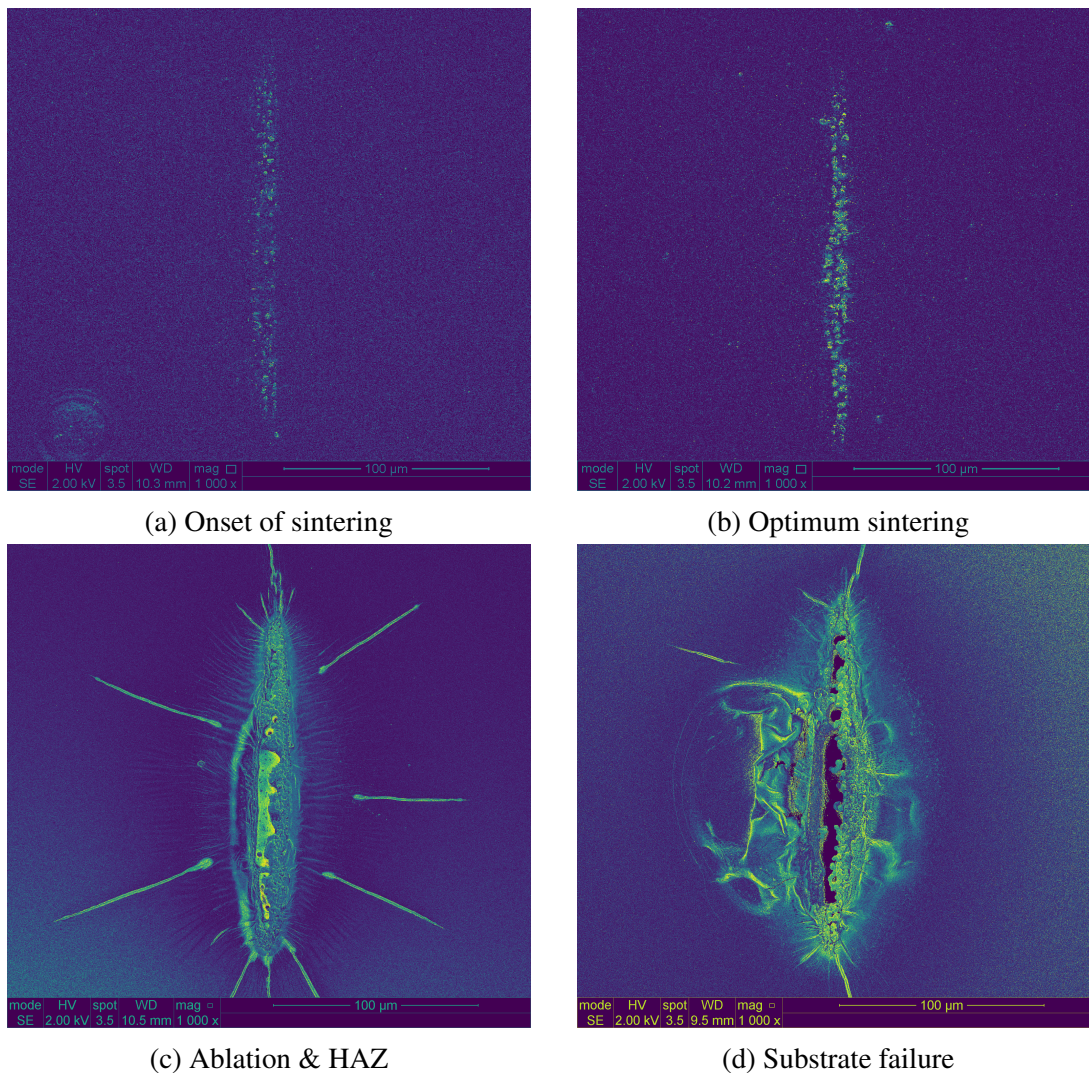


Fig. 5.22 Figure (a) represents the partially sintered copper nanoparticles on the Kapton PI substrate, (b) represents the completely sintered nanoparticle with the minimal HAZ formation of only 5 % the total irradiated area, (c) represents the completely sintered nanoparticles with a large HAZ (50 %) and crack formation at high fluence values ( $\text{J}/\text{cm}^2$ ), and (d) represents damage to the substrate at extremely high values of fluence ( $\text{kJ}/\text{cm}^2$ ) with the laser beam penetrating through the **Kapton PI substrate**, showing ablation and failure.

Finally, following the analysis of the paper substrate, the results differ from those of the PET and Kapton PI polymer films due to the inherent material composition of the paper substrate, although it is clear that the HAZ formation is dependent on the fluence, which determines the level of sintering of the nanoparticles layer. At low fluence regimes below the optimum threshold, the sintering of the nanoparticles occurs partially without the formation of a HAZ, as shown in Figure 5.23(a). As the fluence increases up to the optimum threshold, the nanoparticles are sintered completely without a noticeable formation of a HAZ, nor any crack formation (Figure 5.23(b)). As the fluence regime increase in the  $J/cm^2$  range, the sintered area increases drastically with a minimal HAZ formation of up to 20 %, although no cracks are observed.

However, as the fluence further increases, the irradiated nanoparticles are vaporised from the target area as shown in Figure 5.23(c) due to the intense fluence at this region. At an even higher fluence regime in the  $kJ/cm^2$  range, there are no nanoparticles left on the paper substrate at the target area, although the surrounding layer is significantly affected with a large HAZ formation greater than 100 % of the total irradiated area, represented by a larger plume formation as shown in Figure 5.23(d). Moreover, the larger plume formation on the paper substrate does not appear to have damaged the paper substrate as much as the other two polymer films which have perforations. The relatively larger plume on the paper substrate can be linked to the heat conduction to the surrounding nanoparticles due to the insulative nature of paper, hence the excess thermal energy in the irradiation being dissipated through the conductive nanoparticle layer.

The larger HAZ formation on the polymer films could be due to the thermal energy transfer through the substrate and the surrounding printed layer, while paper is not as thermally conductive in comparison. Additionally, the larger range of HAZ formation area for the Kapton PI film can be attributed to the higher thermal resistance (i.e. higher  $T_g$ ) in comparison with the PET film. The relatively high  $T_g$  of the Kapton PI substrate allows for more thermal energy dissipation throughout the thickness of the substrate, whilst conducting to the surrounding nanoparticle layer which results in a larger HAZ formation, as supported by Chung et al. [265].

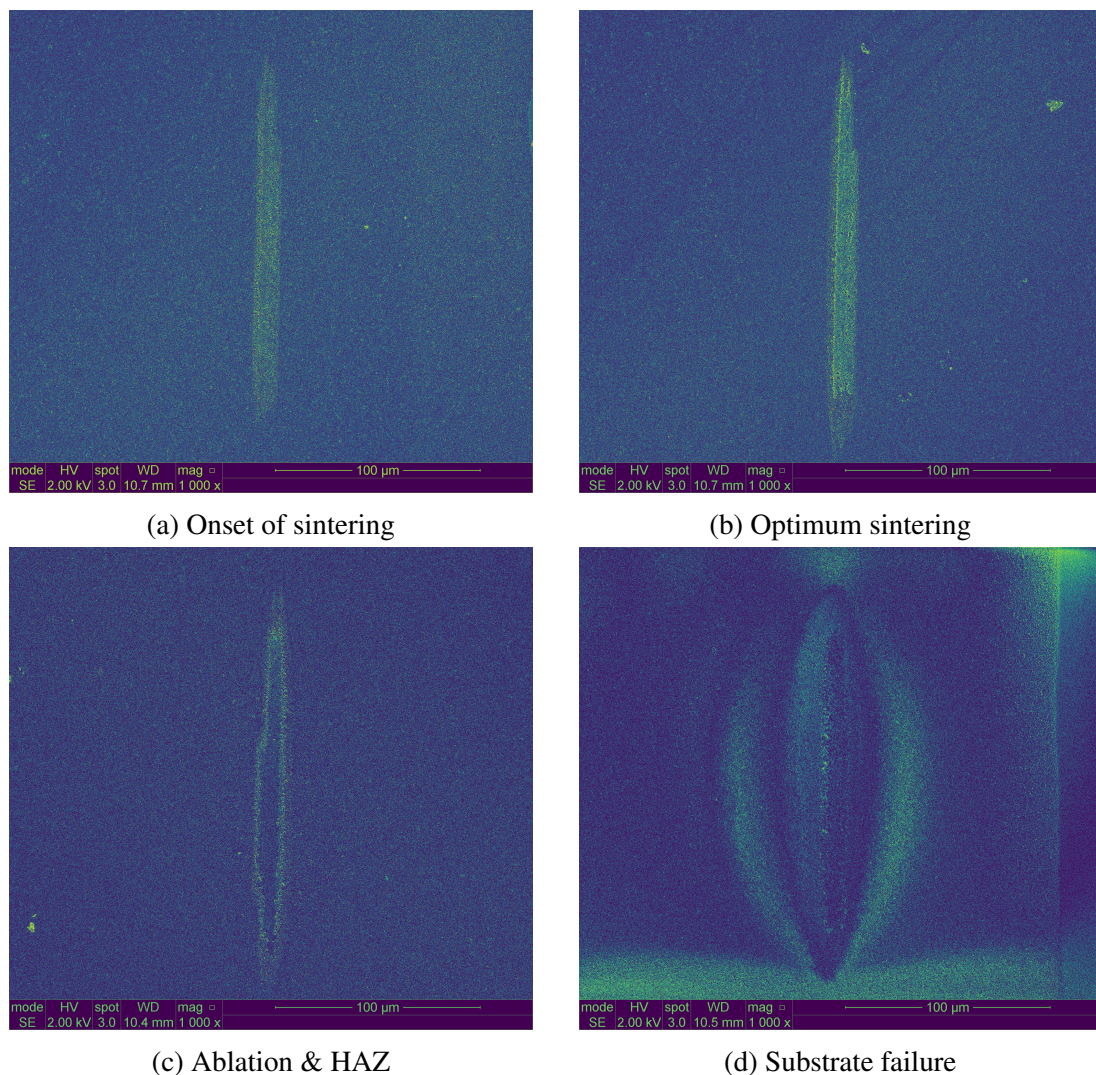


Fig. 5.23 Figure (a) represents the partially sintered copper nanoparticles on the paper substrate, (b) represents the completely sintered nanoparticle with the minimal HAZ formation of less than 5 % the total irradiated area, (c) represents some nanoparticle ablation with some sintered nanoparticles remaining around the plume at high fluence values ( $J/cm^2$ ), and (d) represents some damage to the **paper substrate** at extremely high values of fluence ( $kJ/cm^2$ ) with the formation of a large HAZ much greater than 100 % of the total area.

### Penetration depth of laser beam and structural integrity of the substrates

In addition to investigating the heat affected zone and the sintered area as the laser fluence on each substrate was varied, some understanding of the penetration depth of the laser can be made based on the results of this experiment. The previous research by Ko et al. [266] described the minimal formation of a heat affected zone due to the use of an argon pulsed laser for the ablation of gold nanoparticles. In their research, they mentioned the thermal

penetration of the laser beam irradiation can be minimised by using a pulsed laser during the ablation process, which is partly true to a certain extent. As the laser fluence is increased beyond the optimum sintering threshold, ablation occurs while the excess thermal energy is dissipated throughout the substrate. This thermal energy dissipation relies on the thermal mass of the substrate to prevent excessive thermal stress and a decrease in the structural integrity of the substrate.

In relation to this experiment, the PET film measuring  $350\ \mu\text{m}$  in thickness was able to dissipate the excess thermal energy at fluence variation above several  $\text{mJ}/\text{cm}^2$  until  $2,009\ \text{mJ}/\text{cm}^2$ , at which point the energy at that particular location was too excessive and caused thermal damage to the substrate, as shown in Figure 5.24. At that particular laser fluence, the thermal stress caused (due to the irradiation) was sufficient to cause the failure of the substrate, indicating the penetration depth of the laser beam to be greater than  $350\ \mu\text{m}$ .

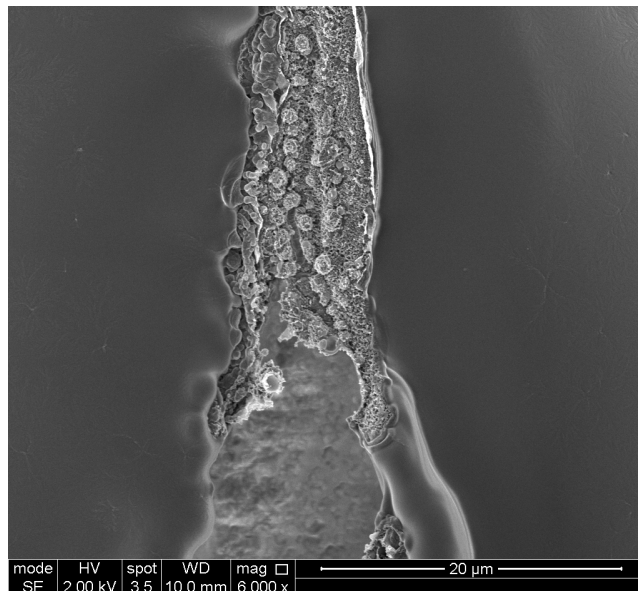


Fig. 5.24 Results from the SEM analysis at laser fluence variation above the optimum sintering threshold, highlighting thermal and structural damage to the PET substrate.

The Kapton PI film measured  $125\ \mu\text{m}$  in thickness and, similarly, was able to withstand excessive laser fluence above the sintering threshold until  $4,018\ \text{mJ}/\text{cm}^2$ , at which point similar observations were made – the excess thermal energy in the laser beam penetrated the substrate, causing thermal and structural damage, described in Figure 5.25, thereby concluding the penetration depth of the laser at this fluence regime can reach  $125\ \mu\text{m}$  on this substrate. Additionally, the surrounding area which was irradiated showed a significant HAZ formation (Appendix B.2).

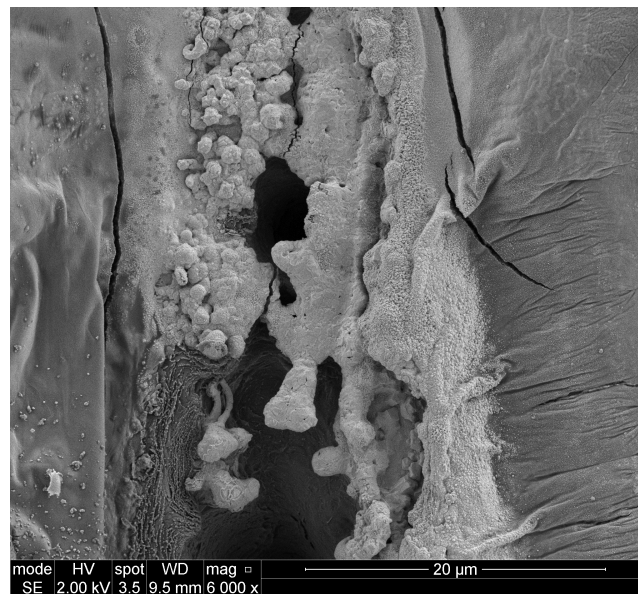


Fig. 5.25 Results from the SEM analysis at laser fluence variation above the optimum sintering threshold, highlighting thermal and structural damage in the form of cracks to the Kapton PI substrate as well as the vaporised deposits around the plume.

For the paper substrate which measured  $400\ \mu\text{m}$  thick, the structural damage through the substrate due to the excessive laser fluence variation was not observed, even at the highest laser fluence. Even though the HAZ formation (Appendix B.2) was very apparent, similar to the HAZ formation on the polymer films, the laser beam did not penetrate through the paper substrate. Based on the analysis of the irradiated area on the paper substrate, it appears that the excess thermal energy was used for the ablation of the nanoparticles from the irradiated area, as well as the vaporisation and formation of a recast layer, as shown in Figure 5.26.

The variation in the penetration depth of the laser highlights the dependence on the thermal mass and thermal energy dissipation throughout the substrate [267]. As heat transfer through the polymer films is facilitated by the movement of polymer ions [268], they are more thermally conductive as compared to paper which is insulative, thus preventing any excessive heat accumulation.

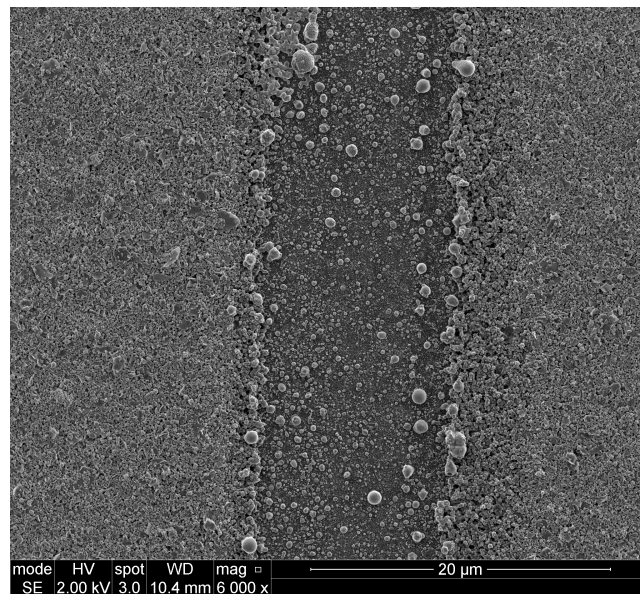


Fig. 5.26 Results from the SEM analysis at laser fluence variation above the optimum sintering threshold, highlighting the ablation of the nanoparticles on the paper substrate at the irradiated area as well as the formation of a recast layer and vaporised deposits surrounding the plume, without any thermal or structural damage to the paper substrate.

#### **Method of laser sintering: Distinct pulses as opposed to a continuous scanning pattern**

In this set of experiments, the pulsed laser sintering was done at a distinct location in order to understand the formation of the heat affected zone on the printed copper nanoparticle layer. As distinct pulses were being used, the HAZ formation was more apparent due to the energy being confined at that particular irradiation location, thereby creating a steep temperature gradient between the irradiated area and the surrounding area which was not being treated with the laser. This method of sintering led to the more obvious formation of the HAZ as the surrounding nanoparticle layer was at a lower temperature than the irradiation zone, which eventually caused the formation of cracks when the laser fluence was exceeded beyond the optimum sintering threshold as described previously. However, this is particularly useful to understand the crack, ablation and heat affected zone formation phenomenon at a  $\mu\text{m}$  scale, and prevent these during the laser scanning mode where the laser is continuously pulsed over a larger area. Due to this scanning approach of the pattern, the incident laser beam is continuously dissipated to a much larger area and the temperature gradient between the irradiated area and the surrounding nanoparticle layer is minimised due to heat conduction through the substrate as well as through the unsintered layer.

### Pulsed laser ablation and long-term stability

Conventional sintering enables the functional material such as metallic nanoparticles in a printed pattern to coalesce gradually without being subjected to steep, abrupt temperature gradients, which eventually improves the ductility of the material [269]. Additionally, the process of removing the printed component from the oven and allowing it to naturally return to atmospheric temperature allows the grain boundary in the microstructure to gradually relax, which ultimately contributes to the ductility of the metallic material as well as its overall strength through a process called normalising.

Alternative sintering processes such as laser sintering have been used to attain similar objectives of sintering for printed electronics, albeit through different ways. Using metallic nanoparticles as an example, the NPs absorb the irradiation which causes the sintering of the material to improve its overall conductivity. However, the area over which the energy is delivered is much smaller as compared to an oven (often in  $\mu\text{m}^2$ ), which may cause severe adverse effects. For example, the sudden burst of high energy from the laser beam creates a steep thermal gradient at that particular location, with a steep temperature rise at the incident surface and a much cooler temperature at the surrounding area. The large temperature gradient, if uncontrolled, creates a large heat affected zone within the material.

The heating of a metallic material beyond its melting point causes a change in the internal microstructure, which can be due to a grain coarsening mechanism, or the relaxation of internal stresses. This change in microstructure is exploited in the case of sintering where a certain control over the grain coarsening mechanism leads to the formation of conductive necks in metallic nanoparticles. However, if performed incorrectly due to unoptimized sintering parameters, this may result in the formation of cracks due to high thermal stress concentrations. The crack formation is more common with laser sintering due to the steep thermal gradients produced at selective locations within the material in a very short period.

In metals which are subjected to a form of heat treatment, the heat affected zone (HAZ) is of particular importance as it is often a source of failure due to the presence of unrelieved stress concentrations. The size of the HAZ is determined by the thermal diffusivity of the material, which is a function of the thermal conductivity, density, and specific heat capacity as well as amount of thermal energy being applied. A material with a high thermal diffusivity will absorb and dissipate heat much quicker than one with a lower thermal diffusivity, and hence produce a smaller HAZ. The formation of a HAZ in metals which are treated with lasers can often be seen in the form of a *plume*. The *plume* is produced as a result of laser material processing which forms a region of mixed vapour and ambient gas above the material surface, as well as material deposits surrounding the irradiated zone [270, 271]. Usually, the formation of a *plume* on a metallic surface after laser treatment indicates a region of failure

and stress concentration, or poor coating of a material. For micromachining operations using laser ablation, this region must be minimised as it indicates a lower machining quality and inferior precision [230].

Laser ablation can be categorised in two processes: *pyrolytic* and *photolytic* ablation. In pyrolytic ablation, the removal of material is due to heating through radiation. If the absorption spectrum of the material coincides with the incident radiation, and the incident laser beam is at a sufficiently extreme power, the electrons in the microstructure of the material will gain sufficient energy to cause restructuring and release from the material surface, leading to a molten ejection, vapourisation, and the formation of a recast layer at the surface. This is more commonly observed in metals. In photolytic ablation, the removal of material is as a result of breakage of chemical bonds, often referred to as “cold ablation”, and generally applies to polymers. In this method of ablation, the energy level of the incident photons in the laser beam must be higher than the molecular bond energy of the polymer materials, resulting in the breaking of polymer chains into monomers and ultimately material removal in the form of vapours or small particles.

The micromachining of materials using lasers can be done using either a continuous wave (*cw*) or a pulsed laser, each with distinct properties. As mentioned earlier in Section 2.2.3, the output of a continuous wave laser is always “open”, while that of a pulsed laser is determined by the duration of the pulse. The inherent difference in their mode of operation gives rise to different outcomes when used for micromachining operations such as laser drilling. The constant output of a continuous wave laser will deliver a quicker and more powerful wave of energy which results in the clean material removal, which is often used for industrial applications such as laser cutting, laser welding and laser drilling of metal pipes and tubing. Pulsed laser, on the other hand, can be fine-tuned within very tight margins, which lead to even more precision and accuracy in the machining operation, eventually benefitting the manufacturing of medical grade devices such as stents, heart valves and fine tubing due to their sub-millimetre geometries. Additionally, the heat affected zone of each type of laser output is different due to their mode of energy delivery. Due to the continuous nature of the energy output from a *cw* laser, the surrounding material is heated very quickly and can give rise to a large HAZ and poor geometries if the laser processing parameters are not optimised, as shown in Figure 5.27(a). On the other hand, the repeated short bursts of energy from a pulsed laser minimises the HAZ as it allows for the energy to be dissipated within the material, thereby preventing overheating and the formation of cracks and debris, as shown in Figure 5.27(b).

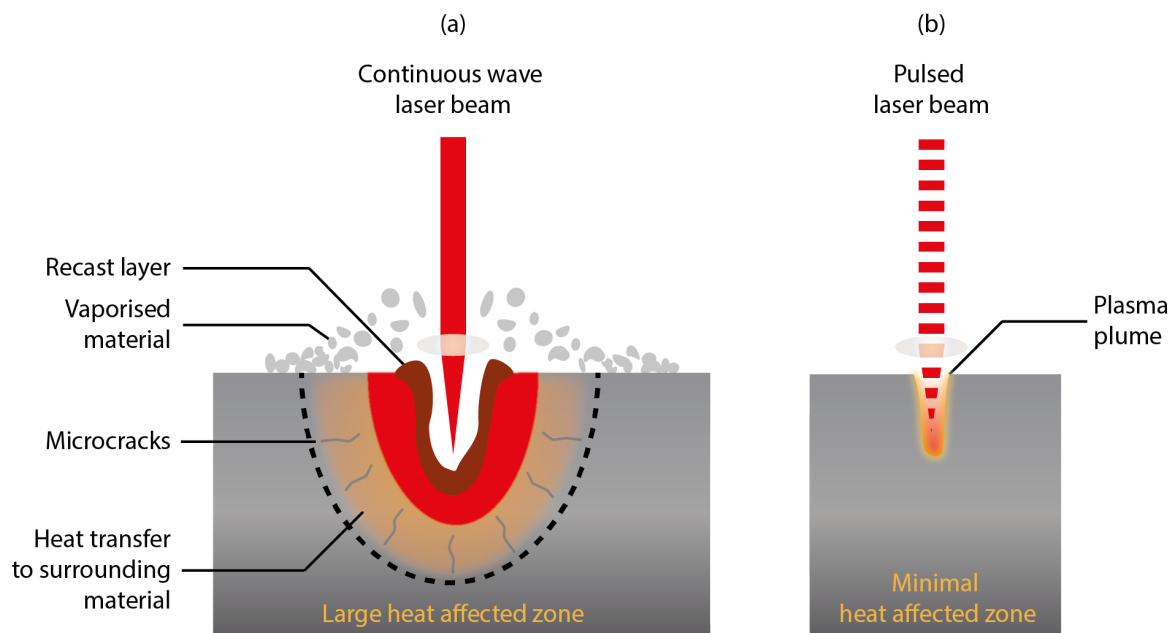


Fig. 5.27 Illustration of the heat affected zone (HAZ) created as a result of laser machining processes, showing (a) the use of a continuous wave, and (b) a pulsed laser.

### 5.3.4 Conclusions

In this set of experiments, the variation of the laser fluence on inkjet-printed copper nanoparticles was investigated in order to understand the formation of the heat affected zone (HAZ) due to the pulsed laser sintering. Three different substrates were investigated: a PET polymer film with a low glass transition temperature, a Kapton PI polymer film with a relatively higher glass transition temperature, and finally a paper substrate which has a more insulative property as compared to the polymer films, but nonetheless remains a thermo-sensitive substrate. As the laser fluence was varied within a wide regime, starting from a few  $mJ/cm^2$  to several  $kJ/cm^2$ , the effects on the printed nanoparticle layer varied from partial sintering, complete sintering, ablation, and substrate failure. The regions of partial and complete sintering on all the substrates showed minimal HAZ formation, and the HAZ formation area increased drastically as the laser fluence was increased significantly beyond the sintering threshold into ablation.

Distinct laser pulses lasting a few nanoseconds were used for the sintering of the copper nanoparticle layer, and despite being known for the ablation effect on metals from previous literature, the consecutive pulses successfully caused the nanoparticles to coalesce at the irradiated location based on SEM analysis and evaluation. As the laser fluence was increased beyond the optimal sintering threshold ( $J/cm^2$ ), the formation of cracks was observed on both polymer films. Furthermore, in the case of even higher fluence regimes ( $kJ/cm^2$ ), the

regions of agglomeration extended to the surrounding plume due to the heat transfer to the surrounding layer from a combination of convective and conductive heat transfer through the localised atmosphere and the substrate, respectively. At such extreme fluence regimes, the ablation phenomenon was clearly visible and manifested in the form of thermal stress on the polymer films which resulted in the structural damage and perforation, as well as the formation of a large HAZ. In the case of the paper substrate irradiated at similar extreme fluence values, the excessive thermal energy in the laser beam was used to form a recast layer at the edges of the irradiated area, in addition to the vaporised deposits and the large HAZ formation.

The thermal mass of the substrates affects the thermal diffusivity property, which is responsible for the heat transfer throughout the entire pattern. As the intensity of the irradiation is increased at a particular location (i.e. the laser fluence), the substrate distributes the thermal energy to prevent excessive heat accumulation. However, due to the excessive incident irradiation, the rate of thermal energy diffusion in the polymer films was slower than the incident thermal energy converted from the radiation in the laser beam, resulting in the thermal failure of the substrate which could be seen in the form of a perforation. This effect was not observed on paper due to its insulative nature, and a closer look at the irradiated region did not reveal any major defects in the form of perforations due to the excessive heat accumulation.

While the use of distinct laser pulses can benefit the selective micro-sintering of nanoparticles, the laser fluence must be optimised to reduce the HAZ formation, particularly when the sintered region is formed of composite materials (e.g. a conductor and an insulator). In contrast, the “snake-scanning” method is beneficial for sintering a larger area without compromising the structural integrity of the printed sample by minimising the formation of a large heat affected zone through thermal energy diffusion over a wider surface area. Finally, the results from this experiment provide a thorough understanding and a baseline for the optimisation of the laser fluence at distinct locations in order to prevent the crack and HAZ formation, and also to avoid ablation and prevent damage to the substrate. This understanding can be extended to perform an even sintering of a larger surface area in the scanning mode, and ensuring the laser beam penetrates through the entire substrate to ensure a complete sintering, particularly for multi-layer printed electronics. Consequently, the electrical performance of the printed pattern can be optimised for optimum conductivity as well as the mechanical properties which can also be improved to ensure the optimum adhesive performance of the nanoparticles to the substrate.



# Chapter 6

## Applications

### Summary

This chapter focuses on potential application areas of the research work conducted in this thesis, particularly for printed sensors, and the central application that forms the focus of this chapter involves carbon fibre laminate samples containing inkjet-printed sensors for structural health monitoring. The sensing behaviour of the copper coils in response to the deformation of specially designed carbon fibre laminate samples is demonstrated, underlining the suitability and practicality of the research performed in the earlier chapters.

The experimental section then elaborates on the comparison of the inkjet-printed copper coils with a wound coil and an off-the-shelf 3D sensor, and the results from the tests demonstrate superior performance of the inkjet-printed coils, particularly a 10-turn monofilar coil. Additionally, the feasibility of the two-step manufacturing process (inkjet printing of copper nanoparticle-based ink, followed by the pulsed laser sintering) is demonstrated by using paper which behaves as a flexible, low-cost, and low thermal resistance substrate, thereby highlighting the capabilities of the pulsed laser sintering process. Finally, the chapter concludes with expanding on the advantages of a reduction in dimensionality due to the thin film nature of the inkjet-printed sensors.

This chapter has been published: (1) Gullapali, A; Beedasy, V; Vincent, JDS; Leong, Z; Smith, P.J; Morley N. Flat inkjet-printed copper induction coils for magnetostrictive structural health monitoring: A comparison with bulk air coils and an anisotropic magnetoresistive (AMR) sensor, **2021**, Sensor. Adv. Eng. Mater. 2100313.

## 6.1 Introduction

Inkjet printing has proven to be a successful method of depositing functional materials on a wide range of substrates for different applications, particularly for printed electronics. The low- to mid-end printed electronics area can benefit from an inkjet perspective for its reduction in production steps and wastage, as mentioned earlier in Chapter 1. By combining functional inks with inkjet printing, some simple electronic circuits can be made in the form of sensors such as RFID tags, strain gauges and coils. These can be manufactured in the form of thin films which can in turn be adhered to multiple surfaces for sensing applications. Polyimide films of a high glass transition temperature can be used as a means to withstand the relatively high sintering temperatures of around 200 °C. Alternatively, for the mid-end applications in industries aiming to use polymer substrates of lower glass transition temperatures such as PET or PEN ( $T_g$  of 70 °C and 120 °C, respectively), combining laser sintering within the manufacturing of printed electronics in the form of thin films can avoid permanent thermal degradation to the substrates. Additionally, a wider range of substrates can be used other than polymer films – for example, a resin-coated paper was used as a demonstration in Chapter 5, and the performance of the printed pattern was compared to other printed patterns on polymer films.

To further expand on this possibility and serve as a proof-of-principle, this chapter details the printing of a copper coil on paper, which was then used as a sensor to detect strain on a carbon fibre composite laminate. This was made possible through the use of the pulsed laser sintering module which:

- (i) prevented damage to the underlying substrate, and;
- (ii) allowed for the **selective** sintering of the final layer of copper nanoink to form interconnects from the centre of the coil to a dedicated area for soldering.

The sensor was used to detect the strain of carbon fibre laminates which were actuated through *magnetostriction*, which is the mechanical deformation of a magnetised structure through the application of a magnetic field. Finally, the inkjet-printed sensor was compared to others of a similar type and purpose and the results described in the later section. The next section elaborates on magnetostriction and the uses in research and industry. It then follows by providing a background of the types of sensors which are used for magnetostrictive applications, leading to the specifications for the inkjet-printed sensor.

### 6.1.1 Magnetostriction

Magnetostriction is a phenomenon which occurs when a ferromagnetic body deforms mechanically as a function of the direction of an applied magnetic field  $H$ , until it reaches a plateau value of  $\lambda$ . From an atomic perspective, magnetostriction is caused by the interaction of the atomic magnetic moments in a crystal lattice and the elastic bond length. To better illustrate this, ferromagnetic materials are internally divided into “domains”, as shown in Figure 6.1(a) – (c) below. In a single “domain”, molecular dipoles are aligned long the same orientation in a way which minimises the interaction with other domains and hence the internal energy of the ferromagnetic material as well. This is also called the relaxation state of the material. When the material is subjected to an applied magnetic field, the field stimulates the realignment of the molecular dipoles along the magnetic field in such a way that it causes an expansion or contraction of the overall material, resulting in a strain. The material is then in a magnetostrictive state, as shown in Figure 6.1(d) below.

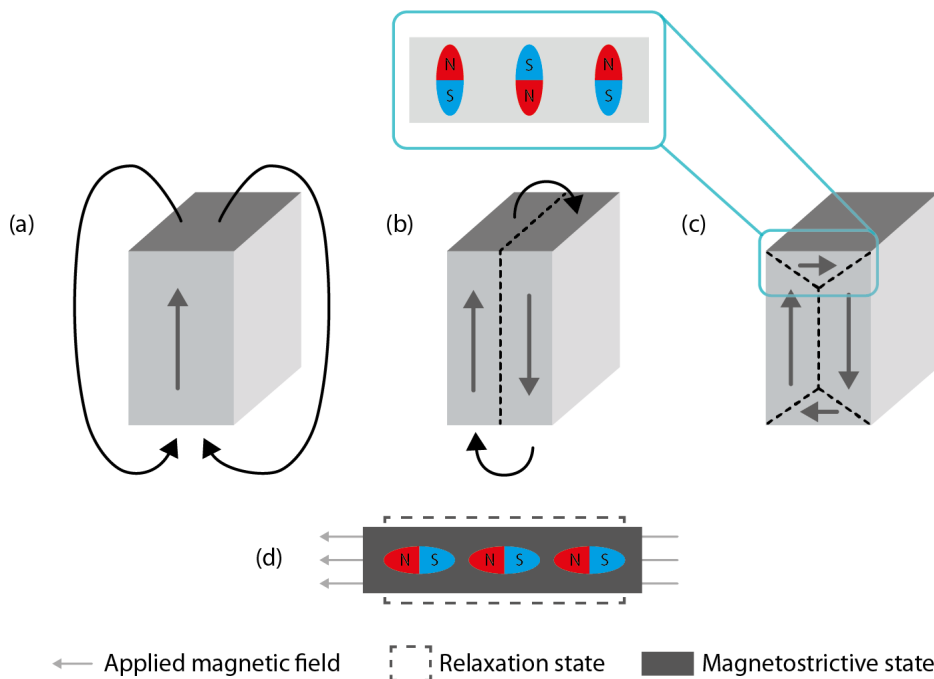


Fig. 6.1 Illustration of the “domains” in a ferromagnetic material with (a) a single domain, (b) two domains equally divided, and (c) four domains resulting in the least internal energy of these three models. (d) represents a ferromagnetic material which expands in the magnetostrictive state when a magnetic field is applied.

This maximum strain is limited by the saturation magnetisation, which varies depending on the type of material as well as the alignment of the applied magnetic field along the crystal axis. The maximum strain also corresponds to a  $90^\circ$  domain rotation over the total volume of

the material, after which no more strain can be observed due to the optimum alignment of the domains. Upon the removal of the applied magnetic field, and subsequently the removal of external stresses, the ferromagnetic material reverts to the inherent crystal anisotropic alignment which results in the least internal energy [272].

There are several uses for magnetostrictive materials due to their ability to convert electromagnetic energy into mechanical energy reversibly, and this is exploited in the form of sensors and actuators. Perhaps the most common application is a transformer which uses magnetostrictive materials obeying Faraday's law to generate an electromotive force in the transformer. This property is, in turn, used to transmit AC voltages across the primary and secondary circuits. The constant rotation of the molecular dipoles in the domains results in the magnetisation and demagnetisation of the core of the transformer, which alters its physical dimensions [273]. This alteration results in the humming sound of the transformer. Other applications prospects of magnetostrictive materials are in the form of sonar transducers, contactless torque sensors, encoders and mechanical vibrators such as ultrasonicators [274]. These have some unique advantages as they can be made into a contactless technology once the ferromagnetic material is encased in an insulative housing, making it impervious to leakages and external contaminations. However, there are many cases where magnetostriction is undesirable, particularly due to the introduction of energy losses in the form of heat or noise related to the material hysteresis.

### 6.1.2 Sensors

Magnetostriction can be measured by using sensors which detect changes in magnetic fields. For example, the most common sensors used for decades are hall-effect sensors, commonly used in the automotive industry to sense position, distance and speed; and strain gauges used to detect the changes due to the applied magnetic field [275]. Nowadays, anisotropic magnetoresistance (AMR) sensors are being used instead due to their more precise sensing capabilities. AMR sensors differ from traditional hall-effect sensors due to their omnipolar sensing (measuring from either north or south pole), and have an increased sensitivity and range. Inherently, these sensors function by the magnetoresistive element, which essentially measures the change in resistance due to the application of a magnetic field. With the addition of amplifiers, comparators and outputs, these AMR sensors can be made extremely sensitive and reliable for long-term applications in integrated circuits. The research by Hott et al. [276] described the increased sensitivity of measured magnetic fields by using an AMR sensor, clearly highlighting the advantages to applications where size is a constraint.

The *magnetostrictive* aspect of quantifying magnetostrictive materials is further investigated in the next section which describes the comparison of inkjet-printed coils and 3D coils on carbon fibre composite laminates actuated by a magnetostrictive ribbon.

## 6.2 Experimental Section

### 2D inkjet-printed copper induction coils for magnetostrictive structural health monitoring: A comparison with 3D air coils and an AMR sensor

#### 6.2.1 Introduction

Carbon fibre reinforced composites (CFRC) consist of a polymer-like matrix that are reinforced by carbon fibres. These CFRCs have a wide range of applications in products that require a low weight but high strength and stiffness such as in bridges, aerospace applications, and wind turbine blades. With decreasing marginal fuel efficiency improvements in the aviation industry [277], these lightweight composite materials are highly sought for the reducing the weight of aerospace components. For example, the Airbus A380 and Boeing 777 introduced in 1995 and 2005 respectively, have structural masses containing about 20 % composites. Recent models such as the Boeing 787 and Airbus A350, introduced in 2011 and in 2015, have an even higher structural mass made of about 50 % composites.

In spite of their unique structural properties owing to their composite strengthening fabrication process, CFRCs are susceptible to failure in multiple different ways, often not apparent to the human eye. Consequently, significant investment is being made for non-destructive testing methods to monitor structural parts during maintenance procedures, real-time operation, or to validate parts before they are used in structural applications. The next generation of non-destructive testing is termed structural health monitoring where repeatable and reliable non-destructive testing is used to ensure continued strength of a composite structure [278, 279]. These technologies allow the remaining service life of the material to be predicted prior to catastrophic failure [280]. Some examples of major SHM techniques currently being studied in composites are fibre optic sensors, piezo-electric sensors, electrical strain gauges, and ultrasonic sensors [281].

Recently there have been numerous research contributions describing the making of “smart” CFRCs with the addition of magnetostrictive materials for applications in aerospace composites for structural health monitoring. Together with 3D sensors, the damage in a composite sample can be detected at multiple levels and monitored in the long run. However, these 3D sensors are bulky and can benefit from a reduction in dimensionality and mass,

without compromising their sensing capabilities in terms of accuracy and high fidelity. In this experiment, inkjet printing and pulsed laser sintering were used to manufacture 2D inductive copper coils (in the form of thin films), which were compared with 3D sensors in the form of hand-wound copper coils and an off-the-shelf AMR sensor. The coils were tested on a variety of fabricated composite samples to determine their sensing efficacies at each instance.

The samples were characterised by measuring their inductance response through induced strain. An increased sensitivity and accuracy of the 10-turn monofilar inkjet-printed sensor was described in respect to (i) a 70-turn hand-wound coils, (ii) a 3-axis off-the-shelf AMR sensor, and (iii) other inkjet-printed sensors with less than 10 turns. The increased performance of the 10-turn monofilar inkjet-printed sensor is attributed to an increased contact area to the composite surface and the minimum sensitivity level achieved by the fine features of the sensor (i.e. number of turns and surface area) for strain detection.

## 6.2.2 Materials and methods

### Composite sample fabrication

To manufacture the first composite laminate, twill weave carbon fibre prepreg sheet VTC-401 supplied by SHD Composites Ltd. were chosen. A 4-ply laminate measuring  $150 \times 100 \times 4.5 \text{ mm}$  was fabricated using the vacuum bagging technique to eliminate the presence of air pockets during the curing process. A  $\text{Fe}_{78}\text{Si}_7\text{B}_{15}$  magnetostrictive ribbon was placed on the top surface of the laminate, followed by a breather layer of fluoropolymer (which is whimsically called “fluffy bunny”) on top of the prepreg stack, and finally vacuum sealed at  $-29 \text{ mmHg}$ . The laminate was then placed in an autoclave set at a pressure of  $6 \text{ bar}$  and the curing cycle was initiated as per the graph in Figure 6.2 below. The curing cycle began with an initial ramp until  $60 \text{ }^\circ\text{C}$  at a rate of  $3 \text{ }^\circ\text{C}/\text{min}$ , followed by a dwell time at this temperature for 60 min. The temperature was then increased to  $120 \text{ }^\circ\text{C}$  at a rate of  $3 \text{ }^\circ\text{C}/\text{min}$ , and maintained for another 60 min. The curing cycle was finally completed and allowed to cool down to room temperature.

The second set of composite laminates was made using a similar method, although instead of placing a magnetostrictive ribbon, a  $300 \text{ }\mu\text{m}$  actuator layer consisting of epoxy impregnated with magnetic particles was placed on top of the prepreg laminate. The composition of the epoxy to hardener ratio was carefully chosen to avoid either actuator failure before composite failure, or the sensitivity of the actuator to an induced strain would be too low. To prevent these two scenarios, a plasticiser was added to improve the control over the mechanical properties of the fabricated actuator. Plasticisers can be categorised into four types: polyimides, carboxyl-terminated polymers, polyglycol diepoxides, and polysulfides

[282]. In spite of introducing a higher level of flexibility in the epoxy, plasticisers have an adverse effect on the strength, chemical and solvent resistance of a sample. Hence, a compromise was made between the plasticiser to epoxy ratio in such a way to optimise the mechanical properties and the flexibility of the actuator layer.

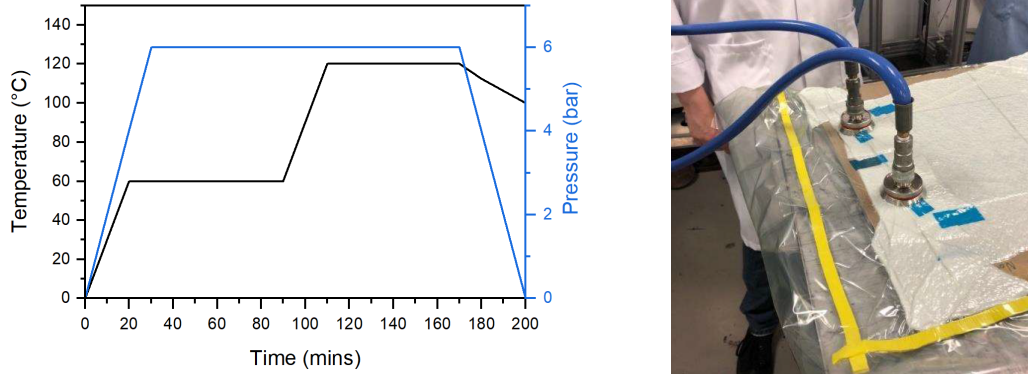
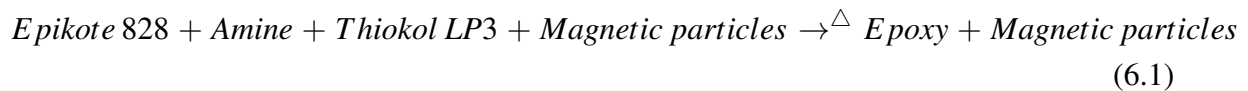


Fig. 6.2 [Left] Graphical representation of the various stages in the curing cycle of the carbon fibre laminates, showing the change of temperature as a function of time as well as the change in pressure. [Right] Snapshot of the vacuum bagging process.

The addition of polyglycol diepoxide to the epoxy resulted in a significant decrease in flexural strength, while the use of carboxyl-terminated polymers (e.g. carboxyl terminated butadiene-acrylonitrile) introduced unsaturated carbon bonds within the structure. During the post-fabrication process these bonds, when exposed to external environmental factors such as heat and atmospheric pressure, can lead to further unwanted curing resulting in a reduction in flexibility. Additionally, the epoxy and carboxyl-terminated polymers mixture is prone to oxidation, which can weaken the end-product over time [283]. Finally, the choice for the remaining two plasticisers can be supported by the previous study by Lim et al. [284] in which they used a polysulfide polymer in a ferrite-epoxy system and showed no adverse effects on strain sensing. This concludes the choice of plasticiser for the experiment, and hence, a Thiokol-LP3 polysulfide polymer purchased from Wessington Group Ltd. was added to the epoxy layer for the second composite laminate. The resin of choice was Epikote-828 purchased from Delta Resins Ltd. and contained bisphenol A and epichlorohydrin. A reaction catalyst (Diethylenetriamine from Alfa Aesar) for the epoxy curing process was also added. The ratio of Epikote-828 to amine was calculated by utilising its equivalent epoxy weight (EEW) of 184 – 190 g/equivalent, and it was averaged to 187g/equivalent. Based on this value, the calculated ratio for a stoichiometric reaction is 100:11 [285].

The reaction process can be summarised below:



The second set of composite laminates were impregnated with iron (Fe) and nickel (Ni) magnetic particles with a range of particle size. An 80  $\mu\text{m}$  sieve was used to separate the particles, which were then co-cured in the epoxy layer. Four samples were manufactured in this second set of laminates:

- (i) CF laminate with Nickel particles of less than 80  $\mu\text{m}$  in diameter (Ni < 80)
- (ii) CF laminate with Iron particles of less than 80  $\mu\text{m}$  in diameter (Fe < 80)
- (iii) CF laminate with Nickel particles ranging from 80 – 200  $\mu\text{m}$  in diameter (Ni: 80 – 200)
- (iv) CF laminate with Iron particles ranging from 80 – 200  $\mu\text{m}$  in diameter (Fe: 80 – 200)

Finally, the CF laminates were cut to the desired testing dimension of 150 × 25 × 4.5 mm using a tile cutter.

### Sensor fabrication

To sense the distortion of the composite samples, five different sensors were compared. Three of them were inkjet-printed with different windings, the next was hand-wound in the form of an air coil sensor, and finally an off-the-shelf AMR sensor was used as a benchmark.

The research by Fuller et al. [62] describe the fabrication of an inkjet-printed circular resonant inductive coil with 10 turns, and the importance of the number of windings as a function of inductance sensitivity. This was also supported by the research by Correia et al. [15] which demonstrated the printing of a high-density coil in the form of a square pad with a turn density of 25, resulting in a high inductance coil. However, the report also suggested that the denser windings resulted in a complicated the printing process which was more susceptible to failure due to shorts, as well as the large area required to print the inductance coils. McKerricher et al. [286], on the other hand, fabricated simpler spiral inductors ranging from 1.5 to 3.5 turns and reported comparable values of inductance once the conductivity of the printed ink was optimised.

In this set of experiments, two spiral coils of a monofilar arrangement were inkjet-printed with 5 and 10 windings, followed by a bifilar coil with a 5/5 winding arrangement, as shown in Figure 6.3(a) – (c) below. The inkjet printing process optimisation is described in a later section below.

The hand-wound copper coil, shown in Figure 6.3(d), was made using copper wire of a diameter of  $224\ \mu\text{m}$  which was turned clockwise around a plastic  $M3$  washer to maintain uniformity. 70 turns were chosen based on the previous experimental results obtained by Vincent et al. [287], which resulted in a better performance and was more sensitive in responding to the induced strain. The hand-wound coil was connected to a handheld LCR meter (Model 880, BK Precision Ltd.) which was used to measure the change in inductance during the experiment.

Finally, the off-the-shelf AMR sensor which was used as a benchmark was a HMC5883L from Honeywell Ltd (Figure 6.3(e)). The sensor was connected to an Arduino microcontroller to record the data.

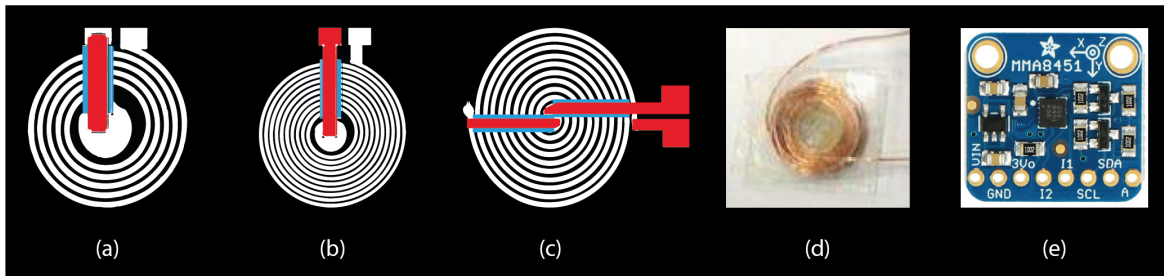


Fig. 6.3 Snapshot of the (a – c) inkjet printed coils, from the monofilar\_5n, monofilar\_10n and bifilar\_5/5 respectively, (d) hand-wound coil, and (e) off-the-shelf HMC5883L AMR sensor.

### Testing rig and procedure

The testing procedure involved replicating a deformation scenario using bending jigs of known radii to replicate the strain which the composite laminate would be subjected to, as shown in Figure 6.4. Bending rigs of test radii 300, 400, 500 and 600 mm were used, corresponding to microstrain values of 1.67, 1.24, 0.98, and 0.81, respectively. The sensors were placed on top and in the middle of the composite laminates above the magnetic actuator component, followed by the application of stress according to the shape of the bending rig. The induced deformation within the composite laminate creates a change in magnetisation of the actuator, which causes a change in inductance within the sensor and eventually recorded by the data acquisition system. The background inductance value, i.e., the inductance prior to the application of strain, of each sensor was measured and used to reduce the background effects, and the change of inductance was used as a comparison to eliminate any systematic error within the system. This process was repeated at least three times for the different bending radii, and the data recorded can be used to compare the different types of sensors.

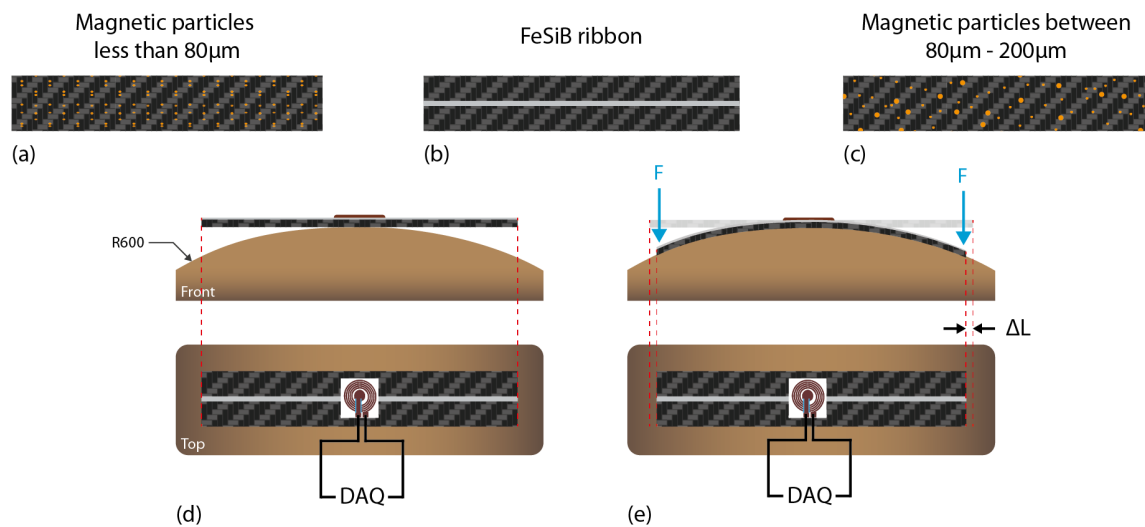


Fig. 6.4 Illustration of (a-c) the twill weave carbon fibre (CF) composite laminates with the different magnetic actuators as labelled, (d) the start of the testing procedure of the carbon fibre sample, showing the placement of the sensor and the data acquisition device (DAQ) on the bending jig of test radii 600 mm, and (e) the end of the testing procedure, showing the application of force  $F$  on both sides of the CF laminate and the subsequent deformation,  $\Delta L$ , when viewed from the top.

### Inkjet printing

Inkjet printing was done using the Jetlab IV printer which can build using a 4 printhead setup, each using a different ink, simultaneously. In this set of experiments, however, only two printheads were used as shown in Figure 6.5, both having the same 60  $\mu\text{m}$  nozzle orifice. The first printhead was used to deposit a functional copper nanoparticle-based ink, and the other a UV-curable insulator ink.

The copper ink was a specially formulated experimental nanoparticle-based ink (Dycotec Materials Ltd.) which was designed for inkjet printing and using flash sintering as a post-processing step. It contains 35 – 37 wt.% of copper nanoparticle stabilised in a mixture of diethylene glycol monoethyl ether and benzyl alcohol. The ink has a matt brown colour as printed from the copper nanoparticles. A filtration step using a 0.45  $\mu\text{m}$  PTFE filter was included before transferring the ink to the reservoir for printing. This was done to eliminate any contaminants which may cause defects or clogs during printing.

The secondary insulator ink was printed to prevent the formation of interconnects between the coils and the top-most layer. The insulator ink was purchased from the same supplier (Dycotec Materials Ltd.) and was specially designed for inkjet printing applications as well as providing a smooth, hydrophilic surface for overprints using other types of inks from the

same supplier. Hence, the combination of the copper nanoparticle-based and the insulator ink eliminated the requirement for additional surface tailoring prior to printing the final layer.

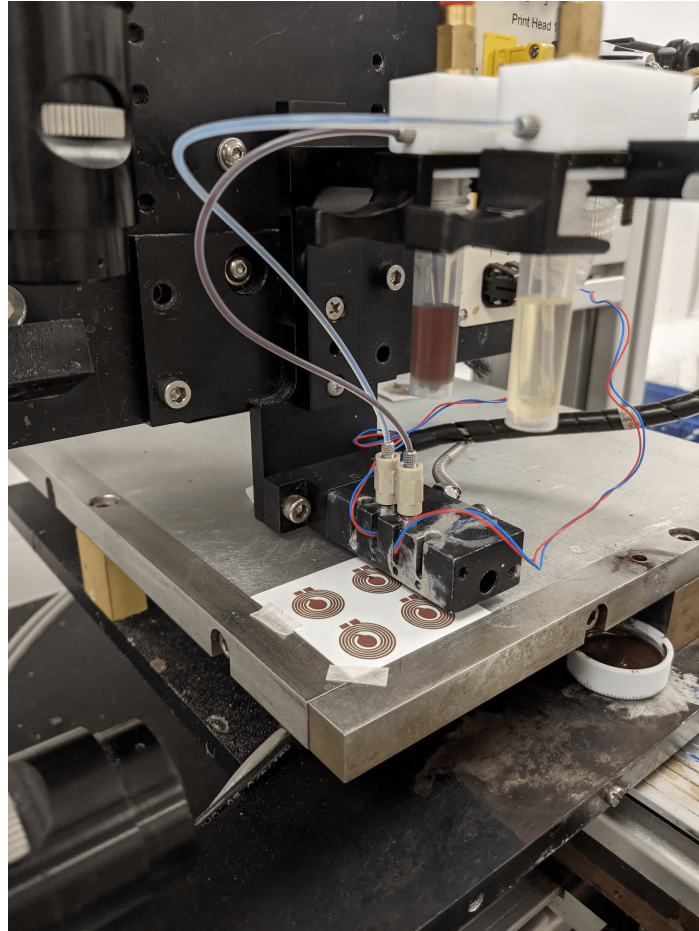


Fig. 6.5 Snapshot of the dual deposition system using the Jetlab IV printer from MicroFab Technologies. The copper ink is shown in the brown reservoir while the insulator ink is contained in the yellow-tinted reservoir. The insulator ink is being printed on the monofilar\_5n coil after the pulsed laser sintering process.

The viscosity of the ink as a variation of temperature is shown in Figure 6.6 below. The insulator ink has a much higher viscosity at room temperature (25 °C) as compared to the copper ink, and hence inkjet printing was done using a heated printhead at 40 °C. At this temperature, the viscosity of the copper ink measured  $7.80 \text{ mPa} \cdot \text{s}$  and the insulator ink  $16.0 \text{ mPa} \cdot \text{s}$ . At this temperature, the printing waveform was further optimised and shown in Figure 6.6 below. The higher viscosity of the insulator ink, despite being heated to 40 °C, required a more intricate waveform with the application of a higher voltage for a longer duration.

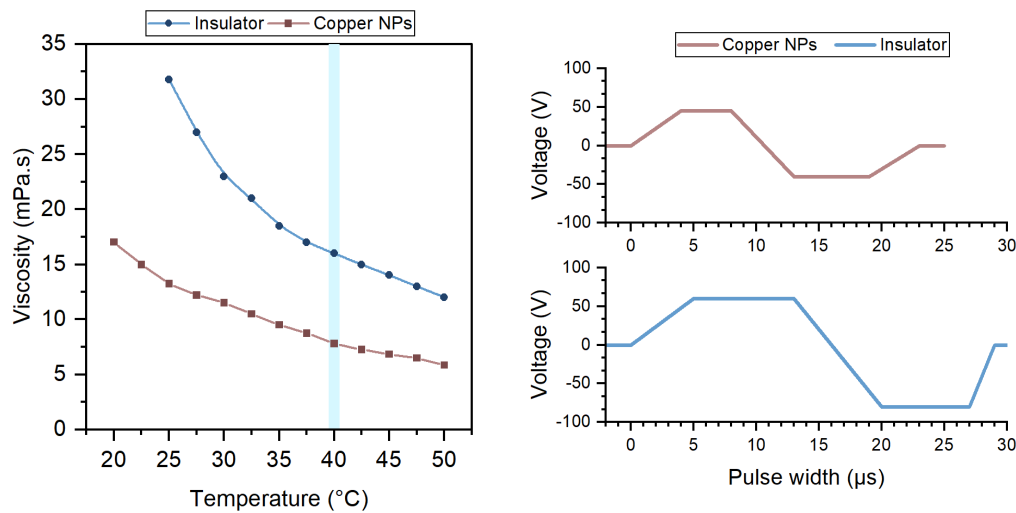


Fig. 6.6 [Left] Plot of the viscosity variation of both the functional copper nanoparticle and the insulator inks as a function of temperature. The printable region chosen was at 40 °C, highlighted in light blue on the plot. [Right] Illustration of the waveform used to print both inks using a 60  $\mu\text{m}$  printhead heated at 40°C.

The substrate chosen was a specially designed 250 *gsm* thick paper with a thin resin hydrophilic polymer coating to allow for printed particles to better adhere to the surface of the paper. The surface temperature was maintained at 40 °C to accelerate the evaporation of the solvent upon deposition and created a pinned contact line.

In this set of experiments, multi-layer coils were printed as shown in Figure 6.7 below. To avoid confusion, the term “layer” refers to the distinct geometries which were stacked. Each layer contains “coatings” of inks, either copper or the insulator ink. The coatings of ink were varied between two and four coats. In the previous chapters, the term “coating” referred to “layers”, hence, for the sake of clarity, this is defined as such due to the geometries involved in this set of experiments.

The droplet spacing was maintained at 50  $\mu\text{m}$  for prints with two coatings, and at 75  $\mu\text{m}$  for prints with four coatings. This was to ensure the spacing between the windings do not merge as the aspect ratio of the printed lines is increased due to the additional two coats. The dimensions of the coils are detailed in Appendix C.2, and are varied according to the chosen droplet spacing for printing. The first layer, described as step 1 in Figure 6.7, was printed out of the copper nanoparticle-based ink followed by pulsed laser sintering after drying (step 2). The second layer was printed using the insulator ink to act as an insulative surface to prevent interconnects (step 3), followed by UV curing (step 4). Finally, the third layer was printed using copper nanoparticle to form interconnects from the centre of the coil to the outer pad (step 5), and was pulsed laser sintered (step 6) to achieve the final product.

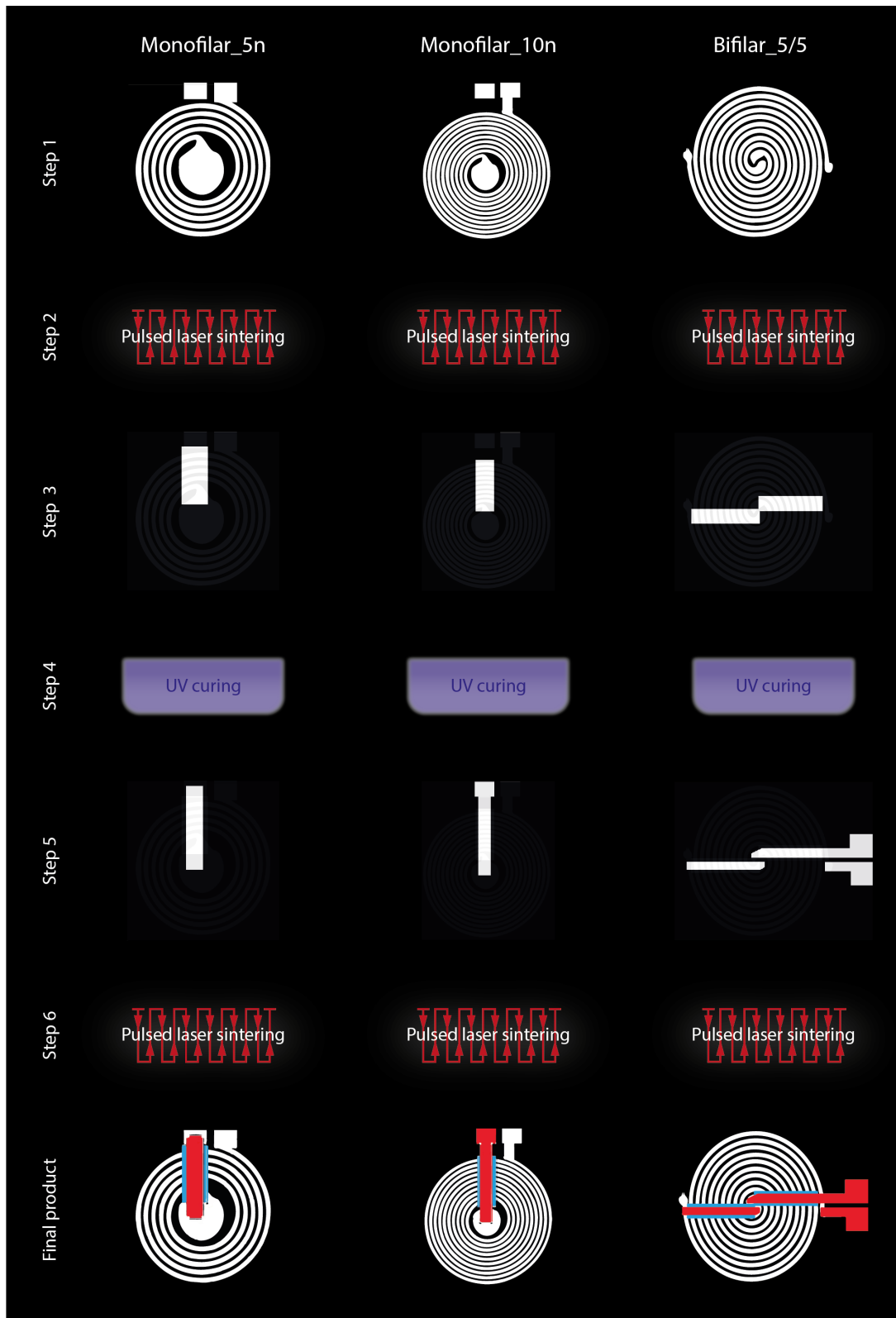


Fig. 6.7 Illustration of the process steps involved in the printing of each set of coils, highlighting the intermediate steps of sintering and curing prior to the printing of additional layers.

## UV curing

The insulator ink which was printed contained a liquid oligomer with a photoinitiator which required UV energy to cross-link into a stable insulative layer. The curing energy recommended by the supplier ranges between  $500 - 1000 \text{ mJ/cm}^2$  and requires incident radiation between  $380 - 390 \text{ nm}$  for optimum curing. The energy was supplied using a UV LED curing lamp from Phoseon Technology Inc. with an emission spectrum ranging from approximately  $390$  to  $420 \text{ nm}$  (shown in figure 6.8), with a peak at  $395 \text{ nm}$ . The irradiance of the UV lamp at the peak wavelength can reach a maximum of  $4 \text{ W/cm}^2$  when the target material is placed close to the output window of the lamp.

Since the insulator ink requires a quarter of the peak irradiance, the sample with the uncured insulator ink was placed at a separation of  $10 \text{ mm}$  from the output window corresponding to an irradiance of  $60 \%$ . The power output of the lamp was set to  $25 \%$ , which corresponds to an output irradiance of  $600 \text{ mJ/cm}^2$  – assuming the emission decreases linearly as a function of output power. The duration of the applied UV energy was set to  $15$  seconds to ensure the printed insulative layer had absorbed enough energy to cross-link.

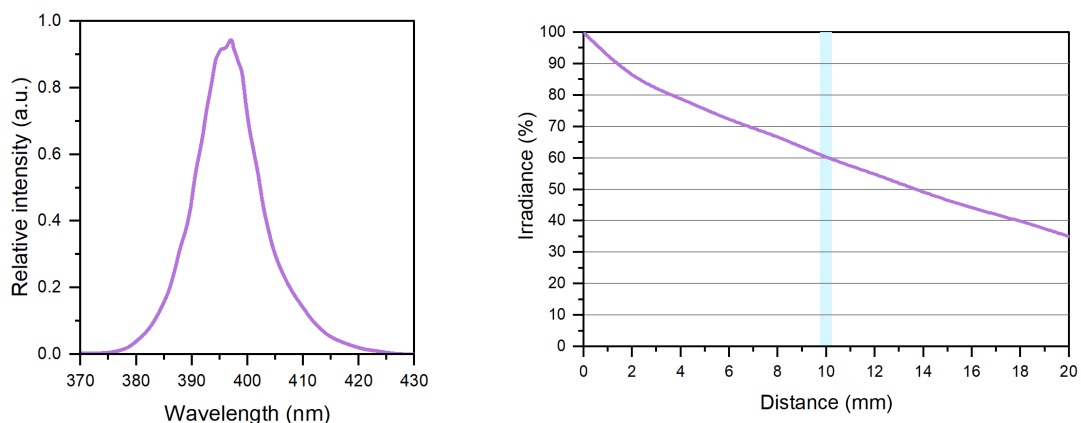


Fig. 6.8 [Left] Emission spectrum of the Phoseon Firefly FF200 UV LED lamp, and [right] the irradiance as a function of distance from the output window. The area highlighted in light blue indicates the position of the sample underneath the lamp.

## Pulsed laser sintering

The laser sintering process was done using the  $905 \text{ nm}$  custom-built pulsed laser system, which has proven successful for sintering the copper nanoparticle-based ink from previous experiments detailed in Chapter 3. Since a similar paper substrate was used as before, the same laser processing parameters for the first layer was employed for an optimum sintering, without causing any ablation of the sample. The fluence values used for the sintering process

is shown in Table 6.1 below. The overlap between each subsequent sintered row of copper was maintained at 15 % of the beam area superimposed next to each other to ensure the formation of a continuously sintered copper track, resulting in the most conductive value of around 35 % bulk conductivity of copper, based on the experimental findings from 3. The third layer of copper which was printed to form the interconnect from the centre of the coil to the contact pad was sintered with a lower fluence value as it was found to cause ablation on the insulator surface. Further process optimisation led to the fluence values shown in Table 6.1, both for two and four coatings of copper ink.

Table 6.1 Table summarising the laser processing parameters for sintering the copper nanoparticle-based ink on the paper substrate. The fluence is varied to ensure optimum sintering of the samples.

Layer	No. of CuNPs coatings	Average power (W)	Laser fluence ( $mJ/cm^2$ )
1	2	0.06430	357
3	2	0.03858	214
1	4	0.08037	446
3	4	0.04822	268

The natural thickness and wetting of the paper substrate resulted in the slight curvature of the paper which affected the quality of the laser sintering process significantly. The focal length of the laser beam must be maintained at 8.80 mm, hence any incremental deviation from this value will affect the focus of the laser beam. Additionally, the paper substrate, being flexible, must be able to be mounted on the carbon fibre laminate, hence any permanent adhesion during the laser sintering stage is undesirable (i.e. the use of double-sided adhesive tape must be avoided). To remedy this problem, the combination of strong neodymium magnets of 10 mm in diameter and a flat 5 mm thick steel sheet as a base was used as a means to apply a temporary localised compressive force to the surface of the paper to ensure it remains flat during the laser sintering process, as shown in Figure 6.9 below.

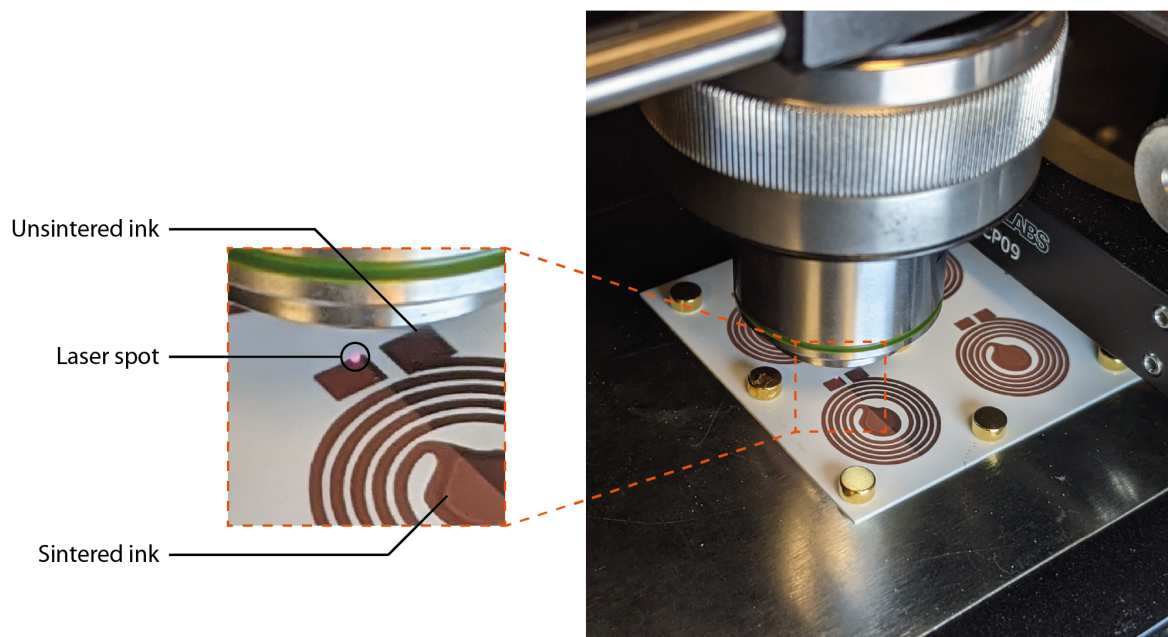


Fig. 6.9 Snapshot of the laser sintering process for the monofilar\_5n coil. The bottom left coil under the objective is being laser sintered, highlighting the distinction between unsintered copper as a dark-brown coating, and sintered copper as a reddish-brown coating, as shown in the detailed view on the left. The 250 *gsm* paper substrate is kept flat to the steel plate by using strong neodymium magnets.

### 6.2.3 Results and discussion

#### Change in inductance after 3-point bend test

The inductance values before and after actuation were recorded from the data acquisition device after three repeats were performed. The average value was then calculated and the result for the change in inductance was plotted for each bending radius, as shown in Figure 6.10 below. This procedure was repeated for each sensor and for each actuator. To simplify the investigation of the sensitivity of the coils in relation to the magnetisation of the various carbon fibre-epoxy laminates, a first order curve fitting regime was employed. Once the data was plotted, a linear fit was calculated for each graph, with the slope represented by “ $m$ ”, the intercept “ $c$ ” and the coefficient of determination “ $R^2$ ”. These values are recorded in Appendix C.1.

The observation from the bending test from the various samples highlighted the inductance response decreases with a decrease in strain, that is, a sample when bent using the bending test rig of radius 300 *mm* yielded a significantly higher response than when bent using the other bending test rigs of a larger radius (i.e. the 400 *mm*, 500 *mm* and 600 *mm* test radii).

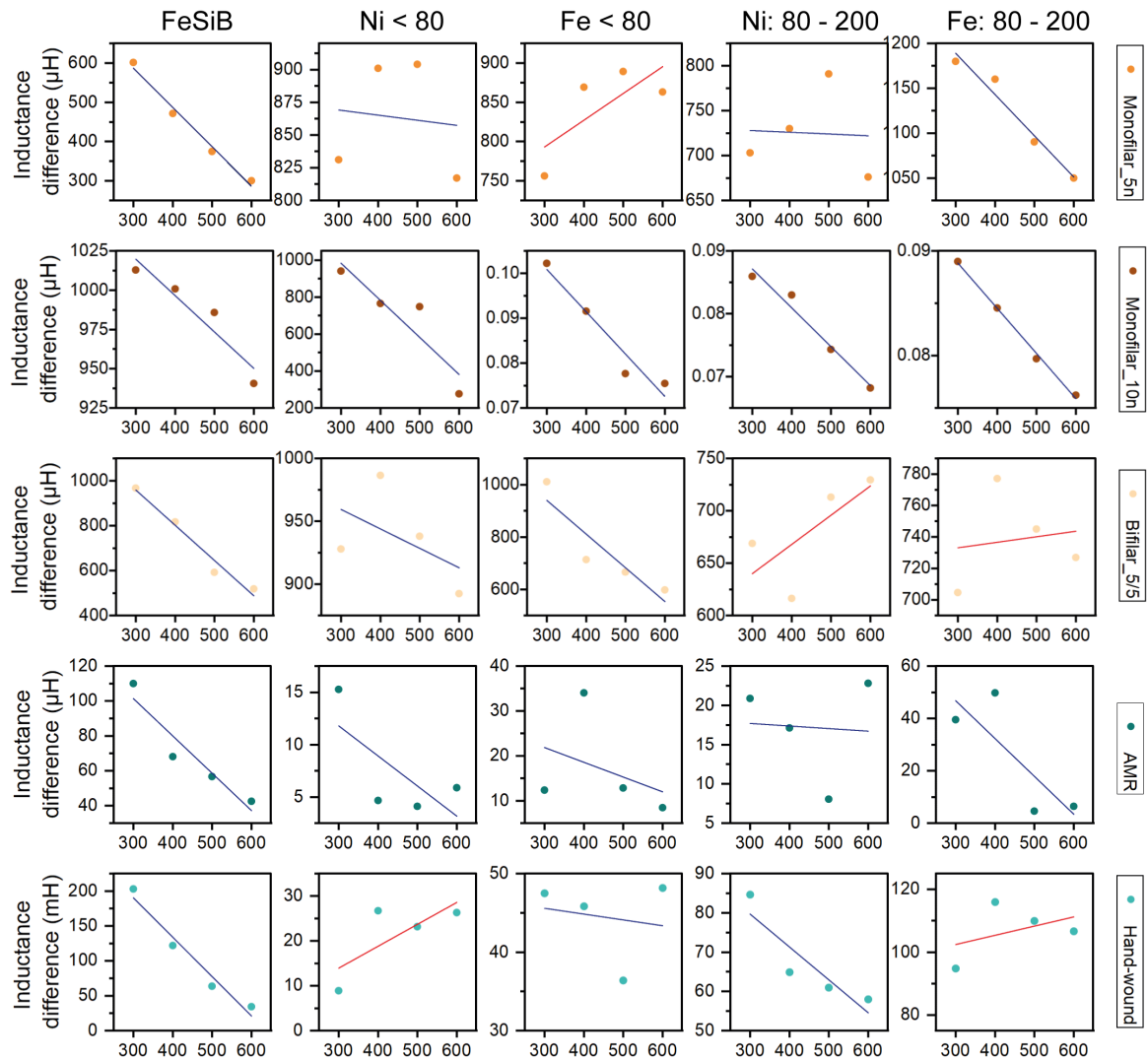


Fig. 6.10 Graphical representation of the inductance response of each sensor on the bending jigs (300, 400, 500 & 600) when actuated with the different composite laminates containing the magnetic component. The results from the inkjet-printed sensors are in the first three rows (monofilar\_5n, monofilar\_10n and bifilar\_5/5).

The coefficient of determination,  $R^2$ , is usually calculated in order to inspect the quality of the curve being fit through the experimentally generated data points. A  $R^2$  value close to 1 explains how accurately the curve is fit. Therefore, a response with a decreasing trend and a  $R^2$  value close to 1 is desired. The slope of the fit,  $m$ , can be understood as the sensitivity of the inductance coil sensor to the change in magnetisation of the sample. Therefore, a high magnitude of the slope ' $m$ ' would justify a decent sensitivity of the sensor, which is indicated with a blue line, while complex/unexpected sensor behaviour is indicated with a red line.

Amongst all the samples, the composite laminate with the FeSiB metal ribbons yielded the best results with an average  $R^2$  value of 0.9422 and a negative slope. This can be attributed to the successful fabrication of the sample and the strong presence of Fe, which is a ferromagnetic material, thereby making it easier for the sensor to detect the change in magnetisation. In comparison, the other samples contain far less metal content, which would make it less responsive to the magnetisation, and eventually this is evidenced by a positive slope.

Another observation from the plots shows that all the sensors are able to record a better magnetisation response to the iron-based samples, and as the iron particle size increases, the response becomes more apparent. A similar trend of an increase in particle size being advantageous to the sensing performance of the coils is observed with the nickel-based samples, although they do not appear to be as sensitive as the iron-based samples.

When comparing the different sensors, the hand-wound coil with 70 turns is the least sensitive ( $R^2$  value 0.5014 and does not respond as well as the other sensors when subject to a change in inductance. However, it may be possible to increase the number of turns in the coil so as to directly increase its sensitivity, although an increase in sensitivity can introduce undesirable noise. Furthermore, increasing the number of turns will also increase the resistance of the coil due to the additional length of copper wire required, thereby introducing inefficiencies which may reflect in a decrease in sensitivity and contribute to the noise factor. As an example, the 70-turn hand-wound coil has a resistance of 1.39  $\Omega$ . If the number of turns were to increase to 100, the resistance of the coil would increase to 2.13  $\Omega$ , indicating a 53 % increase in resistance, and ultimately a reduction in sensitivity.

Moving on to the AMR sensor, the slope of each fitted line pertaining to each individual actuator sample is negative, which indicates a relatively good sensitivity. However, the average  $R^2$  value is 0.4398 which corresponds to a less accurate curve fitting. This can be explained by the additional sensing in the z-axis (hence in three-dimension), in comparison to the other coil sensors which can only sense in the x- and y-axis (two-dimension). As a result, the additional sensing capability of the AMR sensor introduces noise from the surrounding which ultimately affects the accuracy of the recorded values after actuation.

The inkjet -printed copper coils yielded results ranging from good to excellent. The results from the monofilar coil with five turns reported a low average  $R^2$  value of 0.5005, although this sensor was able to record a decent response from the Fe < 80 with a  $R^2$  value of 0.5406, contrary to the AMR coil with a  $R^2$  value of 0.1349 and the hand-wound coil measuring an even lower  $R^2$  value of 0.0305. This highlighted the efficacy of the monofilar coil in quantifying the behaviour of the iron sample which was otherwise difficult to investigate with the hand-wound coil and the AMR sensor. However, it must be noted that this monofilar

coil contains just five turns which can contribute to the pickup of less noisy data, even though the acquisition of the less noisy data might have been obtained at the expense of the coil sensitivity.

To verify this claim, the inkjet-printed bifilar copper coil was tested and the data recorded using this sensor showed a clear improvement with an average  $R^2$  value of 0.6332. This improvement is not necessarily due to the better sensitivity of the coil but due to the ability of the bifilar coil to eliminate undesirable parasitic induction and noise. While the improvement in terms of noise reduction is evident, the  $R^2$  value is still low. Additionally, the coil was unable to record a relatively decent response to the actuation of the nickel-based samples. Therefore, it can be suggested that an improvement in the noise reduction can be made by increasing the number of turns, and hence the magnetic field, thereby making the coil more sensitive to the response upon actuation.

The aforementioned modification was applied to the 10-turn monofilar coil which was inkjet-printed out of copper. The results obtained using this sensor are the most promising both in terms of coil sensitivity ( $m$  value) and the fitting accuracy ( $R^2$  value). The average  $R^2$  value is 0.9265 and all the curves have a steep negative slope, implying a relatively superior sensitivity of this sensor to all the samples. Additionally, the number of turns of the coil are high enough to increase the sensitivity whilst minimising the noise detection.

The gradients of the response of each sensor to the actuator is plotted in Figure 6.11 below and can be used as an indication of the performance of the sensors. A negative, steep gradient indicates superior sensitivity, which can be seen with the 10-turn monofilar coil which was inkjet-printed out of copper.

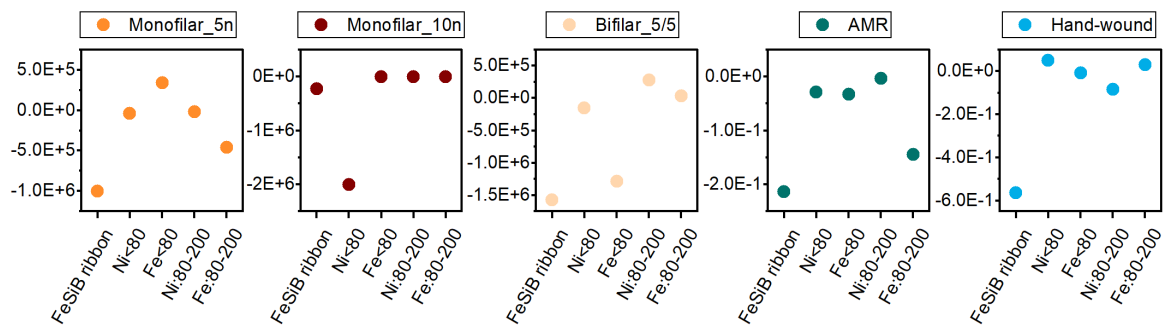


Fig. 6.11 Graphical plot of the gradients for each sensor and actuator design from their inductance response.

### Size dependence of the magnetic particles

The variation of the size distribution of the magnetic particles (Figure 6.12) appear to have an influence on the magnetostrictive properties of the actuators. The dependence of the particle size for the magnetic performance of particle was highlighted by Popplewell and Sakhnini [288] in 1995, and the latest research by Li et al. [289] investigated the correlation between particle size of ferrite oxide particle and their magnetic properties. In their report, they highlighted the magnetic saturation increases as the particle size increases, thereby making the samples more magnetic. However, beyond a certain threshold of particle size (related to the superparamagnetic limit), the internal structure of the particle changes to a multi-domain configuration, leading to a decrease in the overall performance of the overall samples.

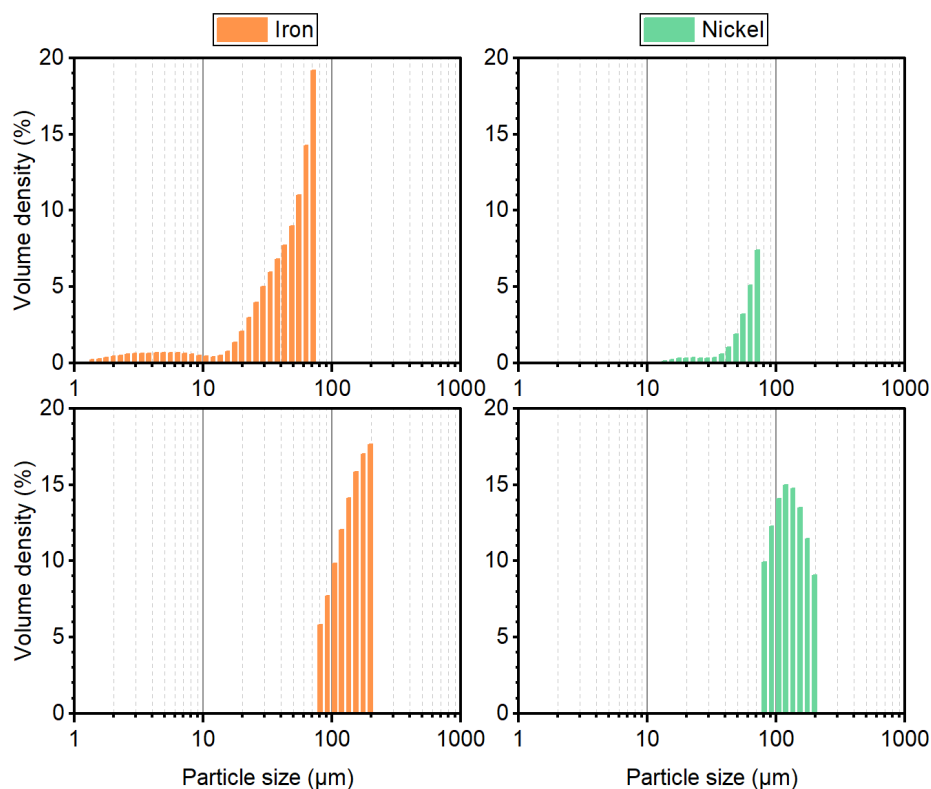


Fig. 6.12 Graphical representation of the size distribution of the iron and nickel particles used for impregnating the epoxy layer for the carbon fibre laminates.

Following Derjaguin-Landau-Verwey-Overbeck (DLVO) theory, the increase in particle size changes the interparticle interactions energies and thus (i) leads to an increase agglomeration which can lead to ‘hot spots’ within the epoxy matrix; and (ii) reduces the secondary stability energy of the agglomeration [290]. In relation to point (i), this was seen from the results here where the increased particle size leads to a reduction in the sensor sensitivity.

With regards to point (ii), the reduction in stability energy means that more energy is available for magnetisation angle reorientation and therefore accuracy increases. This work was also supported by Kamble et al. [291] who investigated the domain size correlation between the magnetic properties of nickel-ferrite particles. In terms of the size distribution, Gokturk et al. [292] experimented with a variation of particle size distribution in nickel-polyethylene composite samples and reported an increase in magnetic performance as the concentration and size variation of the particles increased. In terms of this experiment, the size distribution of the particle is shown in Figure 6.12. The ability of the sensors to detect the change in inductance appears to be more prominent for the particles of a larger size, and a wider size distribution.

### Selective pulsed laser sintering

The third layer of copper which was printed on top of the insulator layer had a lower resolution due to the smooth solid surface created after the cross-linking of the insulator ink. Consequently, four coatings of copper ink caused spreading outside the defined geometry and onto the copper coils from the first layer, which was detrimental to the performance of the copper coils. However, the unsintered copper ink is non-conductive by nature, so it did not cause any shorts unless sintered.

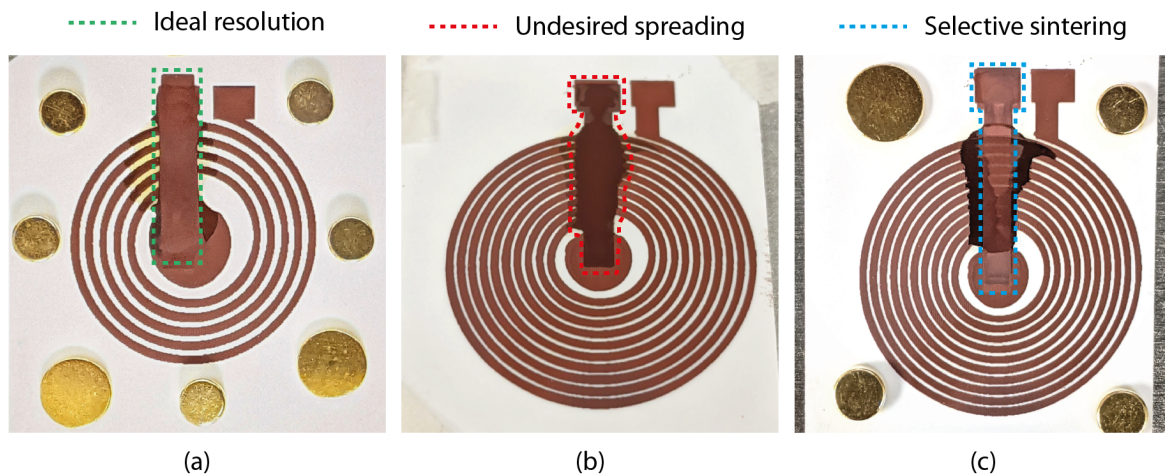


Fig. 6.13 Snapshot of printed copper coils highlighting (a) the ideal desired resolution of the final layer 3 of copper nanoparticle ink on the insulator layer, (b) the undesired spreading of the ink due to four coatings of copper on the insulator layer, and (c) the selective pulsed laser sintering of copper to only render the pattern printed on top of the insulator ink conductive.

The advantage of using laser sintering greatly benefitted this process as the area of sintering could be selected, as compared to conventional sintering processes where the

entirety of the sample was subjected to thermal sintering. This selective laser sintering process ensured only the region above the insulator layer was sintered, thereby preventing the formation of shorts due to the excess ink which had spread, as shown in Figure 6.13.

### Height variation for pulsed laser sintering

The initial set of trials of the copper coils which served as a proof of concept were first sintered without a mechanism to keep the coils level with the surface. As mentioned earlier, the disadvantage of the porous nature of the paper substrate resulted in over-wetting, particularly when four coatings of copper ink were printed. This over-wetting resulted in the surface curvature of the paper, creating incremental height deviations from the level of the surface. As a result, the focus of the laser varied due to few millimetres difference in height, ultimately resulting in a defocussed laser sintering (or no sintering) due to the diffused irradiance, as shown in Figure 6.14.

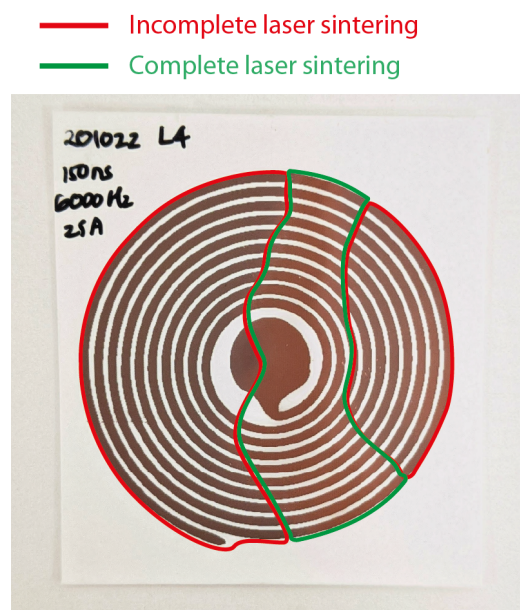


Fig. 6.14 Snapshot of a partially sintered copper coil as a result of a height variation, caused by the bending of paper due to a high moisture content when four coatings of copper were printed. The unsintered region is outlined in red while the sintered region is outlined in green.

This effect could be easily distinguished by the obvious colour change in regions of optimum sintering, while regions of no sintering remained unchanged. To further investigate the uneven sintering (and also the uneven discolouration), a simple two-point probe conductivity test was performed from the centre of the coil to the outer wire. A high resistance value, or in extreme cases no resistance values, served as an indication of poor laser sintering.

Further investigations into testing each section of the coil, particularly the unsintered section, confirmed the high (or no) resistance values within the region, which can be attributed to partial or incomplete sintering due to the diffused irradiance of the defocussed laser beam.

### **Use of laser ablation**

The pulsed laser sintering process had to be carefully tailored for sintering multi-layers in terms of the fluence as the high intensity of the laser caused some ablation on the surface of the cured insulator layer. The reduction in the fluence output by approximately 60 % of the fluence used to sinter the first copper layer resulted in the optimum sintering, without causing any surface defects or vaporisation, of the third layer of copper.

This surface vaporisation can be attributed to the decreased adhesive strength between the interface of the printed copper ink and the insulative layer. The insulator ink contains between 50 – 70 % of 1,4-butanediol diacrylate which is an acrylic used in epoxy, coatings, and inks. Upon cross-linking, the surface of the compound solidifies into a translucent hard surface. The contact angle of the copper ink on top of the insulator ink provides an indication of the spreading of the ink on the surface, and hence the overall adhesive strength. From Figure 6.15 below which shows the contact angle measurements for the copper ink on the cured insulator surface, it can be seen that the contact angle of  $42^\circ$  results in a fairly well-wetted surface when a single drop is deposited on the surface. However, when two drops are deposited consecutively at the same exact location, the drop spreads on the insulator layer, resulting in a relatively poorer resolution of the printed feature.

This phenomenon can be used to support the printing of two coatings of copper ink where the additional volume from the second coating causes the ink to spread more evenly on the surface, thereby creating more localised areas of adhesion to the surface.

In the context of this thesis, pulsed laser ablation is undesired due to its detrimental impact on the additive nature of depositing functional materials. However, in this particular context for the experiment, the ablation properties of the laser can benefit this manufacturing process in the form of a micro-machining finish operation, similar to the research published by Gamaly et al. [193], where the excess material is removed from the surface of the coil particularly where interconnects are likely to be formed.

The samples with four coatings appeared to cause excessive spreading beyond the insulator layer and onto the sintered coils from the first layer. The pulsed laser output can be increased beyond the ablation threshold to remove the excess copper ink. However, the additional volume of material does not appear to affect the performance of the coils from the first sintered layer, hence for this experiment the ablation micro-machining process was not explored, but is worth expanding on in future experiments.

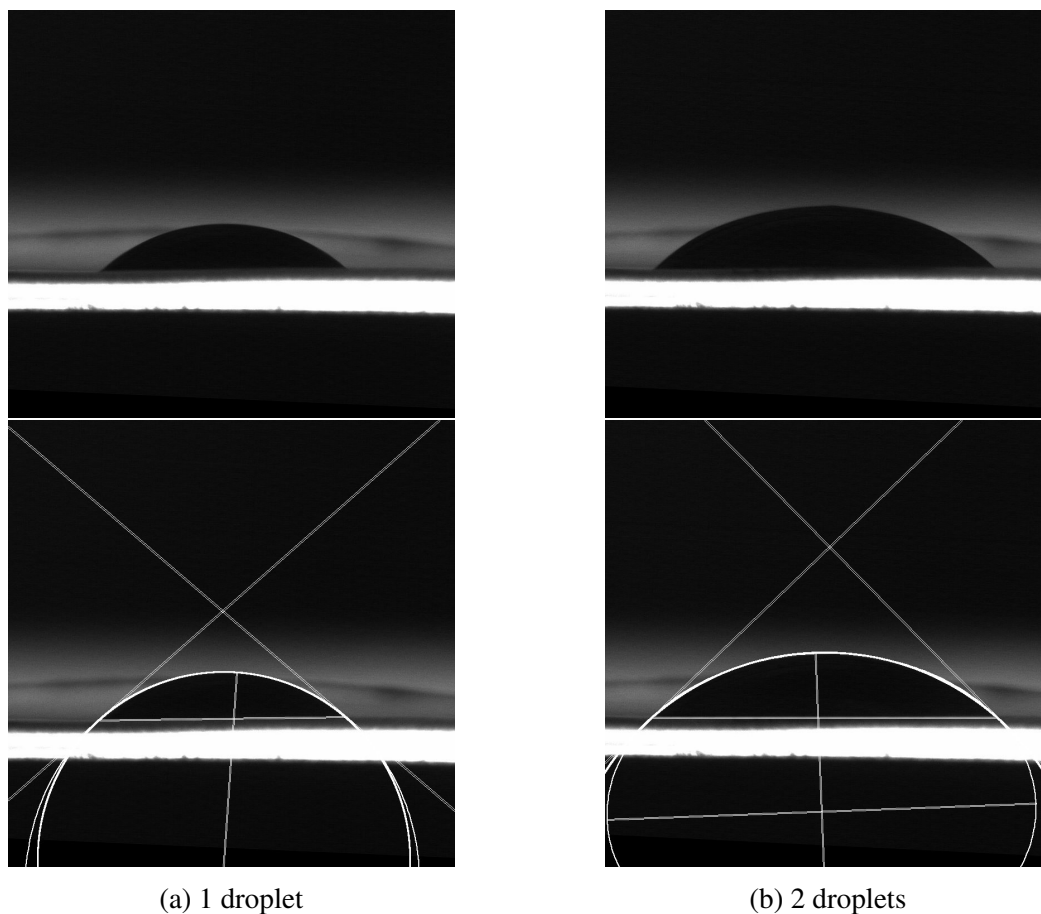


Fig. 6.15 Snapshot of the contact angle measurement for the copper nanoparticle-based ink printed on the cured insulator layer. The contact angle measures  $42^\circ$  on the surface. The first column (a) represents one droplet deposited on the surface, and column (b) represents two droplets deposited at the exact location consecutively. The second row represents the contact angle measurement process using image processing software.

### 6.2.4 Conclusions

In this chapter, inkjet-printed inductive coils were compared with a hand-wound coil as well as an off-the-shelf AMR sensor used for detecting the change in an applied magnetic field. The inkjet-printed coils were manufactured using drop-on-demand deposition technology to deposit functional copper nanoparticle-based ink on a substrate made out of paper, followed by a pulsed laser sintering process to convert the printed patterns into conductive copper.

The sensors were each tested on carbon fibre laminates with different actuators consisting of either a magnetic ribbon or magnetised particles. A series of bending tests were performed using bending jigs of varying radii (and hence varying strain values), and the results from the tests showed a change of inductance for each sensor when actuated. The change of

inductance was recorded and plotted for each bending jig, and the comparison for each sensor and actuator was made. To further elaborate on the sensitivity of each coil, a curve fitting approach was undertaken as a comparison method, similar to previous research works [287, 293], and the parameters for the curve fitting were compared for each plot.

The results from the hand-wound coil appeared to be the least promising where the sensor failed to detect apparent changes in a few cases (success rate 60 %), and in the other cases the sensitivity of the sensor was very poor. The off-the-shelf AMR sensor proved to be successful in detecting inductance changes in every case (success rate 100 %), although the data obtained from the sensor was very noisy due to the three-axis measurement technique of the sensor. Additionally, the sensitivity of the sensor was relatively poorer for some actuators. Finally, the inkjet-printed coils were successful in detecting most of the inductance changes, although the monofilar\_5n and bifilar\_5/5n had a success rate of only 80 %. The sensitivity of these two inkjet-printed sensors was relatively better than the hand-wound and the AMR sensors. The monofilar\_10n sensor, however, had a 100 % success rate and a superior sensitivity compared to all the sensors.

The inkjet-printed sensors have proven to deliver a comparable performance to off-the-shelf sensors, whilst having the key advantage of having a low profile as compared to the 3D AMR sensor. However, the additional process steps in printing and laser sintering the sensors introduce more time-consuming aspects as well as the cost of the overall manufacturing process. The recent works exploring the use of magnetostrictive materials embedded in aerospace-grade composites for structural health monitoring can benefit from the inclusion of inkjet-printing functional material. These sensors can determine damage in the composite samples that have been made "smart" with the addition of co-cured magnetostrictive actuators. Even though the hand-wound copper coils showed lower fidelity compared to the AMR sensor, the 3D coils showed better sensitivity to strain changes when tested. Therefore, a dimensionality reduction of the coils may therefore offer several advantages in terms of overall sensor-actuator weight reduction, the increased sensitivity with a reduced surface area, and an innovative fabrication process which can be expanded for mass production by printing the sensors directly on the "smart" carbon fibre laminates.

Some recommendations such as the fabrication of "smart" carbon fibre actuators are further expanded on in the "Further works" section of the final Chapter 7.2.



# Chapter 7

## Conclusions and Further works

### 7.1 Conclusions

This thesis set out to uncover the effects of pulsed laser sintering on functional materials made out of conductive metallic nanoparticles (e.g. copper nanoparticles), with the aim of producing printed electronics. To achieve this, first a baseline was established with three silver inks (a nanoparticle-based ink, an metallorganic decomposition ink, and a reactive silver ink) which were printed in the form of thin films and converted into functional conductive patterns after exposure to a thermal energy input by conventional means. Once this baseline was established, the novel approach of using pulsed laser sintering was investigated as a potential application for the post-processing step of the inkjet-printed functional material. This approach proved to be a success on both experimental inks which were investigated, a silver and a copper nanoparticle-based ink, and this success was quantified by a comparable electrical conductivity to the respective bulk material, with a maximum of 24.9 % bulk conductivity of silver and 38.7 % bulk conductivity of copper achieved. Additionally, the pulsed laser sintering process was performed at ambient conditions on two thermo-sensitive substrate (PET and paper) without any underlying degradation in the structural integrity, thereby highlighting the novelty of combining pulsed laser sintering with inkjet printing of functional materials.

Upon further investigation and survey from literature, other areas which required further analysis were highlighted and these include the adhesion of the sintered ink to the substrate as well as the formation of a heat affected zone, which is typical of pulsed lasers (more specifically pulsed lasers which emit at nanosecond intervals). These areas, deemed at the interface of the metal-substrate, are not widely reported in literature as researchers have only focussed on improving the conductivity of metal-based functional inks. The few research outputs which mention the adhesion quantification of the functional ink to the substrate have

employed the adhesion quantification guidelines based on current standards (e.g. the ASTM D3359 Cross-cut test), which similarly have some limitation such as subjective bias. In this thesis, the subjective bias limitation was circumvented by the use of digital means, whilst conforming to the guidelines. In terms of pulsed laser sintering, the formation of the heat affected zone on inkjet-printed functional metallic inks have not been reported in literature, hence underlying the novelty of this research. Both the adhesion and heat affected zone were further explored in the following sections and provided some quantitative and qualitative insight into the performance of the pulsed laser sintered copper nanoparticle-based inks. Finally, based on the success of these findings, a novel application scenario was investigated in the last chapter where copper sensors in the form of thin film coils which were pulsed laser sintered on a paper substrate were used to detect an induced deformation. The selective sintering advantage of the pulsed laser was highlighted in this section where only a particular region was converted to conductive copper to prevent the formation of short-circuits in the coils. These coils were then used as strain sensors on carbon fibre composite laminates impregnated with magnetic particles and ribbons to detect the magnetoresistive change upon deformation, and the inkjet-printed sensors demonstrated superior performance to other sensors.

A more detailed summary is as follows:

In Chapter 1, the inkjet printing method was described along with a survey of alternative sintering technique which could be applied to inkjet-printed functional materials. Emphasis was made on the trending use of laser sintering due to the distinct advantage of being selective in the energy deposition method, which can be applied to much finer features within the  $\mu\text{m}$  scale. The laser sintering method can be applied to features printed out of functional materials, where the thermal energy input from the laser beam is used to activate the functional element of the ink. The distinct advantages and disadvantages of inkjet printing in printed electronics are discussed, followed by the latest trends in printing conductive functional inks which highlighted areas for improvement.

Chapter 2 elaborated on functional inks which can be used for printed electronics and using inkjet printing as a deposition technology. The the inkjet-printing parameters such as the printing waveform, droplet spacing and contact angle with the substrate were also discussed, which altogether affect the geometry of the printed pattern. Then, the sintering mechanisms are elaborated upon, particularly what happens when there is a thermal energy input in functional materials. The next section then surveys alternative sintering method, and

lays the focus on LASER sintering for the applications of the research in this thesis. The literature review of laser sintering highlighted a difference between continuous wave and pulsed laser, where continuous wave lasers were limited by the excessive heat generation upon irradiation (hence they require substrates which can sustain the high temperatures), and pulsed laser were mainly portrayed as micro-machining operations due to the ablation phenomenon caused by their inherent “ON/OFF” mode of operation of pulsed lasers. However, there has been a study where screen-printed copper paste on a high glass transition temperature substrate, polyimide, was pulsed laser sinter under an inert atmosphere. Upon closer analysis, the reported successful outcome was due to the irradiation prior to the ablation threshold where the energy in the laser beam is absorbed in the copper paste, and was sufficient to initiate sintering without causing any vaporisation of the material. The interaction of the pulsed laser irradiation with the printed pattern highlighted grounds for investigation in the following chapters, and henceforth a pulsed laser was solely used as a method of sintering the inkjet-printed conductive patterns for the first time.

Chapter 3 provides all the relevant details of the materials and methods used throughout this research, including the theory and experimental techniques for inkjet printing and characterisation. Additionally, the analytical section describes all the testing apparatus used to perform an analysis of all the samples, including the custom-built four-point probe test station, cross-cutter and the bespoke pulsed laser sintering station.

In Chapter 4, the first experimental chapter which sets the baseline, conductive materials such as a silver nanoparticle-based ink, a silver metallorganic decomposition ink, and a reactive silver acetate-based ink, are chosen to explain the particular heat treatment mechanisms such as sintering, thus establishing the baseline. It was found that during the sintering mechanism, the conductivity of the printed patterns improved through agglomeration of the particles, which in turn improved their electrical and mechanical properties. A deeper analysis is done on the electrical conductivity, porosity and particle size distribution after optimum conversion to a conductive pattern to establish the baseline of the expected performance for conductive inkjet-printed patterns.

Chapter 5 investigates the use of a pulsed laser for the sintering of a copper and a silver nanoparticle-based ink, with particular attention to the electrical performance and morphology of the printed patterns, as well as the laser processing parameters such as the overlap and fluence which affect the final pattern. In the first experimental section, the ablation phenomenon was observed at high laser fluence values and also at a high overlap due to the “snake-scanning” approach during sintering. The ablation was mitigated by optimising both the laser fluence and the overlap, which also indicated an area which required investigation due to the poor adhesion to the substrate and the excessive energy input in the

next experimental section II. Due to the inherent nature of pulsed lasers which can be turned ON/OFF in a matter of nanoseconds, or even shorter in picoseconds or femtoseconds for ultra-high performance lasers, the thermal damage is restricted as it allows the target material to absorb and dissipate the energy periodically. The results from the experimental section indicate the comparable performance of using a pulsed laser for the sintering process of copper and silver nanoparticles on a variety of substrates, including two thermo-sensitive substrates such as PET and paper, which indicates the novelty of the combined use of pulsed lasers with inkjet printing at ambient conditions.

Then, the second experimental section of Chapter 5, a copper nanoparticle-based functional ink was preferred throughout this research due to its inherent low cost and the compatibility with the pulsed laser sintering. The special formulation of the copper ink does not require the need of an inert atmosphere for the sintering operation, contrary to conventional thermal sintering which requires the removal of oxygen from the sintering atmosphere to prevent the formation of copper oxide, which is detrimental to the performance of the printed pattern – provided the sintering is done by means of a laser. Since the experimental observations from the previous experimental section I indicated some ablation at some particularly high laser fluence values approaching the ablation threshold, this range of laser fluence was investigated in regard to the adhesion of the printed pattern. First a discussion on different types of adhesion tests was done, highlighting the pros and cons of each method until the decision to follow the cross-cut test procedure based on the ASTM F1842-15 standard, with a modification to eliminate the subjective bias of the observer, was made. As the adhesion properties of a thin film metal-polymer system is seldom reported in experimental findings, this experimental section of Chapter 5 investigated the adhesion of the optimised laser sintered copper nanoparticle-based ink on four substrates: glass, PET, Kapton PI and paper. The top-down method of laser sintering (contrary to the bottom-up conventional sintering regime) resulted in printed features which exhibit good adhesive properties due to a good wettability on substrates of choice, i.e. a contact angle less than  $90^\circ$ . The adhesion tests evaluation revealed the best performance to be the copper printed on the two polymer films, while the paper substrate was classified in a lower category due to the printer copper ink on paper being prone to oxidation if unsintered and left exposed at atmospheric conditions after a few days. Nonetheless, the adhesion classification for the copper printed on all the substrates enabled application in mid- to low-end printed electronics, based on a survey carried out with several industrial manufacturers.

The third experimental section III of Chapter 5 investigated the heat affected zone formation approaching the ablation regime. It was found that below the optimum sintering threshold, the heat affected zone is very minimal, while above the optimum sintering threshold

approaching the ablation threshold, the heat affected zone can be observed on all three substrates – PET, Kapton PI and paper. Laser fluence values above this threshold can either result in the removal of the printed material through vaporisation or damage to the substrate, or a combination of both in extreme cases.

Finally, Chapter 6 set the overall experimental results from Chapter 5 into an application context. Printed electronics can benefit various fields of engineering, and one example is the non-invasive structural health monitoring of carbon fibre reinforced composites (CFRC). By exploring the magnetostrictive aspect of carbon fibre samples impregnated with a magnetic element (either in the form of a ribbon or microparticles), the deformation of these CFRCs can be detected in the form of a strain by using a sensor. The added benefits of using an inkjet-printed sensor include a reduction in size while maintaining comparable (and in some cases, improved) sensing capabilities in terms of accuracy and fidelity to another fabricated sensor and an off-the-shelf sensor. The experimental section of Chapter 6 explored the sensing performance of inkjet-printed copper coils on paper which were pulsed laser sintered and applied to the CRFC actuators, and the results from the experiment indicate the superior performance of a 10-turn inkjet-printed coil, hence demonstrating the clear benefits of inkjet printing technology. Additionally, the pulsed laser sintering aspect enable the sintering to be performed on thermo-sensitive substrate, whilst expanding on the selective sintering aspect to convert only a particular region to prevent the formation of electrical shorts.

## 7.2 Further works

The facilitation of inkjet printing functional material by advances in novel materials on the nanoscale has driven the push for using inkjet deposition technology as a greener, cost-effective and additive implementation in industry. Hence, it is worth exploring alternative metallic nanoinks made out of nickel or aluminium for their attractive prices and different application possibility based on their mechanical properties. The combined use of pulsed laser sintering with inkjet printing can supplement the range of conductive inks, although the compatibility of nickel and aluminium nanoparticles with pulsed lasers must be studied in terms of absorption spectrum and heat affected zone formation. As the pulsed laser used in this research successfully converted copper without the formation of copper oxide, a similar experiment can be carried out with aluminium to prevent the formation of aluminium oxide. Alternative substrates can also be investigated, such as PEN for the optical transparency, to elaborate on the use of pulsed laser sintering without causing damage to the substrate.

The results from the experiment carried out in Chapter 6 illustrated the successful implementation of pulsed laser sintering on a thermo-sensitive substrate at ambient conditions,

as well as the multi-layer aspect of printing a conductor-insulator-conductor circuit. There have been numerous studies of printing a functional metallic nanoparticle-based ink on an epoxy layer, hence a potential next application step is to print directly on the epoxy layer of the carbon-fibre and perform the pulsed laser sintering. Since the pulsed laser has proven to not cause any damage to the substrate, the feasibility of this application can be explored through another experiment with the aim of producing similar inkjet-printed copper coils as sensors and suppressing the use of paper as a substrate. As a first step, the effects of pulsed laser sintering on the carbon-fibre laminate must be investigated to ensure the laser penetration depth does not thermally degrade the epoxy layer or create a heat affected zone, thereby introducing stress concentration areas. An optimisation of the laser fluence used for the sintering of the functional copper nanoparticle-based ink must be made.

As a recourse, if the epoxy layer interacts with the copper ink, or the constituents (e.g. solvent) of the copper ink interacts with the epoxy layer, a surface treatment on the epoxy layer can be made to ensure a smooth and unreactive surface. This can be in the form of a larger insulative layer by using the same insulator ink, or another more inert insulator such as SU-8 or PDMS in case the insulator ink interacts with the carbon-fibre epoxy layer. The final copper layer can be printed on top of the chosen insulator layer, and if there is some overspreading as observed with four coatings of copper, the ablation phenomenon of the pulsed laser can be applied in this scenario with the aim of removing the excess copper ink. This can be made to ensure the excess copper does not interact with the previous layers. In section 6.2.3 of Chapter 6, the uneven sintering of the copper coil was discussed due to the curvature of the wetted sample. As the current flows through the coil, the added heat generation from the interaction with the electrons during current flow may incite electrical sintering over time (as described in section 2.2.1 of Chapter 2) – a topic which raises further questions and investigation.

Finally, to prevent the delamination of the finished copper coil from the CFRC, an encapsulation layer in the form of a similar insulator layer made out of the insulator ink, SU-8 or PDMS can be added to the final layer of copper after the interconnects with the sensors have been made to ensure the longevity of the coils within the CFRC. The encapsulation layer can potentially be combined with the vacuum bagging process whereby the epoxy is co-cured with the copper coil. However, additional research is required to observe the effects of vacuum bagging on the copper nanoparticle-based ink at 120 °C for long durations. This experiment can be targeted at “Embedded electronics”, with the aim of producing “smart” CFRC samples, and a flow chart of the design of experiment can be represented in Figure 7.1 below.

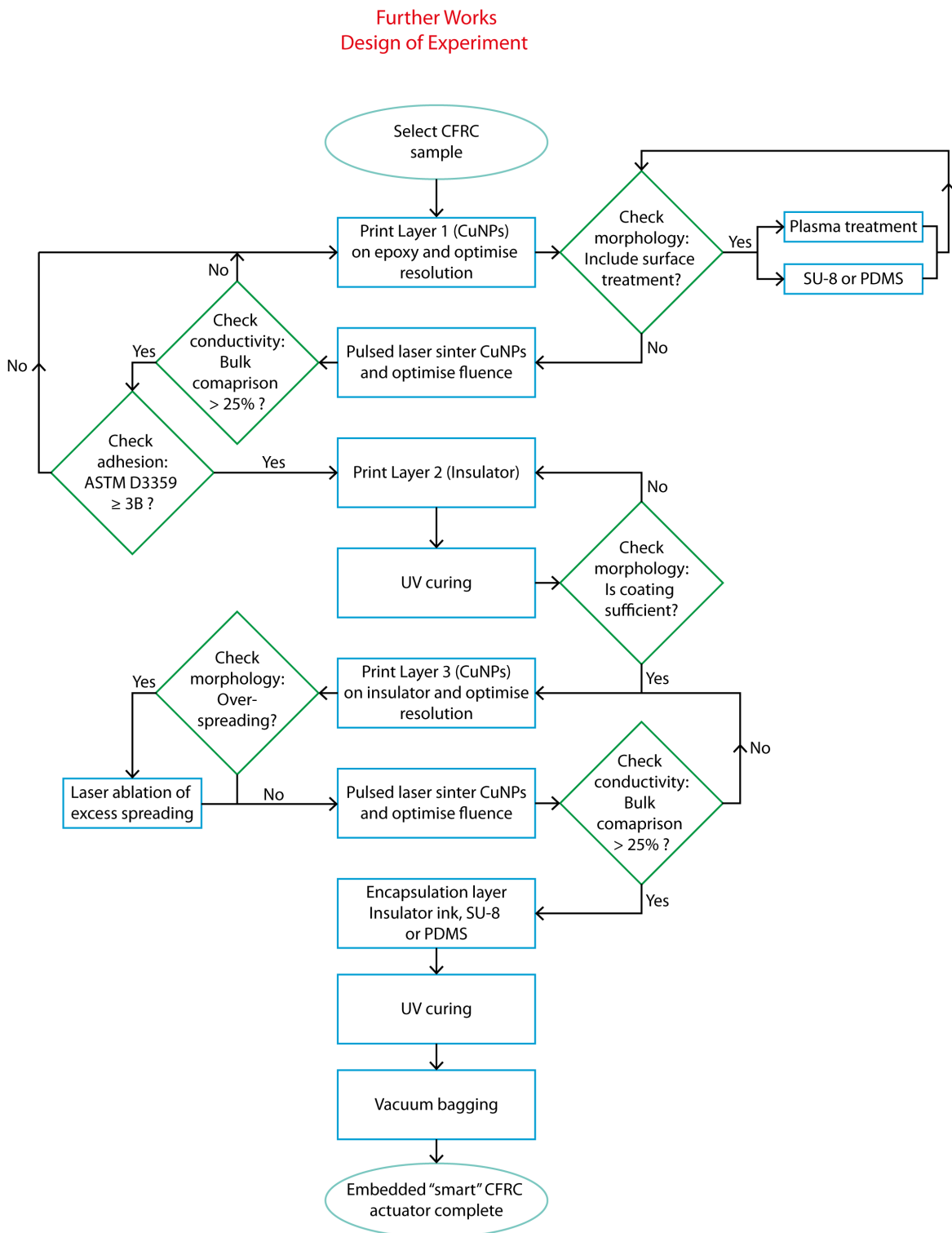


Fig. 7.1 Illustration of the process steps involved in the design of experiment for the “smart” CFRC samples.



# References

- [1] B. Derby, "Inkjet Printing of Functional and Structural Materials: Fluid Property Requirements, Feature Stability, and Resolution," *Annual Review of Materials Research*, vol. 40, no. 1, pp. 395–414, 2010.
- [2] W. Thomson, "Improvements in Telegraphic Receiving and Recording Instruments," 1867.
- [3] W. Thomson, "Improvement in recording instruments for the electric telegraph," nov 1870.
- [4] L. Rayleigh, "On the instability of jets," *Proceedings of the London Mathematical Society*, vol. s1-10, pp. 4–13, nov 1878.
- [5] C. W. Hansell, "Jet sprayer acuted by supersonic waves," jun 1946.
- [6] R. Elmqvist, "Measuring Instrument of the Recording Type," sep 1951.
- [7] R. G. Sweet, "High frequency recording with electrostatically deflected ink jets," *Review of Scientific Instruments*, vol. 36, pp. 131–136, feb 1965.
- [8] Casio, "Chronology of Main Products - History - Corporate - CASIO," 2015.
- [9] Teil1, "Tintendrucktechnologie Paradigma und Motor der Mikrosystemtechnik, Teil 1: Stand der Tintendrucktechnologie - Zwang zur Mikrosystemtechnik," *F&M Feinwerktechnik Mikrotechnik Messtechnik*, vol. 103, no. 6, pp. 318–324, 1995.
- [10] M. Döring, "Ink-jet printing," *Philips tech*, no. 7, pp. 192–198, 1982.
- [11] Hue P. Le, "Progress and Trends in Ink-jet Printing Technology," *Journal of Imaging Science and Technology*, vol. 42, no. 1, pp. 49–62, 1998.
- [12] J. Li, F. Rossignol, and J. Macdonald, "Inkjet printing for biosensor fabrication: Combining chemistry and technology for advanced manufacturing," *Lab on a Chip*, vol. 15, pp. 2538–2558, jun 2015.
- [13] M. Mäntysalo and P. Mansikkamäki, "An inkjet-deposited antenna for 2.4 GHz applications," *AEU - International Journal of Electronics and Communications*, vol. 63, pp. 31–35, jan 2009.
- [14] D. Redinger, S. Molesa, S. Yin, R. Farschi, and V. Subramanian, "An ink-jet-deposited passive component process for RFID," *IEEE Transactions on Electron Devices*, vol. 51, pp. 1978–1983, dec 2004.

- [15] V. Correia, K. Y. Mitra, H. Castro, J. G. Rocha, E. Sowade, R. R. Baumann, and S. Lanceros-Mendez, "Design and fabrication of multilayer inkjet-printed passive components for printed electronics circuit development," *Journal of Manufacturing Processes*, vol. 31, pp. 364–371, 2018.
- [16] J. C. Miers and W. Zhou, "Inkjet Printing at Megahertz Frequency," in *Solid Freeform Fabrication Symposium*, pp. 1275–1293, 2015.
- [17] B. V. Antohe and D. B. Wallace, "Acoustic phenomena in a demand mode piezoelectric ink jet printer," *Journal of Imaging Science and Technology*, vol. 46, no. 5, pp. 409–414, 2002.
- [18] H. Kipphan, *Handbook of Print Media*. Berlin, Heidelberg: Springer Berlin Heidelberg, 2001.
- [19] Y.-M. Kim, S.-U. Son, J.-Y. Choi, D.-Y. Byun, and S.-H. Lee, "Design and Fabrication of Electrostatic Inkjet Head using Silicon Micromachining Technology," *JSTS: Journal of Semiconductor Technology and Science*, vol. 8, no. 2, pp. 121–127, 2008.
- [20] A. Hudd, "Inkjet Printing Technologies," in *The Chemistry of Inkjet Inks* (S. Magdassi, ed.), pp. 3–18, World Scientific, jul 2009.
- [21] K. Takano, T. Kawabata, C. F. Hsieh, K. Akiyama, F. Miyamaru, Y. Abe, Y. Tokuda, R. P. Pan, C. L. Pan, and M. Hangyo, "Fabrication of terahertz planar metamaterials using a super-fine ink-jet printer," *Applied Physics Express*, vol. 3, p. 016701, jan 2010.
- [22] C. C. Ho, K. Murata, D. A. Steingart, J. W. Evans, and P. K. Wright, "A super ink jet printed zinc-silver 3D microbattery," *Journal of Micromechanics and Microengineering*, vol. 19, p. 094013, sep 2009.
- [23] K. Murata, "Direct fabrication of super -fine wiring and bumping by using inkjet process," in *6th International IEEE Conference on Polymers and Adhesives in Microelectronics and Photonics, Polytronic 2007, Proceedings*, pp. 293–296, IEEE, jan 2007.
- [24] J. Brünahl and A. M. Grishin, "Piezoelectric shear mode drop-on-demand inkjet actuator," *Sensors and Actuators, A: Physical*, vol. 101, no. 3, pp. 371–382, 2002.
- [25] Microdrop Technology, "Microdrop Dispenser Heads," 2000.
- [26] M. T. Inc., "Ink-Jet Microdispenser."
- [27] E. L. Kyser and S. B. Sears, "Method and apparatus for recording with writing fluids and drop projection means therefor," jun 1976.
- [28] I. T. Co., "Printheads for High Resolution Inkjet Printers."
- [29] M. Kido, N. Toda, T. Nakagawa, H. Nagashima, J. Furukawa, N. Okada, H. Kobayashi, and R. Co, "Development of New Aqueous Resin Ink for Sign Graphics," in *Printing for Fabrication 2016 (NIP32)*, vol. 2016, pp. 75–78, 2016.

- [30] G. D. Martin, S. D. Hoath, and I. M. Hutchings, "Inkjet printing - The physics of manipulating liquid jets and drops," *Journal of Physics: Conference Series*, vol. 105, p. 012001, mar 2008.
- [31] T. Boland, T. Xu, B. Damon, and X. Cui, "Application of inkjet printing to tissue engineering," *Biotechnology Journal*, vol. 1, pp. 910–917, sep 2006.
- [32] T. Xu, J. Jin, C. Gregory, J. J. Hickman, and T. Boland, "Inkjet printing of viable mammalian cells," *Biomaterials*, vol. 26, pp. 93–99, jan 2005.
- [33] J. D. Kim, J. S. Choi, B. S. Kim, Y. Chan Choi, and Y. W. Cho, "Piezoelectric inkjet printing of polymers: Stem cell patterning on polymer substrates," *Polymer*, vol. 51, pp. 2147–2154, may 2010.
- [34] J. G. Korvink, P. J. Smith, and D. Y. Shin, *Inkjet-Based Micromanufacturing*. Weinheim, Germany: Wiley-VCH Verlag GmbH & Co. KGaA, apr 2012.
- [35] E. Tekin, P. J. Smith, and U. S. Schubert, "Inkjet printing as a deposition and patterning tool for polymers and inorganic particles," *Soft Matter*, vol. 4, pp. 703–713, mar 2008.
- [36] R. W. Vest, "Liquid ink jet printing with MOD inks for hybrid microcircuits," *IEEE Transactions on Components, Hybrids, and Manufacturing Technology*, vol. 10, no. 4, pp. 545–549, 1987.
- [37] K. F. Teng and R. W. Vest, "Application of ink jet technology on photovoltaic metalization," *IEEE Electron Device Letters*, vol. 9, no. 11, pp. 591–593, 1988.
- [38] H. Sirringhaus, T. Kawase, R. H. Friend, T. Shimoda, M. Inbasekaran, W. Wu, and E. P. Woo, "High-resolution inkjet printing of all-polymer transistor circuits," *Science*, vol. 290, pp. 2123–2126, dec 2000.
- [39] J. Perelaer, P. J. Smith, D. Mager, D. Soltman, S. K. Volkman, V. Subramanian, J. G. Korvink, and U. S. Schubert, "Printed electronics: the challenges involved in printing devices, interconnects, and contacts based on inorganic materials," *Journal of Materials Chemistry*, vol. 20, p. 8446, sep 2010.
- [40] L. Yang, A. Rida, R. Vyas, and M. M. Tentzeris, "RFID tag and RF structures on a paper substrate using inkjet-printing technology," *IEEE Transactions on Microwave Theory and Techniques*, no. 12, pp. 2894–2901, 2007.
- [41] J. F. Dijksman, P. C. Duineveld, M. J. J. Hack, A. Pierik, J. Rensen, J.-E. Rubingh, I. Schram, and M. M. Vernhout, "Precision ink jet printing of polymer light emitting displays," *J. Mater. Chem.*, vol. 17, pp. 511–522, jan 2007.
- [42] C. N. Hoth, P. Schilinsky, S. A. Choulis, and C. J. Brabec, "Printing highly efficient organic solar cells," *Nano Letters*, vol. 8, pp. 2806–2813, sep 2008.
- [43] A. Gheno, Y. Huang, J. Bouclé, B. Ratier, A. Rolland, J. Even, and S. Vedraïne, "Toward Highly Efficient Inkjet-Printed Perovskite Solar Cells Fully Processed Under Ambient Conditions and at Low Temperature," *Solar RRL*, vol. 2, p. 1800191, nov 2018.

- [44] S. Norita, D. Kumaki, Y. Kobayashi, T. Sato, K. Fukuda, and S. Tokito, "Inkjet-printed copper electrodes using photonic sintering and their application to organic thin-film transistors," *Organic Electronics*, vol. 25, pp. 131–134, oct 2015.
- [45] W. G. Whittow, a. Chauraya, J. C. Vardaxoglou, L. Yi, R. Torah, K. Yang, S. Beeby, and J. Tudor, "Inkjet Printed Microstrip Patch Antennas Realised on Textile for Wearable Applications," *IEEE Antennas and Wireless Propagation Letters*, vol. 13, pp. 71–74, 2014.
- [46] Y. Mao, N. M. Felix, P. T. Nguyen, C. K. Ober, and K. K. Gleason, "Towards all-dry lithography: Electron-beam patternable poly(glycidyl methacrylate) thin films from hot filament chemical vapor deposition," *Journal of Vacuum Science and Technology B: Microelectronics and Nanometer Structures*, vol. 22, pp. 2473–2478, sep 2004.
- [47] W. Ehrfeld, "Progress in deep-etch synchrotron radiation lithography," *Journal of Vacuum Science & Technology B: Microelectronics and Nanometer Structures*, vol. 6, p. 178, jan 1988.
- [48] E. Sowade, H. Kang, K. Y. Mitra, O. J. Weiß, J. Weber, and R. R. Baumann, "Roll-to-roll infrared (IR) drying and sintering of an inkjet-printed silver nanoparticle ink within 1 second," *Journal of Materials Chemistry C*, vol. 3, no. 45, pp. 11815–11826, 2015.
- [49] L. D. Garma, L. M. Ferrari, P. Scognamiglio, F. Greco, and F. Santoro, "Inkjet-printed PEDOT:PSS multi-electrode arrays for low-cost: In vitro electrophysiology," *Lab on a Chip*, vol. 19, no. 22, pp. 3776–3786, 2019.
- [50] E. Saleh, P. Woolliams, B. Clarke, A. Gregory, S. Greedy, C. Smartt, R. Wildman, I. Ashcroft, R. Hague, P. Dickens, and C. Tuck, "3D inkjet-printed UV-curable inks for multi-functional electromagnetic applications," *Additive Manufacturing*, vol. 13, pp. 143–148, jan 2017.
- [51] P. Q. Nguyen, L. P. Yeo, B. K. Lok, and Y. C. Lam, "Patterned surface with controllable wettability for inkjet printing of flexible printed electronics," *ACS Applied Materials and Interfaces*, vol. 6, pp. 4011–4016, mar 2014.
- [52] E. Halonen, A. Halme, T. Karinsalo, P. Iso-Ketola, M. Mäntysalo, and R. Mäkinen, "Dynamic bending test analysis of inkjet-printed conductors on flexible substrates," in *Proceedings - Electronic Components and Technology Conference*, pp. 80–85, IEEE, may 2012.
- [53] N. C. Raut and K. Al-Shamery, "Inkjet printing metals on flexible materials for plastic and paper electronics," 2018.
- [54] Canon, "Technology Used in Flat Panel Display (FPD) Lithography Equipment," 2018.
- [55] Intel Corporation, "Intel® Core™ i7-8700 Processor (12M Cache, up to 4.60 GHz) Product Specifications."

- [56] C. E. Hendriks, P. J. Smith, J. Perelaer, A. M. J. Van Den Berg, and U. S. Schubert, "'Invisible' silver tracks produced by combining hot-embossing and inkjet printing," *Advanced Functional Materials*, vol. 18, pp. 1031–1038, apr 2008.
- [57] C. W. Sele, T. Von Werne, R. H. Friend, and H. Sirringhaus, "Lithography-free, self-aligned inkjet printing with sub-hundred-nanometer resolution," *Advanced Materials*, vol. 17, pp. 997–1001, apr 2005.
- [58] P. M. Grubb, H. Subbaraman, S. Park, D. Akinwande, and R. T. Chen, "Inkjet printing of high performance transistors with micron order chemically set gaps," *Scientific Reports*, vol. 7, dec 2017.
- [59] W. J. Hyun, S. Lim, B. Y. Ahn, J. A. Lewis, C. D. Frisbie, and L. F. Francis, "Screen Printing of Highly Loaded Silver Inks on Plastic Substrates Using Silicon Stencils," *ACS Applied Materials and Interfaces*, vol. 7, pp. 12619–12624, jun 2015.
- [60] S. K. Garlapati, M. Divya, B. Breitung, R. Kruk, H. Hahn, and S. Dasgupta, "Printed Electronics Based on Inorganic Semiconductors: From Processes and Materials to Devices," *Advanced Materials*, vol. 30, no. 40, pp. 1–55, 2018.
- [61] L. H. Liang, C. M. Shen, S. X. Du, W. M. Liu, X. C. Xie, and H. J. Gao, "Increase in thermal stability induced by organic coatings on nanoparticles," *Physical Review B - Condensed Matter and Materials Physics*, vol. 70, no. 20, 2004.
- [62] S. B. Fuller, E. J. Wilhelm, and J. M. Jacobson, "Ink-jet printed nanoparticle microelectromechanical systems," *Journal of Microelectromechanical Systems*, vol. 11, no. 1, pp. 54–60, 2002.
- [63] D. Kim, S. Jeong, J. Moon, and K. Kang, "Ink-jet printing of silver conductive tracks on flexible substrates," *Molecular Crystals and Liquid Crystals*, vol. 459, pp. 45/[325]–55/[335], dec 2006.
- [64] J. B. Szczech, C. M. Megaridis, J. Zhang, and D. R. Gamota, "Ink jet processing of metallic nanoparticle suspensions for electronic circuitry fabrication," *Microscale Thermophysical Engineering*, vol. 8, pp. 327–339, oct 2004.
- [65] J. Perelaer, A. W. De Laat, C. E. Hendriks, and U. S. Schubert, "Inkjet-printed silver tracks: Low temperature curing and thermal stability investigation," *Journal of Materials Chemistry*, vol. 18, no. 27, pp. 3209–3215, 2008.
- [66] J. Perelaer, M. Klokkenburg, C. E. Hendriks, and U. S. Schubert, "Microwave flash sintering of inkjet-printed silver tracks on polymer substrates," *Advanced Materials*, vol. 21, no. 47, pp. 4830–4834, 2009.
- [67] J. Perelaer, B. J. De Gans, and U. S. Schubert, "Ink-jet printing and microwave sintering of conductive silver tracks," *Advanced Materials*, vol. 18, pp. 2101–2104, aug 2006.
- [68] Z. Radivojevic, K. Andersson, K. Hashizume, M. Heino, M. Mantysalo, P. Mansikkamaki, Y. Matsuba, and N. Terada, "Optimised curing of silver ink jet based printed traces," *Dans Proceedings of 12th International Workshop on Thermal investigations of ICs - THERMINIC 2006*, no. September, pp. 27–29, 2006.

- [69] J. Niittynen and M. Mantysalo, "Characterization of laser sintering of copper nanoparticle ink by FEM and experimental testing," *IEEE Transactions on Components, Packaging and Manufacturing Technology*, vol. 4, no. 12, pp. 2018–2025, 2014.
- [70] J. H. Choi, K. Ryu, K. Park, and S. J. Moon, "Thermal conductivity estimation of inkjet-printed silver nanoparticle ink during continuous wave laser sintering," *International Journal of Heat and Mass Transfer*, vol. 85, pp. 904–909, 2015.
- [71] T. Kumpulainen, J. Pekkanen, J. Valkama, J. Laakso, R. Tuokko, and M. Mäntysalo, "Low temperature nanoparticle sintering with continuous wave and pulse lasers," *Optics and Laser Technology*, vol. 43, no. 3, pp. 570–576, 2011.
- [72] M. L. Allen, M. Aronniemi, T. Mattila, A. Alastalo, K. Ojanperä, M. Suhonen, and H. Seppä, "Electrical sintering of nanoparticle structures," *Nanotechnology*, vol. 19, pp. 17–20, apr 2008.
- [73] G. Xie, O. Ohashi, N. Yamaguchi, and A. Wang, "Effect of surface oxide films on the properties of pulse electric-current sintered metal powders," *Metallurgical and Materials Transactions A: Physical Metallurgy and Materials Science*, vol. 34 A, no. 11, pp. 2655–2661, 2003.
- [74] S. H. Risbud and K. Yamazaki, "Plasma activated sintering of additive-free ain powders to near-theoretical density in 5 minutes," *Journal of Materials Research*, vol. 7, no. 10, pp. 2643–2645, 1992.
- [75] I. Ivanišević, P. Kassal, A. Milinković, A. Rogina, and S. Milardović, "Combined Chemical and Thermal Sintering for High Conductivity Inkjet-printed Silver Nanoink on Flexible Substrates," *Chemical and Biochemical Engineering Quarterly*, vol. 33, no. 3, pp. 377–384, 2019.
- [76] S. Amendola, A. Palombi, and G. Marrocco, "Inkjet printing of epidermal RFID antennas by self-sintering conductive ink," *IEEE Transactions on Microwave Theory and Techniques*, vol. 66, pp. 1561–1569, mar 2018.
- [77] S. F. Jahn, T. Blaudeck, R. R. Baumann, A. Jakob, P. Ecorchard, T. Ruffer, H. Lang, and P. Schmidt, "Inkjet printing of conductive silver patterns by using the first aqueous particle-free MOD ink without additional stabilizing ligands," *Chemistry of Materials*, vol. 22, pp. 3067–3071, may 2010.
- [78] E. Halonen, T. Viiru, K. Östman, A. L. Cabezas, and M. Mantysalo, "Oven sintering process optimization for inkjet-printed Ag Nanoparticle ink," *IEEE Transactions on Components, Packaging and Manufacturing Technology*, vol. 3, no. 2, pp. 350–356, 2013.
- [79] K. Black, J. Singh, D. Mehta, S. Sung, C. J. Sutcliffe, and P. R. Chalker, "Silver ink formulations for sinter-free printing of conductive films," *Scientific Reports*, vol. 6, p. 20814, aug 2016.
- [80] E. Balliu, H. Andersson, M. Engholm, T. Öhlund, H. E. Nilsson, and H. Olin, "Selective laser sintering of inkjet-printed silver nanoparticle inks on paper substrates to achieve highly conductive patterns," *Scientific Reports*, vol. 8, pp. 1–9, dec 2018.

- [81] J. S. Kang, H. S. Kim, J. Ryu, H. Thomas Hahn, S. Jang, and J. W. Joung, "Inkjet printed electronics using copper nanoparticle ink," *Journal of Materials Science: Materials in Electronics*, vol. 21, no. 11, pp. 1213–1220, 2010.
- [82] M. Zenou, O. Ermak, A. Saar, and Z. Kotler, "Laser sintering of copper nanoparticles," *Journal of Physics D: Applied Physics*, vol. 47, p. 025501, jan 2014.
- [83] J. Niittynen, E. Sowade, H. Kang, R. R. Baumann, M. Mäntysalo, M. Mäntysalo, E. Sowade, J. Niittynen, H. Kang, E. Sowade, H. Kang, R. R. Baumann, M. Mäntysalo, M. Mäntysalo, E. Sowade, J. Niittynen, H. Kang, E. Sowade, H. Kang, R. R. Baumann, and M. Mäntysalo, "Comparison of laser and intense pulsed light sintering (IPL) for inkjet-printed copper nanoparticle layers," *Scientific Reports*, vol. 5, p. 8832, mar 2015.
- [84] O. H. Huttunen, T. Happonen, J. Hiitola-Keinänen, P. Korhonen, J. Ollila, and J. Hiltunen, "Roll-To-Roll Screen-Printed Silver Conductors on a Polydimethyl Siloxane Substrate for Stretchable Electronics," *Industrial and Engineering Chemistry Research*, vol. 58, pp. 19909–19916, oct 2019.
- [85] M. Medina-Sánchez, C. Martínez-Domingo, E. Ramon, and A. Merkoçi, "An inkjet-printed field-effect transistor for label-free biosensing," *Advanced Functional Materials*, vol. 24, pp. 6291–6302, oct 2014.
- [86] W. R. Cox, T. Chen, and D. J. Hayes, "Microjet Fabrication of Microlens Arrays," *IEEE Photonics Technology Letters*, vol. 6, no. 9, pp. 1112–1114, 1994.
- [87] A. Voigt, U. Ostrzinski, K. Pfeiffer, J. Y. Kim, V. Fakhfouri, J. Brugger, and G. Gruetznier, "New inks for the direct drop-on-demand fabrication of polymer lenses," *Microelectronic Engineering*, pp. 2174–2179, aug 2011.
- [88] Y. Yang, S. C. Chang, J. Bharathan, and J. Liu, "Organic/polymeric electroluminescent devices processed by hybrid ink-jet printing," *Journal of Materials Science: Materials in Electronics*, vol. 11, no. 2, pp. 89–96, 2000.
- [89] T. R. Hebner, C. C. Wu, D. Marcy, M. H. Lu, and J. C. Sturm, "Ink-jet printing of doped polymers for organic light emitting devices," *Applied Physics Letters*, vol. 72, pp. 519–521, feb 1998.
- [90] V. V. Pokropivny and V. V. Skorokhod, "Classification of nanostructures by dimensionality and concept of surface forms engineering in nanomaterial science," *Materials Science and Engineering C*, vol. 27, pp. 990–993, sep 2007.
- [91] S. V. Kuchibhatla, A. S. Karakoti, D. Bera, and S. Seal, "One dimensional nanostructured materials," *Progress in Materials Science*, vol. 52, pp. 699–913, jul 2007.
- [92] D. Pradhan and K. T. Leung, "Vertical growth of two-dimensional zinc oxide nanostructures on ITO-coated glass: Effects of deposition temperature and deposition time," *Journal of Physical Chemistry C*, vol. 112, pp. 1357–1364, feb 2008.
- [93] Q. Shen, L. Jiang, H. Zhang, Q. Min, W. Hou, and J. J. Zhu, "Three-dimensional dendritic Pt nanostructures: Sonoelectrochemical synthesis and electrochemical applications," *Journal of Physical Chemistry C*, vol. 112, pp. 16385–16392, oct 2008.

- [94] X. Teng, X. Liang, S. Maksimuk, and H. Yang, "Synthesis of porous platinum nanoparticles," *Small*, vol. 2, pp. 249–253, feb 2006.
- [95] H. Lee, S. E. Habas, S. Kveskin, D. Butcher, G. A. Somorjai, and P. Yang, "Morphological control of catalytically active platinum nanocrystals," *Angewandte Chemie - International Edition*, vol. 45, pp. 7824–7828, nov 2006.
- [96] J. N. Tiwari, R. N. Tiwari, and K. S. Kim, "Zero-dimensional, one-dimensional, two-dimensional and three-dimensional nanostructured materials for advanced electrochemical energy devices," *Progress in Materials Science*, vol. 57, pp. 724–803, may 2012.
- [97] D. J. Finn, M. Lotya, and J. N. Coleman, "Inkjet printing of silver nanowire networks," *ACS Applied Materials and Interfaces*, vol. 7, no. 17, pp. 9254–9261, 2015.
- [98] Q. Huang, K. N. Al-Milaji, and H. Zhao, "Inkjet Printing of Silver Nanowires for Stretchable Heaters," *ACS Applied Nano Materials*, vol. 1, no. 9, pp. 4528–4536, 2018.
- [99] T. Rai, P. Dantes, B. Bahreyni, and W. S. Kim, "A stretchable RF antenna with silver nanowires," *IEEE Electron Device Letters*, vol. 34, no. 4, pp. 544–546, 2013.
- [100] T. J. Foley, C. E. Johnson, and K. T. Higa, "Inhibition of oxide formation on aluminum nanoparticles by transition metal coating," *Chemistry of Materials*, vol. 17, pp. 4086–4091, aug 2005.
- [101] D. Li, D. Sutton, A. Burgess, D. Graham, and P. D. Calvert, "Conductive copper and nickel lines via reactive inkjet printing," *Journal of Materials Chemistry*, vol. 19, p. 3719, jun 2009.
- [102] P. J. Wojcik, L. Santos, L. Pereira, R. Martins, and E. Fortunato, "Tailoring nanoscale properties of tungsten oxide for inkjet printed electrochromic devices," *Nanoscale*, vol. 7, pp. 1696–1708, feb 2015.
- [103] C. Costa, C. Pinheiro, I. Henriques, and C. A. Laia, "Inkjet printing of sol-gel synthesized hydrated tungsten oxide nanoparticles for flexible electrochromic devices," *ACS Applied Materials and Interfaces*, vol. 4, pp. 1330–1340, mar 2012.
- [104] Y. N. Liang, B. K. Lok, L. Wang, C. Feng, A. C. W. Lu, T. Mei, and X. Hu, "Effects of the morphology of inkjet printed zinc oxide (ZnO) on thin film transistor performance and seeded ZnO nanorod growth," in *Thin Solid Films*, vol. 544, pp. 509–514, Elsevier B.V., oct 2013.
- [105] S. Sharma, S. S. Pande, and P. Swaminathan, "Top-down synthesis of zinc oxide based inks for inkjet printing," *RSC Advances*, vol. 7, pp. 39411–39419, aug 2017.
- [106] K. Sun, S. Zhang, P. Li, Y. Xia, X. Zhang, D. Du, F. H. Isikgor, and J. Ouyang, "Review on application of PEDOTs and PEDOT:PSS in energy conversion and storage devices," jul 2015.

- [107] A. K. Sarker, J. Kim, B. H. Wee, H. J. Song, Y. Lee, J. D. Hong, and C. Lee, "Hydroiodic acid treated PEDOT:PSS thin film as transparent electrode: an approach towards ITO free organic photovoltaics," *RSC Advances*, vol. 5, pp. 52019–52025, jun 2015.
- [108] U. Lang, N. Naujoks, and J. Dual, "Mechanical characterization of PEDOT:PSS thin films," *Synthetic Metals*, vol. 159, pp. 473–479, mar 2009.
- [109] X. Fan, W. Nie, H. Tsai, N. Wang, H. Huang, Y. Cheng, R. Wen, L. Ma, F. Yan, and Y. Xia, "PEDOT:PSS for Flexible and Stretchable Electronics: Modifications, Strategies, and Applications," oct 2019.
- [110] W. F. Quirós-Solano, N. Gaio, C. Silvestri, G. Pandraud, and P. M. Sarro, "PEDOT:PSS: A conductive and flexible polymer for sensor integration in organ-on-chip platforms," in *Procedia Engineering*, vol. 168, pp. 1184–1187, Elsevier Ltd, 2016.
- [111] G. Cummins and M. P. Desmulliez, "Inkjet printing of conductive materials: A review," *Circuit World*, vol. 38, pp. 193–213, nov 2012.
- [112] M. F. Mabrook, C. Pearson, and M. C. Petty, "Inkjet-printed polypyrrole thin films for vapour sensing," *Sensors and Actuators, B: Chemical*, vol. 115, pp. 547–551, may 2006.
- [113] D. D. Ateh, H. A. Navsaria, and P. Vadgama, "Polypyrrole-based conducting polymers and interactions with biological tissues," 2006.
- [114] Y. M. Lin, C. Dimitrakopoulos, K. A. Jenkins, D. B. Farmer, H. Y. Chiu, A. Grill, and P. Avouris, "100-GHz transistors from wafer-scale epitaxial graphene," feb 2010.
- [115] J. A. Desai, S. Chugh, M. Michel, and A. B. Kaul, "Inkjet printed graphene as an interconnect for optoelectronic devices," *Journal of Materials Science: Materials in Electronics*, vol. 30, pp. 12500–12509, jul 2019.
- [116] L. Huang, Y. Huang, J. Liang, X. Wan, and Y. Chen, "Graphene-based conducting inks for direct inkjet printing of flexible conductive patterns and their applications in electric circuits and chemical sensors," *Nano Research*, vol. 4, no. 7, pp. 675–684, 2011.
- [117] J. Li, M. C. Lemme, and M. Östling, "Inkjet printing of 2D layered materials," *ChemPhysChem*, vol. 15, pp. 3427–3434, nov 2014.
- [118] F. Torrasi, T. Hasan, W. Wu, Z. Sun, A. Lombardo, T. S. Kulmala, G. W. Hsieh, S. Jung, F. Bonaccorso, P. J. Paul, D. Chu, and A. C. Ferrari, "Inkjet-printed graphene electronics," *ACS Nano*, vol. 6, no. 4, pp. 2992–3006, 2012.
- [119] T. Vuorinen, J. Niittynen, T. Kankkunen, T. M. Kraft, and M. Mäntysalo, "Inkjet-printed graphene/PEDOT:PSS temperature sensors on a skin-conformable polyurethane substrate," *Scientific Reports*, vol. 6, oct 2016.
- [120] M. Baklar, P. H. Wöbkenberg, D. Sparrowe, M. Goncalves, I. McCulloch, M. Heeney, T. Anthopoulos, and N. Stingelin, "Ink-jet printed p-type polymer electronics based on liquid-crystalline polymer semiconductors," *Journal of Materials Chemistry*, vol. 20, pp. 1927–1931, feb 2010.

- [121] S. K. Park, J. E. Anthony, and T. N. Jackson, "Solution-processed TIPS-pentacene organic thin-film-transistor circuits," *IEEE Electron Device Letters*, vol. 28, pp. 877–879, oct 2007.
- [122] S. H. Eom, H. Park, S. H. Mujawar, S. C. Yoon, S. S. Kim, S. I. Na, S. J. Kang, D. Khim, D. Y. Kim, and S. H. Lee, "High efficiency polymer solar cells via sequential inkjet-printing of PEDOT:PSS and P3HT:PCBM inks with additives," *Organic Electronics*, vol. 11, pp. 1516–1522, sep 2010.
- [123] D. Kim, S. Jeong, S. H. Lee, J. Moon, and J. K. Song, "Ink-jet printing of organic semiconductor for fabricating organic thin-film transistors: Film uniformity control by ink composition," *Synthetic Metals*, vol. 159, pp. 1381–1385, jul 2009.
- [124] C. Linghu, S. Zhang, C. Wang, and J. Song, "Transfer printing techniques for flexible and stretchable inorganic electronics," *npj Flexible Electronics*, vol. 2, p. 26, dec 2018.
- [125] A. B. Phillips, R. R. Khanal, Z. Song, R. M. Zartman, J. L. DeWitt, J. M. Stone, P. J. Roland, V. V. Plotnikov, C. W. Carter, J. M. Stayancho, R. J. Ellingson, A. D. Compaan, and M. J. Heben, "Wiring-up carbon single wall nanotubes to polycrystalline inorganic semiconductor thin films: Low-barrier, copper-free back contact to CdTe solar cells," *Nano Letters*, vol. 13, pp. 5224–5232, nov 2013.
- [126] G. Zhang, M. Zhang, X. Ye, X. Qiu, S. Lin, and X. Wang, "Iodine modified carbon nitride semiconductors as visible light photocatalysts for hydrogen evolution," *Advanced Materials*, vol. 26, pp. 805–809, feb 2014.
- [127] S. Dasgupta, R. Kruk, N. Mechau, and H. Hahn, "Inkjet printed, high mobility inorganic-oxide field effect transistors processed at room temperature," *ACS Nano*, vol. 5, pp. 9628–9638, dec 2011.
- [128] C. L. Fan, M. C. Shang, M. Y. Hsia, S. J. Wang, B. R. Huang, and W. D. Lee, "Poly(4-vinylphenol) gate insulator with cross-linking using a rapid low-power microwave induction heating scheme for organic thin-film-transistors," *APL Materials*, vol. 4, no. 3, p. 36105, 2016.
- [129] S. H. Ko, J. Chung, H. Pan, C. P. Grigoropoulos, and D. Poulikakos, "Fabrication of multilayer passive and active electric components on polymer using inkjet printing and low temperature laser processing," *Sensors and Actuators, A: Physical*, vol. 134, pp. 161–168, feb 2007.
- [130] S. J. Kim, M. Jang, H. Y. Yang, J. Cho, H. S. Lim, H. Yang, and J. A. Lim, "Instantaneous Pulsed-Light Cross-Linking of a Polymer Gate Dielectric for Flexible Organic Thin-Film Transistors," *ACS Applied Materials and Interfaces*, vol. 9, pp. 11721–11731, apr 2017.
- [131] C. L. Cho, H. ling Kao, Y. H. Wu, L. C. Chang, and C. H. Cheng, "Direct Fabrication of Inkjet-Printed Dielectric Film for Metal–Insulator–Metal Capacitors," *Journal of Electronic Materials*, vol. 47, pp. 677–683, jan 2018.
- [132] C. Mariotti, B. S. Cook, L. Roselli, and M. M. Tentzeris, "State-of-the-art inkjet-printed metal-insulator-metal (MIM) capacitors on silicon substrate," *IEEE Microwave and Wireless Components Letters*, vol. 25, pp. 13–15, jan 2015.

- [133] V. Sanchez-Romaguera, M. B. Madec, and S. G. Yeates, "Inkjet printing of 3D metal-insulator-metal crossovers," *Reactive and Functional Polymers*, vol. 68, pp. 1052–1058, jun 2008.
- [134] J. Wu, R. Wang, H. Yu, G. Li, K. Xu, N. C. Tien, R. C. Roberts, and D. Li, "Inkjet-printed microelectrodes on PDMS as biosensors for functionalized microfluidic systems," *Lab on a Chip*, vol. 15, pp. 690–695, feb 2015.
- [135] J. Jiang, B. Bao, M. Li, J. Sun, C. Zhang, Y. Li, F. Li, X. Yao, and Y. Song, "Fabrication of Transparent Multilayer Circuits by Inkjet Printing," *Advanced Materials*, vol. 28, no. 7, pp. 1420–1426, 2016.
- [136] M. T. Inc., "Microdispensing."
- [137] J. Fukai, Z. Zhao, D. Poulikakos, C. M. Megaridis, and O. Miyatake, "Modeling of the deformation of a liquid droplet impinging upon a flat surface," *Physics of Fluids A: Fluid Dynamics*, vol. 5, pp. 2588–2599, nov 1993.
- [138] J. E. Fromm, "Numerical Calculation of the Fluid Dynamics of Drop-on-Demand Jets," *IBM Journal of Research and Development*, vol. 28, pp. 322–333, may 1984.
- [139] B.-J. de Gans and U. S. Schubert, "Inkjet Printing of Well-Defined Polymer Dots and Arrays," *Langmuir*, vol. 20, pp. 7789–7793, aug 2004.
- [140] N. Reis and B. Derby, "Ink Jet Deposition of Ceramic Suspensions: Modeling and Experiments of Droplet Formation," *MRS Proceedings*, vol. 625, p. 117, jan 2000.
- [141] P. C. Duineveld, M. M. de Kok, M. Buechel, A. Sempel, K. A. H. Mutsaers, P. van de Weijer, I. G. J. Camps, T. van de Biggelaar, J.-E. J. M. Rubingh, and E. I. Haskal, "Ink-jet printing of polymer light-emitting devices," in *International Symposium on Optical Science and Technology* (Z. H. Kafafi, ed.), vol. 4464, p. 59, International Society for Optics and Photonics, feb 2002.
- [142] C. D. Stow and M. G. Hadfield, "An Experimental Investigation of Fluid Flow Resulting from the Impact of a Water Drop with an Unyielding Dry Surface," *Proceedings of the Royal Society A: Mathematical, Physical and Engineering Sciences*, vol. 373, pp. 419–441, jan 1981.
- [143] K. Range and F. Feuillebois, "Influence of surface roughness on liquid drop impact," *Journal of Colloid and Interface Science*, vol. 203, pp. 16–30, jul 1998.
- [144] A. Yarin, "Drop impact dynamics: Splashing, spreading, receding, bouncing," *Annual Review of Fluid Mechanics*, vol. 38, pp. 159–192, jan 2006.
- [145] L. Xu, "Liquid drop splashing on smooth, rough, and textured surfaces," *Physical Review E - Statistical, Nonlinear, and Soft Matter Physics*, vol. 75, p. 056316, may 2007.
- [146] L. Xu, W. W. Zhang, and S. R. Nagel, "Drop splashing on a dry smooth surface," *Physical Review Letters*, vol. 94, p. 184505, may 2005.

- [147] R. Bhola and S. Chandra, "Parameters controlling solidification of molten wax droplets falling on a solid surface," *Journal of Materials Science*, vol. 34, no. 19, pp. 4883–4894, 1999.
- [148] B. Derby, "Additive Manufacture of Ceramics Components by Inkjet Printing," *Engineering*, vol. 1, pp. 113–123, mar 2015.
- [149] J. P. Dear and J. E. Field, "High-speed photography of surface geometry effects in liquid/solid impact," *Journal of Applied Physics*, vol. 63, pp. 1015–1021, feb 1988.
- [150] M. B. Lesser and J. E. Field, "Impact of Compressible Liquids.," *Annual Review of Fluid Mechanics*, vol. 15, pp. 97–122, jan 1983.
- [151] Z. Levin and P. V. Hobbs, "Splashing of Water Drops on Solid and Wetted Surfaces: Hydrodynamics and Charge Separation," *Philosophical Transactions of the Royal Society A: Mathematical, Physical and Engineering Sciences*, vol. 269, pp. 555–585, may 1971.
- [152] L. Cheng, "Dynamic Spreading of Drops Impacting onto a Solid Surface," *Industrial & Engineering Chemistry Process Design and Development*, vol. 16, pp. 192–197, apr 1977.
- [153] T. Young, "An Essay on the Cohesion of Fluids," *Philosophical Transactions of the Royal Society of London*, vol. 95, pp. 65–87, jan 1805.
- [154] R. D. Deegan, O. Bakajin, T. F. Dupont, G. Huber, S. R. Nagel, and T. A. Witten, "Capillary flow as the cause of ring stains from dried liquid drops," *Nature*, vol. 389, pp. 827–829, oct 1997.
- [155] H. Hu, R. G. Larson, , . Hua Hu\*, and R. G. Larson, "Marangoni effect reverses coffee-ring depositions," *Journal of Physical Chemistry B*, vol. 110, no. 14, pp. 7090–7094, 2006.
- [156] B.-J. de Gans and U. S. Schubert, "Inkjet Printing of Well-Defined Polymer Dots and Arrays," *Langmuir*, vol. 20, pp. 7789–7793, aug 2004.
- [157] R. M. German, "History of sintering: Empirical phase," *Powder Metallurgy*, vol. 56, pp. 117–123, apr 2013.
- [158] P. Buffat and J. P. Borel, "Size effect on the melting temperature of gold particles," *Physical Review A*, vol. 13, no. 6, pp. 2287–2298, 1976.
- [159] R. Garrigos, P. Cheyssac, and R. Kofman, "Melting for lead particles of very small sizes; influence of surface phenomena," *Zeitschrift für Physik D Atoms, Molecules and Clusters*, vol. 12, pp. 497–500, mar 1989.
- [160] G. L. Allen, R. A. Bayles, W. W. Gile, and W. A. Jesser, "Small particle melting of pure metals," *Thin Solid Films*, vol. 144, pp. 297–308, nov 1986.
- [161] P. W. Voorhees, "The theory of Ostwald ripening," *Journal of Statistical Physics*, vol. 38, pp. 231–252, jan 1985.

- [162] A. K. Datye, Q. Xu, K. C. Kharas, and J. M. McCarty, "Particle size distributions in heterogeneous catalysts: What do they tell us about the sintering mechanism?," in *Catalysis Today*, vol. 111, pp. 59–67, Elsevier, jan 2006.
- [163] J. R. Greer and R. A. Street, "Thermal cure effects on electrical performance of nanoparticle silver inks," *Acta Materialia*, vol. 55, pp. 6345–6349, oct 2007.
- [164] S. Singh, D. Gupta, V. Jain, and A. K. Sharma, "Microwave processing of materials and applications in manufacturing industries: A Review," jan 2015.
- [165] D. Agrawal, "Microwave sintering of ceramics, composites and metallic materials, and melting of glasses," *Transactions of the Indian Ceramic Society*, vol. 65, no. 3, pp. 129–144, 2006.
- [166] J. Perelaer and U. S. Schubert, "Novel approaches for low temperature sintering of inkjet-printed inorganic nanoparticles for roll-to-roll (R2R) applications," *Journal of Materials Research*, vol. 28, no. 4, pp. 564–573, 2013.
- [167] P. Mishra, G. Sethi, and A. Upadhyaya, "Modeling of microwave heating of particulate metals," *Metallurgical and Materials Transactions B: Process Metallurgy and Materials Processing Science*, vol. 37, pp. 839–845, oct 2006.
- [168] J. Perelaer, R. Abbel, S. Wünscher, R. Jani, T. Van Lammeren, and U. S. Schubert, "Roll-to-roll compatible sintering of inkjet printed features by photonic and microwave exposure: From non-conductive ink to 40% bulk silver conductivity in less than 15 seconds," *Advanced Materials*, vol. 24, no. 19, pp. 2620–2625, 2012.
- [169] K. S. Kim, B. G. Park, K. H. Jung, J. W. Kim, M. Y. Jeong, and S. B. Jung, "Microwave sintering of silver nanoink for radio frequency applications," *Journal of Nanoscience and Nanotechnology*, vol. 15, pp. 2333–2337, mar 2015.
- [170] J. J. Valetton, K. Hermans, C. W. Bastiaansen, D. J. Broer, J. Perelaer, U. S. Schubert, G. P. Crawford, and P. J. Smith, "Room temperature preparation of conductive silver features using spin-coating and inkjet printing," *Journal of Materials Chemistry*, vol. 20, no. 3, pp. 543–546, 2010.
- [171] Z. Hui, Y. Liu, W. Guo, L. Li, N. Mu, C. Jin, Y. Zhu, and P. Peng, "Chemical sintering of direct-written silver nanowire flexible electrodes under room temperature," *Nanotechnology*, vol. 28, jun 2017.
- [172] S. Magdassi, M. Grouchko, O. Berezin, and A. Kamyshny, "Triggering the sintering of silver nanoparticles at room temperature," *ACS Nano*, vol. 4, pp. 1943–1948, apr 2010.
- [173] A. T. Alastalo, H. Seppä, J. H. Leppäniemi, M. J. Aronniemi, M. L. Allen, and T. Mattila, "Modelling of nanoparticle sintering under electrical boundary conditions," *Journal of Physics D: Applied Physics*, vol. 43, p. 485501, dec 2010.
- [174] S. Jang, D. J. Lee, D. Lee, and J. H. Oh, "Electrical sintering characteristics of inkjet-printed conductive Ag lines on a paper substrate," *Thin Solid Films*, vol. 546, pp. 157–161, nov 2013.

- [175] H. Lee, D. Kim, I. Lee, Y. J. Moon, J. Y. Hwang, K. Park, and S. J. Moon, "Stepwise current electrical sintering method for inkjet-printed conductive ink," *Japanese Journal of Applied Physics*, vol. 53, pp. 5–07, apr 2014.
- [176] C. Werner, D. Godlinski, V. Zöllmer, and M. Busse, "Morphological influences on the electrical sintering process of Aerosol Jet and Ink Jet printed silver microstructures," *Journal of Materials Science: Materials in Electronics*, vol. 24, no. 11, pp. 4367–4377, 2013.
- [177] I. Reinhold, C. E. Hendriks, R. Eckardt, J. M. Kranenburg, J. Perelaer, R. R. Baumann, and U. S. Schubert, "Argon plasma sintering of inkjet printed silver tracks on polymer substrates," *Journal of Materials Chemistry*, vol. 19, pp. 3384–3388, may 2009.
- [178] F. M. Wolf, J. Perelaer, S. Stumpf, D. Bollen, F. Kriebel, and U. S. Schubert, "Rapid low-pressure plasma sintering of inkjet-printed silver nanoparticles for RFID antennas," *Journal of Materials Research*, vol. 28, pp. 1254–1261, apr 2013.
- [179] S. Wünscher, S. Stumpf, A. Teichler, O. Pabst, J. Perelaer, E. Beckert, and U. S. Schubert, "Localized atmospheric plasma sintering of inkjet printed silver nanoparticles," *Journal of Materials Chemistry*, vol. 22, pp. 24569–24576, dec 2012.
- [180] S. Wünscher, S. Stumpf, J. Perelaer, and U. S. Schubert, "Towards single-pass plasma sintering: Temperature influence of atmospheric pressure plasma sintering of silver nanoparticle ink," *Journal of Materials Chemistry C*, vol. 2, pp. 1642–1649, mar 2014.
- [181] J. Niittynen, R. Abbel, M. Mäntysalo, J. Perelaer, U. S. Schubert, and D. Lupo, "Alternative sintering methods compared to conventional thermal sintering for inkjet printed silver nanoparticle ink," *Thin Solid Films*, vol. 556, pp. 452–459, apr 2014.
- [182] M. Yu, S. Grasso, R. Mckinnon, T. Saunders, and M. J. Reece, "Review of flash sintering: materials, mechanisms and modelling," *Advances in Applied Ceramics*, vol. 116, pp. 24–60, jan 2017.
- [183] S. H. Park, S. Jang, D. J. Lee, J. Oh, and H. S. Kim, "Two-step flash light sintering process for crack-free inkjet-printed Ag films," *Journal of Micromechanics and Microengineering*, vol. 23, p. 015013, jan 2013.
- [184] J. Ryu, H.-S. Kim, and H. T. Hahn, "Reactive sintering of copper nanoparticles using intense pulsed light for printed electronics," *Journal of Electronic Materials*, vol. 40, pp. 42–50, jan 2011.
- [185] H.-S. S. Kim, S. R. Dhage, D.-E. E. Shim, and H. T. Hahn, "Intense pulsed light sintering of copper nanoink for printed electronics," *Applied Physics A: Materials Science and Processing*, vol. 97, pp. 791–798, dec 2009.
- [186] H. J. Chan, B. C. Huang, L. W. Wang, K. H. Liao, and C. Y. Lo, "Porosity reduction in inkjet-printed copper film by progressive sintering on nanoparticles," *Thin Solid Films*, vol. 627, pp. 33–38, 2017.
- [187] Y. H. Son, J. Y. Jang, M. K. Kang, S. Ahn, and C. S. Lee, "Application of flash-light sintering method to flexible inkjet printing using anti-oxidant copper nanoparticles," *Thin Solid Films*, vol. 656, pp. 61–67, jun 2018.

- [188] K. Shimoda, *Introduction to laser physics*. Springer-Verlag, 2nd ed. ed., 1986.
- [189] F. Mafuné, J. Y. Kohno, Y. Takeda, T. Kondow, and H. Sawabe, “Formation and size control of silver nanoparticles by laser ablation in aqueous solution,” *Journal of Physical Chemistry B*, vol. 104, pp. 9111–9117, oct 2000.
- [190] F. Mafuné, J. Y. Kohno, Y. Takeda, T. Kondow, and H. Sawabe, “Structure and stability of silver nanoparticles in aqueous solution produced by laser ablation,” *Journal of Physical Chemistry B*, vol. 104, pp. 8336–8337, sep 2000.
- [191] A. V. Kabashin and M. Meunier, “Synthesis of colloidal nanoparticles during femtosecond laser ablation of gold in water,” *Journal of Applied Physics*, vol. 94, no. 12, pp. 7941–7943, 2003.
- [192] V. D. Ta, A. Dunn, T. J. Wasley, J. Li, R. W. Kay, J. Stringer, P. J. Smith, E. Esenturk, C. Connaughton, and J. D. Shephard, “Laser textured surface gradients,” *Applied Surface Science*, vol. 371, pp. 583–589, 2016.
- [193] E. G. Gamaly, A. V. Rode, B. Luther-Davies, and V. T. Tikhonchuk, “Ablation of solids by femtosecond lasers: Ablation mechanism and ablation thresholds for metals and dielectrics,” *Physics of Plasmas*, vol. 9, p. 949, mar 2002.
- [194] M. D. Shirk and P. A. Molian, “A review of ultrashort pulsed laser ablation of materials,” *Journal of Laser Applications*, vol. 10, pp. 18–28, feb 1998.
- [195] H. Horn, S. Beil, D. A. Wesner, R. Weichenhain, and E. W. Kreutz, “Excimer laser pretreatment and metallization of polymers,” *Nuclear Instruments and Methods in Physics Research, Section B: Beam Interactions with Materials and Atoms*, vol. 151, pp. 279–284, may 1999.
- [196] A. A. Serafetinides, M. I. Makropoulou, C. D. Skordoulis, and A. K. Kar, “Ultra-short pulsed laser ablation of polymers,” *Applied Surface Science*, vol. 180, pp. 42–56, aug 2001.
- [197] S. Y. Ji, C. M. Ajmal, T. Kim, W. S. Chang, and S. Baik, “Laser patterning of highly conductive flexible circuits,” *Nanotechnology*, vol. 28, p. 165301, apr 2017.
- [198] P. Zhao, J. Huang, J. Nan, D. Liu, and F. Meng, “Laser sintering process optimization of microstrip antenna fabricated by inkjet printing with silver-based MOD ink,” *Journal of Materials Processing Technology*, vol. 275, p. 116347, jan 2020.
- [199] C. El Hajjaji, N. Delhote, S. Verdeyme, M. Piechowiak, L. Boyer, and O. Durand, “Optimization of the conductivity of microwave components printed by inkjet and aerosol jet on polymeric substrates by IPL and laser sintering,” *International Journal of Microwave and Wireless Technologies*, pp. 1–11, 2021.
- [200] M. Joo, B. Lee, S. Jeong, and M. Lee, “Laser sintering of Cu paste film printed on polyimide substrate,” *Applied Surface Science*, vol. 258, pp. 521–524, oct 2011.
- [201] E. Halonen, E. Heinonen, and M. Mäntysalo, “The Effect of Laser Sintering Process Parameters on Cu Nanoparticle Ink in Room Conditions,” *Optics and Photonics Journal*, vol. 03, no. 04, pp. 40–44, 2013.

- [202] M. K. Rahman, Z. Lu, and K. S. Kwon, "Green laser sintering of copper oxide (CuO) nano particle (NP) film to form Cu conductive lines," *AIP Advances*, vol. 8, p. 95008, sep 2018.
- [203] J. C. Hernandez-Castaneda, B. K. Lok, and H. Zheng, "Laser sintering of Cu nanoparticles on PET polymer substrate for printed electronics at different wavelengths and process conditions," *Frontiers of Mechanical Engineering*, vol. 15, pp. 303–318, jun 2020.
- [204] Edmund Optics, "The Correct Material for Infrared (IR) Applications," no. Figure 4, pp. 1–7, 2016.
- [205] S. F. Ray, "Optical materials," in *Applied Photographic Optics*, pp. 99–111, 2019.
- [206] C. T. Yen and W. C. Chen, "Effects of molecular structures on the near-infrared optical properties of polyimide derivatives and their corresponding optical waveguides," *Macromolecules*, vol. 36, no. 9, pp. 3315–3319, 2003.
- [207] K. Han, K. You, W. H. Jang, and T. H. Rhee, "Synthesis and properties of chlorinated polyimides," *Macromolecular Chemistry and Physics*, vol. 201, no. 6, pp. 747–751, 2000.
- [208] A. A. Serkov, H. V. Snelling, S. Heusing, and T. M. Amaral, "Laser sintering of gravure printed indium tin oxide films on polyethylene terephthalate for flexible electronics," *Scientific Reports*, vol. 9, no. 1, 2019.
- [209] J. Luo, W. Deng, F. Yang, Z. Wu, M. Huang, and M. Gu, "Gold nanoparticles decorated graphene oxide/nanocellulose paper for NIR laser-induced photothermal ablation of pathogenic bacteria," *Carbohydrate Polymers*, vol. 198, pp. 206–214, oct 2018.
- [210] A. Basch, T. Wasserman, and M. Lewin, "Near-Infrared Spectrum of Cellulose: a New Method for Obtaining Crystallinity Ratios.," *J Polym Sci Part A-1 Polym Chem*, vol. 12, no. 6, pp. 1143–1150, 1974.
- [211] L. J. Walker SB, Ahn BY, "Reactive Silver Inks for High-performance Printed Electronics," *Sigma Aldrich Technical Documents*, 2015.
- [212] D. B. Bogy and F. E. Talke, "Experimental and Theoretical Study of Wave Propagation Phenomena in Drop-on-Demand Ink Jet Devices," *IBM Journal of Research and Development*, vol. 28, pp. 314–321, may 1984.
- [213] N. Reis, C. Ainsley, and B. Derby, "Ink-jet delivery of particle suspensions by piezoelectric droplet ejectors," *Journal of Applied Physics*, vol. 97, p. 094903, may 2005.
- [214] J. Eggers, "Nonlinear dynamics and breakup of free-surface flows," *Reviews of Modern Physics*, vol. 69, pp. 865–930, jul 1997.
- [215] H.-C. Wu, T.-R. Shan, W.-S. Hwang, and H.-J. Lin, "Study of Micro-Droplet Behavior for a Piezoelectric Inkjet Printing Device Using a Single Pulse Voltage Pattern," *Materials Transactions*, vol. 45, no. 5, pp. 1794–1801, 2004.

- [216] H. Wijshoff, "Drop formation mechanisms in piezo-acoustic inkjet," *Technical Proceedings of the 2007 NSTI Nanotechnology Conference and Trade Show*, vol. 31, pp. 732–735, 2007.
- [217] W. T. Pimbley and H. C. Lee, "Satellite Droplet Formation in a Liquid Jet," *IBM Journal of Research and Development*, vol. 21, pp. 21–30, jan 1977.
- [218] D. Soltman and V. Subramanian, "Inkjet-printed line morphologies and temperature control of the coffee ring effect," *Langmuir*, vol. 24, no. 5, pp. 2224–2231, 2008.
- [219] L. Jacot-Descombes, M. R. Gullo, V. J. Cadarso, M. Mastrangeli, O. Ergeneman, C. Peters, P. Fatio, M. A. Freidy, C. Hierold, B. J. Nelson, and J. Brugger, "Inkjet printing of high aspect ratio superparamagnetic SU-8 microstructures with preferential magnetic directions," *Micromachines*, vol. 5, pp. 583–593, aug 2014.
- [220] ASTM Standards, "Standard Test Method for Determining Ink or Coating Adhesion on Flexible Substrates for a Membrane Switch or Printed Electronic Device," Tech. Rep. F1842 - 15, ASTM, 2015.
- [221] A. International, "Standard Test Methods for Measuring Adhesion by Tape Test," Tech. Rep. December 2007, 2013.
- [222] I. O. for Standardization, "Cross-cut test ISO 2409:2007," *The British Standards Institutions*, vol. 3, pp. 9–11, 2013.
- [223] P. Lukacs, A. Pietrikova, and O. Kovac, "Improvement of the evaluation of inkjet printed silver based layers' adhesion," *Journal of Adhesion Science and Technology*, vol. 33, no. 2, pp. 124–136, 2019.
- [224] T. Ridler and S. Calvard, "Picture Thresholding Using," *IEEE Transactions on Systems, Man and Cybernetics*, vol. smc-8, no. 8, pp. 630–632, 1978.
- [225] A. L. Dearden, P. J. Smith, D. Y. Shin, N. Reis, B. Derby, and P. O'Brien, "A low curing temperature silver ink for use in ink-jet printing and subsequent production of conductive tracks," *Macromolecular Rapid Communications*, vol. 26, no. 4, pp. 315–318, 2005.
- [226] D. Mitra, K. Y. Mitra, M. Hartwig, and R. R. Baumann, "Intense pulsed light dithering of an inkjet printed silver nanoparticle ink depending on the spectral absorption and reflection of the background," in *Printing for Fabrication 2016 (NIP32)*, 2016.
- [227] J. F. Ready, "Effects due to absorption of laser radiation," *Journal of Applied Physics*, vol. 36, pp. 462–468, feb 1965.
- [228] A. Henglein, "Formation and absorption spectrum of copper nanoparticles from the radiolytic reduction of  $\text{Cu}(\text{CN})_2^-$ ," *Journal of Physical Chemistry B*, vol. 104, pp. 1206–1211, feb 2000.
- [229] D. Deng, S. Feng, M. Shi, and C. Huang, "In situ preparation of silver nanoparticles decorated graphene conductive ink for inkjet printing," *Journal of Materials Science: Materials in Electronics*, vol. 28, no. 20, pp. 15411–15417, 2017.

- [230] M. K. Mohammed, U. Umer, O. Abdulhameed, and H. Alkhalefah, "Effects of laser fluence and pulse overlap on machining of microchannels in alumina ceramics using an Nd: YAG laser," *Applied Sciences (Switzerland)*, vol. 9, no. 19, pp. 1–14, 2019.
- [231] D. Guo, G. Xie, and J. Luo, "Mechanical properties of nanoparticles: Basics and applications," *Journal of Physics D: Applied Physics*, vol. 47, no. 1, 2014.
- [232] S. C. Park, S. H. Cho, H. C. Jung, J. W. Joung, and Y. B. Park, "A study on improvement of interfacial adhesion energy of inkjet-printed Ag thin film on polyimide by CF4 plasma treatment," *Korean Journal of Materials Research*, vol. 17, no. 4, pp. 215–221, 2007.
- [233] S. Joo and D. F. Baldwin, "Interfacial adhesion of nano-particle silver interconnects for electronics packaging application," in *Proceedings - Electronic Components and Technology Conference*, pp. 1417–1423, IEEE, 2008.
- [234] M. P. Larsson and M. M. Ahmad, "Improved polymer-glass adhesion through micro-mechanical interlocking," *Journal of Micromechanics and Microengineering*, vol. 16, no. 6, pp. 161–168, 2006.
- [235] S. Joo and D. F. Baldwin, "Adhesion mechanisms of nanoparticle silver to substrate materials: Identification," *Nanotechnology*, vol. 21, no. 5, 2010.
- [236] P. S. Ho, P. O. Hahn, J. W. Bartha, G. W. Rubloff, F. K. LeGoues, and B. D. Silverman, "Chemical bonding and reaction at metal/polymer interfaces," *Journal of Vacuum Science & Technology A: Vacuum, Surfaces, and Films*, vol. 3, pp. 739–745, may 1985.
- [237] C. Ochoa-Putman and U. K. Vaidya, "Mechanisms of interfacial adhesion in metal-polymer composites - Effect of chemical treatment," *Composites Part A: Applied Science and Manufacturing*, vol. 42, pp. 906–915, aug 2011.
- [238] M. Zenou, O. Ermak, A. Saar, and Z. Kotler, "Laser sintering of copper nanoparticles," *Journal of Physics D: Applied Physics*, vol. 47, p. 025501, jan 2014.
- [239] E. Halonen, S. Koskinen, I. Leino, P. Heljo, and M. Mäntysalo, "Sintering of inkjet-printed Cu-nanoparticle ink in ambient conditions using a continuous wave 808 nm diode laser," in *Materials Research Society Symposium Proceedings*, vol. 1529, pp. 45–50, Cambridge University Press, feb 2012.
- [240] J. Mei, M. R. Lovell, and M. H. Mickle, "Formulation and processing of novel conductive solution inks in continuous inkjet printing of 3-D electric circuits," *IEEE Transactions on Electronics Packaging Manufacturing*, vol. 28, no. 3, pp. 265–273, 2005.
- [241] E. Halonen, V. Pynttäre, J. Lilja, H. Sillanpää, M. Mäntysalo, J. Heikkinen, R. Mäkinen, T. Kaija, and P. Salonen, "Environmental protection of inkjet-printed Ag conductors," *Microelectronic Engineering*, vol. 88, pp. 2970–2976, sep 2011.
- [242] K. L. Mittal, "Adhesion Measurement of Thin Films," *ElectroComponent Science and Technology*, vol. 3, no. 1, pp. 21–42, 1976.

- [243] R. A. Bowling, "An Analysis of Particle Adhesion on Semiconductor Surfaces," *Journal of The Electrochemical Society*, vol. 132, p. 2208, sep 2006.
- [244] W. W. Gerberich and M. J. Cordill, "Physics of adhesion," *Reports on Progress in Physics*, vol. 69, no. 7, pp. 2157–2203, 2006.
- [245] D. B. Marshall and A. G. Evans, "Measurement of adherence of residually stressed thin films by indentation. I. Mechanics of interface delamination," *Journal of Applied Physics*, vol. 56, no. 10, pp. 2632–2638, 1984.
- [246] C. S. Litteken and R. H. Dauskardt, "Adhesion of polymer thin-films and patterned lines," *International Journal of Fracture*, vol. 120, no. 1-2, pp. 475–485, 2003.
- [247] R. P. Birringer, P. J. Chidester, and R. H. Dauskardt, "High yield four-point bend thin film adhesion testing techniques," *Engineering Fracture Mechanics*, vol. 78, pp. 2390–2398, aug 2011.
- [248] S. R. Dupont, M. Oliver, F. C. Krebs, and R. H. Dauskardt, "Interlayer adhesion in roll-to-roll processed flexible inverted polymer solar cells," in *Solar Energy Materials and Solar Cells*, vol. 97, pp. 171–175, North-Holland, feb 2012.
- [249] S. R. Dupont, E. Voroshazi, P. Heremans, and R. H. Dauskardt, "Adhesion properties of inverted polymer solarcells: Processing and film structure parameters," *Organic Electronics*, vol. 14, pp. 1262–1270, may 2013.
- [250] A. Sridhar, D. J. van Dijk, and R. Akkerman, "Inkjet printing and adhesion characterisation of conductive tracks on a commercial printed circuit board material," *Thin Solid Films*, vol. 517, pp. 4633–4637, jun 2009.
- [251] U. Caglar, K. Kaija, and P. Mansikkamaki, "Analysis of mechanical performance of silver inkjet-printed structures," in *2008 2nd IEEE International Nanoelectronics Conference*, pp. 851–856, IEEE, 2008.
- [252] J. Schirmer, J. Roudenko, M. Reichenberger, S. Neermann, and J. Franke, "Adhesion Measurements for Printed Electronics: A Novel Approach to Cross Cut Testing," *Proceedings of the International Spring Seminar on Electronics Technology*, vol. 2018-May, pp. 1–5, 2018.
- [253] D. Materials, "DM-CUP-5080 - Dycotec Materials."
- [254] D. Materials, "DM-SIJ-3200 - Dycotec Materials."
- [255] D. Materials, "DM-INI-7003 - Dycotec Materials."
- [256] Sigma-Aldrich, "Copper inkjet ink | Sigma-Aldrich."
- [257] Sigma-Aldrich, "SunTronic® conductive silver ink for screen printing."
- [258] Sigma-Aldrich, "Reactive Silver Inks for High-Performance Printed Electronics."
- [259] D. Group, "Durst Ink Systems."

- [260] Y. Hirayama and M. Obara, "Heat-affected zone of metals ablated with femtosecond laser pulses," in *Photon Processing in Microelectronics and Photonics II* (A. Pique, K. Sugioka, P. R. Herman, J. Fieret, F. G. Bachmann, J. J. Dubowski, W. Hoving, K. Washio, D. B. Geohegan, F. Traeger, and K. Murakami, eds.), vol. 4977, p. 417, SPIE, jul 2003.
- [261] Y. Hirayama and M. Obara, "Heat-affected zone and ablation rate of copper ablated with femtosecond laser," *Journal of Applied Physics*, vol. 97, p. 064903, mar 2005.
- [262] R. Le Harzic, N. Huot, E. Audouard, C. Jonin, P. Laporte, S. Valette, A. Fraczkiewicz, and R. Fortunier, "Comparison of heat-affected zones due to nanosecond and femtosecond laser pulses using transmission electronic microscopy," *Applied Physics Letters*, vol. 80, pp. 3886–3888, may 2002.
- [263] J. J. Chang, B. E. Warner, E. P. Dragon, and M. W. Martinez, "Precision micromachining with pulsed green lasers," *Journal of Laser Applications*, vol. 10, pp. 285–291, dec 1998.
- [264] J. Hermann, S. Noël, T. E. Itina, E. Axente, and M. E. Povarnitsyn, "Correlation between ablation efficiency and nanoparticle generation during the short-pulse laser ablation of metals," *Laser Physics*, vol. 18, pp. 374–379, apr 2008.
- [265] J. Chung, S. Ko, C. P. C. C. P. C. Grigoropoulos, N. R. N. R. Bieri, C. Dockendorf, and D. Poulikakos, "Microconductors on Polymer by Nanoink Printing and Pulsed Laser Curing," in *ASME 2004 Heat Transfer/Fluids Engineering Summer Conference*, vol. 4, pp. 597–605, ASME, 2004.
- [266] S. H. Ko, J. Chung, Y. Choi, C. P. Grigoropoulos, N. R. Bieri, T.-y. Choi, C. Dockendorf, and D. Poulikakos, "Laser based hybrid inkjet printing of nanoink for flexible electronics," *Photon Processing in Microelectronics and Photonics IV*, vol. 5713, no. April 2005, p. 97, 2005.
- [267] F. J. Romero, A. Salinas-Castillo, A. Rivadeneyra, A. Albrecht, A. Godoy, D. P. Morales, and N. Rodriguez, "In-depth study of laser diode ablation of Kapton polyimide for flexible conductive substrates," *Nanomaterials*, vol. 8, p. 517, jul 2018.
- [268] J. Lawrence, A. B. Patel, and J. G. Brisson, "Thermal conductivity of Kapton HN between 0.5 and 5 K," *Cryogenics*, vol. 40, pp. 203–207, mar 2000.
- [269] A. Roshanghias, "Sinter bonding of inkjet-printed Ag die-attach as an alternative to Ag paste," *Journal of Materials Science: Materials in Electronics*, vol. 29, pp. 11421–11428, jul 2018.
- [270] K. R. Kim and D. F. Farson, "CO<sub>2</sub> laser-plume interaction in materials processing," *Journal of Applied Physics*, vol. 89, no. 1, pp. 681–688, 2001.
- [271] T. E. Itina, J. Hermann, P. Delaporte, and M. Sentis, "Laser-generated plasma plume expansion: Combined continuous-microscopic modeling," *Physical Review E - Statistical Physics, Plasmas, Fluids, and Related Interdisciplinary Topics*, vol. 66, no. 6, p. 12, 2002.

- [272] E. du Trémolet de Lacheisserie, “Magnetostrictive materials,” in *Magnetism*, pp. 213–234, Springer New York, 2005.
- [273] J. Marks and S. Vitolina, “Modelling of magnetostriction of transformer magnetic core for vibration analysis,” *Open Physics*, vol. 15, pp. 803–808, dec 2017.
- [274] A. G. Olabi and A. Grunwald, “Design and application of magnetostrictive materials,” *Materials and Design*, vol. 29, no. 2, pp. 469–483, 2008.
- [275] N. B. Ekreem, A. G. Olabi, T. Prescott, A. Rafferty, and M. S. Hashmi, “An overview of magnetostriction, its use and methods to measure these properties,” *Journal of Materials Processing Technology*, vol. 191, pp. 96–101, aug 2007.
- [276] M. Hott, P. A. Hoehner, and S. F. Reinecke, “Magnetic communication using high-sensitivity magnetic field detectors,” *Sensors (Switzerland)*, vol. 19, no. 15, pp. 1–14, 2019.
- [277] A. A. Vicario, S. M. Shanmuga Ramanan, and S. Arun, “Composites in missiles and launch vehicles,” in *Comprehensive Composite Materials II*, pp. 131–152, Elsevier, jan 2017.
- [278] I. Herszberg, M. K. Bannister, H. C. Li, R. S. Thomson, and C. White, “Structural health monitoring for advanced composite structures,” *ICCM International Conferences on Composite Materials*, pp. 1–15, 2007.
- [279] D. P. Roach and T. M. Rice, “A Quantitative Assessment of Advanced Nondestructive Inspection Techniques for Detecting Flaws in Composite Laminate Aircraft Structures,” p. 348, 2016.
- [280] C. L. Wilson, K. Lonkar, S. Roy, F. Kopsaftopoulos, and F. K. Chang, “Structural health monitoring of composites,” in *Comprehensive Composite Materials II*, pp. 382–407, Elsevier, jan 2017.
- [281] V. Giurgiutiu, *Structural health monitoring of aerospace composites*. Elsevier Inc., sep 2015.
- [282] R. A. Shanks and I. Kong, “General Purpose Elastomers: Structure, Chemistry, Physics and Performance,” pp. 11–45, Springer, Berlin, Heidelberg, 2013.
- [283] A. Christopoulos, E. Hristoforou, and G. Tsamasphyros, “Strain sensing capabilities of iron/epoxy composites,” *Smart Materials and Structures*, vol. 21, p. 085030, aug 2012.
- [284] S. H. Lim, S. R. Kim, S. Y. Kang, J. K. Park, J. T. Nam, and D. Son, “Magnetostrictive properties of polymer-bonded Terfenol-D composites,” *Journal of Magnetism and Magnetic Materials*, vol. 191, pp. 113–121, jan 1999.
- [285] M. Abdouss, T. Farajpour, and M. Derakhshani, “Investigating of polysulfide and epoxy-polysulfide copolymer curing,” *Materialwissenschaft und Werkstofftechnik*, vol. 41, no. 10, pp. 884–888, 2010.

- [286] G. McKerricher, J. G. Perez, and A. Shamim, "Fully inkjet printed RF inductors and capacitors using polymer dielectric and silver conductive ink with through vias," *IEEE Transactions on Electron Devices*, vol. 62, no. 3, pp. 1002–1009, 2015.
- [287] J. D. S. Vincent, M. Rodrigues, Z. Leong, and N. A. Morley, "Design and development of magnetostrictive actuators and sensors for structural health monitoring," *Sensors (Switzerland)*, vol. 20, p. 711, jan 2020.
- [288] J. Popplewell and L. Sakhnini, "The dependence of the physical and magnetic properties of magnetic fluids on particle size," *Journal of Magnetism and Magnetic Materials*, vol. 149, pp. 72–78, aug 1995.
- [289] Q. Li, C. W. Kartikowati, S. Horie, T. Ogi, T. Iwaki, and K. Okuyama, "Correlation between particle size/domain structure and magnetic properties of highly crystalline Fe<sub>3</sub>O<sub>4</sub> nanoparticles," *Scientific Reports*, vol. 7, no. 1, pp. 1–4, 2017.
- [290] Z. Laherisheth, K. Parekh, and R. V. Upadhyay, "Role of inter-particle force between micro and nano magnetic particles on the stability of magnetorheological fluid," *AIP Advances*, vol. 7, no. 2, 2017.
- [291] R. B. Kamble, V. Varade, K. P. Ramesh, and V. Prasad, "Domain size correlated magnetic properties and electrical impedance of size dependent nickel ferrite nanoparticles," *AIP Advances*, vol. 5, p. 017119, jan 2015.
- [292] H. S. Göktürk, T. J. Fiske, and D. M. Kalyon, "Effects of particle shape and size distributions on the electrical and magnetic properties of nickel/polyethylene composites," *Journal of Applied Polymer Science*, vol. 50, pp. 1891–1901, dec 1993.
- [293] L. Zhaoyuan, L. Chan, N. Walters, J. Clarke, W. Holmes, and S. Hayes, "Structural health monitoring using magnetostrictive sensors," *2018 IEEE International Magnetic Conference, INTERMAG 2018*, pp. 1–5, 2018.
- [294] L. B. Valdes, "Resistivity Measurements on Germanium for Transistors," *Proceedings of the IRE*, vol. 42, no. 2, pp. 420–427, 1954.
- [295] F. M. Smits, "Measurement of Sheet Resistivities with the Four-Point Probe," *Bell System Technical Journal*, vol. 37, pp. 711–718, may 1958.
- [296] L. Swartzendruber, "Four-point probe measurement of non-uniformities in semiconductor sheet resistivity," *Solid-State Electronics*, vol. 7, no. 6, pp. 413–422, 1964.

# Appendix A

## Chapter 3 Supporting Information

### A.1 Python script for pulse overlap % calculation

```
C3_Overlap%.py — C:\Users\viman\Desktop\py4e — Atom
File Edit View Selection Find Packages Help
C3_Overlap%.py
1 print("Input xy coordinate of the first pulse:")
2 x1, y1 = map(float, input().split())
3 print("Input coordinate of the second pulse:")
4 x2, y2 = map(float, input().split())
5
6 # Specify the dimensions of the rectangular Laser beam
7 h = 10
8 w = 200
9
10 area_beam = h * w
11
12 from shapely.geometry import box
13 rect1 = box(x1, y1, x1+w, y1+h)
14 rect2 = box(x2, y2, x2+w, y2+h)
15 rect_list = [rect1, rect2]
16
17 # Find total area of two overlapping beams
18 # Return total Area of two overlap beams
19
20 def overlappingArea(l1, r1, l2, r2):
21     x = 0
22     y = 1
23
24 # The length of intersecting beam starts from
25 # max(l1[x], l2[x]) of x-coordinate, and ends at
26 # min(r1[x], r2[x]) of x-coordinate.
27 # By subtracting the end from the start
28 # we get the required lengths.
29
30 areaI = abs((min(r1[x], r2[x]) - max(l1[x], l2[x])) *
31            (min(r1[y], r2[y]) - max(l1[y], l2[y])))
32
33 return (areaI)
```

```

C3_Overlap%.py — C:\Users\viman\Desktop\py4e — Atom
File Edit View Selection Find Packages Help
C3_Overlap%.py
33     return (areal)
34
35 # Driver's Code
36 l1 = [x1, y1]
37 r1 = [x1+w, y1+h]
38 l2 = [x2, y2]
39 r2 = [x2+w, y2+h]
40
41 olperc = 1 - abs((overlappingArea(l1, r1, l2, r2) - area_beam) / area_beam)
42
43 # Output
44 print("Overlapped beam area = ", overlappingArea(l1, r1, l2, r2))
45 print("Overlap percentage = ", "{:.1%}".format(olperc))
46
47 # To find the intersection of the beams
48 for rect in rect_list[1:]:
49     rectI = rect1.intersection(rect)
50 intersection = rectI
51
52 from matplotlib import pyplot as plt
53 from matplotlib.collections import PatchCollection
54 from matplotlib.patches import Polygon
55
56 # plot the rectangles before and after merging
57 patches = PatchCollection([Polygon(a.exterior) for a in rect_list],
58     + facecolor="blue", linewidth=.5, alpha=.5)
59 intersect_patch = PatchCollection([Polygon(intersection.exterior)],
60     + facecolor="crimson", linewidth=.5, alpha=.5)
61
62 # make figure
63 fig, ax = plt.subplots(1,2, subplot_kw=dict(aspect=5))
64 ax[0].add_collection(patches, autolim=True)
65 ax[0].autoscale_view()
66 ax[0].set_title("Overlapped beams")
67 ax[1].add_collection(intersect_patch, autolim=True)
68 ax[1].set_title("Intersected area of beams")
69 ax[1].set_xlim(ax[0].get_xlim())
70 ax[1].set_ylim(ax[0].get_ylim())
71 plt.show()
72
C3_Overlap%.py 70:1 CRLF UTF-8 Python GitHub Git (0)

```

```

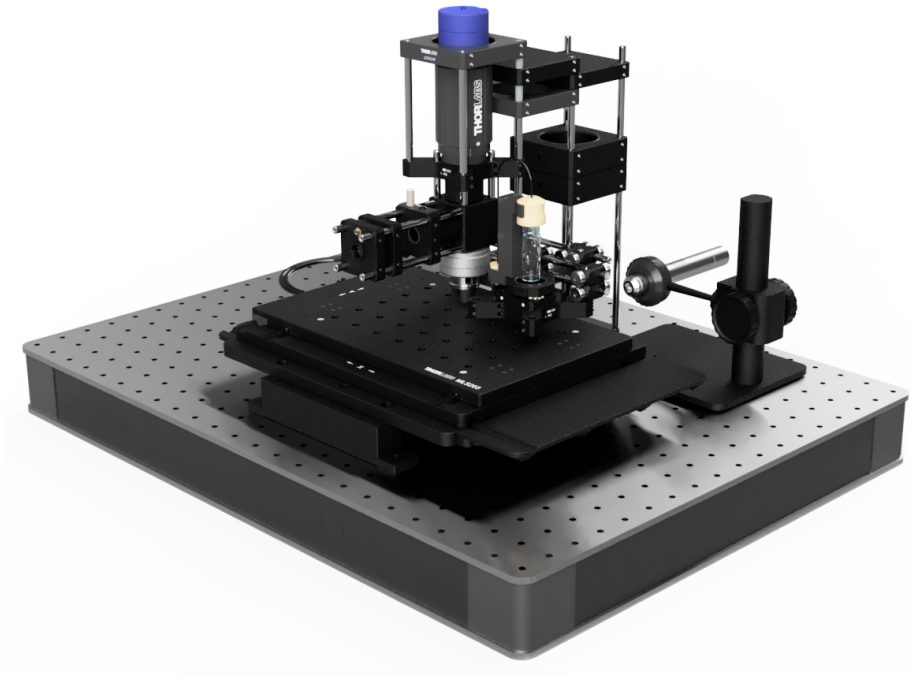
Command Prompt - "C3_Overlap%.py"
Microsoft Windows [Version 10.0.19042.572]
(c) 2020 Microsoft Corporation. All rights reserved.

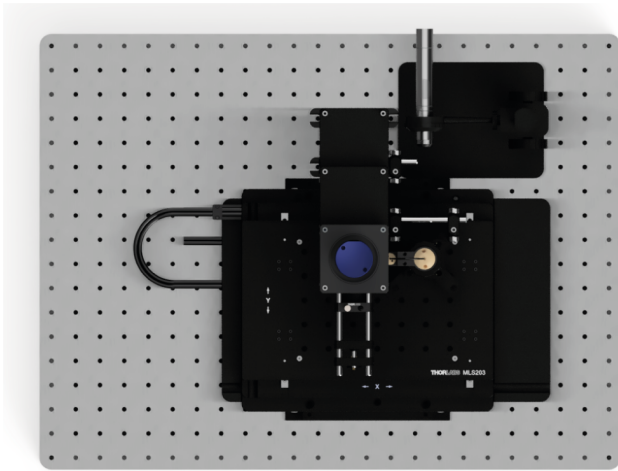
C:\Users\viman>cd Desktop\py4e

C:\Users\viman\Desktop\py4e>"C3_Overlap%.py"
Input xy coordinate of the first pulse:
100 100
Input coordinate of the second pulse:
270 100
Overlapped beam area = 300.0
Overlap percentage = 15.0%

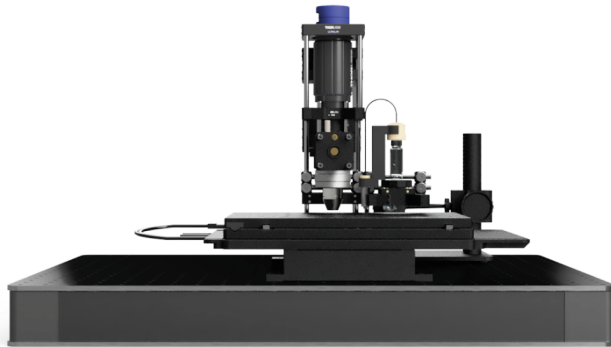
```

## A.2 Pulsed Laser Sintering station

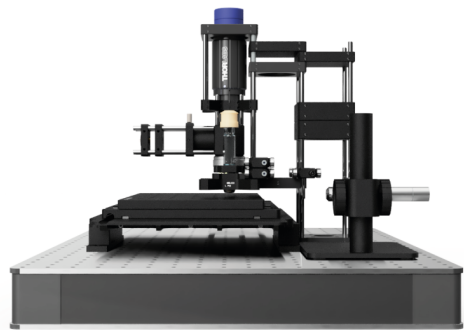




Top view

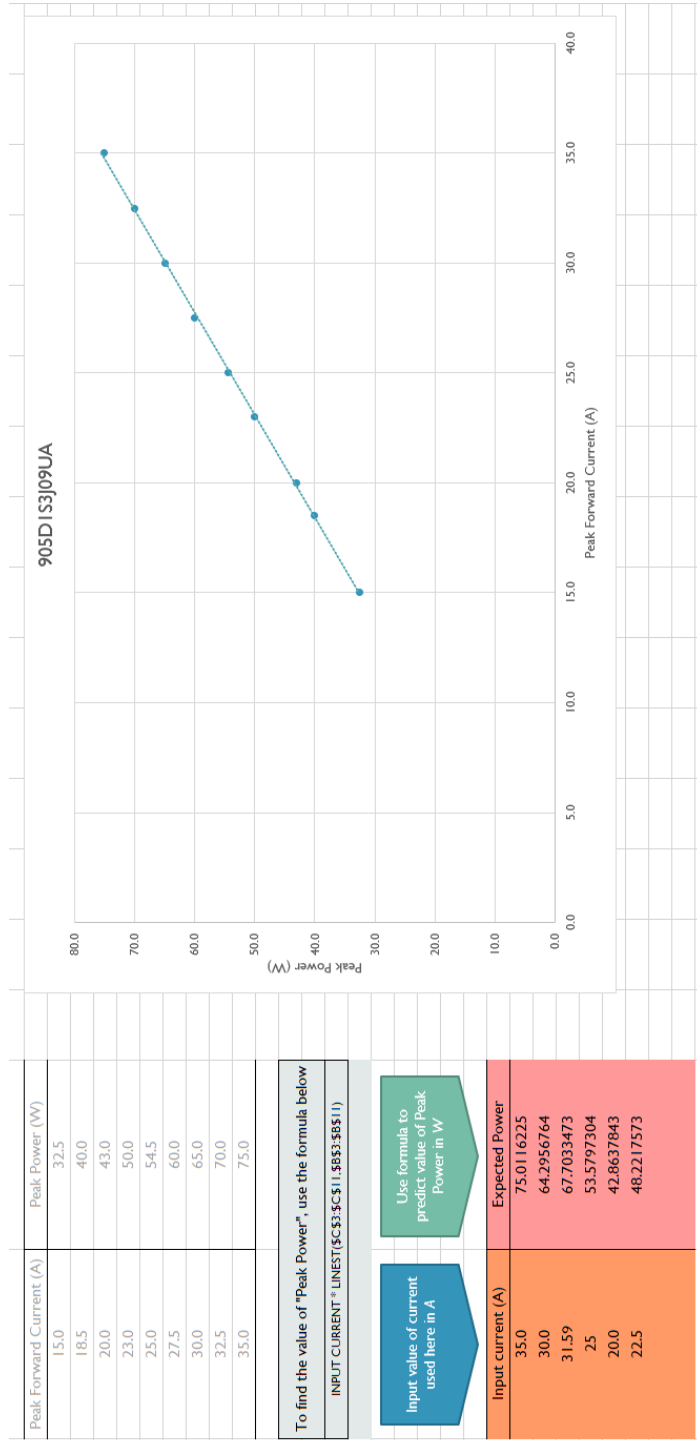


Front view

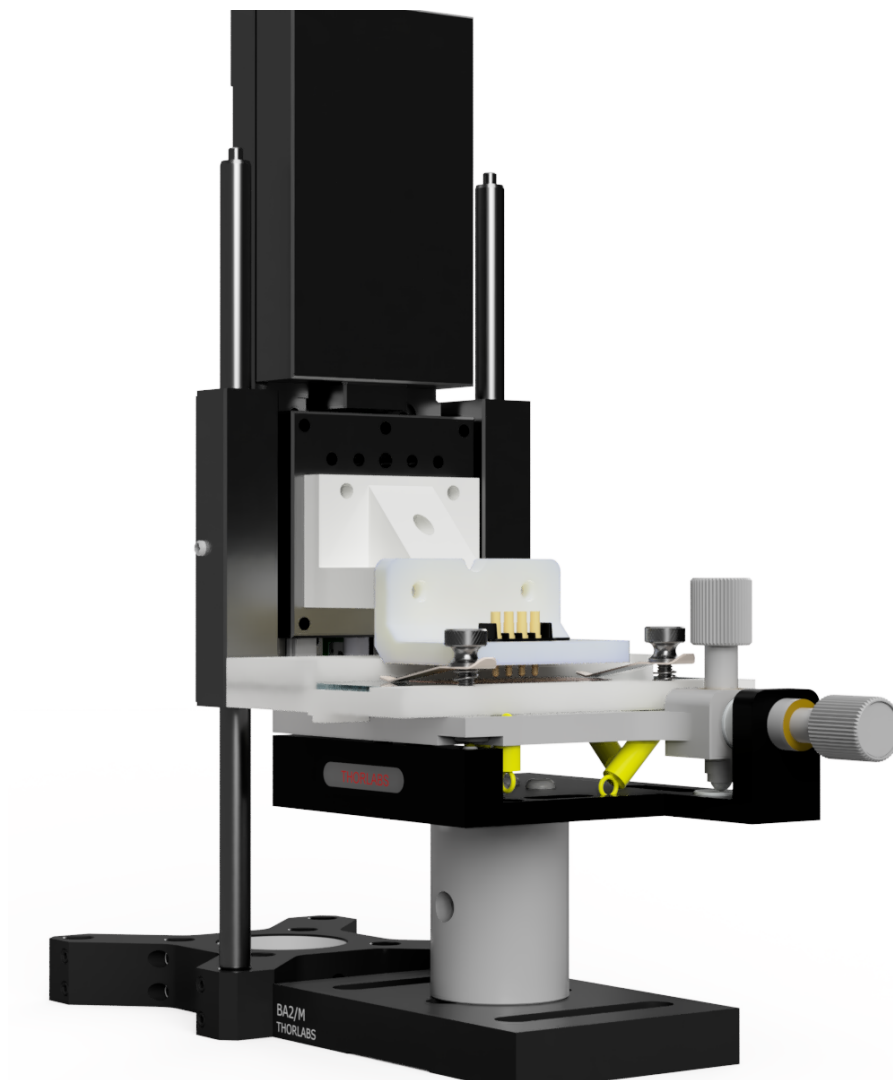


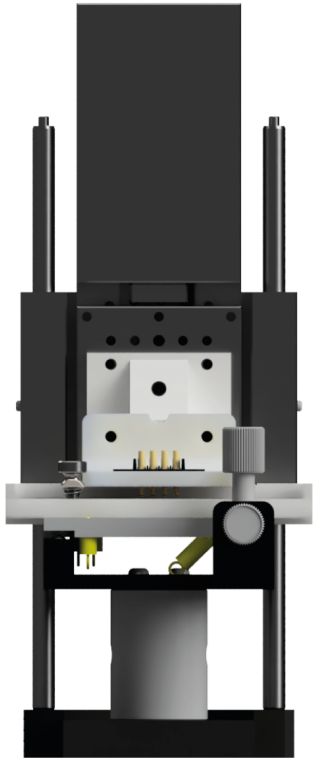
Side view

### A.3 Optical Output Power vs. Current - 905D1S3J09UA

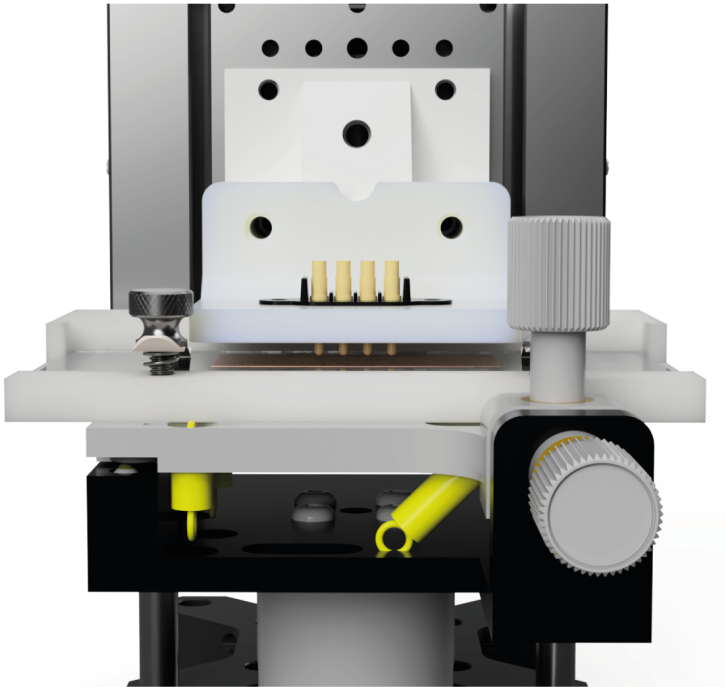


## A.4 Four Point Probe test station

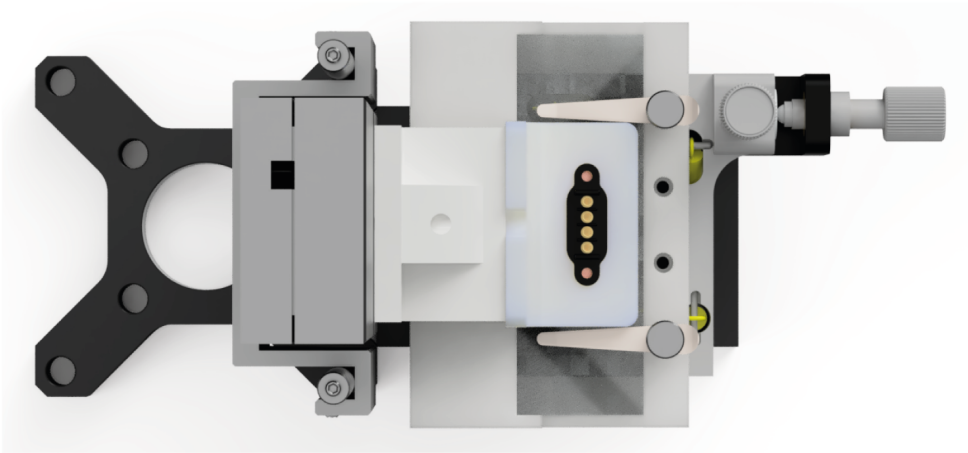




Front view

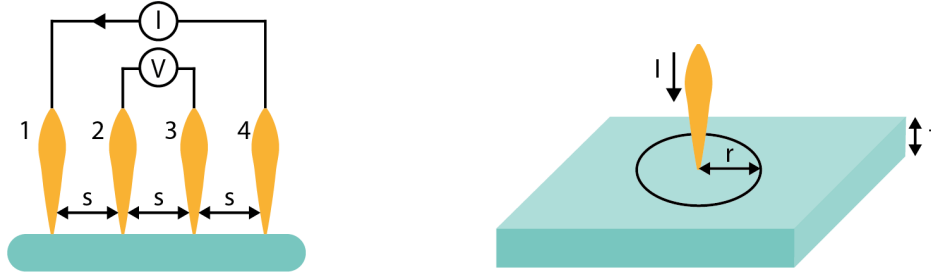


Enlarged front view



Top view

## A.5 Sheet Resistance formula derivation



The following derivation is extracted from references [294–296].

Assuming a sharp probe contacting and injecting current into a thin film of thickness,  $t$ . In this case the current travels away from the probe through the material in short cylindrical shells of equipotential, each having a current density,  $J$ , of:

$$J = \frac{I}{2\pi r t} \quad (\text{A.1})$$

By applying Ohm's law ( $E = \rho J$ ) with the electric field across each shell equal to the voltage drop over the shell thickness, and with the thickness of the shell tending towards zero, the electric field across each shell is:

$$\frac{dV}{dr} = -\rho_s \left( \frac{I}{2\pi r t} \right) \quad (\text{A.2})$$

As the sheet resistivity,  $\rho_s$ , has already been defined as the sheet resistance,  $R_s$ , multiplied by the thickness of the material, the previous equation can be rearranged as:

$$\frac{dV}{dr} = -R_s \left( \frac{I}{2\pi r} \right) \quad (\text{A.3})$$

This can be integrated between  $r$  and  $r'$  to obtain:

$$V - V' = \frac{IR_s}{2\pi} \left( \ln \frac{1}{r} - \ln \frac{1}{r'} \right) = \frac{IR_s}{2\pi} (\ln r' - \ln r) \quad (\text{A.4})$$

As the four-point probe measures the voltage difference between different points, the voltage will never tend to zero. Additionally, we assume the thin film thickness,  $t$ , is negligible compared to the probe spacing,  $s$ . As the current is injected in probe 1 and recovered in probe 4, the equation can be resolved into:

$$V = \frac{IR_s}{2\pi} (\ln r_4 - \ln r_1) \quad (\text{A.5})$$

And the voltages measured at probes 2 and 3 are:

$$V_2 = \frac{IR_s}{2\pi} (\ln 2s - \ln s) \quad (\text{A.6})$$

$$V_3 = \frac{IR_s}{2\pi} (\ln s - \ln 2s) \quad (\text{A.7})$$

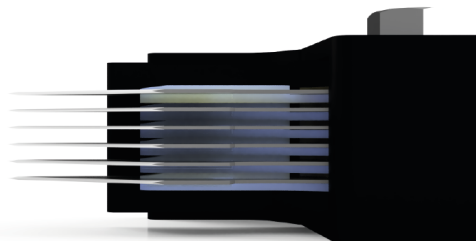
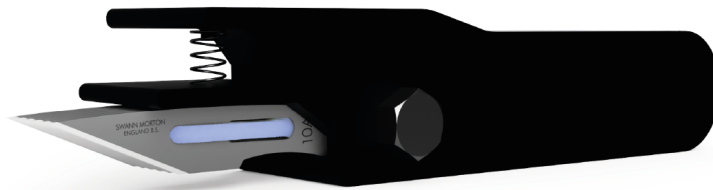
Hence, the change in voltage,  $\Delta V$ , is:

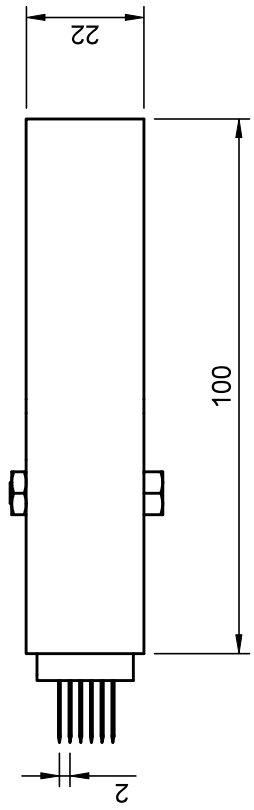
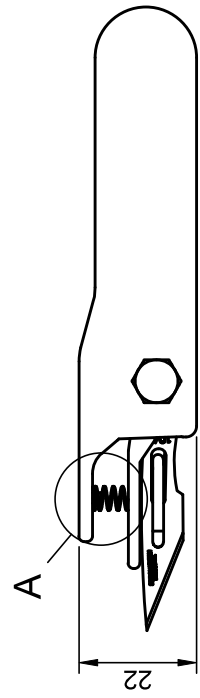
$$\Delta V = V_2 - V_3 = \frac{IR_s}{2\pi} (2 \ln 2s - 2 \ln s) = \frac{IR_s}{2\pi} \ln 2 \quad (\text{A.8})$$

Which can be rearranged for  $R_s$  as:

$$R_s = \frac{\pi}{\ln 2} \frac{\Delta V}{I} = 4.53236 \frac{\Delta V}{I} \quad (\text{A.9})$$

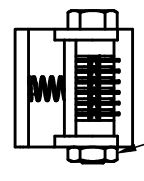
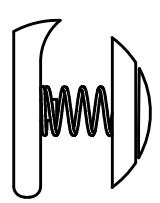
## A.6 Cross-cutter Assembly and Technical Drawing



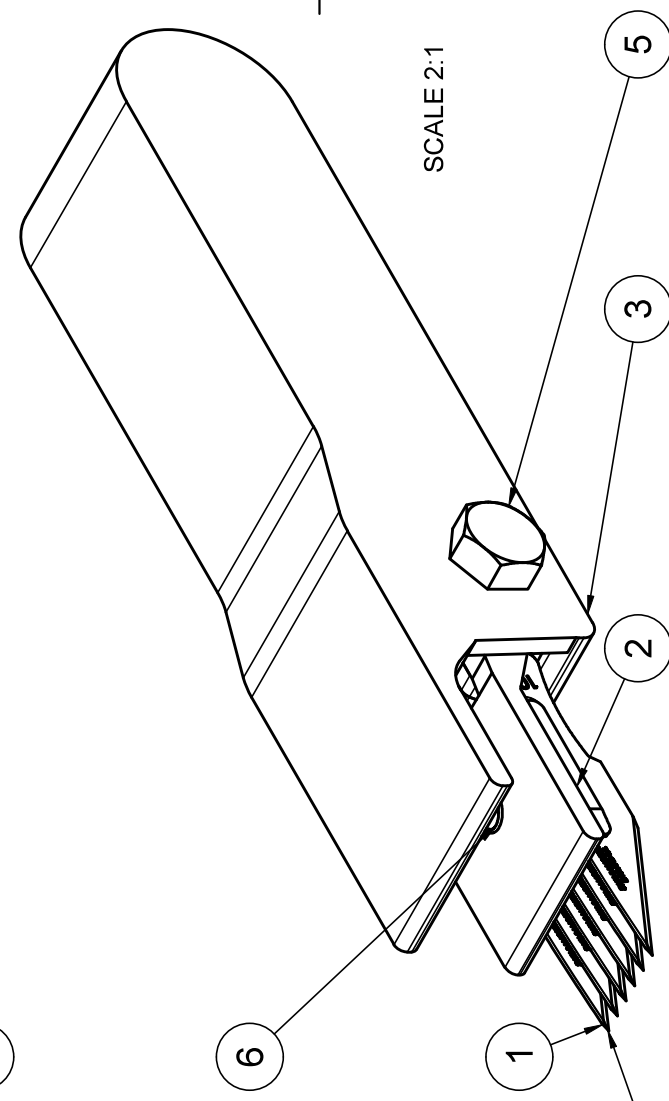


Detailed view of tension spring mechanism

A (2:1)

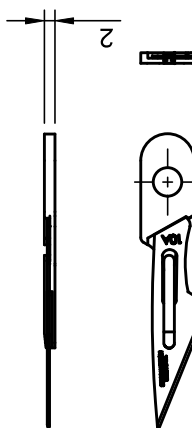


4



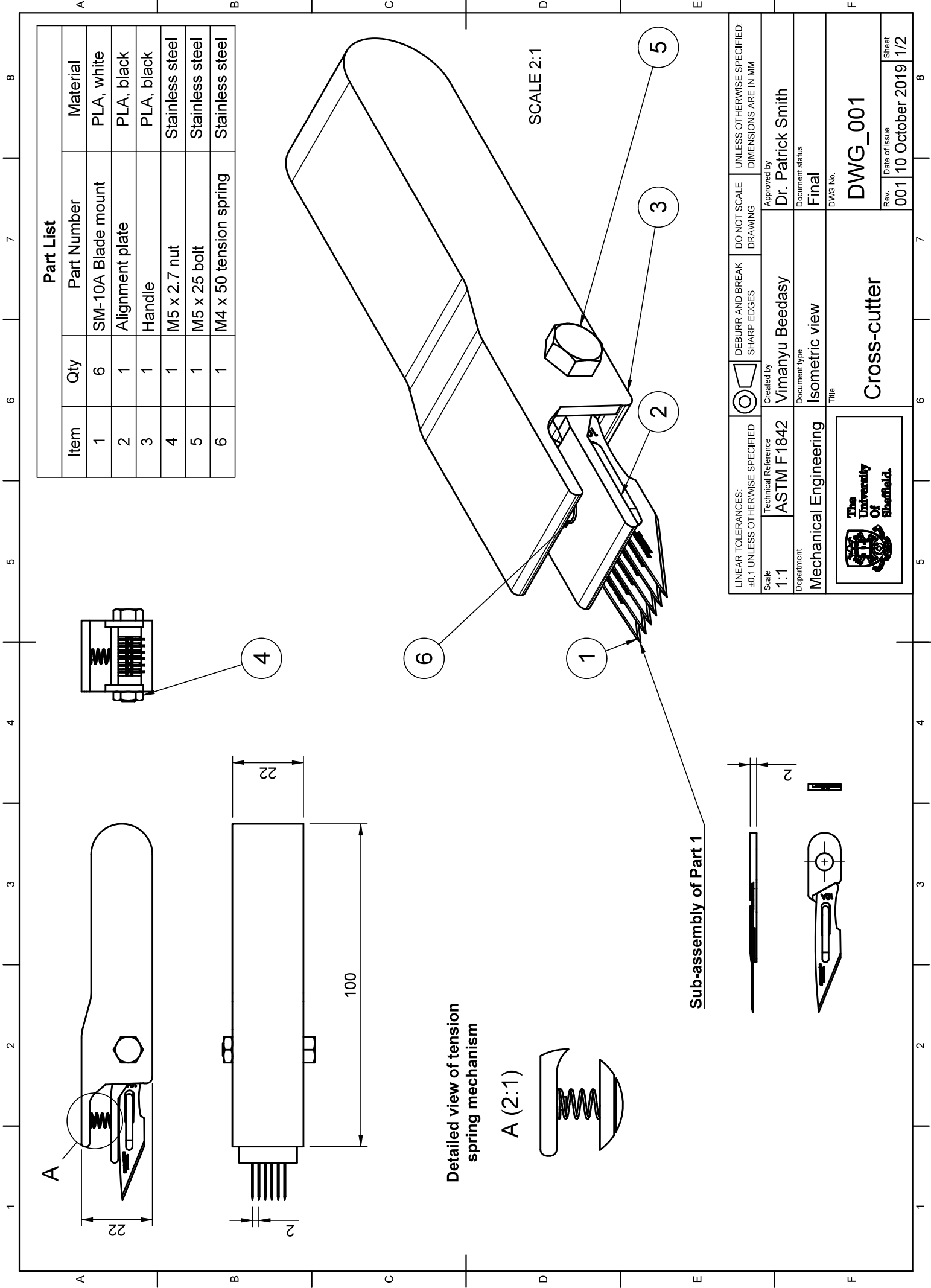
SCALE 2:1

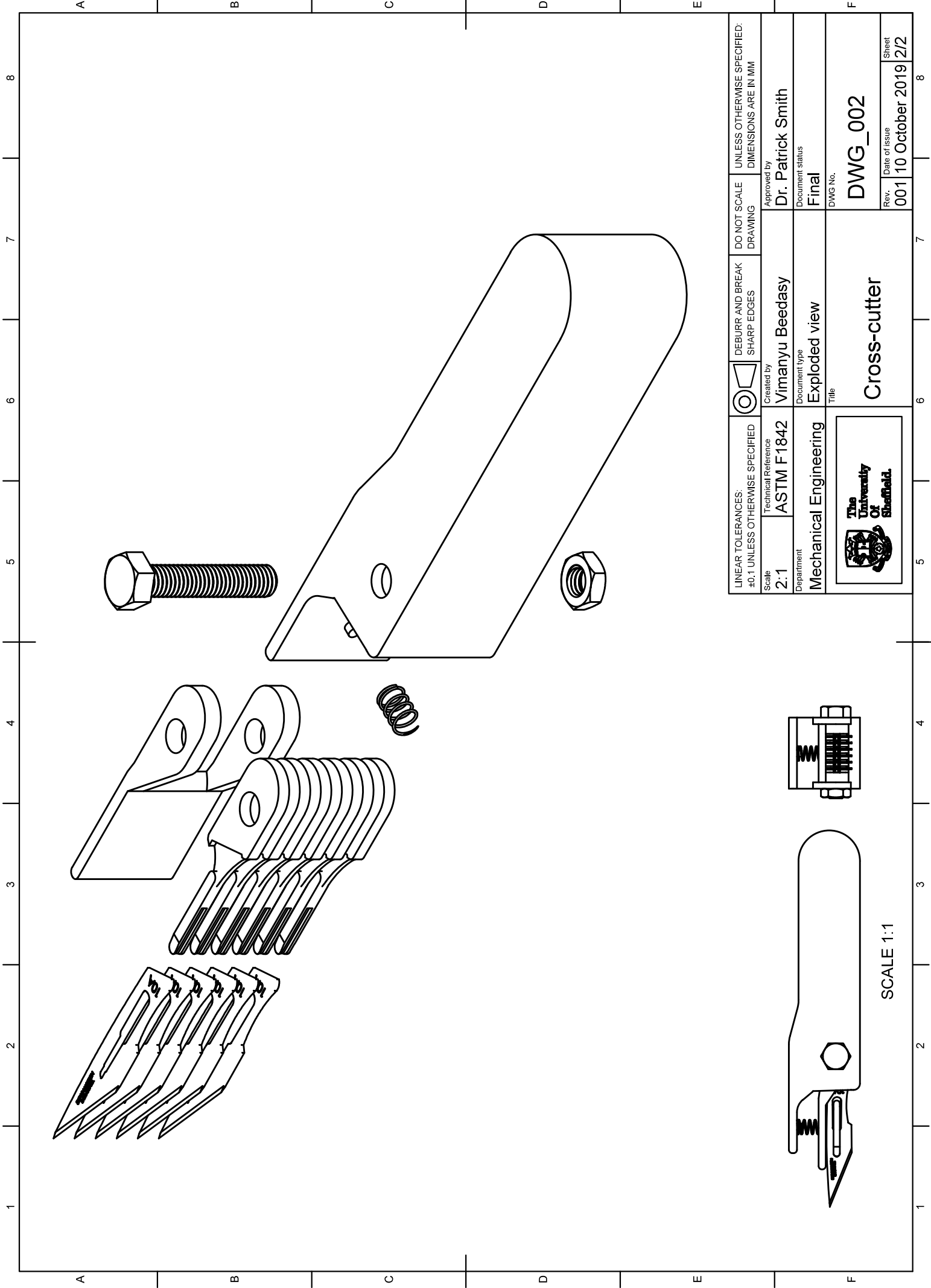
Sub-assembly of Part 1



Part List		
Item	Qty	Material
1	6	SM-10A Blade mount
2	1	Alignment plate
3	1	Handle
4	1	M5 x 2.7 nut
5	1	M5 x 25 bolt
6	1	M4 x 50 tension spring

LINEAR TOLERANCES: ±0.1 UNLESS OTHERWISE SPECIFIED	DEBURR AND BREAK SHARP EDGES	DO NOT SCALE DRAWING	UNLESS OTHERWISE SPECIFIED: DIMENSIONS ARE IN MM
Scale 1:1	Created by Vimanyu Beedasy	Approved by Dr. Patrick Smith	
Department Mechanical Engineering	Document type Isometric view	Document status Final	
		DWG No. DWG_001	
Title Cross-cutter		Rev.	Sheet
		001	1/2





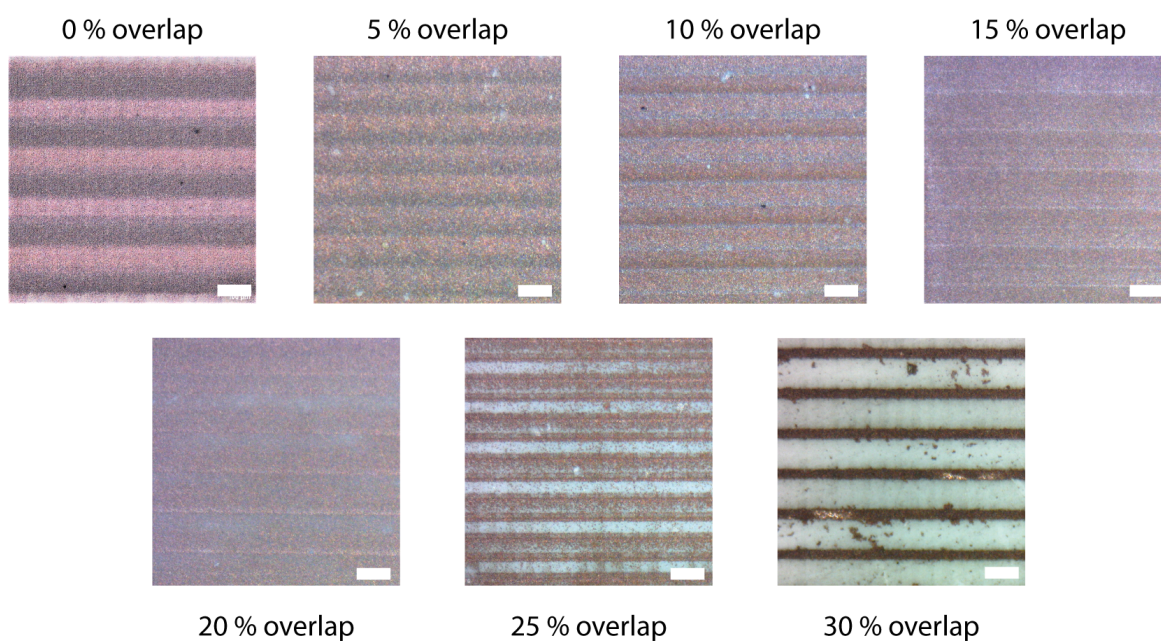
SCALE 1:1

LINEAR TOLERANCES: ±0.1 UNLESS OTHERWISE SPECIFIED	DO NOT SCALE DRAWING	UNLESS OTHERWISE SPECIFIED: DIMENSIONS ARE IN MM
DEBURR AND BREAK SHARP EDGES	Created by <b>Vimanyu Beedasy</b>	Approved by <b>Dr. Patrick Smith</b>
Technical Reference <b>ASTM F1842</b>	Document type <b>Exploded view</b>	Document status <b>Final</b>
Scale <b>2:1</b>	Department <b>Mechanical Engineering</b>	DWG No. <b>DWG_002</b>
		
<b>Cross-cutter</b>		
Rev.	Date of issue	Sheet
001	10 October 2019	2/2

# Appendix B

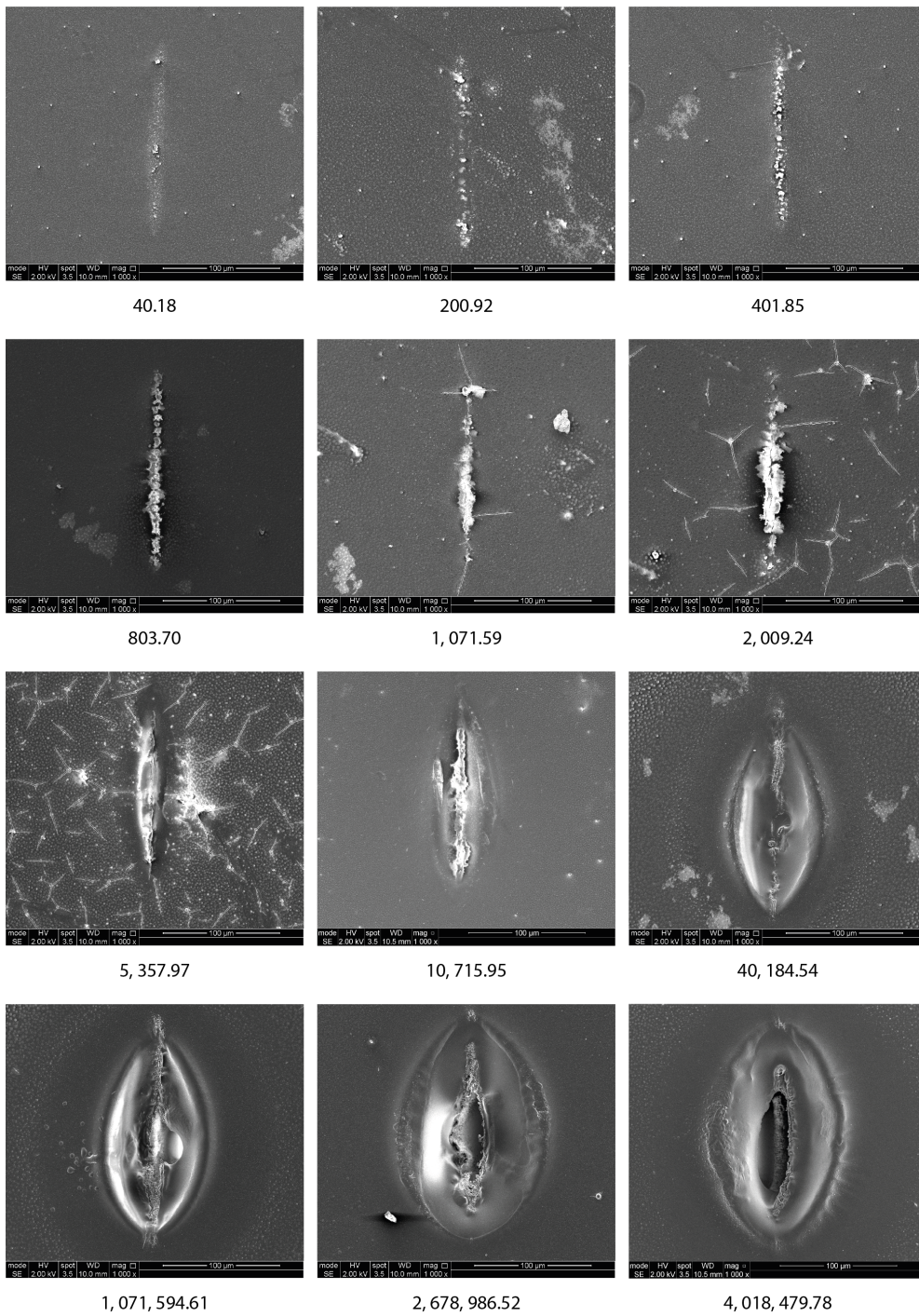
## Chapter 5 Supporting Information

### B.1 Pulse overlap variation analysis

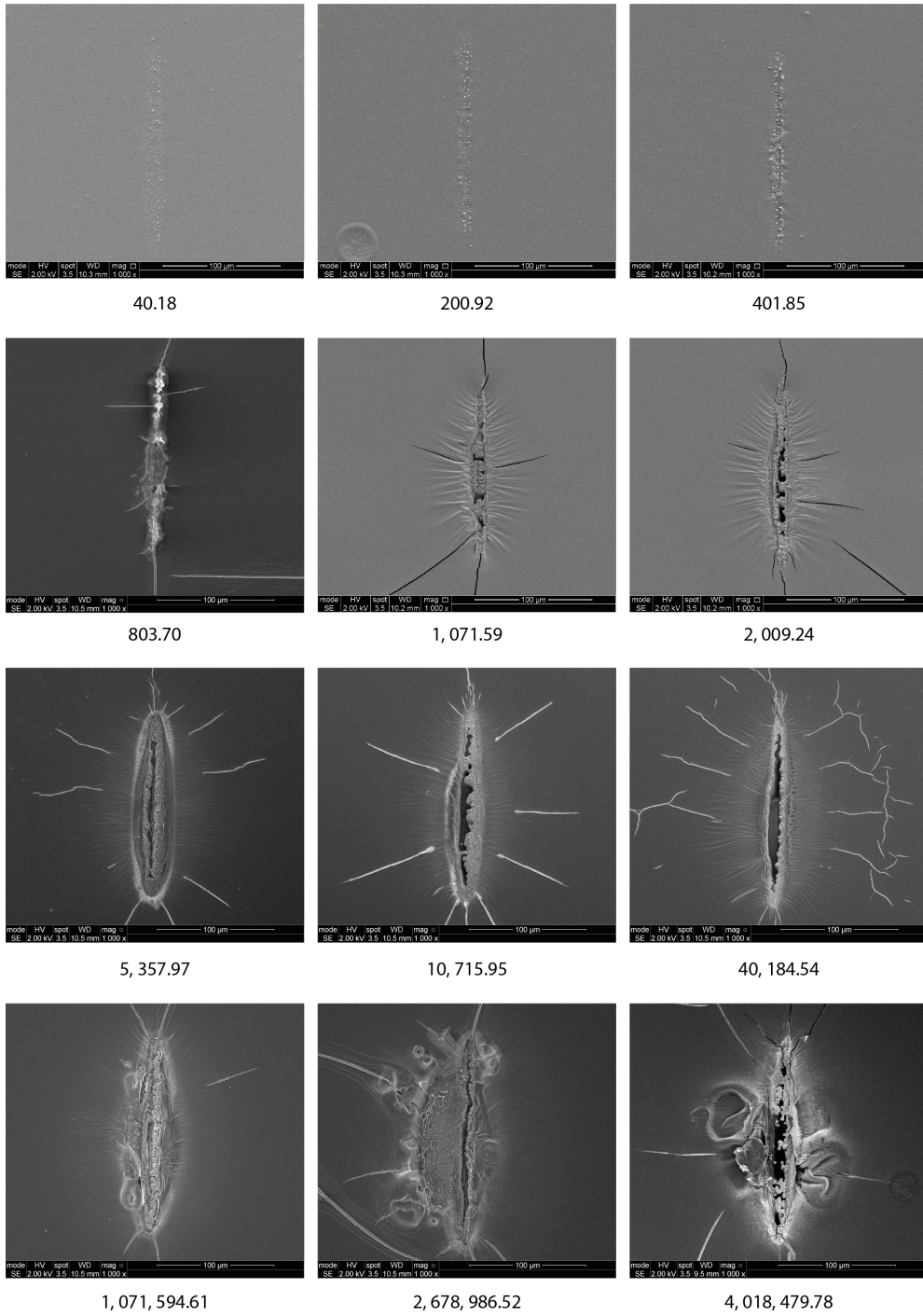


## B.2 Heat Affected Zone RAW SEM data

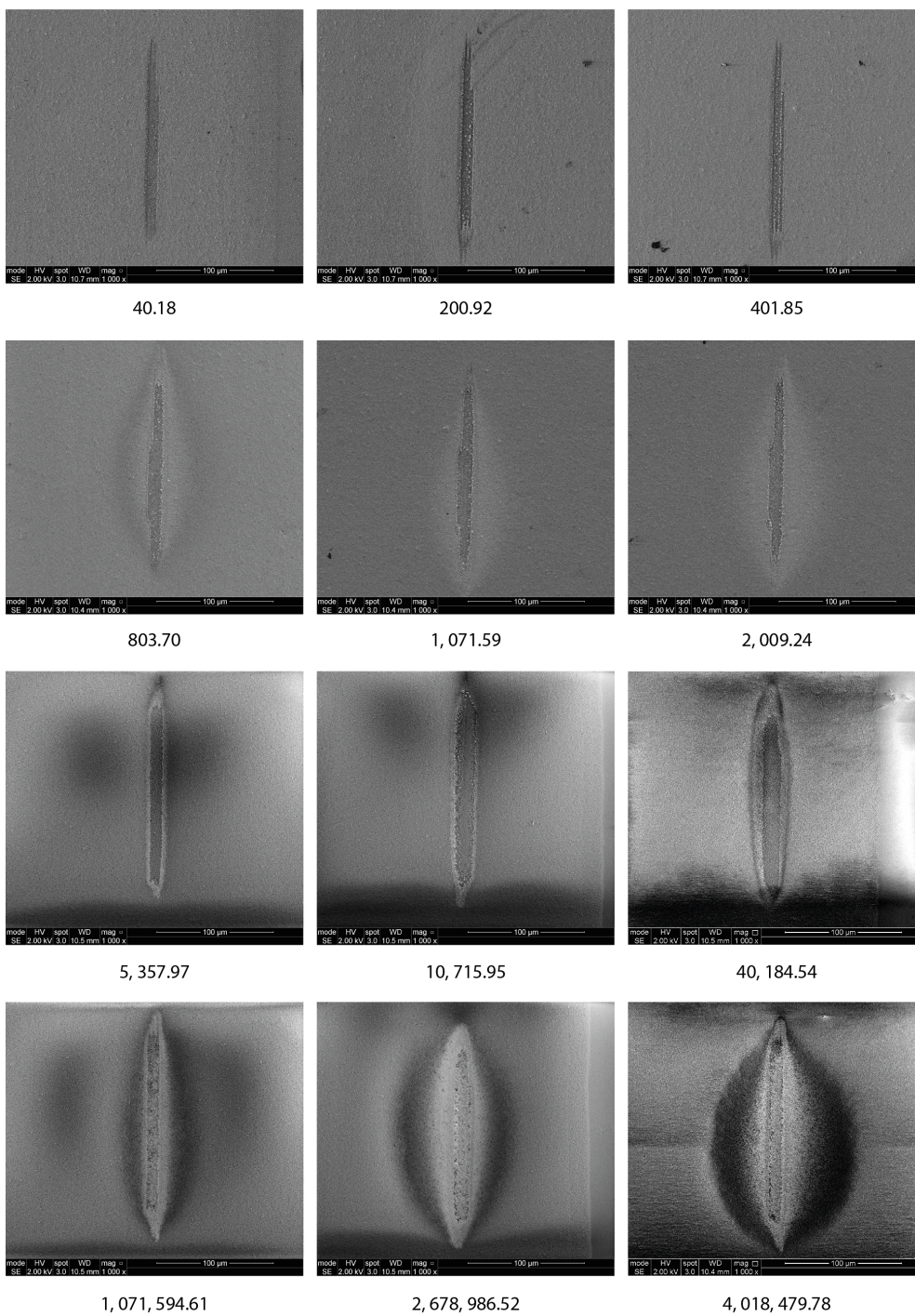
PET film



Kapton PI film



## Paper



# Appendix C

## Chapter 6 Supporting Information

### C.1 Summary of the fitted values for the change of inductance plots of each coil

<i>Sample</i>		<i>Monofilar_5n</i>	<i>Monofilar_10n</i>	<i>Bifilar_5/5</i>	<i>Hand-wound</i>	<i>AMR</i>
<i>FeSiB ribbon</i>	<i>m</i>	-1000312	-231956	-1572641	-0.5644	-0.21402
	<i>c</i>	8.86965 x10 <sup>8</sup>	1.08934 x10 <sup>9</sup>	1.43129 x10 <sup>9</sup>	359.58	165.574
	<i>R</i> <sup>2</sup>	0.98494	0.89638	0.96826	0.95973	0.90172
<i>Ni&lt;80</i>	<i>m</i>	-39000	-2008886.921	-154886.523	0.04888	-0.02875
	<i>c</i>	8.808 x10 <sup>8</sup>	1.58618 x10 <sup>9</sup>	1.00589 x10 <sup>9</sup>	-0.736	20.41569
	<i>R</i> <sup>2</sup>	0.01214	0.83112	0.26504	0.56237	0.50018
<i>Fe&lt;80</i>	<i>m</i>	341000	-94.42237	-1288837.81	-0.0074	-0.03294
	<i>c</i>	6.908 x10 <sup>8</sup>	129207	1.32657 x10 <sup>9</sup>	47.8	31.7333
	<i>R</i> <sup>2</sup>	0.54060	0.93855	0.83035	0.03053	0.13492
<i>Ni:80-200</i>	<i>m</i>	-20000	-61.93039	279311.69643	-0.0838	-0.00327
	<i>c</i>	7.34 x10 <sup>8</sup>	105711	5.56164 x10 <sup>8</sup>	104.83	18.67643
	<i>R</i> <sup>2</sup>	0.00275	0.97033	0.50522	0.81222	0.00416
<i>Fe:80-200</i>	<i>m</i>	-460000	-43.19395	35176.15583	0.02928	-0.14459
	<i>c</i>	1.327 x10 <sup>8</sup>	101798	7.22559 x10 <sup>8</sup>	93.644	90.14672
	<i>R</i> <sup>2</sup>	0.96182	0.99597	0.02186	0.18081	0.65817

## C.2 Dimensions of the three inkjet-printed copper coils

